UNIVERSITÀ DI PARMA

UNIVERSITA' DEGLI STUDI DI PARMA

Dottorato di Ricerca in Ingegneria Industriale

CICLO XXXV

Heat Pipes: Novel Experimental Insights into the Phenomenological Understanding

Coordinatore:
Chiar.mo Prof. Ing. Gianni Royer Carfagni

Tutore:
Chiar.mo Prof. Ing. Fabio Bozzoli

Dottorando: Luca Pagliarini

Anni Accademici 2019/2020 – 2021/2022

“What we know is a drop, what we don't know is an ocean.”

Isaac Newton

Dedication

Three years of PhD have passed in the blink of an eye, yet leaving behind vivid and indissoluble memories that I will carry with me forever.

Looking back, I understand how much I have grown both professionally and humanly during this tough journey, though full of satisfaction - because achievements, without challenges, would be meaningless. Now that I am about to write the last pages of my report, pouring tears of pain and joy, I finally realize the effort I devoted to this boundless project, under whose heaviness I would have surely given up if I hadn't received selfless support from my parents, Irene and Giorgio, my sister Ilaria and my nephews Diego and Caterina, my close friends, including Gallo, Babbe and Edo, and my colleagues. My supervisor, Professor Fabio Bozzoli, has introduced me with profound intellect and remarkable patience to the impervious path of research. Professor Sara Rainieri has genuinely helped me in dealing with any task. I would have been lost in the academic jungle without the light-heartedly aid of Matteo Malavasi, Doctor Naoko Iwata, Doctor Luca Cattani and Doctor Pamela Vocale.

During the PhD course, I have been given the priceless opportunity to travel around Europe, cooperating with other research groups and experiencing new realities - who explores the world, discovers himself. The energetic commitment and established experience of Professor Marco Marengo has given me a strong basis for tackling complex issues. The outstanding skills of Professor Vincent Ayel and Doctor Maksym Slobodeniuk have guided me during hard experimentations. Professor Sauro Filippeschi and Professor Mauro Mameli have led me through the steep way of professional self-consciousness.

An important chapter of my life is coming to an end: every people I have met, every face I have smiled to during the last three years, they will always hold a special place in my heart. And - since I don't often bet on myself - I sincerely thank each one of them from the bottom of my soul for having returned the smile and believed in me!

Abstract

The present dissertation reports the most meaningful outcomes referred to global and local heat transfer investigations on different Heat Pipe devices, either wicked or wickless. The experimental campaigns have been carried out in the framework of the ESA MAP project TOPDESS (grant 4000128640/19/NL/PG/pt) through fruitful collaborations between the University of Parma and the University of Poitiers (France), the University of Pisa (Italy), the University of Brighton (United Kingdom) and the Federal University of Santa Catarina (Brazil).

The newly proposed post-processing methods, which allow the estimation of thermofluidic interactions due to inner convection, are based on infrared acquisitions on the outer wall of the investigated systems. The non-intrusive feature of such techniques strongly enhances their applicative appeal in terms of experimentation since no substantial alterations of the original layouts are required. By a systematic data reduction of the evaluated quantities, which also relies on statistical approaches, interesting thermo-fluid dynamic patterns have been identified. Despite the studied devices present different geometries and thermal performances, their local behaviours have been proven to be linked by a common thread.

The provided remarks are of crucial importance for the phenomenological understanding of two-phase passive heat transfer devices working under highly transient conditions. Moreover, they set the basis for the improvement and proper validation of existing numerical models, opening to reliable designing approaches and consequent large-scale applications of modern and still immature thermal management solutions. Future works are needed to fully characterize the local heat transfer in a wide range of devices and working conditions.

KEYWORDS: Pulsating Heat Pipes; Loop Heat Pipes; Infrared Thermography; Inverse Heat Conduction Problem; Working Modes; Fluid Oscillation Frequency; Flow Modes.

Table of contents

Part I: Two-phase passive heat transfer devices and pulsating heat pipes phenomenology

Chapter 1 Traditional two-phase passive heat transfer devices and modern passive heat transfer techniques

1.1 Introduction

The electrical energy demand for thermal management solutions by active two-phase heat transfer devices is more and more increasing especially in the field of electronic components, where a continuous miniaturization process results in higher power densities to be dissipated [1]. This is valid not only on ground, but also for space applications, where the design of cooling devices is even more challenging due to the extreme operative conditions. Recent studies showed that the electrical energy required for electronic thermal management in industries and data centres contributes to a large amount with respect to the total (up to 50%). Indeed, nowadays heat dissipation is achieved by means of forced convection liquid loops or fans, which require a large amount of energy to operate [2]. For this reason, two-phase passive systems, in which phase-change phenomena can improve the overall heat exchange without the aid of electric devices or pumps to sustain the convective motion, are becoming useful tools to dissipate high heat power inputs, and they need to be deeply investigated.

In the present Chapter, the working principles of two-phase passive heat transfer devices are described. An excursus of typical passive heat transfer systems is provided, along with basic concepts regarding the understanding of their operational behaviour. In particular, wicked and wickless devices are presented to give an overview of some viable thermal management solutions in terms of advantages and disadvantages.

1.2 Physics underlying two-phase passive heat transfer

In general, the operation of modern passive heat transfer devices is based on the combination of three physical phenomena: phase-change, gravity and capillarity.

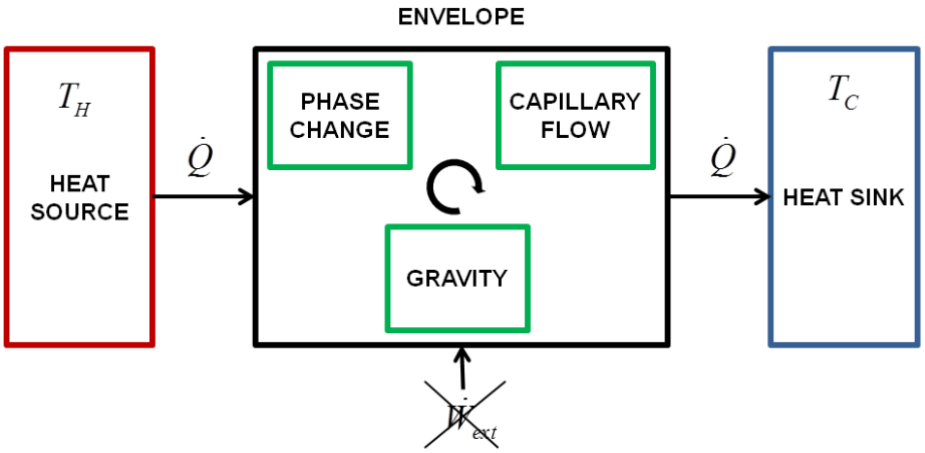

Figure 1.1: Schematic of phenomena governing two-phase passive heat transfer systems.

In Figure 1.1, a schematic of such phenomena is presented: heat transfer is achieved without providing electrical energy to the system. This general scheme can be adapted to different devices, depending on the phenomena specifically occurring: in some passive systems, capillary forces are negligible, while, in others, effects of the gravity field might be less important. Boundary conditions (heat source/sink) always result in phase-change phenomena, which promote heat transfer and consequent heat dissipation. In other words, heat transport is due to the heating power provided to the system; capillary and gravity forces additionally play a significant role in the achievement of an adequate pumping force for the continuous working fluid motion, i.e., continuous device operation. Compared to single-phase systems, two-phase systems have the additional advantage of improved heat transfer capability due to phase change.

Depending on geometry and physical phenomena, different two-phase passive heat transfer devices can be identified, including:

- ThermoSyphons (TSs);
- Heat Pipes (HPs);
- Loop Heat Pipes (LHPs);
- Pulsating Heat Pipes (PHPs).

1.3 Thermosyphons

TSs are the first two-phase passive devices ever proposed; their conceptualization and application date back to the XIX century. These systems are intrinsically based on the effect of gravity, while capillary forces are negligible (tubes with high inner diameters). Heat provided at the lowest end promotes evaporation of liquid laying at the bottom of the tube due to gravity; the resulting vapour crosses the tube by buoyancy from bottom to top, where it condenses. Condensate eventually sticks to

the inner wall, and liquid film is pushed back to the bottom by gravity. The TS operation is depicted in Figure 1.2 [3].

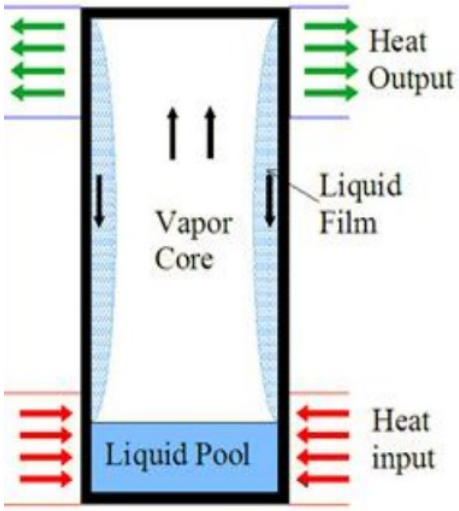

Figure 1.2: TS working principle [3].

Since the cold liquid backflow, which is crucial for preventing dry-out of the heated area, depends on the gravity field, the device operates only when heat is provided at the lowest end of the tube, i.e., in vertical orientation and ground conditions. To solve this operative limit, in the last decades, particular attention has been given to the design of TSs layouts able to operate against gravity, such as reverse TSs [4]. In other modern devices (e.g., HPs and LHPs) such limitation is instead overcome by attaching a wick structure on the tube inner surface to promote liquid flow from the heat sink to the heat source by capillarity through the porous structure rather than by gravity.

1.4 Heat pipes

Similarly to other passive heat transfer devices, heat transfer in HPs occur over a relatively long distance between a heat source and a heat sink through latent heat of vaporization of the working fluid. The presence of a wick structure guarantees a satisfactorily operation at almost any inclination angle, depending on the wick geometry. The three sections constituting HPs are the evaporator (heating section), the condenser (cooling section) and the adiabatic section (in between the others, negligible heat exchange with the external environment), as shown in Figure 1.3 [5].

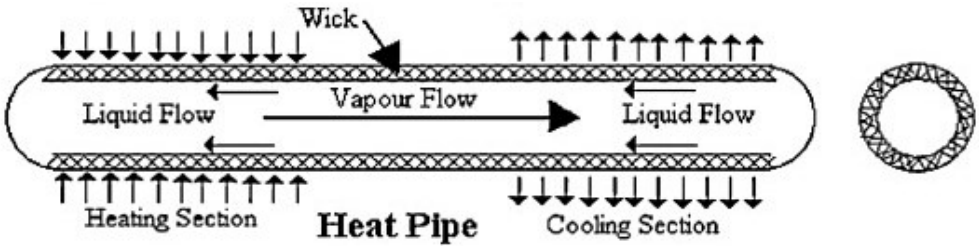

Figure 1.3: HP working principle [5].

Liquid flows spontaneously from the condenser to the evaporator due to a difference in capillary pressure. In the evaporator, vapour generation results in a receding liquid meniscus into the wick structure. Mass addition by condensation at the opposite end results instead in an advancing meniscus. The difference between capillary radii leads to a positive pressure difference between the condenser and the evaporator, acting as a continuous driving force for the liquid which feeds the heating section.

However, depending on the working fluid, operating temperature and geometrical properties, HPs undergo various heat transfer limitations, such as the capillary limit, the boiling limit, the entrainment limit, the viscous limit, and the sonic limit. Concerning the capillary limit, the driving capillary pressure is insufficient, and the evaporator dries since cold liquid cannot be supplied to the heated section. The boiling limit occurs when liquid also evaporates in the wick due to high heat loads or operating temperatures, partially blocking the liquid backflow to the evaporator. The entrainment limit is instead due to high shear forces generated by the vapour flow over the capillary structure, which overcome the capillary forces and push the liquid back to the condenser.

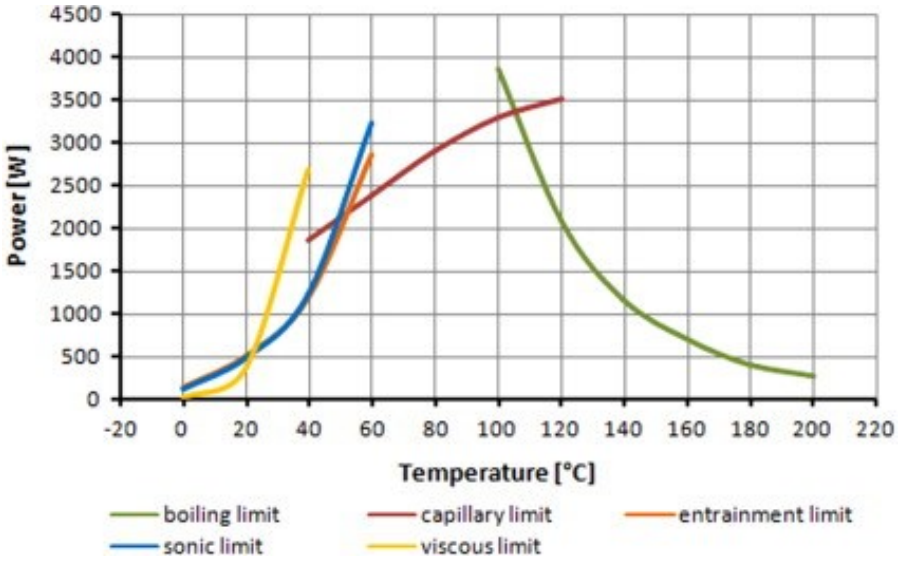

Figure 1.4: Operational limits of HPs [6].

At low operating temperatures, the saturation pressure of vapour is not high enough to overcome the pressure drops along the pipe, thus preventing the HP activation (viscous limit). Finally, at low

vapour densities, the sonic limit may be experienced due to the onset of a chocked flow. All the mentioned limits are depicted in the graph of Figure 1.4 [6], depending on the heat load provided to the evaporator and the working fluid temperature.

Moreover, the morphology of the wick strongly influences the HP operation; three main porous structures are generally adopted:

- Sintered wick (Figure 1.5a). It works at high heat fluxes to the evaporator, and it allows the HP operation at every orientation;
- Mesh wick (Figure 1.5b). The heat flux limit is lower than in sintered powder, and it well operates between -5°C and 90°C in the vertical orientation (evaporator below condenser);
- Axial groove wick (Figure 1.5c). They offer good performances at very low heat fluxes, and in horizontal orientation.

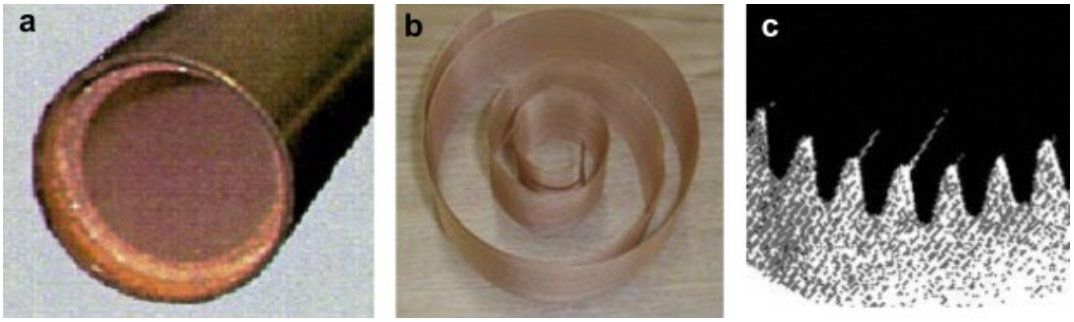

Figure 1.5: Conventional wick structures: sintered (a), mesh (b), groove (c) [7].

1.5 Loop heat pipes

LHPs are two-phase thermal control devices which take advantage of capillary forces to promote heat transfer from an evaporator to a condenser section. When compared to HPs, LHPs provide many advantages in terms of overall reliability, orientation-free operation and distance between the heat transfer areas, despite their more complex geometry. LHPs are constituted by an evaporator, also called capillary pump, a compensation chamber (also called reservoir), a condenser and two fluid transport lines, namely the vapour and the liquid lines (Figure 1.6 [8]). The wick structure is only present in the evaporator and in the compensation chamber. The reservoir accommodates excess liquid during standard operation of the device, and it ensures a regular liquid flow to the capillary pump. The wick in the evaporator (primary wick) has the purpose of developing high capillary pressure for circulating the working fluid around the loop; a secondary wick connects the evaporator and the compensation chamber to promote liquid supplying to the evaporator. Both vapour and liquid lines are made of smooth tubes (often thermally insulated from the environment) that can be arranged differently depending on the required compactness.

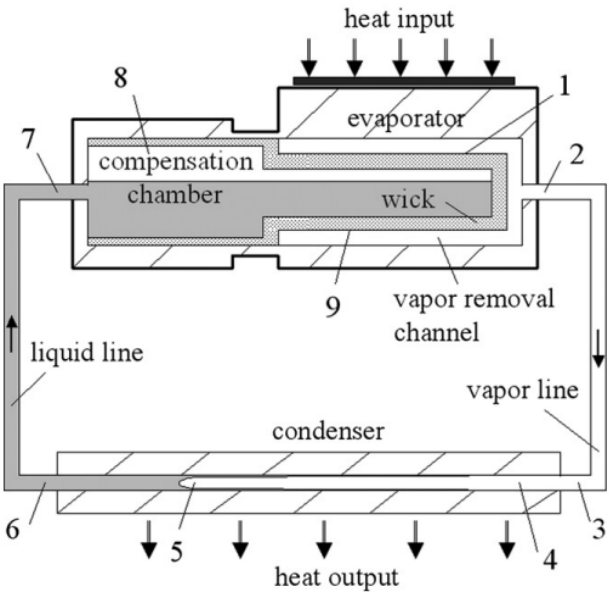

Figure 1.6: Geometry of a LHP [8].

In steady state operation, the heat input vaporises the liquid and the resulting menisci at the liquid-vapour interface in the evaporator wick lead to capillary forces that pump the liquid from the compensation chamber. The vapour pressure and temperature in the evaporator, where heat is supplied, is higher than the temperature and pressure in the reservoir. Moreover, vapour cannot penetrate in the compensation chamber because of the the capillary forces developed in the secondary wick soaked with liquid. Due to the combined effect of the primary wick, which guarantees high capillary pressure, and the secondary wick, which acts as a hydraulic lock, the vapour is forced to flow to the condenser through the vapour, eventually condensing and returning to the compensation chamber through the liquid line.

It has to be pointed out that the total heat load given to the evaporator Q_e is partially used for liquid vaporization ($Q_{e,vap}$), and partially exchanged by conduction through the device walls/wick ($Q_{e,cc}$). Such a thermal behaviour may significantly undermine the LHP operation.

The heat leak magnitude is proportional to the difference between saturation temperature at the evaporator, T_e, and at the reservoir, T_{cc}. The LHP thermo-fluid dynamics can be described as follows:

$$Q_e = Q_{e,vap} + Q_{e,cc} \tag{1.1}$$

$$Q_{e,vap} = \dot{m} h_{diff} \tag{1.2}$$

$$Q_{e,cc} = \lambda_{e-cc}(T_e - T_{cc}) \tag{1.3}$$

where $\dot{m}$ is the mass flow rate, h_{diff} is the latent heat of vaporization, and λ_{e-cc} is the thermal conductivity between the evaporator and the compensation chamber (usually hard to estimate). In transient conditions, heat conduction to the compensation chamber leads to an increase in its temperature, eventually decreasing the $Q_{e,vap}$ magnitude as well as the two-phase flow rate, for a fixed value of Q_e. From Equations (1.1) and (1.2), it is readily noticeable that heat leaks hamper vapour generation at the condenser. The T_{cc} and consequent $Q_{e,cc}$ increase is counteracted by subcooled liquid coming from the condenser; in fact, the heat leak to the reservoir can be also expressed as:

$$Q_{e,cc} = \dot{m} cp_l (T_{cc} - T_{in,cc}) \tag{1.4}$$

where cp_l is the liquid specific heat and $T_{in,cc}$ is the liquid temperature at the compensation chamber inlet. Part of the heat leak will be therefore compensated by $T_{in,cc}$ (i.e., by heat dissipation at the condenser). Hence, the LHP reaches a steady state operation, with self-sustained and stable flow motion along the loop, as the heat leak is totally compensated by the liquid subcooling. In other words, the LHP saturation temperature will be adjusted until the energy balances at the evaporator, compensation chamber and condenser are satisfied (LHP auto-regulation).

Similarly to HPs, the LHP functioning is affected by a number of heat transfer limitations, depending on the specific design of the device. Specifically, viscous, sonic, capillary, entrainment and boiling limits can be defined.

1.6 Closure

To deal with the increasing electrical energy demand for thermal management applications in the industry, passive two-phase heat transfer devices represent an advantageous solution. Nevertheless, the lack of active equipment for the fluid motion (heat transport) significantly decreases the full effectiveness of passive devices, which only rely on capillary and/or gravity forces. To enhance the adaptability of such devices to different operating conditions, wicked solutions have been proposed. However, the proper design of porous structures requires a deep understanding of the developed capillary effects, not to mention the high manufacturing cost and low flexibility of wicked pipes. For this reason, part of the scientific effort is nowadays devoted to the study of modern wickless devices, such as PHPs. In the following Chapter, a description of these heat transfer systems will be provided.

Chapter 2 Introduction on the pulsating heat pipes operational behaviour

2.1 Introduction

PHPs are the last evolution of the wickless heat pipe technology: the capillary effect is provided by the capillary dimension of the channel rather than by the presence of a wick structure (HPs, LHPs). In addition to its simple, cheap and flexible layout, PHP is able to work against and even without gravity. All these features have been considered as highly appealing by the scientific community since the PHP first conceptualization in 1990 [9], and the works dealing with the study of such heat transfer devices have been growing exponentially, especially during the last decade.

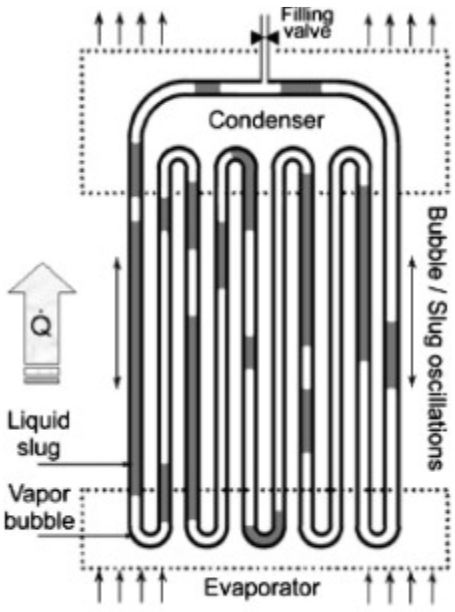

Figure 2.1: Typical PHP layout and heat transfer sections [10].

In their simplest, tubular layout, PHPs are made of a single metallic tube arranged in a planar, serpentine manner (Figure 2.1, [10]) and filled with a working fluid in saturation conditions. Devices usually exhibit small vapour quality, hence presenting an alternation of vapour plugs and liquid slugs. The PHP geometry is generally defined by three zones: the evaporator, where heat is provided to the system by an external source, the condenser, where the heat is dissipated to the external environment, and the adiabatic section, where the system does not thermally interact in a significant way with the surroundings. However, a PHP could operate without an adiabatic zone, even if a physical contact between the other two areas is not desirable and practical.

The most employed PHP is the closed-loop one (Figure 2.2b), although other PHPs have been proposed in the literature [11]: the closed-end PHP (Figure 2.2a), the closed-loop PHP with check-valve (Figure 2.2c) and the PHP with open ends (Figure 2.2d).

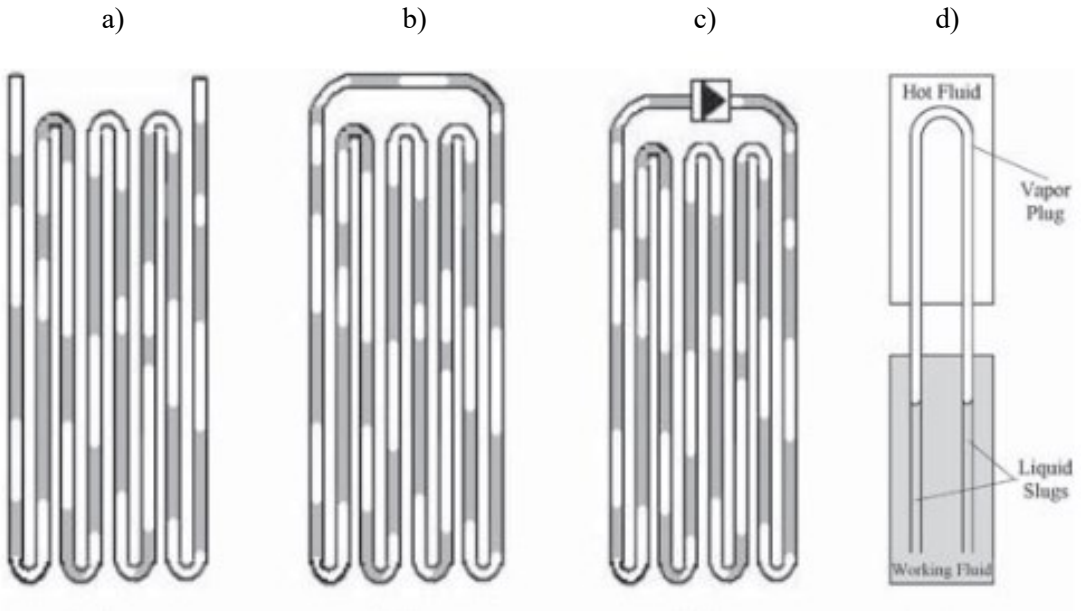

Figure 2.2: Different types of PHP [11].

Except for tubular layouts, PHPs can be furtherly categorized as Flat Plate PHPs (FPPHPs) and micro-PHPs. Specifically, in flat plate layouts, the path for the working fluid is machined on a metallic flat surface (Figure 2.3a), while, in micro-PHPs (Figure 2.3b), the channels are usually carved on a silicon wafer, and manufactured by MEMS (MicroElectroMechanical Systems) technique; the inner diameter of such devices is much lower than that of tubular and flat plate layouts (hydraulic diameter lower than 500 μm, [12]).

a) b)

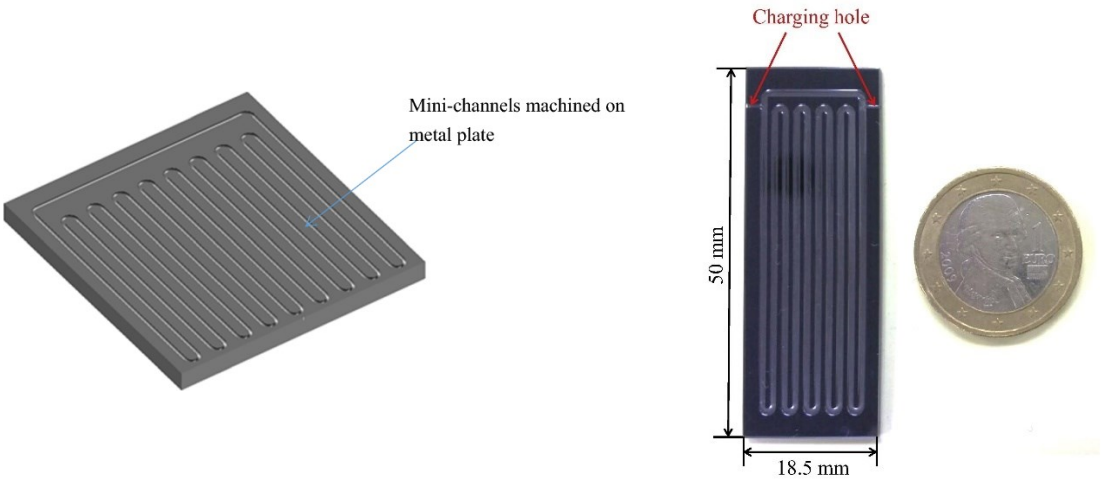

Figure 2.3: Additional PHP layouts: FPPHP (a, [13]); micro-PHP (c, [14]).

Also, three-dimensional geometries can be obtained: three-dimensional PHPs (Figure 2.4) are manufactured by locating each area (evaporator, adiabatic section and condenser) on different planes in the three-dimensional space.

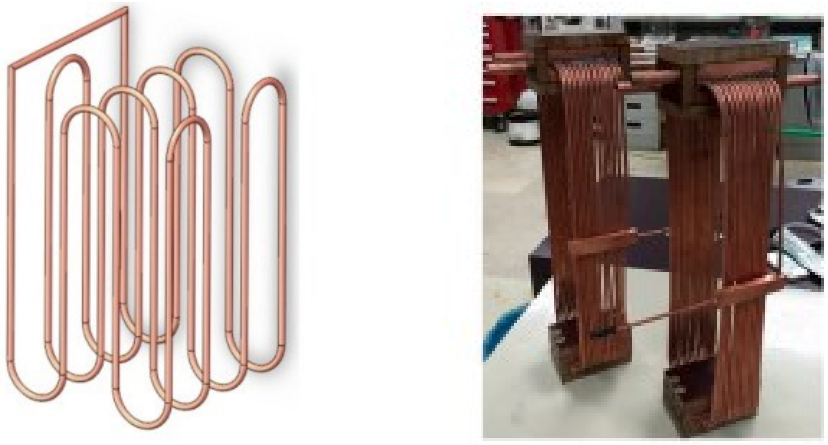

Figure 2.4: Three-dimensional PHP configurations (left, [15]; right, [16]).

2.2 Working principle

The PHP operation is mainly characterized by thermally driven oscillations of the working fluid. In fact, when heat is provided for the first time at the evaporator section, the fluid temperature and, consequently, the fluid pressure locally increases. Such a difference in pressure between the evaporator and the condenser results in a self-sustained motion of the fluid through the adiabatic section, typically occurring in the pattern of fluid oscillations (for this reason, PHPs are also called oscillating heat pipes). In other words, the device operation is guaranteed by continuous thermal instabilities in the overall system. Hence, the PHP cannot be described by a single thermodynamic state, even though the exact

features of the thermodynamic cycle are still unknown. By considering the pressure-enthalpy diagram of Figure 2.5 [17], when evaporation and bubbles expansion occur at the evaporator section, the local thermodynamic state of the working fluid tends to move from A to B, i.e., at higher pressure/temperature and vapour quality, by evaporation at constant pressure combined with isentropic pressure increase due to bubble expansion [11]. At the same time, vapour condensation at the condenser (constant pressure and negative isentropic work) tends to move the local thermodynamic state from A to C, i.e., at lower pressure/temperature and vapour quality, thus furtherly increasing the pressure difference between the evaporator and the condenser. Such a non-equilibrium condition results in the driving force for the fluid motion: the system consequently tends to restore the equilibrium state by equalizing the internal pressure. Motion of liquid slugs and vapour plugs from the evaporator towards the condenser in a generic channel will push the colder fluid at the condenser towards the evaporator in the adjacent channel, hence working as a restoring force. The coupled effect of driving and restoring forces in the PHP branches finally lead to fluid oscillations.

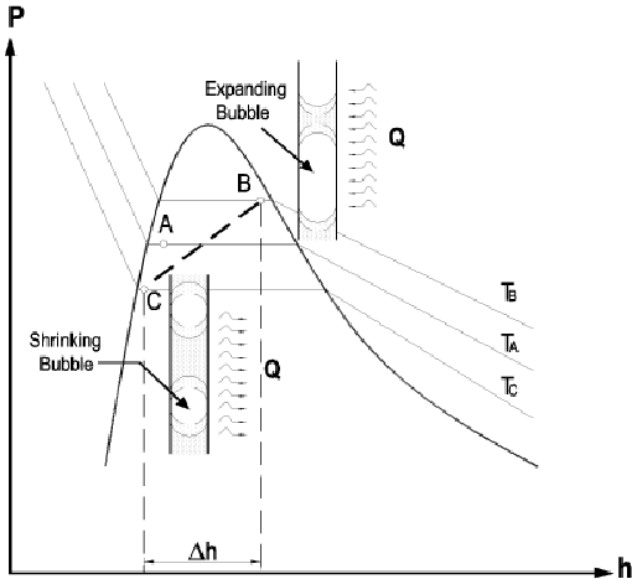

Figure 2.5: Pressure-enthalpy diagram for a PHP [17].

However, the local thermodynamic state of the working fluid might not always lay within the saturation curve, contrarily to what qualitatively shown in Figure 2.5. In fact, the fluid may also be either in superheated or subcooled conditions, or even presenting metastable states, such as superheated liquid or subcooled vapour.

By considering a control volume belonging to either PHP sections, the physics governing the PHP behaviour is described by far more complex thermo-fluid dynamics. In Figure 2.6, the magnification of a typical slug-plug pattern is presented [18]. Although a complete outline of the phenomena locally occurring in PHPs is hard to achieve, some considerations about fundamental processes can be drawn.

Regarding fluid-dynamic and hydrostatic phenomena, menisci are formed due to surface tension and capillary dimension of the channel. Liquid films additionally surround vapour plugs. The menisci contact angle and the liquid film dynamics depends on both the fluid-solid combination and the fluid properties. During motion, either advancing (positive contact angle) or receding (negative contact angle) menisci could be observed. The pressure drop along the capillary channel axis is mainly due to liquid slugs and the shape (either advancing or receding) of the liquid-vapour interfaces. Moreover, pressure forces are exerted on liquid and bubbles by adjoining plugs. Even if surface tension forces predominate, gravity also influences, with a not yet fully clarified extent, the slug-plug flow. Fluid is also subjected by internal viscous dissipation and wall shear stress, depending on the flow field motion. During the PHP operation, pressure waves and pulsations generated in each channel interact with each other, thus leading to a complex propagation of perturbations.

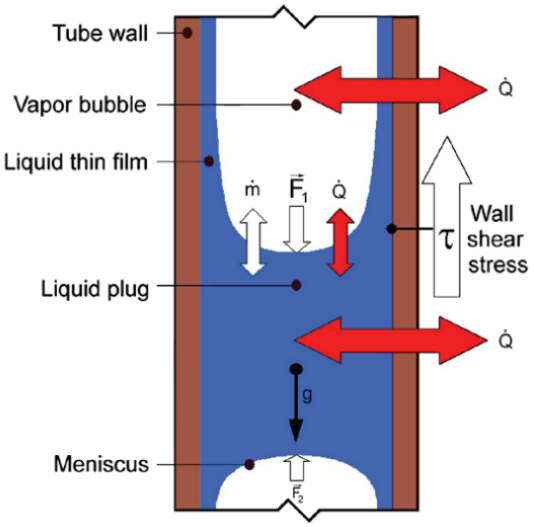

Figure 2.6: Typical slug-plug pattern in a confined, capillary environment [18].

For what concerns thermodynamic processes, slugs and plugs mainly exchange heat in the radial direction, even though heat transfer may also axially occur. In the evaporator, sensible or latent heat may be exchanged, despite latent heat exchange is more likely to occur; when fluid entering the evaporator is in saturated conditions, liquid evaporation will either expand existing bubbles or create new bubbles by breaking up processes due to nucleate boiling. Liquid film evaporation is the main phase-change phenomenon occurring in the evaporator. On the other hand, the condenser is mainly interested by vapour condensation, leading to either bubble shrinking or merging of small bubbles. In the adiabatic section, the working fluid goes from high-pressure, high-temperature conditions given by the evaporator to low-temperature, low-pressure conditions existing in the condenser. Such a variation in terms of thermodynamic conditions is achieved by internal enthalpy balancing through evaporation mass transfer from liquid slugs to vapour plugs, since nearly saturated conditions are imposed in the

system. Nevertheless, with non-equilibrium metastable conditions, interactions between liquid and vapour passing through the adiabatic section could be described by more complex phenomena.

2.3 Influencing parameters

The PHP working behaviour is influenced by several parameters, linked, for example, to the device geometry, the working fluid properties, or the operating conditions. Specifically, their effect on the PHP operation, as well as their inter-play, is still not fully understood. In the present Paragraph, the main influencing parameters are described and discussed.

2.3.1. Tube inner diameter

The internal diameter is the first geometrical parameter to be considered when dealing with PHPs. In fact, in order for the employed heat transfer device to fully work as a PHP, a capillary flow must be always ensured. Since the pressure difference for the working fluid motion is generated by bubble expansion and shrinking at the evaporator and condenser, respectively, a full effectiveness of the pumping force is obtained when the confined flow presents a slug-plug pattern. This can only be achieved when the inner diameter is lower than a critical one. The capillary limit criterion is defined in [19] through the Bond dimensionless number as follows:

$$Bo < 4 \quad ; \quad Bo = \frac{g(\rho_l - \rho_v)d^2}{\sigma} \tag{2.1}$$

where g is the gravity acceleration, ρ_l and ρ_v are the liquid-phase and vapour-phase densities, respectively, d is the inner diameter of the channel and σ is the fluid surface tension. All the listed fluid properties should be evaluated in terms of average fluid temperature during the PHP operation, considering the fluid in saturation conditions unless the fluid temperature/pressure is locally known in the device through direct fluid measurements.

By rearranging Equation (2.1), the definition of capillary limit by the critical diameter, which depends on the gravity field and the working fluid properties, reads as:

$$d_{crit} = 2\sqrt{\frac{\sigma}{g(\rho_l - \rho_v)}} \tag{2.2}$$

The Eötvos number ($E\ddot{o}$) is sometimes used in place of Bo, $Bo = \sqrt{E\ddot{o}}$. In Figure 2.7, the critical diameter for different working fluids is shown.

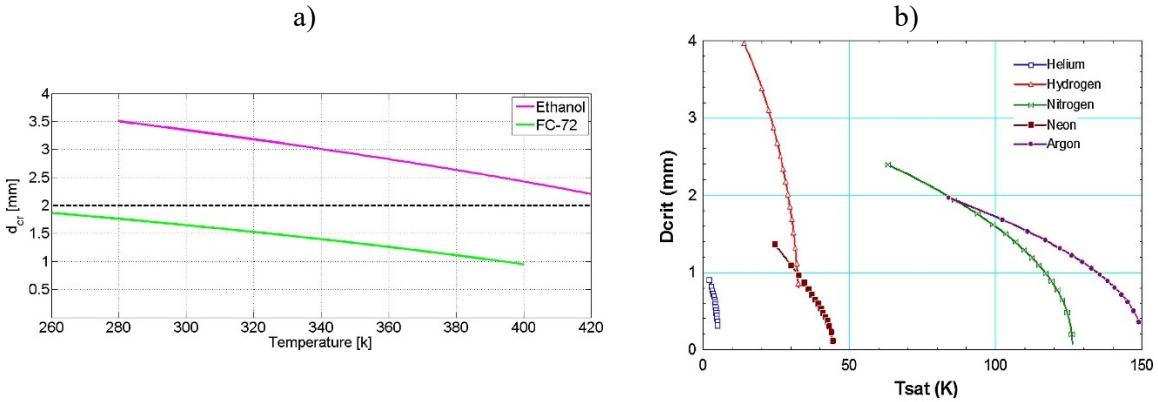

Figure 2.7: Critical diameter versus temperature for different working fluids. (a), [20]; (b), [21].

For the correct PHP operation, it also exists a capillary limit of Bo > 0.4 for very low inner diameters, as highlighted by Taft et al. [22] for the case of micro-PHPs. It has to be pointed out that the Bond criterion is true for static conditions, while its validity is undermined by the presence of either flow or bulk accelerations, i.e., inertial forces, which could prevent the occurrence of capillary flows. The inertial effects can be evaluated by means of the Weber number (We), $We = \rho_l U_l^2 d/\sigma$, with a capillary threshold of $We < 4$ [23]; U_l is the liquid slug velocity. To also take into account viscous dissipations, Harirchian and Garimella [24] proposed a more comprehensive criterion based on the Garimella number (function of Bond and Reynolds numbers), $Ga = \sqrt{Bo}Re < 160$.

2.3.2. Filling ratio

The Filling Ratio (FR) is defined as the ratio between liquid volume inside the PHP (at room temperature) and total inner volume of the device. Obviously, the two limits for FR are defined by FR = 0% (empty device) and FR = 100% (device entirely filled with liquid). In the case of FR = 0%, the heat is only transferred by conduction through the device wall, and the PHP becomes a simple series of inefficient fins. With FR = 100%, pulsation is prevented since no vapour bubbles are present. Heat is transferred both by conduction through the device wall and the liquid, as well as by buoyancy of the liquid itself. At the two heat transfer sections, only sensible heat is inefficiently exchanged. For FR values approaching the mentioned limits, the PHP operation is still highly ineffective. On one side, FR close to 100% will result in very few bubbles inside the system, which cannot generate the required perturbations for the fluid motion. On the other hand, a little fluid inventory inside the PHP will lead to premature dry-out phenomena, i.e., absence of liquid in the evaporator section. Hence, the evaporator wall temperature will dramatically increase due to a sharp drop in the inner heat transfer coefficient. In general, it can be stated that the optimal FR for a PHP is around 50%, whereby the amount of vapour is enough for ensuring fluid motion, and the amount of liquid is enough for avoiding early evaporator dry-outs.

2.3.3. Heat load

The heat load given to the evaporator is the solely source of thermal instabilities in PHPs. For a given geometry, the input heat flux is responsible for the level of perturbations and flow patterns existing in the channels. For low heat loads, the pumping action for the fluid motion is limited, and the bubbles oscillate with high frequency and low amplitude. Either complete absence of fluid motion or extremely weak oscillations results in a low heat transfer performance of the device. As along as the heat load increases, the device undergoes an activation phase, where the fluid oscillation amplitudes become comparable with the device length. Such an oscillatory condition is maintained for higher power inputs to the evaporator, until different flow patterns, namely semi-annular and annular flows, occur (details will be provided in Paragraph 3.3.1). Also, during oscillations at high heat loads, the fluid may cross the condenser section, reaching the evaporator in the adjacent branch. Such an overextension will lead to fluid circulation phenomena, where the fluid moves in a preferential direction. Once furtherly increased the power input to the evaporator, the PHP will reach its operational limit, mainly governed by dry-outs at the evaporator. Nonetheless, a full description of the phenomena occurring at the operational limit is not yet available in the literature.

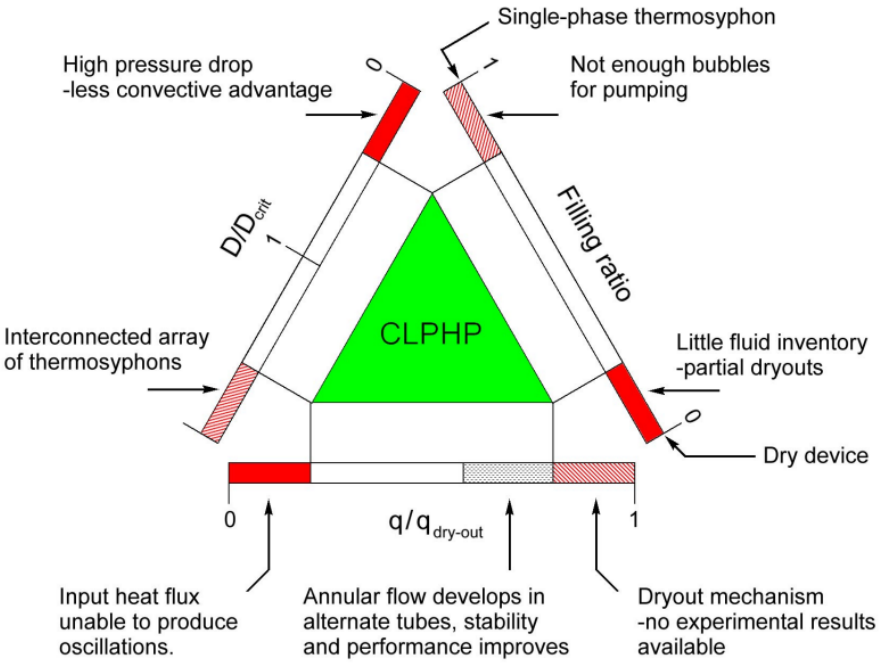

Figure 2.8: Boundary effects of inner diameter, filling ratio and heat load on a CLPHP [25].

The boundary effects of inner diameter, filling ratio and heat load on a generic CLPHP are qualitatively resumed in Figure 2.8. To note that “no experimental results available” referred to dry-out

mechanisms is a strong statement, despite the number of works dealing with operational limits at high heat loads is nowadays still limited, especially due to the critical test conditions.

2.3.4. Working fluid properties

Working fluid properties also influence the PHP working behaviour. The main influencing properties are the surface tension, the latent heat, the $\partial P/\partial T|_{sat}$, the specific heat and viscosity. Regarding the former property, high surface tensions increase the critical diameter, according to Equation (2.2). Hence, capillary flows will be allowed for larger inner tubes diameters, thus increasing the stored volumes of liquid and the heat transfer areas. As a drawback, pressure drops will similarly increase, resulting in higher pumping forces (higher thermal instabilities) needed to maintain fluid motion. Low latent heat enhances the fluid evaporation at a given temperature and high pressure, promoting fluid oscillation at higher velocity; the thermal performance will increase accordingly. However, dry-outs may occur at lower heat loads. High $\partial P/\partial T|_{sat}$, which is provided by the Clausius-Clapeyron equation, offers a greater driving force for a given temperature increase at the evaporator; this beneficially influences the start-up phase, as well as the general fluid motion. In Figure 2.9, $\partial P/\partial T|_{sat}$ is shown for different fluids as a function of their temperature [26]. Low boiling points have same beneficial effects on the device activation. High specific heat leads to higher sensible heat exchange, which plays a significant role in the PHP heat transfer behaviour. Large dynamic viscosity always acts to damp oscillations, hampering the PHP operation.

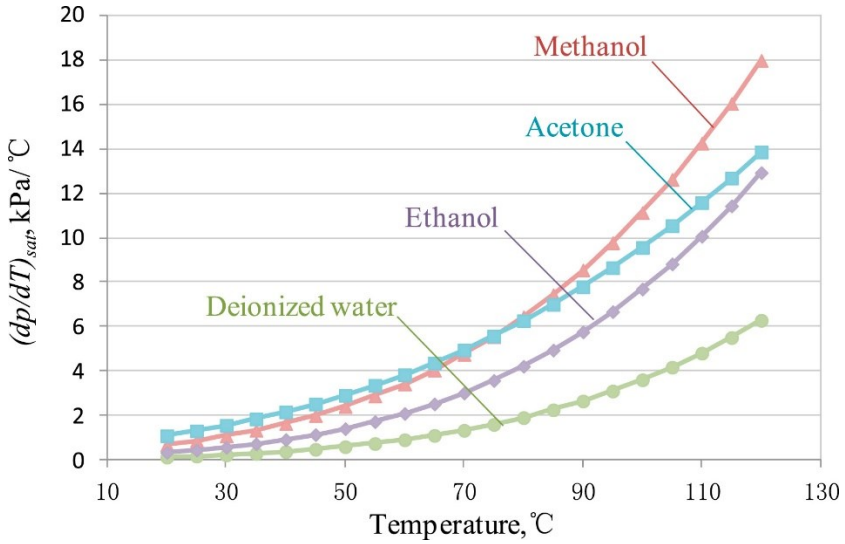

Figure 2.9: $\partial P/\partial T|_{sat}$ for some working fluids [26].

Moreover, the use of fluid mixtures, particular fluids or nanoparticles can enhance the device heat transfer capability [27]. Combination of fluids, such as binary or ternary mixtures, under certain mixing conditions, improves the thermal performance. The addition of surfactants will increase the fluid surface

tension, reducing the start-up time. Self-rewetting fluids (surface tensions increases with temperature) will be pushed to the evaporator section by the Marangoni effect, promoting a constant backflow hence shifting the operational limit (evaporator dry-out event) at higher heat loads. Nanoparticles improve heat transfer; also, their deposition increases nucleation sites, resulting in higher fluid thermal conductivity and different flow patterns experienced during the device operation.

2.3.5. Orientation

The device performance could be furtherly affected by its inclination angle, such as by the branches position with respect to the gravity field. Usually, best performances are achieved in the vertical Bottom Heated Mode (BHM, evaporator located at the bottom), where buoyancy forces help the fluid motion from the evaporator to the condenser. The Top Heated Mode (THM, evaporator located at the top) generally provides the worst performances due to the operation against gravity. The horizontal orientation will similarly result in lower performances, when compared with the BHM. Also, devices presenting low number of turns are usually more influenced by the orientation [28], while PHPs with higher number of turns will operate independently of the tilt angle [29]. Three-dimensional configurations usually guarantee a significant independency of inclination, allowing acceptable performances even in the most unfavourable cases [30].

2.3.6. Geometrical features

The PHP geometry in terms of length of its sections influences in a complex way the device behaviour. In fact, for low values of power input over the heat transfer surface (i.e., heat flux given to the evaporator), the PHP does not activate. Moreover, low heat dissipation capabilities of the condenser will prevent an effective heat transfer; in fact, the condenser area is supposed to be always larger than the evaporator one. The adiabatic section length must be also considered, since longer transport section results in higher pressure drops between the evaporator and condenser. Similarly, the turn radius leads to local pressure drops, hampering the fluid motion.

Regarding the evaporator, the heat transfer capability increases as long as the evaporator length decreases, since colder fluid from the condenser/adiabatic section will cool down the whole evaporator zone more easily. When the evaporator is longer, the driving force for the working fluid might not be high enough to allow colder fluid to refresh the overall evaporator section, resulting in the formation of hot spots and dry areas. Anyway, the optimal evaporator length is affected by different conditions, such as the working fluid, the filling ratio and the heating power input [31].

2.3.7. Non-condensable gases

The presence of Non-Condensable Gases (NCGs) in the device, such as air, negatively affects the PHP operation. In fact, NCGs increase the fluid pressure and saturation temperature, leading to the sub-cooling of the system. An example of system sub-cooling is shown in Figure 2.10 for some NCGs percentages [32].

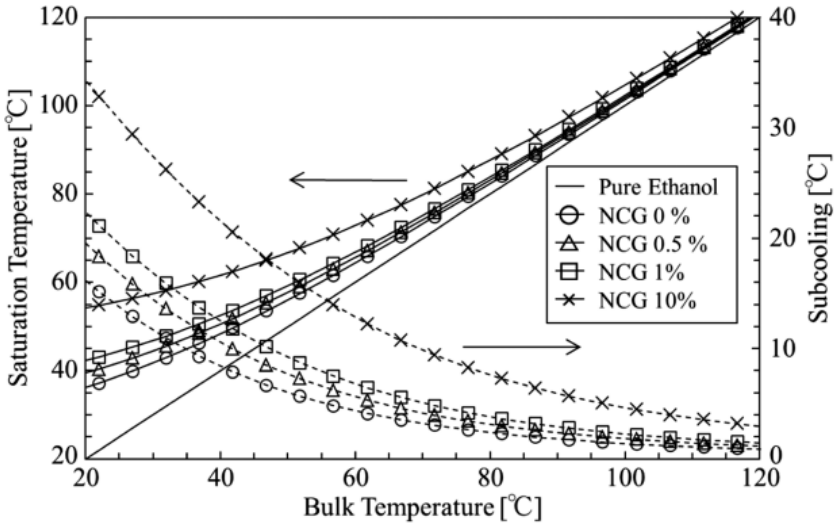

Figure 2.10: Saturation temperature and sub-cooling for varying NCGs percentages [32].

This results in a rise in operating temperature and pressure, decreasing the PHP thermal performance (inhibition of nucleation and bubble expansion). Operating PHPs with a non-negligible quantity of diluted NCGs is generally due to an incorrect filling procedure. Before filling the device with working fluid, the system has to be satisfactorily vacuumed, considering that different evacuation pressures result in different percentages of NCGs remaining into the system [33].

2.4 Applications

Despite PHPs are not yet intensively employed from an industrial point of view, many different applications have been investigated, spanning from the automotive sector to the space industry. The main applicative purposes of PHPs regard thermal management and heat recovery. In Figure 2.11, possible applications of PHPs are gathered [34].

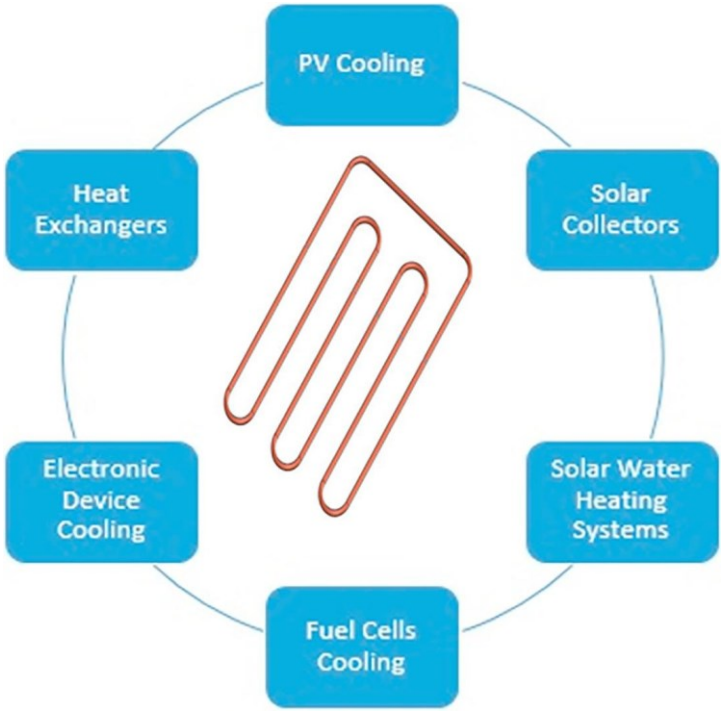

Figure 2.11: List of possible PHPs applications [34] (PV: photovoltaic).

2.4.1. Flexible and deployable systems

PHPs made of polymeric, flexible materials are suitable for deployable systems, since their shape can be easily modelled without compromising their integrity (Figure 2.12, [35]). The low material cost in the manufacturing process is suitable for large-scale production, however their thermal performance is lower with respect to metallic devices due to lower thermal conductivity of flexible materials.

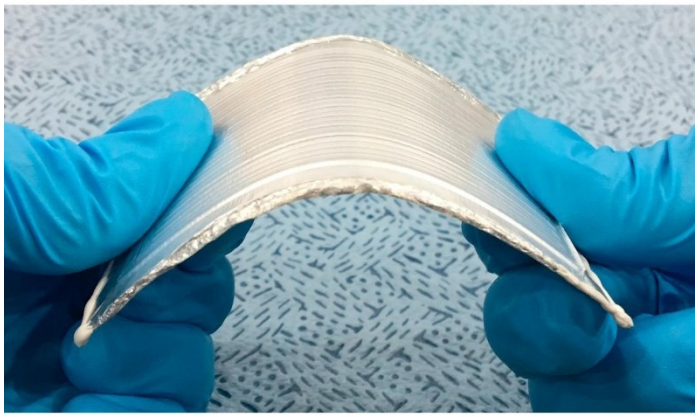

Figure 2.12: Example of flexible PHP for deployable systems [35].

2.4.2. Fuel cells and batteries

Efficient thermal management of fuel cells and batteries is needed during charge/discharge phases to increase the lifetime of energy storage systems. Integrated solutions are especially desirable in the automotive field to cool down batteries in a passive way during summer (Figure 2.13, [36]) or to transport heat inside the cabin during winter. Compactness and passive heat transport can be achieved thanks to PHP systems. Their application might be extended to batteries warm-up in winter conditions by transferring heat from a heat source, e.g., endothermic engine.

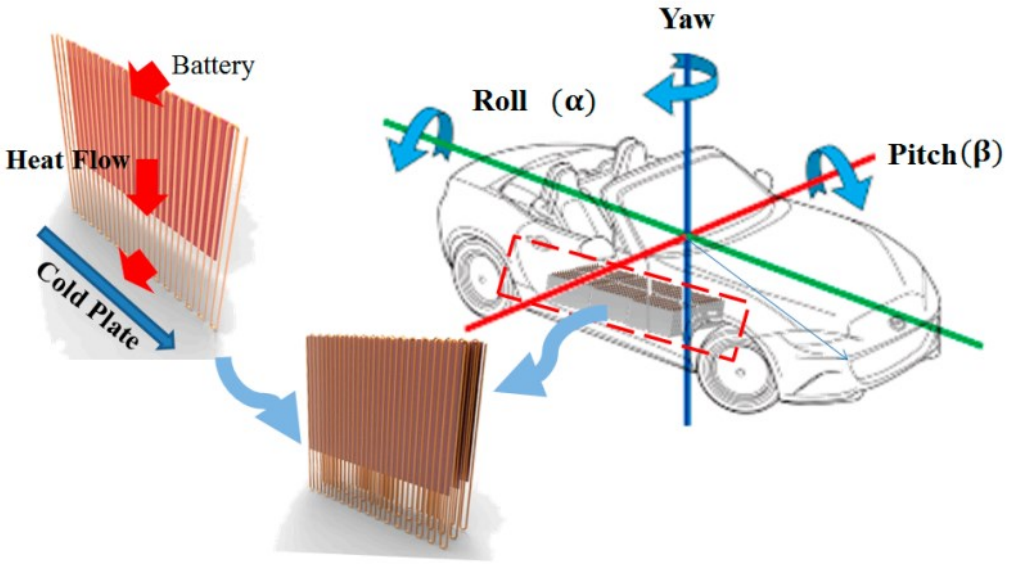

Figure 2.13: Cooling of battery packs through a PHP in an electric vehicle [36].

A big limitation is represented by the mutual position of heat sources and heat sinks: longer distances will result in ineffective PHPs operation due to higher pressure drops, which cannot be overcome by the only thermal instabilities driving the working fluid.

2.4.3. Micro-electronics cooling

One of the most important applications of PHPs is represented by the thermal management of micro-electronics, especially for CPUs and LEDs cooling. Effective and efficient cooling devices are more and more needed to prevent fatal failures of electronic systems due to rapid increases in temperature. Due to their high flexibility, PHPs can be embedded directly in the printed circuit boards, satisfying the requirements of the powers electronic packaging. PHPs can be also used in place of typical finned surfaces on top of CPUs for better heat spreading. In Figure 2.14, a prototype for CPU cooling application is shown [37].

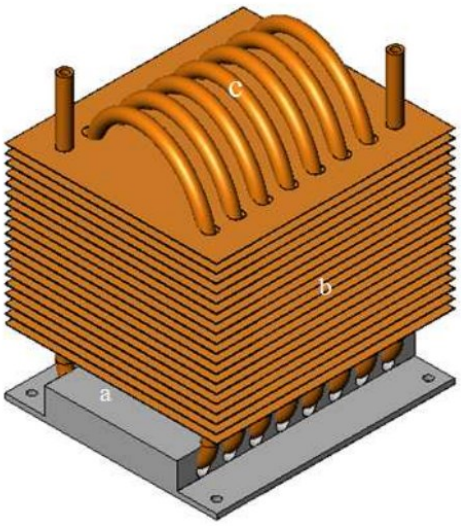

Figure 2.14: Closed-end PHP prototype for CPU cooling [37].

Moreover, metallic FPPHPs (either standard or micro) represent a suitable cooling solution since their geometry ensures a good thermal contact between their surface and the heating components, while the amount of conductive material is capable of efficiently spreading thermal power generated by miniaturised sources.

2.4.4. Cryogenics and high-power applications

Another PHP application is found in the cryogenic and pre-cryogenic field, hence, when heat transfer occurs at low temperatures (even approaching the absolute zero). Among possible applications, PHPs can be used to replace thermal conductive links, which connect high-temperature superconductor magnets with cryocoolers. Also, PHPs could be employed for the cooling of electronics or general facilities on satellites.

Low saturation temperatures of the working fluids are required to allow two-phase flows at cryogenic temperature operation: helium, hydrogen, nitrogen, neon and argon are generally used.

On the contrary, when high-temperature conditions (over 500°C) are considered, with high powers to be dissipated, liquid metals are adopted.

2.4.5. Space applications

PHP systems are more and more involved in space applications due to their low heaviness, low cost and reliable, long-term operation in weightlessness. To give a graphical overview of possible PHP applications in space at different operating temperatures, the scheme by Pietrasanta et al. [38] is reported in Figure 2.15. The temperature scale in the abscissa is referred to that of a black sphere exposed to sunlight at the distance of different planets from the Sun.

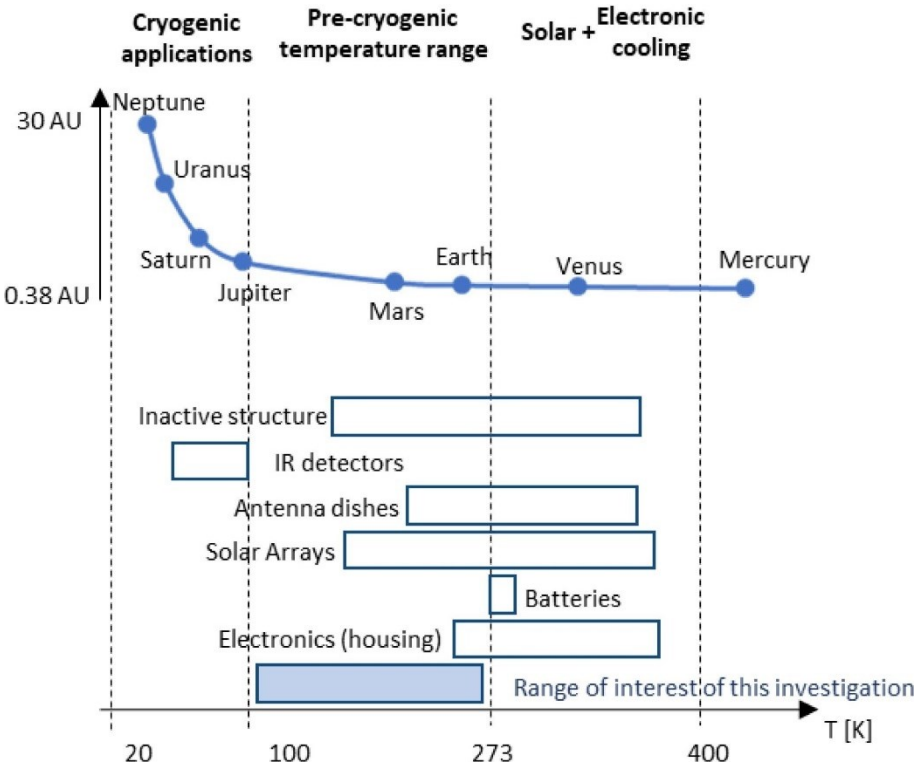

Figure 2.15: Space applications by range of operating temperature [38].

2.4.6. Solar collectors

The potential use of PHPs has been investigated for solar collectors, where solar energy can be adopted for power generation, heating, desalination and other purposes. When compared with conventional solar collectors, PHPs solar collectors represent a cheap and efficient alternative, with the additional advantages of corrosion-free operation and absence of icing at low temperatures.

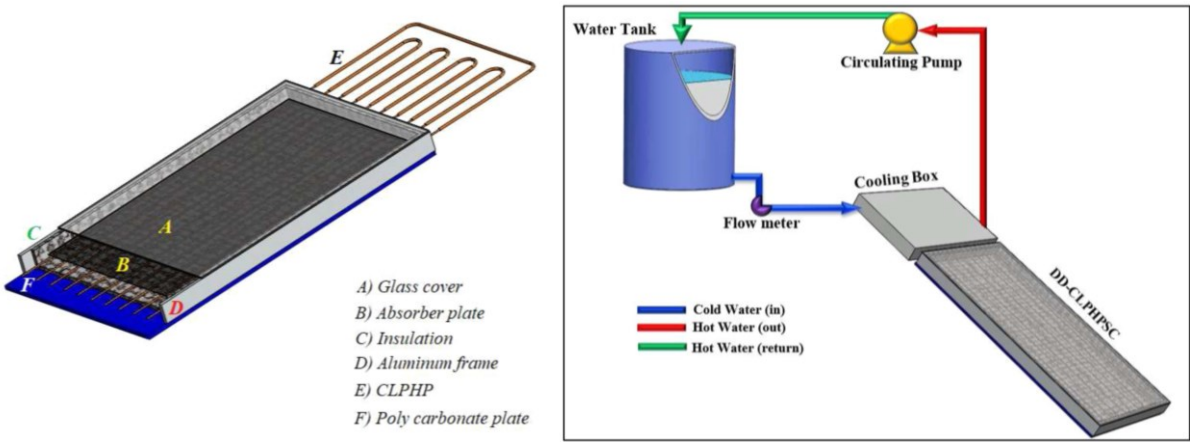

Figure 2.16: PHP solar collector [39].

In Figure 2.16, a PHP solar collector is shown [39].

2.4.7. Heat recovery

The process of waste heat recovery is one of the approaches used in many engineering applications concerning heating, ventilation, and air conditioning (HVAC) systems. PHPs can be used, for example, to recover part of the heat in counter-flowing streams in air conditioning systems, or exhaust heat recovery from a chimney. PHP heat exchanger for heat recovery in a HVAC system is depicted in Figure 2.17 [40].

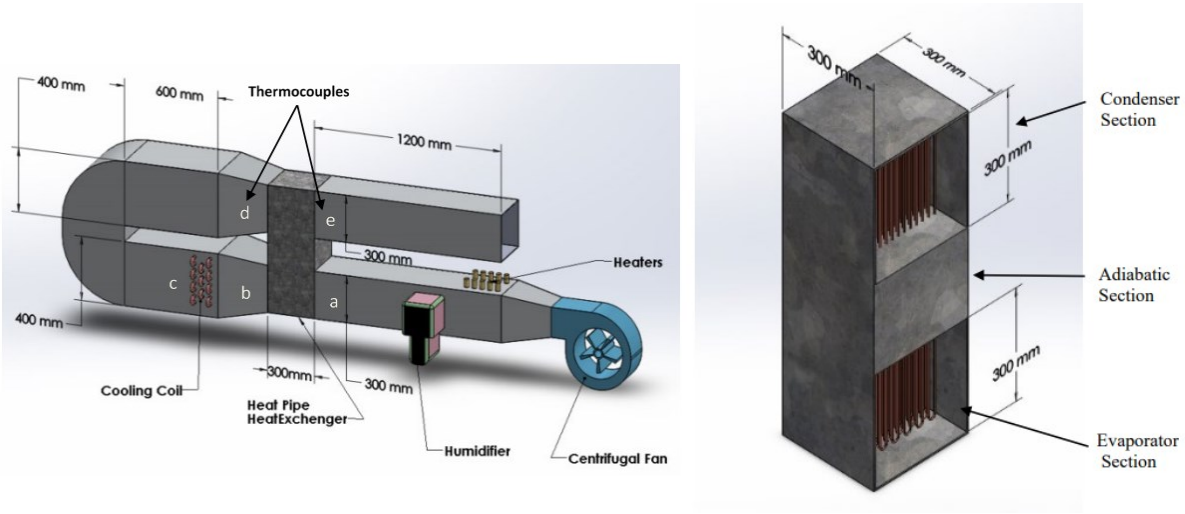

Figure 2.17: HVAC system based on a PHP heat exchanger [40].

2.5 Closure

PHPs are promising two-phase passive heat transfer devices belonging to the wickless family. They are characterized by high flexibility, low manufacturing cost and good reliability even in absence of gravity. Despite the promising features, which consecrated the PHP systems as highly advantageous thermal management solutions, their operational behaviour is far from being completely understood. In fact, due to the absence of controllable parameters, such as the wick structure properties, their functioning is mainly chaotic and hardly predictable from an engineering standpoint. The number of parameters influencing the PHP behaviour is massive, spanning from geometric characteristics to working fluid properties. The experimental effort has been thus focusing on a complete assessment of the thermo-dynamic principles underlying the PHP operation by means of different experimental approaches, which will be described in the next Chapter.

Chapter 3 Experimental techniques, perceived physical phenomena and feasibility

3.1 Introduction

The present Chapter aims at providing a general description of the experimental techniques adopted for the investigation of PHPs performance and behaviour. Their practical implementation is discussed in a critical way, and the main outcomes provided by each method are examined. Such an extended discussion proposes to provide references for choosing the most suitable experimental set-up. Also, it gives an insight into typical or potentially achievable remarks for the sake of future experimentations.

3.2 Basic investigation methods

As already mentioned in Chapter 2, the PHPs thermal performance depends on many different influencing parameters. Evaluation of the PHP heat transfer efficiency is thus crucial for understanding their effects on the studied layouts, and for comparing PHPs thermal effectiveness with other (either singe phase or two-phase) heat transfer solutions. Specifically, the PHP heat transfer capability is assessed by carrying out a thermal characterization, based on the quantification of the PHP equivalent thermal resistance R_{eq} (or, by also considering the device length, equivalent thermal conductivity) defined by Equation (3.1) as a function of the net power input provided to the evaporator Q_{net} [41]:

$$R_{eq} = \frac{T_{eva} - T_{cond}}{Q_{net}} \tag{3.1}$$

In particular, Q_{net} identifies the heat load given to the evaporator section of the device, net of power losses to the environment, while T_{eva} and T_{cond} are the evaporator and condenser temperatures,

respectively, averaged over time. With thermally insulated evaporators (negligible heat losses), Q_{net} can be replaced by the total electrical power input given to the system; both evaporator and condenser temperatures are usually referred to temperatures measured on the device outer surface (wall temperature at the two heat transfer sections).

Despite the equivalent thermal resistance represents the most employed quantity for the PHPs description due to the relatively simple implementation of wall temperature measurements, it cannot be generally used, in a quantitative way, when different experimental set-ups are compared. This great lack of generality is confirmed by the fact that the existing semi-empirical models [31,42–45] either have low accuracy or inability to predict the PHP thermal performance. At the state-of-the-art, the only models capable of satisfactorily reducing a relevant part of the massive amount of literature data are the ones based on artificial neural networks [46,47]. However, these data reduction approaches are not based on a real understanding of the physical phenomena, and they could not be reliably extended to new layouts for unexplored applications or configurations. The design of novel thermal management solutions based on the PHP technology is consequently hampered: according to [48], most of the PHP systems are at a Technological Readiness Level from 5 to 7, hence with still limited industrial applications.

To attempt an explanation of such a low degree of generality and proficient comparison between different experimental works, the following issues concerning the definition of equivalent thermal resistance are considered:

- the chaotic nature of working fluid oscillations, which may lead to different heat transfer capabilities of each channel, could result in space variations of either the evaporator or the condenser temperature distributions. A correct estimation of the T_{eva} and T_{cond} terms might not be achievable in a repeatable way, given a finite number of measurement points;
- different ways of providing or dissipating heat at the two heat transfer sections (e.g., free convection with air or forced convection with liquid) could modify the thermal interactions at the wall-fluid interface, resulting in different phase-change phenomena and overall device behaviour. Hence, the generality of the equivalent thermal resistance could be hampered by different boundary conditions for the studied device, undermining quantitative comparisons between different experimental apparatuses;
- the thermal resistance cannot be satisfactorily rescaled for any possible geometry, i.e., it cannot describe the PHP thermal performance when lengths or diameters vary.

In general, the former issue is overcome by achieving a high thermal inertia of the evaporator and condenser, such that the PHP wall temperature does not substantially fluctuates. The condition of high thermal inertia could be obtained by engraving the PHP channels, within the two heat transfer sections, in thermal spreaders made of conductive material (either aluminium or copper). Drawings provided by Takawale et al. [49] in their experimental work well depicts the common configuration adopted for the

evaporator and condenser sections (Figure 3.1), which take advantage of thermal spreaders for ensuring a high thermal uniformity.

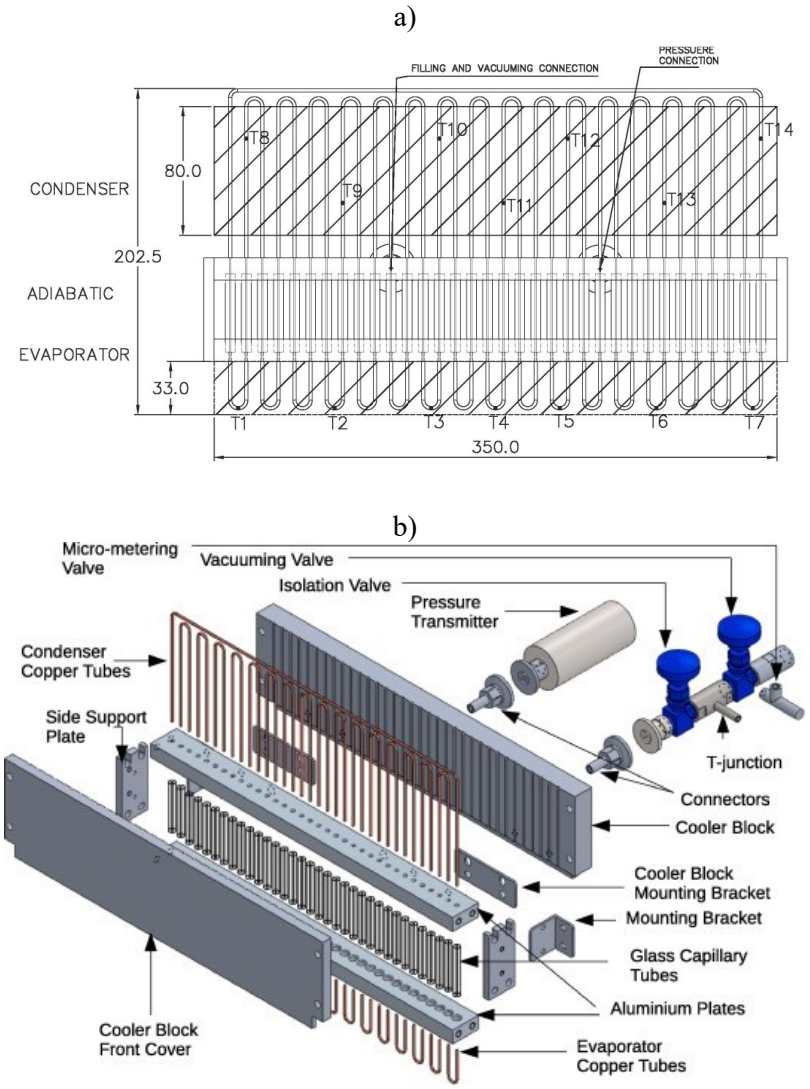

Figure 3.1: Schematic of the sections constituting a common PHP set-up (a) and exploded view (b) [49]; the evaporator and condenser are usually engraved in thermal spreaders.

In the shown configuration, the evaporator is usually warmed up by electrical resistances, either placed inside the spreaders or attached to the spreaders' outer surfaces. On the other hand, the condenser is often cooled by a plate heat exchanger, attached on the outer surface of the spreader, and connected to a cooling loop (Figure 3.2a). Thermocouples are directly attached on the outer wall of the device by drilling paths in the thermal spreaders. Such a configuration is not only adopted for tubular layouts, but also extensively employed in FPPHPs due to high feasibility of implementation. The condenser part may also fit into a shell exchanger connected to a thermal bath (Figure 3.2b), i.e., the condenser is totally immersed in cooling fluid, whereas leading to an obvious need for sealing of the cooling system.

a) b)

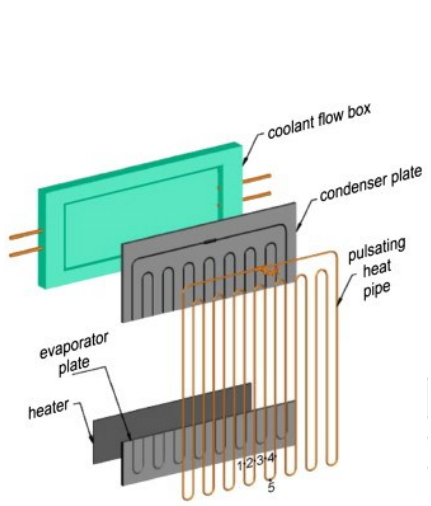

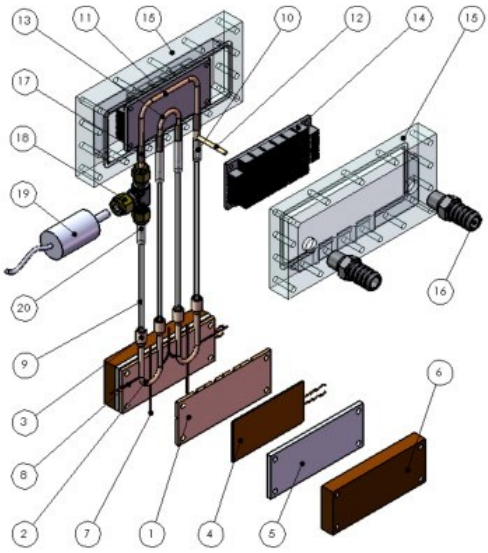

N°	ITEM
1	Evap. copper plate
2	Evap. copper U-turns
3	Copper joint
4	Heater
5	Mica sheet
6	Bakelite back plate
7	TC fluid side
8	TC wall side
9	Glass tube
10	Silicon joint
11	Condenser tube
12	Branch (vacuum/filling)
13	Cond. copper tube
14	Heat sink
15	Cooler shell
16	Cooler connector
17	Silicon seal
18	T-junction
19	Pressure transducer
20	Copper fitting

Figure 3.2: Typical condenser configurations. Karthikeyan et al. [50] (a); Mameli et al. [51] (b).

Hence, the evaporator section is usually subjected to a hybrid boundary condition of constant heat flux/temperature, while heat dissipation at the condenser is dominated by a nearly-fixed temperature boundary condition. Additionally, both the adiabatic section and the evaporator are generally thermally insulated from the external environment to have higher control on the heat load and dissipations. However, it has to be pointed out that a number of other experimental investigations have been based on different evaporator/condenser configurations. For what concerns the heated section, power can be provided to the system by a heating wire twisted around the PHP channels, as shown by the representative picture of Figure 3.3 (Qian et al. [52]). When metallic tubes having low wall thickness are considered, the heat transfer conditions at the evaporator sections are subjected to a purely constant heat flux constraint, thus modifying the thermal interactions between the PHP wall and the evaporating working fluid.

Hence, the evaluation of equivalent thermal resistance could be influenced by the lower thermal inertia of the heat transfer section, and, consequently, by the specific positioning of thermocouples.

Regarding the condenser section, heat dissipation could be achieved, at the device wall without the adoption of thermal spreaders, by forced air convection [15,26,53–57] or, more rarely, by free air convection [52,58]. Again, the different convective conditions might vary the condensation phenomena inside the system, eventually influencing the overall behaviour of the studied device. Such heat transfer configurations have been recently investigated by Ahmad and Jung [59], who studied the thermal response and flow behaviour of a 2-turn PHP made of glass, working in BHM under passive and active cooling regimes with ambient air. Over a total length of 210 mm, the evaporator occupied 30 mm, while

the condenser section varied from free convection (160 mm) to forced convection (60 mm). A total of 4 K-type thermocouples were located at the evaporator and condenser to assess temperature oscillations and evaluate the thermal resistance of the device at heat loads to the evaporator varying from 5 to 80 W.

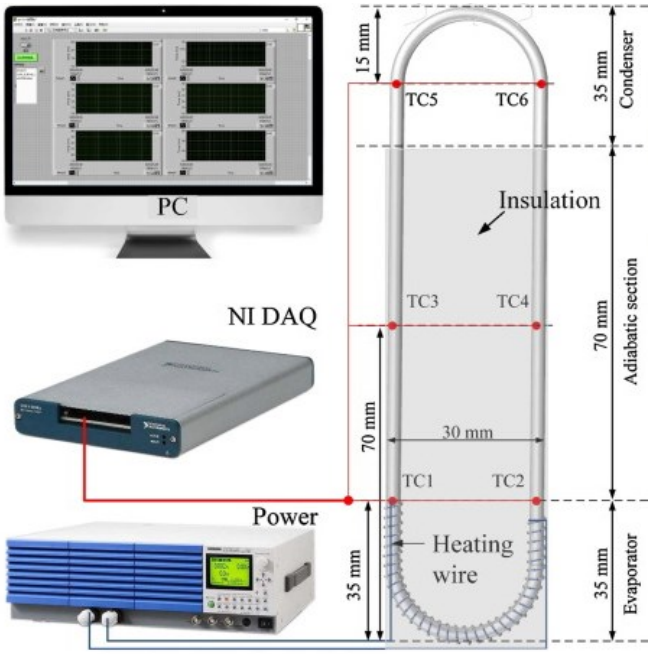

Figure 3.3: Evaporator constituted by a heating wire twisted around the PHP channel [52].

The results highlighted a higher thermal performance (lower thermal resistance) in the free convection case, despite the forced convection guaranteed lower evaporator temperature and satisfying operation even at high heat loads without dry-outs phenomena. Also, the flow transition from slug-plug to annular flow was more gradual in forced convection than in free convection. Yet, two main considerations should be drawn: the length of the condenser section in forced convection, arbitrary chosen by the Authors [59], might not have been suitable for a consistent comparison, and the paucity of temperature measurement points might have undermined the thermal performance evaluation. In fact, having big condenser sections and great temperature differences along the channels can result in unreliable thermal resistance estimations. This is confirmed in [60], where the values of equivalent thermal resistance, evaluated for a copper PHP in vertical orientation and cooled by forced air convection, highlighted low repeatability at low heat loads, i.e., when the device operation was less stable. Nonetheless, such different heat transfer performances at the start-up could also be due to the intrinsic instabilities introduced by gravity, as clarified in [61].

To resume, R_{eq} provides useful pieces of information when evaluated in experimental studies dealing with the effects of influencing parameters on the PHP operation under same test and boundary conditions. It can be also helpful to experimentally assess the effectiveness of new layouts for practical

applications, while it is not reliable when layouts under different experimental approaches and boundary conditions are considered. In fact, the equivalent resistance is a parameter whose meaningfulness is based on the specific test conditions rather than on a complete understanding of the physical phenomena. Moreover, boundary conditions adopted during experimentations usually differ from those defined in real applications. Such an intrinsic limitation undermines an accurate description of the device and consistent individuation of the interplay between different influencing parameters.

A final point worth of discussion is the optimal time window for the average evaporator/condenser temperature computation in (3.1). Since the thermal resistance is based on average quantities, its definition is only valid when temperatures are almost constant over time, with low-amplitude fluctuations. In other words, the thermal resistance must be evaluated during steady or pseudo-steady state conditions of the device, and temperatures are usually averaged over few minutes. In general, the pseudo-steady state conditions are empirically identified from observations of the evaporator/condenser temperature, i.e., when both evaporator and condenser temperatures are stable enough. From the temperature data, qualitative conclusions on the PHPs working regimes can be also drawn. In particular, four main working modes can be usually identified during the pseudo-steady state as follows [48]:

- pure conduction (or device inactivity), where the wall temperature at both the evaporator and condenser sections presents no fluctuations (the heat is only transferred by conduction);
- start-up (or device activation), where wall temperature variations start to be perceivable within the evaporator section at least in one channel;
- intermittent flow, where the evaporator temperature does not stabilize due to the occurrence of multiple stop-overs;
- full activation, where the evaporator temperature either abruptly decreases or exhibits weak fluctuations.

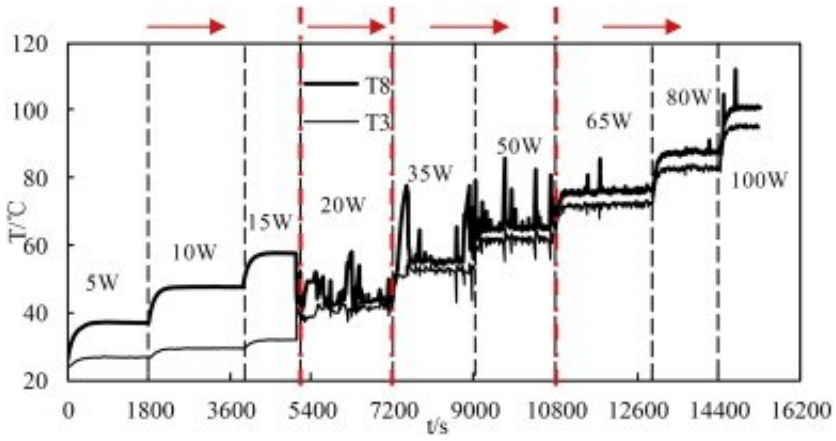

Figure 3.4: Typical temperature profiles evolution with the heat load to the evaporator (thick line: evaporator temperature; thin line: condenser temperature) [62].

A typical evolution of PHPs temperature profiles from low to high heat loads can be found in [62], and shown in Figure 3.4. In this experimental case, the condenser temperature was free to vary due to the imposed forced convection with air at the condenser section. From 5 to 15 W, the device was inactive; at 20 W, its activation occurred, but the intermittent flow regime persisted until 65 W, at which the PHP underwent a full activation.

The measured outer wall temperatures (either at the evaporator or at the condenser) are sometimes used for the further evaluation of fluid oscillation frequencies. Such a quantitative estimation is usually carried out by means of different reduction methods: the Fourier transform, the short-time Fourier transform, the Hilbert-Huang transform and the wavelet method. Being PHPs behaviour extremely chaotic and identified by impulsive fluid motions, both strong and weak oscillations, having non-fixed oscillation frequency, may be perceived. Hence, the dominant oscillation frequency, i.e., oscillation frequency mainly observed, is adopted as quantity for characterizing oscillatory flows. However, regardless the employed approach, some Authors observed dominant fluid oscillation frequencies, while others concluded that the great chaoticity of the system prevented the identification of any main fluid oscillation frequency. Such a discrepancy between experimental works could be due to either the unsuitable reduction methods or to the ineffective wall temperature measurement procedure. Zhao et al. [63] performed a Fourier transform analysis on outer wall temperature data acquired in the condenser at 60 Hz through thermocouples with an accuracy of 0.25°C. Evaporator and condenser, along with thermal spreaders, were placed on one side of the device, while thermocouples were located on the outer wall of the device at the opposite side. The device was made of copper, with wall thickness of 1.53 mm. The results showed no particular dominant frequency; this remark was confirmed by adopting wavelet transforms on the same set of data. Similar outcomes were provided by Monroe et al. [64], who applied the Fourier transform to the outer wall temperature sampled at 300 Hz (accuracy = 0.25°C) in the adiabatic section. The PHP was made of copper, with a wall thickness of 1.55 mm. On the contrary, the work by Xu et al. [65] highlighted perceivable dominant frequencies related to the fluid oscillation phenomenon. The PHP wall was made of copper, with thickness equal to 0.5 mm. The thermocouples were placed on the PHP outer wall (evaporator heated by a heating wire, condenser cooled by free convection with air), with accuracy of about 0.1°C, although no sampling frequency was reported. Similar dominant frequencies were evaluated through outer wall temperature signals at the evaporator, condenser and adiabatic section in the same branch, highlighting that the fluid was flowing in the whole device at same characteristic frequency. It can be concluded that the capability of evaluating dominant fluid oscillation frequencies starting from outer wall temperatures might be strongly hampered, for same reduction method and measurement procedure (i.e., thermocouples on the PHP outer surface), by a number of characteristics of the considered experimental set-up, such as the material and the wall thickness, together with the accuracy and thermal response of the measurement equipment. In other words, the features of the studied device (wall thickness/material) could either allow or prevent a significant observation of temperature variations at the outer wall for a given measurement accuracy.In

addition, slow thermal response may undermine the assessment of fast, transient temperature fluctuations, perhaps suggesting the non-full suitability of thermocouples for the sake of frequency analyses.

3.3 Advanced investigation methods

The here called advanced investigation methods are the ones that propose to provide either qualitative or quantitative information on the heat transfer modes or flow behaviour by means of advanced experimental approaches. The word "advanced" has been intentionally used to underline the higher complexity of experimental set-ups required for such investigations (e.g., complex manufacturing or expensive peripheral facilities) with respect to those required for the equivalent thermal resistance evaluation. In particular, the typical advanced investigations are the ones based on high-speed visualizations (optical or neutron radiography), infrared thermography or fluid temperature/pressure measurements. Each technique will be described in detail, focusing on feasibility and implementation procedures; obtainable results will be also discussed.

3.3.1. High-speed visualization

High-speed visualizations on the working fluid in PHPs are usually achieved by means of two main techniques: visible light imaging and neutron radiography. Specifically, visible light imaging represents a simple and effective tool for the PHPs investigation. In fact, no special auxiliary devices are needed, although the relatively high cost of high-speed cameras might be inaccessible to some research facilities. However, visible light imaging cannot be adopted, for obvious reasons, when PHP walls are either opaque or reflective to visible light. Such a drawback leads to a critical limitation for the method: in fact, only transparent branches (either made of glass or plastic) can be explored, while metallic layouts, which are representative of most of applications, cannot be investigated by this mean. Due to the greatly different thermal properties of transparent materials, the device behaviour is supposed to significantly vary, therefore resulting in experimental remarks that might not be comparable with those found for metallic PHPs. For this reason, two main experimental approaches through direct visualizations can be found in the literature:

- Studies on devices entirely made of transparent materials [65–69]. The aim is providing a complete description of all the PHP sections, including the evaporator and condenser. However, the heating/cooling conditions could be perturbed by the different thermal properties of transparent materials;
- Studies on devices presenting few transparent inserts [15,49,51,70–75]. The aim is giving instead a partial description of the device, without perturbing the heating/cooling conditions.

Regarding the former group of experiments, the usual PHP set-up involves heating wires at the evaporator section (Figure 3.5a, [68]), while heat dissipation at the condenser is often achieved by either free/forced convection with air [15,66,67] or by means of shell heat exchangers with transparent windows (Figure 3.5b, [69]).

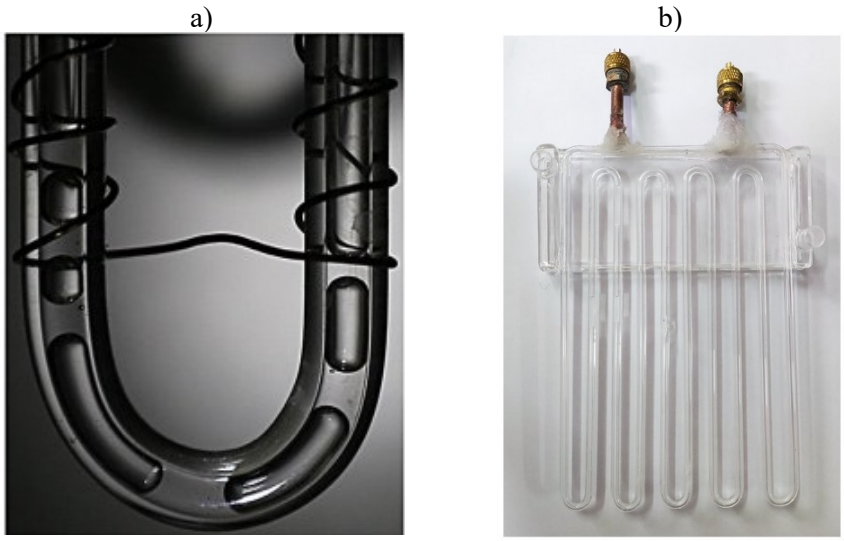

Figure 3.5: Heating wire at the evaporator, Xue and Qu [68] (a); shell heat exchanger at the condenser, Zhang et al. [69] (b).

It is worth to underline that, for what concerns the evaporator section, the adoption of heating wires is clearly needed for visualization purposes, although it may significantly influence the local evaporative processes. In fact, a correct thermal contact between the PHP wall and the wires should be always achieved to guarantee a uniform delivery of heating power. Such a manufacturing issue is perhaps less severe for metallic evaporator sections, where the high thermal diffusivity of the material promotes a redistribution of the heat flux, while it may be crucial for poorly conductive materials. In addition, an uneven contact or dry-out phenomena may result in the wires burnout during the device operation. On the other hand, Authors do not generally provide neither practical nor phenomenological reasons for preferring air convection over liquid convection as heat dissipation mean at the condenser in visualization apparatuses.

Nonetheless, most of the works dealing with full visualizations are the ones concerning investigations of flat plates layout [76–82]. In fact, due to their favourable geometry, FPPHPs are suitable for simultaneous visualizations of the fluid flow in every channel by placing transparent windows, i.e., by using sheets of glass or polymeric materials, with a rather low manufacturing effort. Here, the transparent windows could be generally compressed by clamping structures or glued on the metallic substrates. In Figure 3.6, examples of both solutions are shown; while compressing the transparent window may lead to unwanted by-pass of fluid between adjacent channels, glue spreading

might modify the channels cross-section, and non-optimal curing might result in incondensable gases release over time.

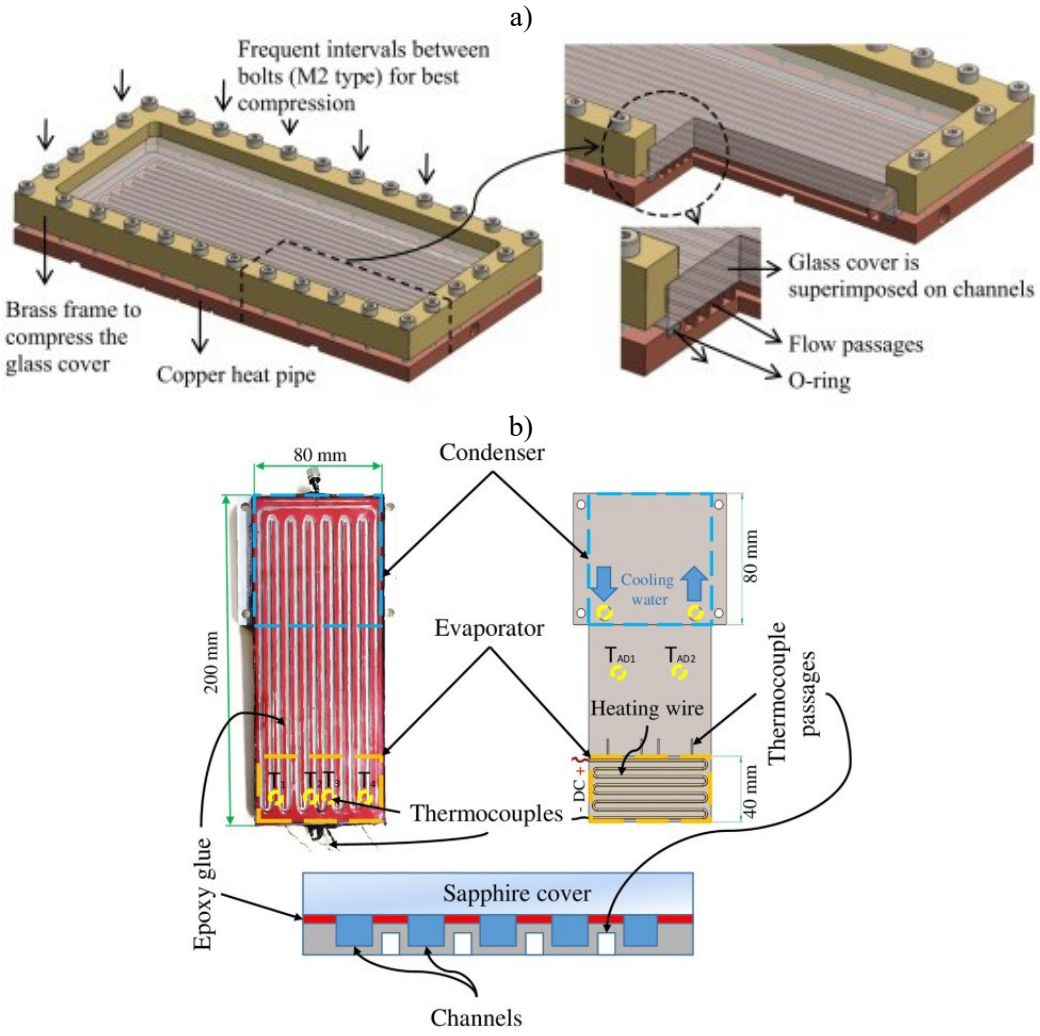

Figure 3.6: Compressed window solution, Markal et al. [78] (a); glued window solution, Slobodeniuk et al. [79] (b).

Moreover, both in fully metallic and partially transparent FPPHP set-ups, heat is usually provided and dissipated on one side of the device (Figure 3.7). This represents a further advantage with respect to tubular layouts in terms of comparison between different experimental works since the heating/cooling conditions remain nearly unchanged even for the full visualization case. Nevertheless, the presence of poorly conductive material on one face of the device might somehow influence the overall conductive phenomena and thermal interactions between the wall and the working fluid.

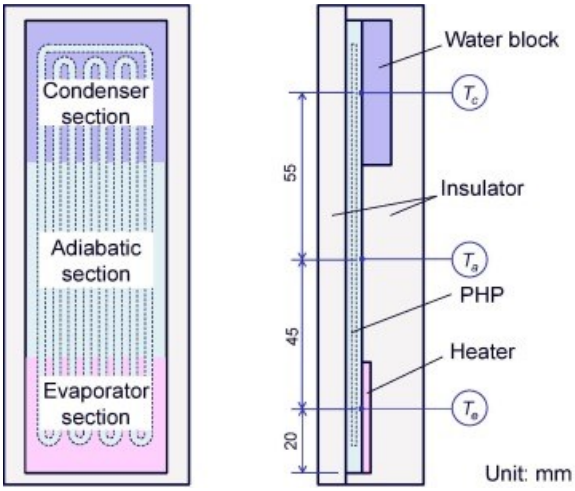

Figure 3.7: Typical heater and condenser (heat exchanger) location in FPPHPs (set-up by Arai and Kawaji [82]).

Regarding the second mentioned group of experimental approaches, transparent channels are placed along the device layout. Usually, the section investigated by transparent inserts in tubular layouts is the adiabatic one. In fact, the adiabatic section is mainly a heat transport section which does not significantly take part in heat transfer or phase change. Hence, placing transparent inserts in such a PHP area is supposed not to affect heating or cooling phenomena, while ensuring, at the same time, a high degree of insight into the device flow behaviour. The location of such inserts depends, in terms of fabrication, on the accessibility to different areas and on the trade-off between complexity of the test rig and desired number of investigated branches. Some experimental works investigated set-ups having all the channels in the adiabatic section replaced with transparent inserts [49,51,70,71]; other studies proposed instead set-ups with fewer transparent channels or smaller transparent zones [15,72–75]. In all the cases, connections between metallic pipes and transparent inserts should prevent fluid leaks and preserve the original pipe section to reduce local perturbations on the fluid stream. Such a double condition of flow continuity and sealing is usually achieved by using either commercial or home-made joints, fixed to the transparent channels by following different approaches: Mangini et al. [74] sealed a glass tube between two T-junctions by using a low vapour pressure glue. Patel and Mehta [70] performed connections with copper joints and Teflon rings as ferrules; the sealing was guaranteed by only mechanical compression on the channels' ends. Mameli et al. [51] connected the condenser tubes with the glass ones in the adiabatic section by simply fitting silicon tubes; the method was not used for those connections close to the evaporator due to its high temperature (i.e., due to a possible thermal deformation of silicon).

From visible light imaging, interesting remarks linked to boiling/condensation, bubble/liquid film dynamics and fluid flow can be drawn. In general, when the heater is activated for the first time,

temperature at the evaporator increases until the PHP wall reaches the needed superheat, and nucleate boiling is triggered (Figure 3.8a).

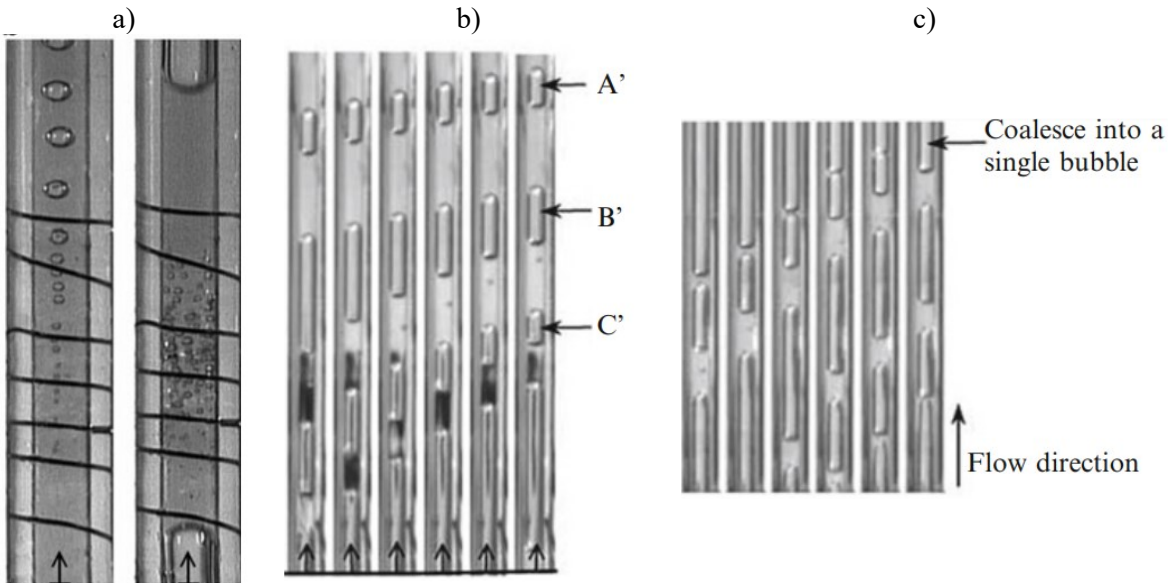

Figure 3.8: Nucleate boiling at the evaporator (a, Tong et al. [83]); bubble shrinking (b) and coalescence (c) at the condenser (Xu et al. [66]).

The nucleation sites activation is favoured during visualization experiments, where low transmissive walls lead to an uneven heating. Nucleate boiling is responsible for pressure increase at the evaporator section, which results in fluid motion towards the condenser. Here, the time needed for the nucleation sites to activate is higher than the time required for the fluid to perform a complete oscillation between the evaporator and the condenser. Hence, during fluid motion, nucleate boiling is suppressed and replaced by thin liquid film boiling. On the other hand, at the condenser section, heat transfer phenomena promote bubble shrinking accompanied by bubble coalescence (Figure 3.8b-c). Nevertheless, coalescence may take place also in other sections of the device; in general, the bubble dynamics can be summarised by four typical behaviours [84], such as:

- Bubbles move nearly at the same velocity without significantly expanding (Figure 3.9a);
- One bubble is nearly stationary, while another is moving/expanding towards it. This results in the merge of the two bubbles (Figure 3.9b);
- Bubbles move nearly at the same velocity while expanding, eventually merging together (Figure 3.9c);
- Bubbles move/expand in opposite directions, merging together to form a larger bubble (Figure 3.9d).

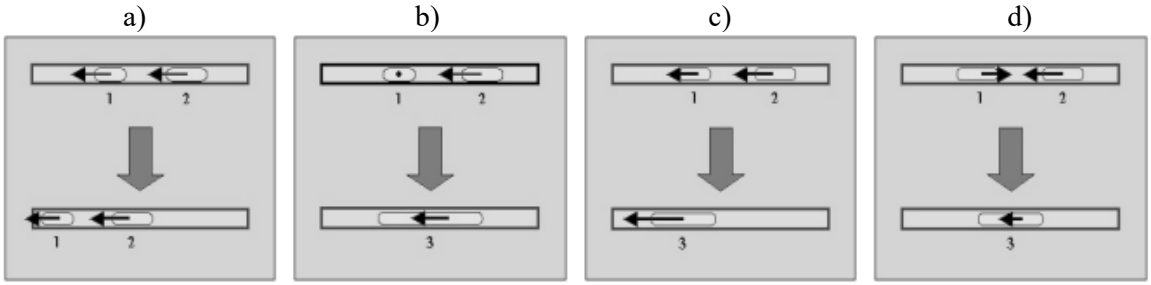

Figure 3.9: Schematics of the usual bubble dynamics in PHPs [84].

Depending on the heating power, different flow patterns can be also observed. Liu et al. [85] performed visualization experiments on different PHP layouts, identifying three typical flow patterns in the adiabatic section: slug-plug, semi-annular and annular flows (Figure 3.10). During the slug-plug flow, trains of liquid slugs and vapour plugs cross the channels; in the semi-annular flow, the tube is mostly filled with vapour surrounded by liquid film, while the annular flow exhibits a continuous vapour column, and the liquid film becomes thinner. Transition between the mentioned flows was observed in [85] from low to high power inputs to the evaporator, even though the annular flow was hardly achievable for high filling ratios. The Authors also highlighted that the annular flow took place just before the PHP operational limit, and it guaranteed the best device performance.

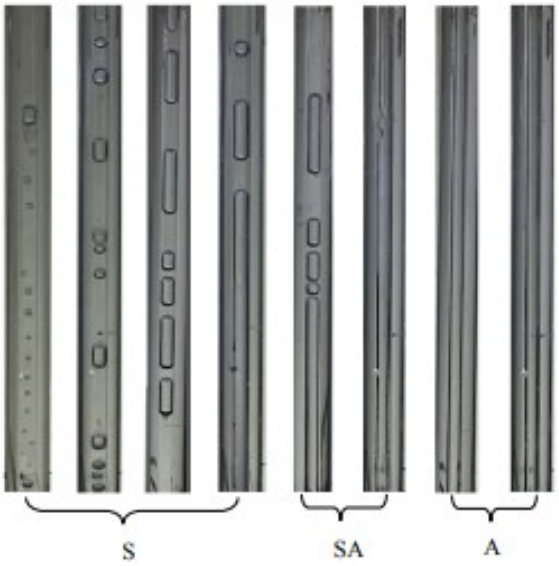

Figure 3.10: Typical flow patterns; S: slug-plug, SA: semi-annular, A: annular [85]. Slug-plug flow usually occur at low/average power inputs, while semi-annular and annular flows take place at high power inputs.

Moreover, the flow direction is generally assessed through visualization during the PHP operation, so that the oscillatory flow (fluid oscillating between the evaporator and condenser) is discerned from

circulatory flows (net fluid circulation with preferential direction). In particular, while the PHP is mainly interested by oscillating flows, net fluid circulation could be spontaneously promoted in particular working conditions, including those with high heat load, high filling ratio, low number of channels and vertical BHM orientation. Circulation may occur for either short or long periods, and it could be accompanied by flow direction reversals or partial oscillations in some branches [50,66,83]. When compared to purely oscillatory flows, circulatory flows enhance the PHP performance [61,86]; different technologies for the onset of circulation have been thus proposed. Check-valves or asymmetries in the design (heating areas, geometry) have been proven to force the fluid to flow with a preferential direction, even for the most unfavourable test cases or layouts [87–90].

The mentioned remarks on the fluid flow characteristics are completed by a quantitative evaluation of the main features defining the working fluid stream in PHPs. Specifically, the analysis is generally based on the evaluation of fluid displacement by means of the bubble tracking technique. This method takes advantage of differences in terms of pixel intensity in high-speed videos, representative of liquid-vapour interfaces. As a drawback, it relies on the presence of stable and recognizable fluid menisci, which could not be always obtained for every test condition, i.e., for every flow pattern. Starting from the fluid displacement, other derived quantities, such as the fluid velocity or oscillation frequency, could be evaluated.

It has to be furtherly highlighted that direct fluid visualization has been also used for fluid temperature measurements by Kim et al. [91] in a micro-PHP (flat layout) through a laser induced fluorescence technique. Here, the transparent window, made of borosilicate glass, was simultaneously investigated by a high-speed camera and irradiated by a laser beam, opportunely adjusted to obtain a power density of about 1.06 mW/mm^2 on the surface of interest. The reflection of the laser radiation on the glass window was considered negligible due to the flat plate geometry of the studied device. The working fluid (ethanol) was mixed with rhodamine B as fluorescent dye, and an optical filter was placed in front of the camera to separate the laser wavelength from the whole emission wavelength. The method was calibrated by varying the fluid temperature from 20 up to 75°C, underlining an inversely proportional relationship between temperature and intensity of light emitted by the used additive. From the resulting grey-scale images intensity, temperature fields were obtained, and hydrodynamic considerations about liquid-vapour interfaces break-up for the onset of annular flows were additionally drawn. However, the need for special optics/laser emitters and a dedicated calibration increases the method complexity, while reflective phenomena related to the section of interest might undermine its applicability to capillary tubes having circular section. In addition, the effects of rhodamine B on the overall phase-change behaviour should be taken into account. Other few works have used high-speed cameras to measure the outer wall temperature by means of temperature-sensitive paints. Ishii and Fumoto [92] investigated the evaporator of a FPPHP constituted by three different layers: a machined substrate made of aluminium, a thin layer coated with temperature-sensitive paint, and a glass window (Figure 3.11a). The paint was framed by a high-speed camera (macro zoom lens + band pass optical filter) and excited by a UV LED lamp. From a calibration

procedure, the relative intensity of the fluorescent radiation emitted by the paint in between 50°C and 90°C was found to follow the relation $exp(-0.0243T+1.35)/1.059$. The employed procedure allowed temperature measurements at the fluid-glass interface and at the aluminium-glass interface, rather than an estimation of the fluid temperature. The results gave a complete outline of the temperature distribution in the evaporator section, showing local temperature fluctuations probably due to evaporation phenomena and flow motion. A fast Fourier transform analysis was carried out, highlighting no significant dominant frequencies except for few heat loads. Temperature differences in terms of vapour or liquid passage were also reported, even though the chosen set-up prevented direct fluid visualizations, thus undermining a reliable validation of the two-phase flow identification. To overcome such a limitation, Francom and Kim [93] proposed a test rig with two cameras, one framing the temperature-sensitive paint coating (on a stainless-steel layer), and one observing the inner fluid through an acrylic base on which the PHP channels were machined (Figure 3.11b).

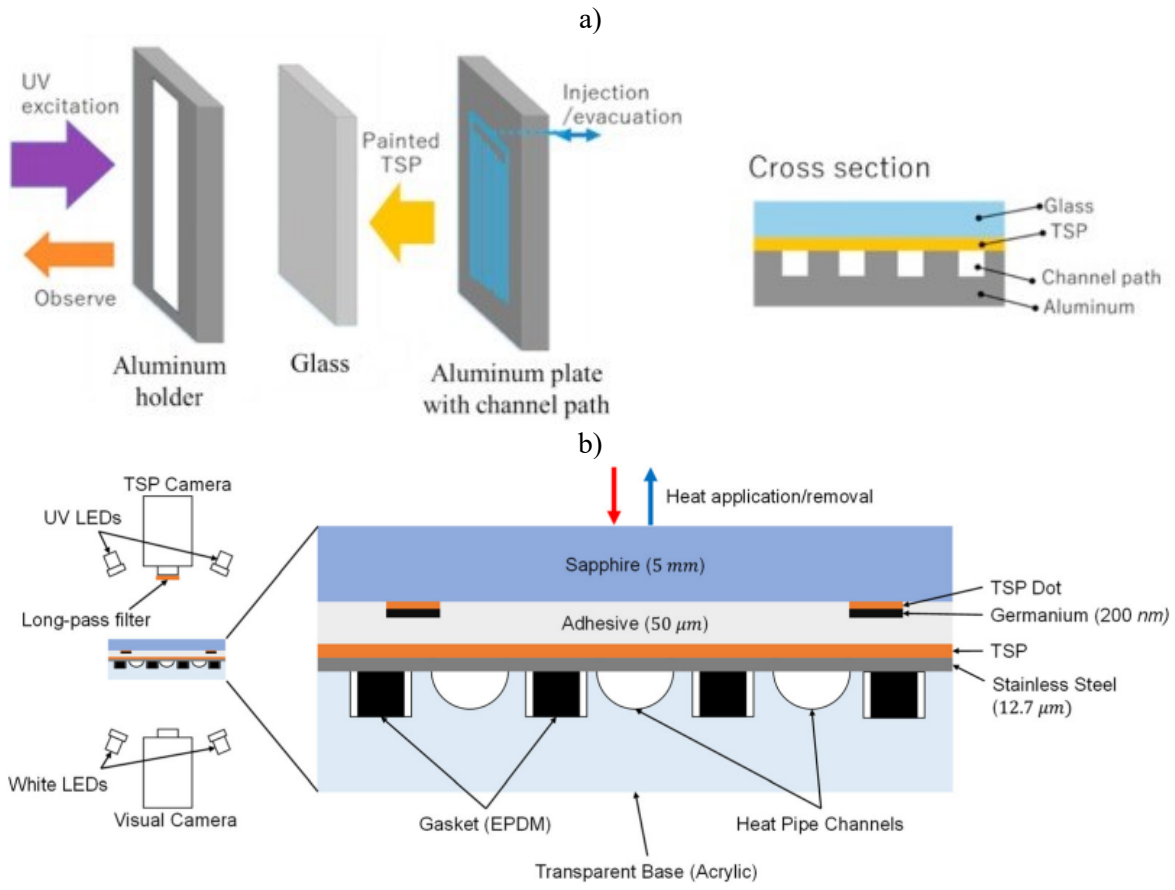

Figure 3.11: Specifics of the device adopted in [92] for the temperature measurement of the fluid-glass and aluminium-glass interfaces by temperature-sensitive paint (a); set-up used in [93] for the simultaneous acquisition of wall temperature and fluid visualization (b).

Heat fluxes exchanged across an adhesive layer were also locally calculated to provide a quantitative description of the sensible-latent heat transfer, strengthened by direct fluid visualizations. However, the overall uncertainties of the estimated quantities were significantly high; moreover, the weak approximations of latent heat mainly transferred by vapour plugs and sensible heat mainly transferred by liquid slugs should be carefully considered. The forehead mentioned and not fully explored methods based on visualizations might be useful tools for the PHP thermo-fluid dynamics study, although their outcomes could not be fully reliable, and their implementation requires an in-depth know-how and complex manufacturing.

Alike direct fluid visualizations, indirect visualizations by neutron radiography have been adopted for the study of the PHPs fluid dynamics [94–99]. Such a technique is based on neutrons penetration through metallic surfaces and attenuation by hydrogen atoms. Specifically, the attenuation coefficient is higher for the liquid phase, while lower for the vapour phase. In practice, when a metallic PHP filled with fluid containing hydrogen (e.g., water or acetone) is exposed to a neutron beam, the radiation passes through walls and vapour plugs, while it is attenuated by liquid slugs. The implementation of such a method is thus challenging due to expensive experimental facilities, such as neutron emitters and receivers, which are not commonly available in research labs due to high costs and great health hazard. Nonetheless, when compared to visible light imaging, this method presents the great advantage of granting visualizations of fully opaque devices without any need for low-conductivity, transparent inserts. Hence, the remarks obtained by neutron radiography can be more quantitatively extended to the phenomenological description of other metallic PHPs, usually studied by other typical techniques. The outcomes provided by this visualization approach are generally similar to those found by means of visible light imaging, and they are not here presented in detail. However, it has to be highlighted that the attenuation of neutron beams is linked to the void fraction in PHPs by the Beer-Lamber law, $I=I_0 exp(-\mu x)$. In fact, the intensity of the radiation I measured by the receiver, i.e., the intensity of grey-scale neutron images, depends on the incident intensity I_0 of the neutron beam, the attenuation coefficient μ for the attenuating material, and the distance x travelled through the material. Yoon et al. [97] took advantage of this relationship to thoroughly evaluate the volume fraction of liquid and vapour in the sections of a closed-loop PHP at varying heat loads to the evaporator, underlining that liquid is mainly present in the condenser section. Time evolutions of the liquid fraction were also reported and compared with wall temperature measurements through thermocouples.

3.3.2. Infrared thermography

Together with visualization techniques, infrared measurements can be classified among non-intrusive experimental methods for the PHPs analysis. When compared to visible light imaging, infrared thermography is still an undergrown technique for what concerns PHPs, and its potential has not been already fully disclosed. Specifically, such a method is based on the measurement of infrared radiations emitted by the observed body through specific equipment, i.e., InfraRed (IR) cameras. Radiative heat

fluxes are eventually converted into temperature signals, depending on the radiative properties of the investigated object. IR cameras provide two main advantages with respect to other temperature sensors: much higher space discretization of the temperature field (depending on the number of pixels of the sensor) and better assessment of temperature variations. On the contrary, absolute temperatures are generally measured with lower accuracy. Due to the relatively high cost of IR cameras, IR thermography might not be affordable for low-budget experimentations, especially when high-accuracy and high-speed acquisitions (with great pixel resolution) are required. The need for highly emissive objects for quantitative measurements represents another limitation of the method, which prevents its direct applicability to many experimental set-ups (e.g., presenting glass or metallic tubing). However, when focusing on the PHPs outer wall temperature, such a drawback can be easily overcome by opportunely treating either metallic or glass surfaces with high-emissivity coatings, i.e., by opaque paints or tapes.

In this case, IR measurements are mainly carried out with the aim of providing a description of wall temperature fluctuations in different PHP sections. Consequently, qualitative remarks on the fluid motion at varying operating conditions (e.g., varying power inputs to the evaporator) can be shown. A complete outline of the device behaviour can be proficiently achieved by means of thermography, since temperature is recorded at multiple locations over time. The work by Karthikeyan et al. [50] well represents the usual outcomes collected by infrared investigations on PHPs. Here, both the evaporator and part of the adiabatic section of a multi-turn PHP made of copper were coated with a high-emissivity black paint, and IR acquisitions were therefore carried out during its operation. The PHP working regimes were clearly identified, from inactivity up to a quasi-circulatory flow (Figure 3.12). Specifically, the interpretation of the global PHP thermal behaviour is greatly eased with IR, space-time temperature maps, when compared with the adoption of few thermocouples, arbitrarily placed on top of the device wall. Apart from qualitative conclusions, meaningful heat transfer quantities could be furtherly provided, starting from IR acquisitions, although their evaluation has been achieved in few experimental works. Specifically, Cattani et al. [100] performed IR measurements on the outer wall of a sapphire channel in a single-loop PHP. Half of the channel surface was coated with a thin, uniform layer of high-emissivity paint. The resulting raw data were then used as inputs for the Inverse Heat Conduction Problem (IHCP) resolution approach, leading to the evaluation of heat fluxes locally exchanged between the working fluid and the device wall within the adiabatic section. The Tikhonov method was used as inverse method (for additional details, see Paragraph 4.4.1).

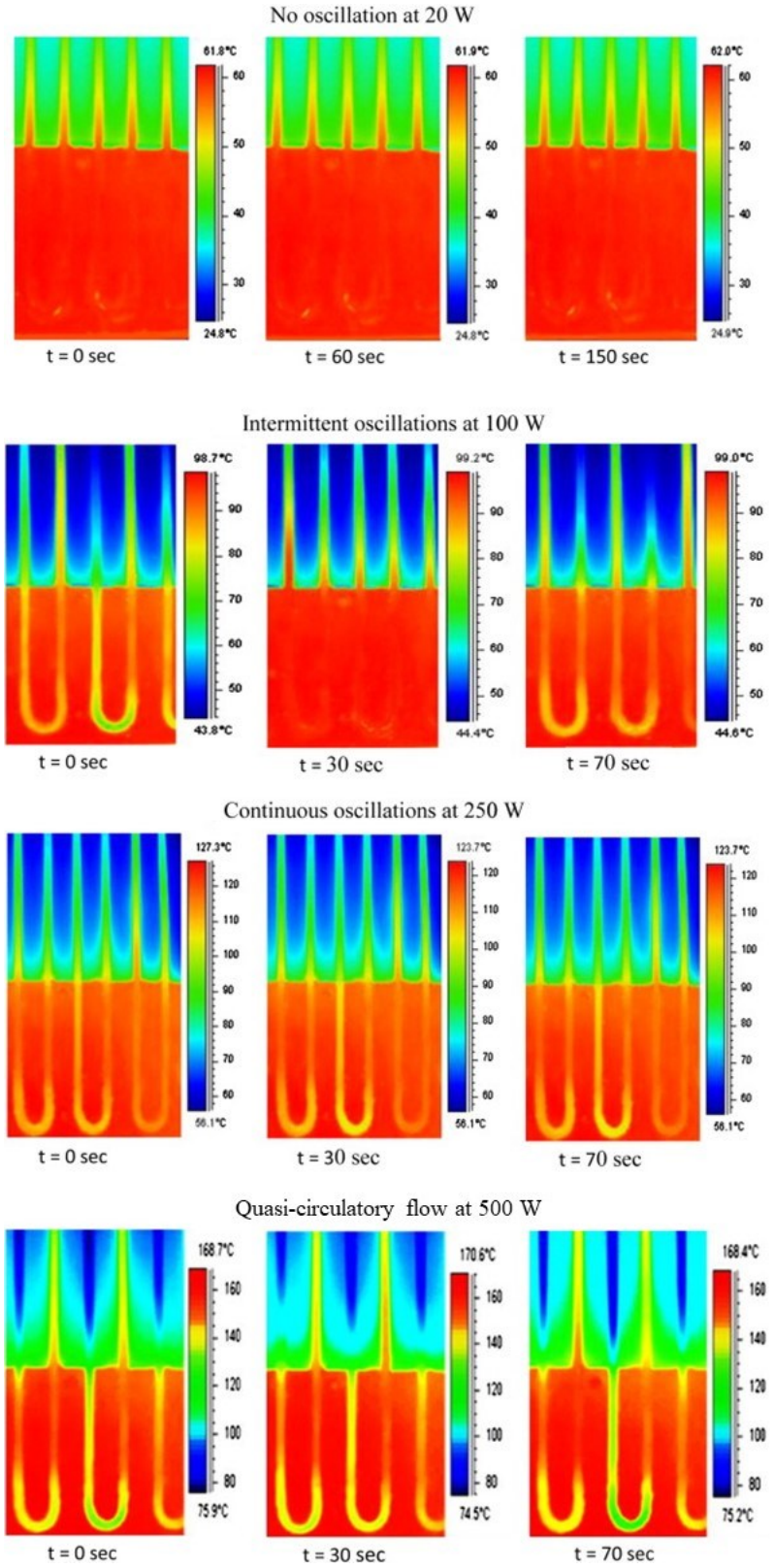

Figure 3.12: Typical IR observations of the PHP outer wall temperature for different working regimes [50].

Jo et al. [101] focused on the estimation of the same heat transfer quantity (wall-to-fluid heat flux) through thermography, whereas investigating a different PHP layout with a different post-processing

method. In particular, the studied device was a micro-PHP made of a glass piece, machined for the fluid path, and a substrate constituted by Indium Tin Oxide (ITO), polyimide and silicon layers (Figure 3.13).

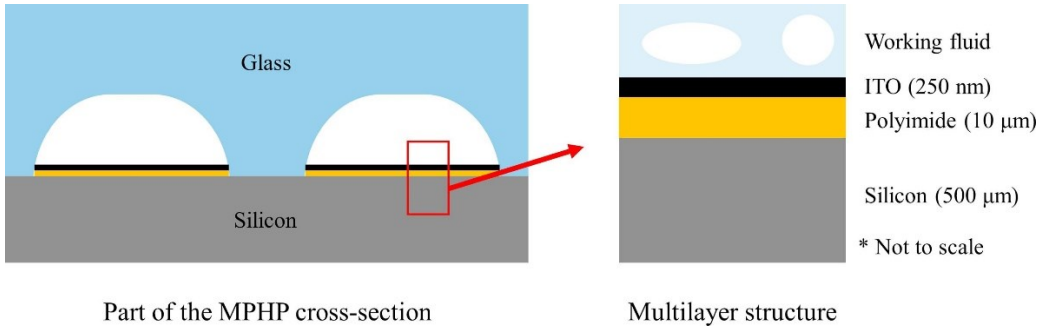

Figure 3.13: Cross-section of the micro-PHP by Jo et al. [101], magnified at the multilayer substrate (conduction/radiation problem resolution).

The IR camera framed the opaque section of the device, i.e., the multilayer substrate. Different radiative properties of each substrate layer (e.g., transparency of silicon in the infrared spectrum) were adopted for evaluating both the outer (polyimide) and inner wall (ITO) temperature by means of the conduction/radiation problem resolution, finally resulting in the estimation of wall-to-fluid heat flux distributions. The estimation procedure by Kim et al. [102] concerning temperature and heat flux distribution measurements on a boiling surface by thermography was replicated in this work. However, it has to be pointed out that the adopted multilayer wall can be hardly implemented, from a manufacturing point of view, on tubular layouts, due to difficulties in obtaining tubes made of circular-shaped layers.

A few other IR investigations focused instead on direct fluid temperature measurements [101,103–106]. Nonetheless, similarly to visible light imaging, the evaluation of fluid temperature in PHPs requires inserts transparent to infrared radiations. In the case of tubular layouts, the most employed transparent inserts are those made of sapphire, which has, at rather low thicknesses (≈ 1 mm), transmission coefficient equal to about 0.9, as well as transparency to visible light. Alike glass tubing, the first manufacturing difficulty is represented by obtaining connections between metallic and sapphire channels. Since sapphire tubes are generally fragile and hardly commercially available, the best solution might be fixing inserts with epoxy glue rather than applying mechanical stress. Secondly, fluid investigations by IR method can be generally achieved on few parts of the device, especially in the adiabatic section, since the option of manufacturing a PHP entirely made of sapphire could not be feasible. Issues regarding the fluid emissivity should be finally discussed: in fact, the possibility of carrying out quantitative fluid temperature measurements depends on the radiative properties of the analysed fluid. Specifically, vapour is almost fully transparent to infrared radiations (null emissivity), preventing any vapour-phase measurements by means of thermography, while the liquid-phase is

usually highly emissive. However, when considering confined flows inside small, capillary tubes, liquid thickness also plays a significant role: below a certain value (which depends on the considered fluid), the liquid emissivity falls, eventually undermining correct fluid temperature measurements. In other words, IR fluid measurements cannot be quantitatively performed either when the liquid completely fills a channel of low inner diameter or when thin liquid films surround vapour bubbles. Unless previous literature studies already analysed the correlation between liquid thickness and emissivity for the chosen working fluid (this is, for instance, the case of [107] for methanol, ethanol and FC-72, below 2 mm), dedicated tests should be performed.

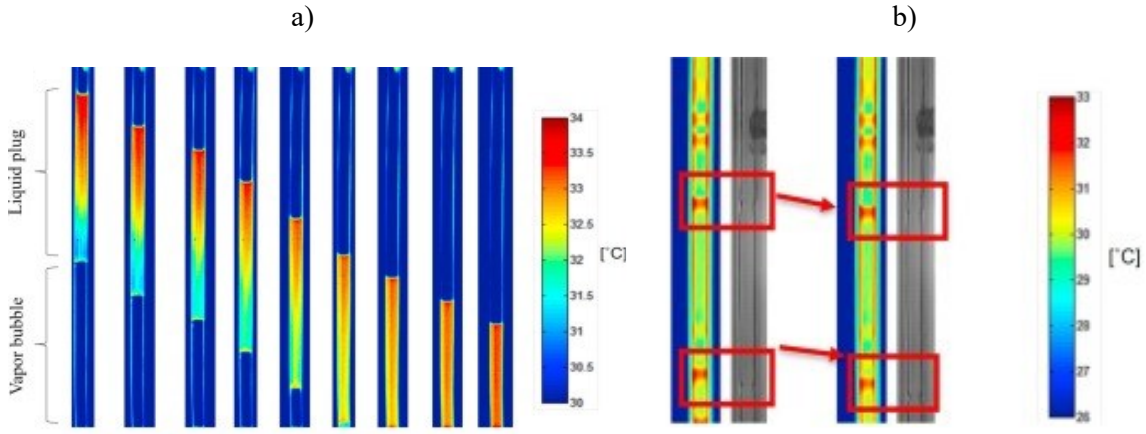

Figure 3.14: Typical IR samples referred to slug-plug flow (a) and annular flow (b) [103].

Typical fluid temperature acquisitions by IR thermography are depicted in the work by Mangini et al. [103], where a sapphire insert belonging to a single-loop PHP was investigated both visually and by thermography. The device was filled with pure ethanol, and the tube had an inner diameter equal to 2 mm. In Figure 3.14a, a slug-plug flow is observed; the temperature field of liquid slugs is quantitatively perceived, while vapour plugs provide same temperature as the colder background, i.e., they are fully transparent to IR radiations. It is interesting to notice that, when annular flows occur (Figure 3.14b), portions interested by vapour columns surrounded by liquid result in a perceived temperature in between the fluid and the background ones. In fact, in annular flows, the liquid thickness is greater than that of thin liquid films typical of slug-plug flows, leading to fairly higher emissivity and opacity of the liquid layer. In [103], the Authors also stated that, during annular flows, IR analysis could be used for further quantitative measurements of the liquid film thickness by taking advantage of the relationship between liquid thickness and emissivity, even though no specific methods were here suggested.

3.3.3. Intrusive techniques

Different intrusive techniques for the study of PHPs can be found in the literature [51,64,67,74,105,108–112]: such methods include temperature or pressure sensors directly inserted in

the fluid stream to provide data about its local thermofluidic behaviour during the device operation. Usually, the sensors are placed inside joints, inevitably introducing discontinuities in the layout. Such discontinuities might result in either a local change in tube section (similarly to transparent inserts) or undesired thermofluidic interactions between the sensors probes and the working fluid. Nonetheless, the introduced perturbations may be usually considered negligible with respect to the overall behaviour of the device. This might not be the case of micro-devices, where the operational behaviour could be strongly influenced by bulky connections. The adopted T-junctions are generally commercial; however, some Authors have underlined the need for specifically designed joints to prevent discontinuities. Mameli et al. [110] took advantage, in the adiabatic section of a multi-turn PHP, of an in-house fabricated brass joint to host a pressure transducer and a K-type micro-thermocouple, whose drawing is shown in Figure 3.15. Both sensors were fixed with epoxy glue.

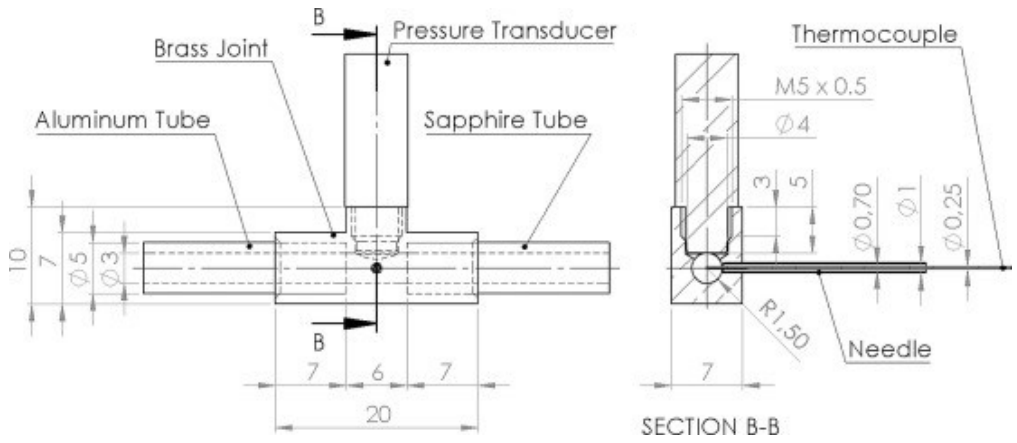

Figure 3.15: Drawing of the T-junction used in [110] for the local acquisition of both fluid pressure and temperature signals (dimensions in mm).

On the contrary, other solutions could significantly modify the device layout, as in the case of Noh and Kim [109], where two pressure sensors were connected to two extruded pipes at the evaporator section (Figure 3.16a). Reliable pressure measurements might be undermined by the presence of vapour bubbles in the auxiliary branches.

For what concerns flat plate layouts, inserting sensors could require complex and scarcely leak-proof solutions, as the one depicted in [113] (Figure 3.16b). Here, an aluminium block and one side of the device (made of polymeric material) were drilled to create a T-junction. The pressure transducer was then mounted on the block, which was glued on top of the PHP surface and secured by two bolts.

Finally, pressure sensors could be inserted in the filling-vacuuming branch; however, since such a portion of dead volume is regarded not to actively participate in the overall thermofluidic behaviour, the resulting measurements might not provide any interesting remark.

a)

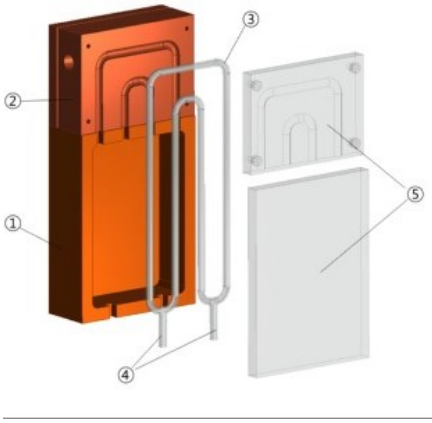

No.	Items
1	Bakelite chamber
2	Copper water jacket
3	Glass PHP
4	Taps for pressure sensors
5	Acrylic window

b)

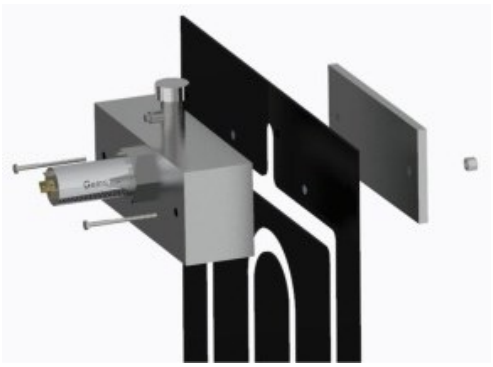

Figure 3.16: Additional solutions for performing local fluid pressure acquisitions. Tubular layout (a), Noh and Kim [109]; flat plate layout (b), Der et al. [113].

From an operative standpoint, fluid pressure measurements in PHPs are used to check whether the device underwent fluid leaks over time; in fact, when the filled device is in thermal equilibrium with the environment, any deviation from the saturation pressure at room temperature denotes that the channels are not perfectly sealed. Such a leak test is especially viable when the layout presents many critical junctions, or the device is made of flexible materials, potentially permeable to incondensable gases [113]. In addition, fluid pressure fluctuations give an insight into the working fluid oscillations, since pressure instabilities are responsible for fluid motion: device activations or stopovers are typically accompanied by pressure oscillations or slightly fluctuating pressure trends, as demonstrated in [74] and [111]. Due to such a strict relationship between fluid motion and pressure variations, hydrodynamic quantities can be evaluated by means of an adequate experimental set-up. Perna et al. [105] reduced pressure signals referred to two transducers placed at both ends of a sapphire channel in the adiabatic section of a multi-turn PHP (microgravity conditions). Raw data were recorded with sampling frequency of 200 Hz, while the distance between the two measurement points was equal to 140 mm. The pressure measurements were used as inputs for the wavelet method, resulting in the evaluation of fluid oscillation frequencies; in addition, the phase between both signals was used to estimate the fluid velocity. Further processing of IR acquisitions validated, with good agreement, the previously found values of velocity. Estimations of fluid oscillation frequencies by means of pressure signals were also performed by Khandekar et al. [86], Mameli et al. [51] and Takawale et al. [49]. The Fourier transform was employed in all the mentioned works, considering one single measurement point, although dominant frequencies were only assessed in [86]. Such a remark raises once again doubts about the best experimental signal to be used for the dominant fluid oscillation frequency evaluation in PHPs, along with the best reduction approach.

Fluid temperature measurements in PHPs are achieved for multiple reasons, mainly linked (but not only) to the device thermodynamics: Sun et al. [67] inserted thermocouples at different locations of a

glass PHP (poor thermal conductivity) to achieve a better evaluation of temperature variations with respect to that obtainable by thermocouples placed on the outer wall. Mameli et al. [51] provided values of heat transfer coefficient by simultaneously measuring the fluid and the wall temperature at the same locations. In Mameli et al. [110], the degree of fluid superheating and subcooling near the two heat transfer sections was estimated by means of coupled fluid temperature-pressure measurements, providing pieces of information on the local thermodynamic state of the working fluid (FC-72). A comparison between outer wall and inner fluid temperature data was carried out by Monroe et al. [64] in terms of fast Fourier transform analysis. While, by considering fluid temperature signals, dominant frequencies could be estimated, the tube thermal inertia prevented the identification of any peaks in the power spectrum through the outer wall temperature. Besides, results by Karthikeyan et al. [114] on direct fluid measurements highlighted no dominant frequency. The frequency analysis was carried out through the fast Fourier transform of the fluid temperature signal acquired within the evaporator section of a PHP entirely made of glass (heating wire at the evaporator, free convection at the condenser). These remarks suggests that the temperature sensors position plays a crucial role in the fluid oscillations assessment, confirming the considerations discussed in Section 3.2, though underlining that the optimal test conditions and post-processing tools for a proper frequency analysis in PHPs (without the aid of direct fluid visualizations) are far from being fully defined.

3.4 Closure

The main techniques adopted for the study of PHPs have been introduced in the present Chapter, highlighting strengths and weaknesses of each approach. The coupled description of implementation and perceived physical phenomena gives useful guidelines to new experimenters and researchers, along with interesting pieces of information to experienced workers in the PHP field. Typical manufacturing solutions are presented, underlining the critical issues related to their application in terms of different device response. The outcomes provided so far by taking advantage of each mentioned method are also outlined. The potentiality of the explored investigation approaches is shown, together with a more critical understanding of the most suitable experimental set-ups for the improvement of the existing literature. Few uncommon and unexplored methods are also introduced as reference for future, possible developments.

The main experimental techniques for the PHP study are summarized in Table 3.1, along with the manufacturing/implementation costs, a rough estimation of the number of works dealing with each method, the set-up and implementation solutions, and the observed physical phenomena.

Every implementation solution depends on many factors, such as the availability of some experimental equipment or the feasibility of modifying the device layout in particular sections of interest.

In particular, the review analysis has highlighted that there is not a clear standardization of the experimental set-ups, which greatly hampers univocal and quantitative comparisons between experimental works. This is mainly due to different ways of providing/dissipating heat, i.e., to the different boundary condition. Power input can be provided by electrical resistance inside thermal spreaders or by wire resistances twisted around the tubes. The condenser section might be interested by free/forced convection with air or cooled by liquid flowing at controlled temperature. Set-ups might present transparent inserts both in the adiabatic section and the heat transfer areas, modifying the heat transfer behaviour of the device. Junctions for the connection of transparent inserts or for intrusive measurements of the working fluid thermodynamic properties might perturb the fluid stream. All these dissimilarities could lead to different values of investigated quantities, such as the equivalent thermal resistance, the fluid velocity/oscillation frequency or the fluid temperature. Apart from qualitative investigations, the study on the PHPs operation and overall physical behaviour should be thus carried out by defining a standard procedure of implementation for the experimental set-ups. Alternatively, more general parameters, i.e., which are not influenced by the specific set-up conditions, should be employed as characteristic quantities for the device description.

Table 3.1: Experimental techniques typically used for the PHPs investigation.

Experimental procedure	Cost	Number of studies	Peripherals facilities	Implementation solutions	Observed phenomena and estimated quantities
Temperature sensors placed on the outer wall	↓↓	↑↑	Thermocouples, RTDs	Grooved/drilled paths (simple attachment)	• Equivalent thermal resistance • Working regimes • Fluid oscillation frequencies
Visible light imaging	↓	↑	• High-speed camera • Lamps (optional)	• Transparent windows/inserts (glass or plastic materials), glued or mechanically jointed • Fully transparent devices	Fluid displacement (velocity/oscillation frequency/flow direction)
	↑	↓↓	• High-speed camera • UV LEDs • Optical filters • Temperature sensitive paint	Multilayer substrates	Fluid temperature
Neutron radiography	↑↑	↓	• Neutron emitters/receivers • Neutron shields (potential health hazard)	None	• Fluid displacement/velocity/oscillation frequency • Void fraction
IR visualization	↑	↓	IR camera	• Multilayer substrates • Coated sections (high-emissivity coatings)	• Outer/inner wall temperature (working regimes) • Wall-to-fluid heat flux
				Transparent windows/inserts (sapphire), glued	• Fluid temperature (liquid phase) • Liquid film thickness (not verified)

Temperature and pressure sensors inserted in the fluid stream	↓	↓	• Micro-thermocouples • Pressure sensors	Junctions (glued sensors)	• Fluid thermodynamic state • Fluid motion (velocity, oscillation frequency) • Heat transfer coefficient

Part II: Thermal behaviour assessment in pulsating heat pipes (Inverse Heat Conduction Problem resolution approach)

Chapter 4 Inverse Heat Conduction Problem

4.1 Introduction

The present Chapter introduces the reader to inverse problems, with specific reference to the Inverse Heat Conduction Problem. Its general formulation is provided, and some common regularisation methods for a reliable outputs' evaluation are described. Specifically, the Tikhonov method and the filtering approach are presented along with the criteria usually employed for the choice of the optimal regularisation parameters.

4.2 Classification and ill-posed nature of inverse problems

In science, an inverse problem is defined as the process of estimating the causal factors that produce a given set of experimental observations. Its solution is represented by those causes that cannot be directly observed, starting from the study of their physical effects. Inverse problems therefore differ from direct problems, which concern the evaluation of the effects starting from the causes (Figure 4.1) [115].

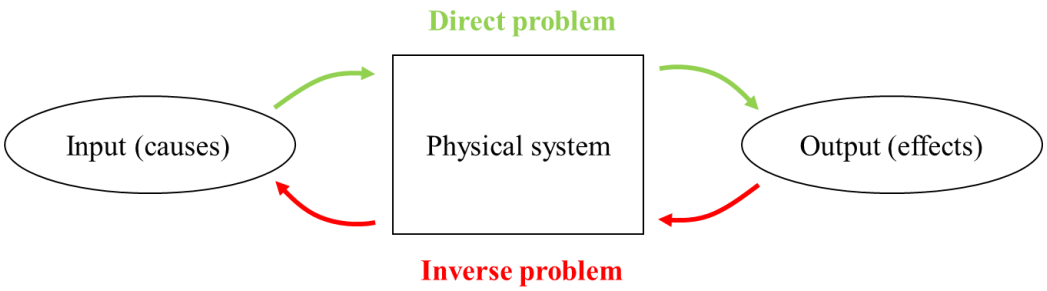

Figure 4.1: Direct vs inverse problem.

If the physics underlying the considered system is adequately understood, causes (b) and effects (x) can be related by specifying a known relationship G such that [116]:

$$G(b) = x \tag{4.1}$$

where d may represent a function of time and/or space, or a collection of discrete observations. In direct problems, x is evaluated given b. Computing $G(b)$ might involve ODEs or PDEs, integrals or algorithms for which there is no explicit analytical formula for $G(b)$. On the other hand, in inverse problems b is evaluated starting from x. When some information is available on the functional form of the unknown quantity b, the inverse problem is reduced to the estimation of few unknown parameters and defined as a parameter estimation problem. By considering, for example, the unknown quantity b as a function of time, and described by a polynomial of the form [117]:

$$b = f(t) = B_1 + B_2 t + B_3 t^2 + \cdots B_N t^{N-1} \tag{4.2}$$

$$f(t) = \sum_{j=1}^{N} B_j C_j(t) \tag{4.3}$$

where B_j are unknown constants and $C_j(t)$ are known functions, the evaluation of b reduces to the problem of estimating a finite number of parameters B_j (N defined in advance). When, instead, the functional form of b is neither available nor assumed, the inverse problem can be regarded as a function estimation problem.

A class of mathematical models for which many useful results exist are linear systems. They obey superposition $G\ (b_1 + b_2) = G(b_1) + A(b_2)$ and scaling $G(\xi b) = \xi G(b)$. In this case, the general formulation of Equation (4.1) can always be written in the form of a linear system of algebraic equations:

$$\boldsymbol{Ab} = \boldsymbol{x} \tag{4.4}$$

where $\boldsymbol{x} \in X$ and $\boldsymbol{b} \in B$, being X and B metric spaces, and $\boldsymbol{A}$ is an operator so that $\boldsymbol{A}X \subset B$. Many important physical problems, spanning from gravitational and magnetic field problems to seismic wave propagation and heat conduction, are characterized by linearity. On the contrary, nonlinear mathematical models arise when the parameters of interest have an inherently nonlinear relationship to the observables. This situation commonly occurs, for example, in electromagnetic field problems.

Anyway, solutions can be found not only for linear problems, but also for non-linear problems, whose resolution will not be dealt with in this dissertation.

A key issue is related to the ill-posed nature of inverse problems (while direct problems are often well-posed, inverse problems are usually classified as ill-posed). In fact, according to Hadamard's definition [118], the following requirements on the solution are needed for an inverse problem to be considered as well-posed:

- Existence;
- Uniqueness;
- Stability.

For the specific case of linear problems, Equation (4.4) represents a well-posed problem when [118]:

- The solution exist for any $\boldsymbol{b} \in B$;
- The solution is unique;
- The solution is stable for even small perturbations of $\boldsymbol{b}$, in other words, when the operator $\boldsymbol{A^{-1}}$ is the defined and continuous in every part of B.

In ill-posed problems, the inverse operator $\boldsymbol{A^{-1}}$ is not continuous in its domain, leading to the fact that the solution is not continuously dependent on the input data $\boldsymbol{b}$. In general, the solution of an ill-posed problem does not continuously depend on the measured data, and the structure of the solution might not have a significant link to the measured data. In addition, even small perturbations on the input data, e.g. noise, may lead to unacceptable perturbation of the solution itself, thus violating the stability requirement.

4.3 Inverse Heat Conduction Problems definition

Engineering filed problems are defined by governing equations, shape and size of the domain, boundary and initial conditions, material properties of the media contained in the field and by internal sources and external forces or inputs. When all these pieces of information are known, the field problems are regarded as well-posed and generally solvable ones.

Focusing on thermal engineering, heat conduction problems are defined by the following governing equations and boundary/initial conditions:

$$\rho c_p \frac{\partial T}{\partial t} = k\nabla^2 T + \dot{Q}_v, \qquad (x, y, z) \in \mathbb{R}^3 \tag{4.5}$$

$$T(x, y, z, t) = T_b(x, y, z, t), \qquad (x, y, z, t) \in S_D \tag{4.6}$$

$$-k\frac{\partial T(x,y,z,t)}{\partial n} = q(x,y,z,t), \qquad (x,y,z,t) \in S_N \tag{4.7}$$

$$-k\frac{\partial T(x,y,z,t)}{\partial n} = h[T(x,y,z,t) - T_e(x,y,z,t)], \qquad (x,y,z,t) \in S_R \tag{4.8}$$

$$T(x,y,z,0) = T_0(x,y,z), \qquad (x,y,z) \in \Omega \tag{4.9}$$

In particular, Equation (4.5) represents the general, three-dimensional formulation for the energy balance equation in the considered domain, where ρ, c_p and k are, respectively, the density, specific heat and thermal conductivity of the material, T is the temperature distribution, ∇^2 is the Laplacian operator and $\dot{Q}_v$ is the volumetric heat generation rate. The energy balance equation is completed by any combinations of conditions on the boundary S of the domain Ω: Equation (4.6) is the Dirichlet boundary condition, Equation (4.7) is the Neumann boundary conditions, while Equation (4.8) is the Robin boundary condition. Lastly, an initial condition, defined by Equation (4.9), might also define the heat conduction problem. T_b, T_e and T_0 are generic functions, while q and h are the heat flux and the heat transfer coefficient, respectively.

In direct heat conduction problems, the temperature distribution throughout the domain is the unknown quantity, and it can be evaluated starting from the given governing equations and boundary/initial conditions. On the contrary, when the temperature distribution is somehow known in either part or totality of the domain, and some of the intrinsic, causal characteristics of the domain need to be evaluated, the problem assumes the definition of Inverse Heat Conduction Problem (IHCP). Depending on the combinations of boundary/initial conditions, IHCPs are classified as follows:

- Boundary value determination inverse problems;
- Initial value determination inverse problems;
- Material properties determination inverse problems;
- Source determination inverse problems;
- Shape determination inverse problems.

In the present discussion, the only boundary determination inverse problems will be considered. In this kind of inverse problems, part of the boundary of a given domain has unknown conditions. Instead, in some points, some results of temperature measurements or anticipated values of temperature are prescribed. While estimating the boundary heat flux is represented by the resolution of a linear problem (low computational effort), the evaluation of other heat transfer quantities as unknowns, such as the convective heat transfer coefficient, is strongly hampered since it involves the minimization of a non-quadratic functional, and the problem cannot be formulated as a linear one.

From a mathematical point of view, while direct problems are often well-posed, inverse problems are usually classified as ill-posed problems. In fact, in inverse problems, the condition of stability is

often violated since, when experimental measurements are considered, small noisy perturbations in the input data could generate great variations of the solution.

4.4 Resolution methods

As already mentioned, when practical, experimental cases are considered, inverse problems give unstable results due to the presence of noise in the input data. Since such a statement might not be readily understandable, a simple one-dimensional conduction example is here provided.

Consider a sphere with isotropic, constant thermal properties, whose temperature T does not substantially vary from point to point (lumped capacitance), and subjected to a time-dependent, sinusoidal heat flux q on the outer surface (Neumann boundary condition). The study case can be investigated by considering four different problems:

1. q is known analytically, T is unknown (direct problem: analytical formulation);
2. q is measured, T is unknown (direct problem: experimental, discrete formulation);
3. T is known analytically, q is unknown (boundary determination inverse problem: analytical formulation);
4. T is measured, q is unknown (boundary determination inverse problem: experimental, discrete formulation).

By combining the governing equation with the given boundary condition, the energy balance equation assumes the form:

$$\rho c_p \frac{dT}{dt} V = qS \tag{4.10}$$

where V and S are the volume and outer surface of the sphere, respectively. For the first problem, the solution can be easily found by analytical means, and T readily assumes the dimensionless distribution of Figure 4.2a. In the second problem, q exhibits a certain noise level due to a whatever experimental procedure. The discrete solution is found by numerical means, e.g., by finite difference method, and shown in Figure 4.2b. Here, the output remains basically unchanged, despite the noisy input data. The analytical problem can be easily and reliably inverted (third problem, Figure 4.2c), evaluating back the heat flux distribution given at the boundary of the domain. However, when an experimental distribution of T is considered (Figure 4.2d), the inverse problem gives an unstable and unreliable solution. This remark has to be accounted for the presence of a first-order derivative in the problem formulation, which amplifies the small, noisy variations of the input data. Such an issue becomes more and more severe as soon as space variations of temperature occur, since the inverse approach is greatly undermined by the additional presence of the Laplacian operator.

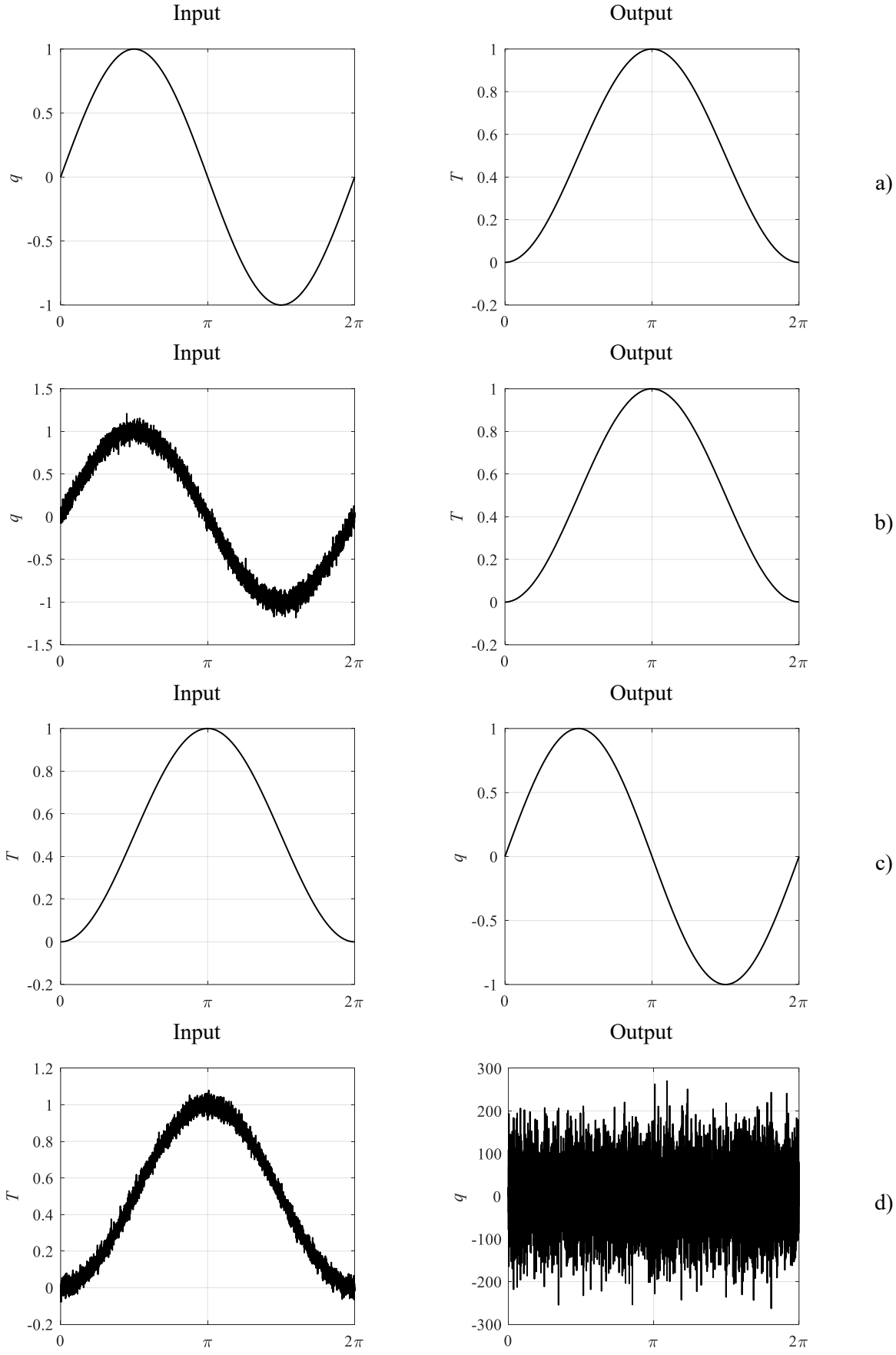

Figure 4.2: Practical example of possible issues faced in dealing with inverse, ill-posed problems.

For a long time, inverse problems had been thought as unsolvable due to their ill-posed nature; nevertheless, in the 60's and 70's, many methods attempting to solve ill-posed unstable problems were formalized, which are based on the idea of reformulating inverse problems as well-posed, stable problems by means of regularisation.

In general, the resolution methods for IHCPs should obey the following criteria [116]:

- The predicted quantity should be accurate if the measured data are of high accuracy.
- The method should be stable with respect to measurement errors.
- The method should have a statistical basis and permit various statistical assumptions for the measurement errors. The method should not require the input data to be a priori smoothed.
- The method should be stable for small time steps or intervals. This permits a better resolution of the time variation of the unknown quantity than is permitted by large time steps.
- Temperature measurements from one or more sensors should be permitted.
- The method should not require continuous first derivatives of unknown functions. Furthermore, the method should be able to recover functions containing jump discontinuities.
- Knowledge of the precise starting time of the application of an unknown surface heat flux or source term should not be required.
- The method should not be restricted to any fixed number of measurements.
- The method should be able to treat complex physical situations, including, among others, composite solids, moving boundaries, temperature dependent properties, convective and radiative heat transfer, combined modes of heat transfer, multi-dimensional problems and irregular geometries.
- The method should be easy for computer programming.
- The computer cost should be moderate.
- The user should not have to be highly skilled in mathematics in order to use the method.
- The method should permit extension to more than one unknown.

For the sake of further applications, the only Tikhonov method and filtering approach will be described in the next Sections.

4.4.1. Tikhonov method

The Tikhonov method, originally formulated in [119], is perhaps the most successful and well-known resolution method for inverse problems of all times. In particular, such a method explicitly

incorporates the regularity requirement in the formulation of the problem. The solution x_λ is found by solving the following minimization problem on the general formulation of Equation (4.4):

$$\min_x \{\|Ax - b\|_2^2 + \lambda^2 \|x\|_2^2\} \tag{4.11}$$

where $\|\cdot\|_2^2$ stands for the square of the 2-norm, and λ is the regularisation parameter. Specifically, the first term $\|Ax - b\|_2^2$ measures the goodness-of-fit, i.e., how well the solution *x* predicts the given (noisy) data *b*. Obviously, if this term is too large, then *x* cannot be considered as a good solution. The same conclusion, on the other hand, can be drawn if this term is too small, i.e., when the residual becomes smaller than the average size of the errors. In fact, this leads to the unwanted result of fitting the noise in the data.

The second term $\|x\|_2^2$ measures the regularity of the solution. The presence of this term comes from the assumption that the naive solution is dominated by high-frequency components with large amplitudes. Hence, by controlling the norm of x, most of the large noisy components are hopefully suppressed. The balance between the two terms is eventually controlled by the factor λ^2. The larger the regularisation parameter λ, the more weight is given to the minimization of the solution norm and thus the regularity of the solution ($x \to 0$ as $\lambda \to \infty$). On the other hand, the smaller the λ, the more weight is given to fitting the noisy data, resulting in solutions that are less regular (the original, naive solution is obtained when $\lambda = 0$).

The goal of the minimization approach is to find an optimal balance between the described terms through a suitable value of λ, such that the regularized solution x_λ is sufficiently regular and it fits well the input data. In other words, the successfulness of the method is achieved when the regularized solution approximates the exact one. Moving deeper into the method, Equation (4.11) represents a linear least squares problem in *x*. In fact, by adopting the following definition, generalized for two arbitrary vectors *y* and *z*:

$$\left\| \begin{pmatrix} y \\ z \end{pmatrix} \right\|_2^2 = \begin{pmatrix} y \\ z \end{pmatrix}^T \begin{pmatrix} y \\ z \end{pmatrix} = y^T y + z^T z = \|y\|_2^2 + \|z\|_2^2 \tag{4.12}$$

the Tikhonov problem can be reformulated as:

$$\min_x \left\| \begin{pmatrix} A \\ \lambda I \end{pmatrix} x - \begin{pmatrix} b \\ 0 \end{pmatrix} \right\|_2 \tag{4.13}$$

where *I* is the identity matrix. The commonly adopted normal equation for this problem assumes the form:

$$(A^TA + \lambda^2 I)x = A^Tb \Leftrightarrow x_\lambda = (A^TA + \lambda^2 I)^{-1}A^Tb \tag{4.14}$$

To obtain more insight into the solution x_λ, the Singular Value Decomposition (SVD) is introduced. In particular, SVD of a given matrix $M \in R^{n\times m}$ $(n \geq m)$ is a factorization of the form $M = U\Sigma V^T = \sum_{i=1}^{n} u_i\sigma_i v_i^T$. Here, $\Sigma = diag(\sigma_1, \dots, \sigma_n)$, where $\sigma_1 \geq \cdots \geq \sigma_n \geq 0$ are the singular values. $U \in \mathbb{R}^{m\times n}$ and $V \in \mathbb{R}^{n\times n}$ are instead constituted by the singular vectors $U = (u_1, \dots, u_n)$, $V = (v_1, \dots, v_n)$, and both matrices have orthonormal columns so that $U^TU = V^TV = I$. When the SVD of A and the relation $I = VV^T$ are included in Equation (4.17), the solution x_λ assumes the form:

$$x_\lambda = V(\Sigma^2 + \lambda^2 I)^{-1}\Sigma \mathrm{U}^{\mathrm{T}} b \tag{4.15}$$

and, by adopting the singular values and vectors:

$$x_\lambda = \sum_{i=1}^{n} \frac{\sigma_i}{\sigma_i^2 + \lambda^2} u_i^T b v_i = \sum_{i=1}^{n} \frac{\sigma_i^2}{\sigma_i^2 + \lambda^2} \frac{u_i^T b}{\sigma_i} v_i = \sum_{i=1}^{n} \varphi_i^{[\lambda]} \frac{u_i^T b}{\sigma_i} v_i \tag{4.16}$$

In Equation (4.17), $\varphi_i^{[\lambda]}$ is the filter factor, whose filtering behaviour is shown in Figure 4.3. The magnitude of $\varphi_i^{[\lambda]}$ determines how strongly the SVD components influence x_λ.

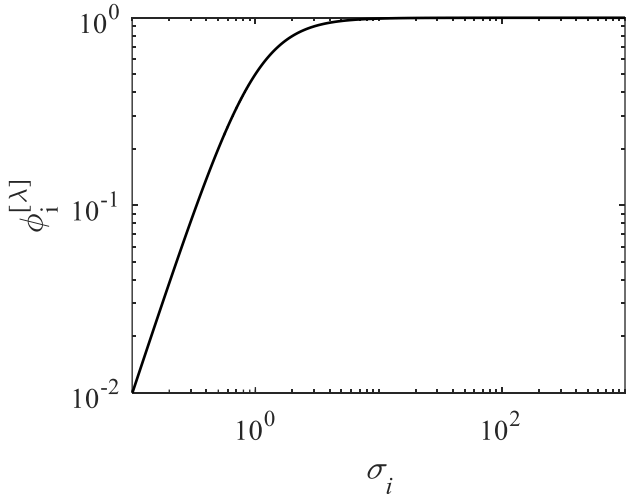

Figure 4.3: Filter factors as functions of the singular values; $\lambda = 1$.

Hence, from the SVD analysis, it can be concluded that the Tikhonov solution is indeed a filtered solution, whose response can be controlled by varying λ. For the estimation of the optimal regularisation

parameter, the Tikhonov method usually relies on the L-curve method. A deeper insight into such a method (application to a circular pipe) will be provided along the text.

4.4.2. Filtering approach

The filtering approach is a technique in which the solution for the inverse problem is directly aimed without involving any minimization processes. Such an approach represents an atypical resolution method, since the starting inverse problem is not here reformulated as a well-posed one, and it involves smoothing of the input data. Depending on the analysed case, the robustness of this method is consequently lower when compared to other techniques, even though its easy formalization and poor computational requirements are responsible for its great appeal from an applicative standpoint.

In this approach, the noisy input data are filtered by means of anyhow formulated filtering function: many assumptions on the nature of noise affecting input data could be drawn, thus leading to the potential choice of different filtering functions. Usually, when experimental data are considered, the noise distribution can be regarded as Gaussian. For these applications, the Gaussian filter represents a suitable filtering function, widely employed in image denoising [120]. In particular, the transfer function *H* of the Gaussian filter in the frequency domain is defined, according to its one-dimensional formulation, by:

$$H(u) = e^{-u^2/2u_c^2} \tag{4.17}$$

where u_c is the cut-off frequency. The transfer function is plotted, in Figure 4.4, as a function of the frequency component *u*.

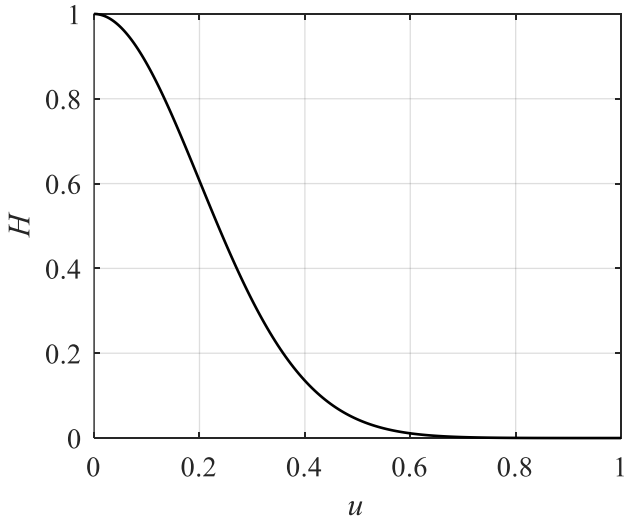

Figure 4.4: Transfer function of the one-dimensional Gaussian filter, u_c = 0.2; the responsive value at the cut-off frequency is almost equal to 0.6.

It has to be noted that u_c acts here alike the regularisation parameter λ in the Tikhonov method. The smoothness and regularity of the inverse problem solution is thus guaranteed by adopting an optimal cut-off frequency. However, such a value cannot be known a priori; in fact, its choice relies on the discrepancy principle, which will be described in the next Paragraph.

4.5 Optimal regularisation parameters choice

4.5.1. L-curve method

The L-curve method is a graphical tool for the evaluation of the optimal regularisation parameter in different resolution methods for invers problems, such as the Tikhonov method. In fact, the optimal trade-off between regularity of the solution and its fit to input data is always aimed in minimization approaches. Considering Equation (4.11), the two discussed terms can be plotted one versus the other in the same, logarithmic graph, as a function of the regularisation parameter λ. The resulting curve is precisely the L-curve. In Figure 4.5, a typical L-curve is shown [121]: the optimal trade-off is visually obtained by identifying the λ value such that the curve presents a corner.

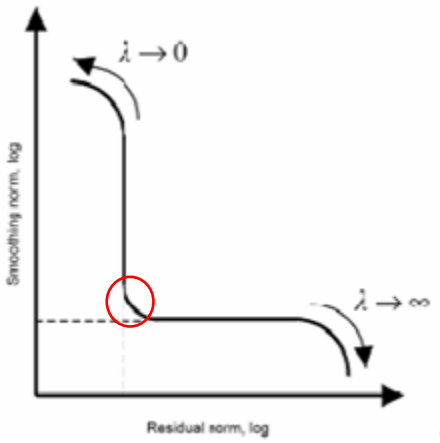

Figure 4.5: Typical trend of an L-curve [121]; the smoothing norm of the solution is plotted against the residual norm of the solution.

4.5.2. Discrepancy principle

The discrepancy principle is a simple and widely used criterion adopted for the choice of the optimal regularisation parameter in the context of inverse problems. Such a method, originally formulated by Morozov [122], predicts that the optimum value is obtained when the discrepancy between the

calculated and measured input ($\tilde{b}$ and b, respectively) coincides with the noise level σ_b. In other terms, it is defined as:

$$\frac{\left\|\tilde{b} - b\right\|_2^2}{N} \cong \sigma_b \tag{4.18}$$

where N is the dimension of b. In particular, $\tilde{b}$ generally comes from the adoption of the regularised solution in the direct problem; hence, the method represents a stopping criterion for the iterative evaluation of regularised solutions, until the optimal one is found.

4.6 Closure

In inverse problems, causes of physical phenomena are evaluated starting from the observed effects. In inverse heat transfer problems, temperature and/or heat flux measurements allow the estimation of unknown quantities appearing in the analysis of physical problems in thermal engineering. Specifically, in inverse problems dealing with heat conduction, the boundary heat flux (cause) is usually estimated, while the temperature field in the body (effect) is measured.

However, inverse problems are inherently ill-posed from a mathematical standpoint. In other words, their solution might be extremely unstable due to the presence of noise in the threated raw experimental data. Their resolution is thus obtained through regularisation methods, such as the Tikhonov method and the filtering approach. The choice of the optimal regularisation parameters is usually achieved by means of the L-curve method or the discrepancy principle. In the next Chapter, some applications of the IHCP resolution approach to the case of PHPs will be presented.

Chapter 5 Inverse Heat Conduction Problem in pulsating heat pipes

5.1 Introduction

The present Chapter deals with the newly proposed techniques for the local heat flux exchanged between the working fluid and the device wall in PHPs. Specifically, the here described approaches are referred to both bidimensional problems, such as cylindrical pipes in which the conduction phenomena mainly occur along one spatial dimension over time, and three-dimensional problems, where two spatial coordinates are taken into account. First, a robust yet demanding method in terms of computational burden is described, with reference to the Tikhonov method for the regularisation of the solution. Secondly, a fast and reliable method based on the Gaussian filtering is addressed. All the methods are applied on the adiabatic section of the devices, i.e., where the boundary condition of free convection with air and radiation is uniformly present over the entire outer wall surface.

5.2 Tubular geometries

5.2.1. Sapphire inserts

A channel whose thermal and geometric properties result in a low thermal response of the conductive medium to perturbations is considered. This is the case of transparent inserts, e.g., sapphire channels, in PHPs. Specifically, the considered channel belongs to the adiabatic section of the device, without thermal insulation from the environment, and it is interested by inner convection due to working fluid oscillations. The sketch of the solid domain is shown in Figure 5.1, with reference to the geometrical coordinates of interest. The conduction problem is here defined by the following conditions and assumptions:

- Time-dependent heat flux at the inner wall surface;
- Combination of free convection and radiation towards the environment at the outer wall surface;
- Isotropic and constant thermal properties of the material;
- Negligible variations of temperature along the circumferential coordinate α;
- Temperature distribution at the outer surface is experimentally measured at J locations over N time instants.

Hence, in the solid domain, the temperature distribution is considered to vary along the radial coordinate r, the axial coordinate z, and time.

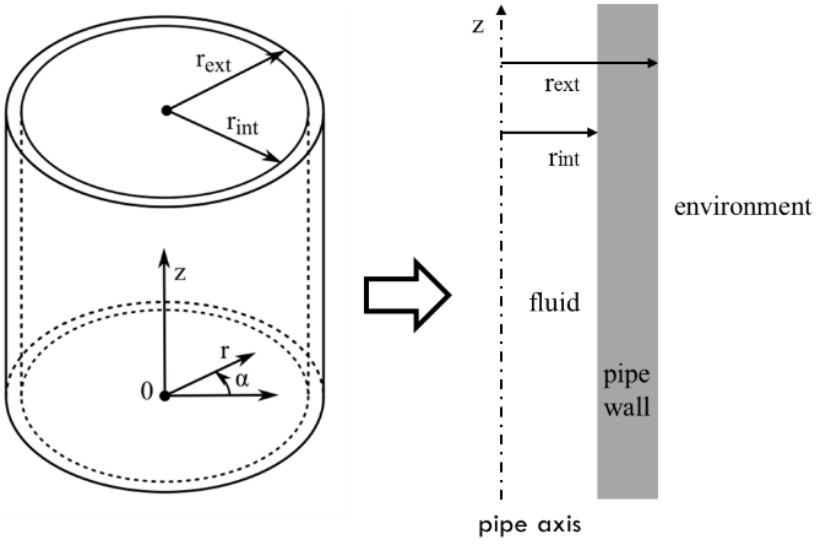

Figure 5.1: Sketch of the considered solid domain.

The problem, according to its general formulation relying on Equation (4.4), can be defined as follows:

$$\boldsymbol{Xq} + \boldsymbol{T_0} = \boldsymbol{T} \tag{5.1}$$

where $\boldsymbol{T}$ is the discrete vector of experimental data, $\boldsymbol{q}$ is the heat flux distribution at the inner wall surface, $\boldsymbol{T_0}$ is the homogenous term resulting from a null heat flux, and $\boldsymbol{X}$ is the sensitivity matrix.

Specifically, $\boldsymbol{T}$ and $\boldsymbol{q}$ are respectively defined as:

$$\boldsymbol{T} = \begin{pmatrix} T_1(1) \\ \vdots \\ T_J(1) \\ \vdots \\ T_1(N) \\ \vdots \\ T_J(N) \end{pmatrix} \quad , \quad \boldsymbol{q} = \begin{pmatrix} q_1(1) \\ \vdots \\ q_K(1) \\ \vdots \\ q_1(N) \\ \vdots \\ q_K(N) \end{pmatrix} \tag{5.2}$$

where q is referred to k different locations. In other words, $\boldsymbol{T}$ is a column vector having $J \times N$ rows, while $\boldsymbol{q}$ is a column vector having $K \times N$ rows.

The sensitivity matrix is instead a lower triangular matrix defined as:

$$\boldsymbol{X} = \begin{pmatrix} \boldsymbol{x(1)} & 0 & 0 & 0 \\ \boldsymbol{x(2)} & \ddots & 0 & 0 \\ \vdots & \cdots & \ddots & 0 \\ \boldsymbol{x(N)} & \boldsymbol{x(N-1)} & \cdots & \boldsymbol{x(1)} \end{pmatrix} \quad , \quad \boldsymbol{x(n)} = \begin{pmatrix} x_{11}(n) & \cdots & x_{1K}(n) \\ \vdots & \ddots & \vdots \\ x_{J1}(n) & \cdots & x_{JK}(n) \end{pmatrix} \tag{5.3}$$

where $\boldsymbol{x(n)}$ is the component at the n-th time instant. Here, each element is defined, for the j-th and k-th locations, as:

$$x_{jk}(n) = \frac{\partial T_{jn}}{\partial q_k(1)} \tag{5.4}$$

Intuitively, the sensitivity matrix describes the thermal response of the considered conductive medium, i.e., it quantifies temperature variations at prescribed locations j and time instants n when a perturbation is applied at the first time instant and at a generic location k. The sensitivity matrix of the system, for a generic geometry and material, can be usually calculated numerically.

The regularised solution to the problem of Equation (5.1) is therefore obtained by solving the linear least squares problem of Equation (4.14), coupled with the L-curve method for the choice of the optimal regularisation parameter. For computational implementation, the discretization of the linear inverse problem of Equation (5.1) can be employed by means of the SVD method, as expressed in Equations (4.15) and (4.16). Further details about the estimation error of this inverse approach are reported in [75].

5.2.2. Metallic channels

A channel whose thermal and geometric properties result in a significant thermal response of the conductive medium to perturbations is instead considered. The geometrical reference is here the same as the one adopted in Figure 5.1. The inner and outer conditions are basically the same used in the previous Paragraph, except for the thin-wall approximation:

$$T(r,z) \cong T\left(r_{int},z\right) \cong T\left(r_{ext},z\right)\big) \tag{5.5}$$

With this further assumption, the temperature distribution becomes only function of the axial coordinate z and time. Obviously, such an approximation is only valid when the material is highly conductive, and its thickness is rather limited (in general, when the Biot number is lower than 0.1). The governing equation in the solid domain is defined by Equation (4.5) with no heat generation:

$$k\nabla^2 T = \rho c_p \frac{\partial T}{\partial t} \tag{5.6}$$

The boundary conditions of Equation (5.7) and Equation (5.8), applied on the inner surface and on the outer surface of the channel, respectively, complete Equation (5.6):

$$-k\frac{\partial T}{\partial r}\Big|_{r=r_{int}} = q \tag{5.7}$$

$$\frac{\partial T}{\partial r}\Big|_{r=r_{ext}} = -\frac{(T-T_{env})}{R_{env}} \tag{5.8}$$

where q is the exchanged heat flux, T_{env} is the environmental temperature and R_{env} is the overall heat-transfer resistance (natural convection + radiation) between the channel wall and the surrounding environment.

With reference to the infinitesimal wall section of length Δz, described in Figure 5.2, the local energy balance equation assumes the form of Equation (5.9).

$$\frac{dU}{dt} = Q_z - Q_{z+\Delta z} + Q_{r_{int}} - Q_{r_{ext}} \tag{5.9}$$

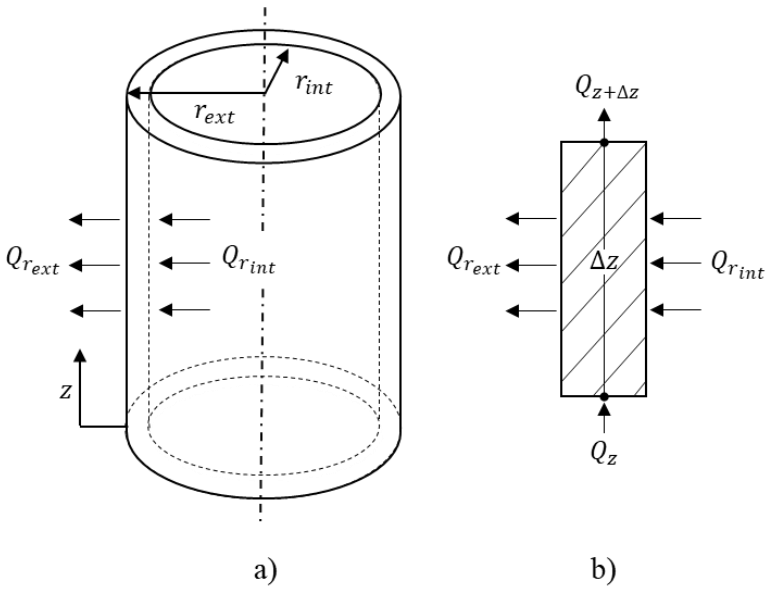

Figure 5.2: Portion of the test section (a) and generic wall element (b).

The equation terms are expressed as follows:

$$Q_z = -k\frac{\partial T}{\partial z}\cdot\pi\left(r_{ext}^2 - r_{int}^2\right) \tag{5.10}$$

$$Q_{z+\Delta z} = -k\frac{\partial T}{\partial z}\cdot\pi\left(r_{ext}^2 - r_{int}^2\right) - k\frac{\partial^2 T}{\partial z^2}\cdot\pi\left(r_{ext}^2 - r_{int}^2\right)\cdot\Delta z \tag{5.11}$$

$$\frac{dU}{dt} = \rho c_p\frac{\partial T}{\partial t}\cdot\pi\left(r_{ext}^2 - r_{int}^2\right)\cdot\Delta z \tag{5.12}$$

$$Q_{r_{ext}} = \frac{(T - T_{env})}{R_{env}}\cdot 2\pi r_{ext}\cdot\Delta z \tag{5.13}$$

$$Q_{r_{int}} = q\cdot 2\pi r_{int}\cdot\Delta z \tag{5.14}$$

By substituting Equations (5.10)-(5.14) into Equation (5.9), the energy balance equation becomes:

$$\rho c_p\frac{\partial T}{\partial t}\cdot\pi\left(r_{ext}^2 - r_{int}^2\right) = k\frac{\partial^2 T}{\partial z^2}\cdot\pi\left(r_{ext}^2 - r_{int}^2\right) + q\cdot 2\pi r_{int} - \frac{(T - T_{env})}{R_{env}}\cdot 2\pi r_{ext} \tag{5.15}$$

Finally, the heat flux on the wall inner surface results:

$$q = \frac{\left(\rho c_p\frac{\partial T}{\partial t} - k\frac{\partial^2 T}{\partial z^2}\right)\cdot\left(r_{ext}^2 - r_{int}^2\right) + \frac{(T - T_{env})}{R_{env}}\cdot 2r_{ext}}{2r_{int}} \tag{5.16}$$

Equation (5.16) can be solved numerically, e.g., by the finite difference method. However, the presence of first and second order derivatives requires the adoption of a regularisation method. In this case, the filtering approach is adopted, thus including in the equation for the wall-to-fluid heat flux the filtered temperature T_f in place of the experimental, noisy one. To apply the filtering approach of Paragraph 4.4.2, the frequency image of the raw temperature is first computed. In particular, for wall temperature samples discretized into M spatial steps Δz and N time increments Δt, the Discrete Fourier Transform of the measured $M \times N$ temperature distribution T results in:

$$\mathcal{F}(T) = \tilde{T}(u,v) = \sum_{g=0}^{M-1}\sum_{h=0}^{N-1} T(g,h) e^{-j2\pi\frac{u}{M}g} e^{-j2\pi\frac{v}{N}h} \tag{5.17}$$

where u and v are the spatial and time coordinates in the frequency domain. By adopting the Gaussian filter, according to its 2D formulation, the Discrete Fourier transform of the filtered temperature becomes:

$$\mathcal{F}(T_f) = \widetilde{T_f}(u,v) = H(u,v) \cdot \tilde{T}(u,v) \tag{5.18}$$

$H(u,v)$ is the transfer function for the Gaussian filter, defined, in two dimensions, as:

$$H(u,v) = e^{-(u^2+v^2)/2u_c^2} \tag{5.19}$$

Last, the Fourier image is converted back to the time-space domain:

$$\mathcal{F}^{-1}(\widetilde{T_f}) = T_f(m,n) = \frac{1}{M \cdot N}\sum_{k=0}^{M-1}\sum_{l=0}^{N-1} \widetilde{T_f}(k,l) e^{j2\pi\frac{k}{M}m} e^{j2\pi\frac{l}{N}n} \tag{5.20}$$

The optimal cut-off frequency is evaluated by means of the discrepancy principle. The steps followed in the filtering procedure are summarized in the flowchart of Figure 5.3.

The estimation error of to the wall-to-fluid heat flux for the present approach is discussed through a dedicated validation in Appendix A for the test cases of Chapter 7 and Chapter 8.

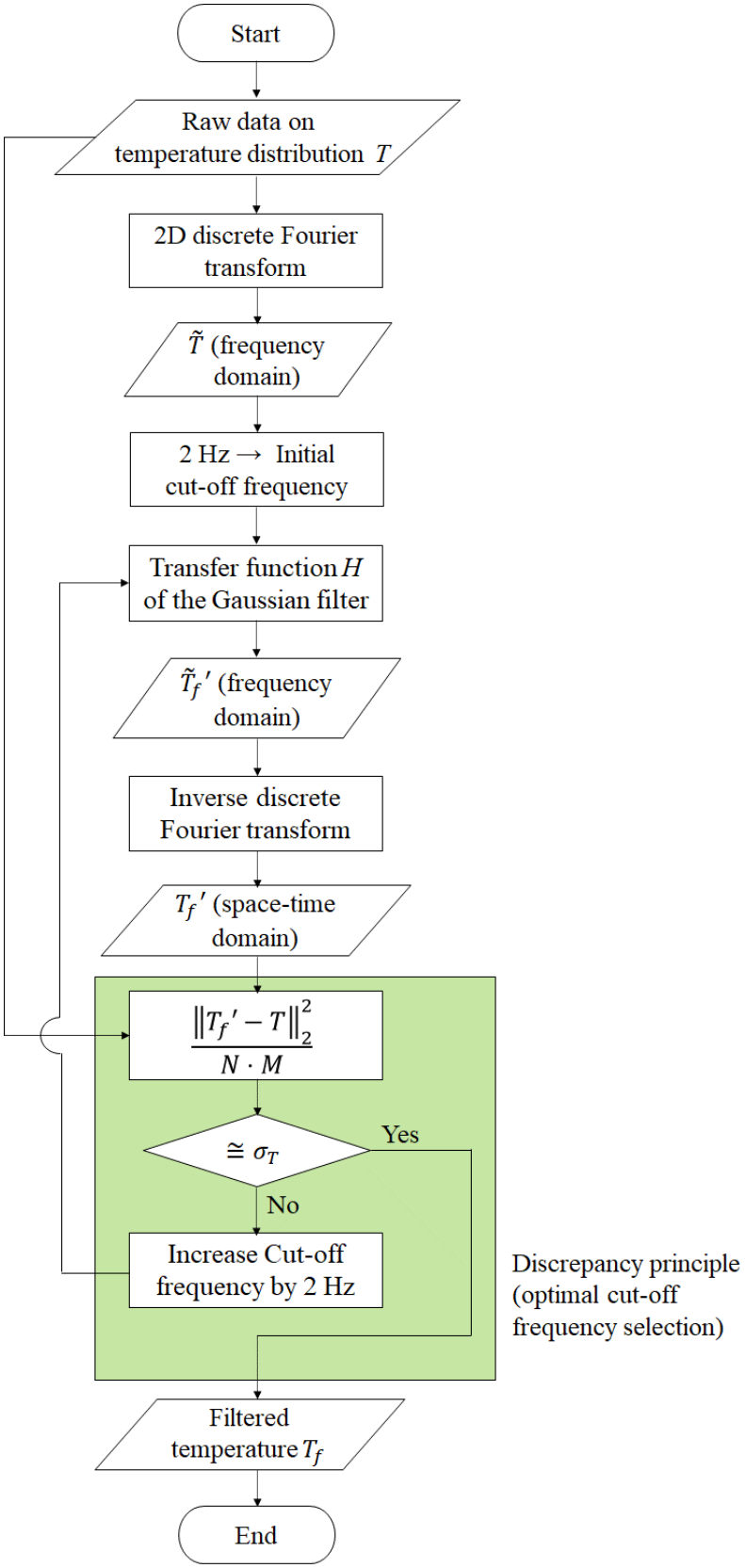

Figure 5.3: Filtering procedure steps.

5.3 Flat plate geometries

In FPPHPs, the evaluation of the wall-to-fluid heat flux becomes intrinsically more challenging due to the complex interplay between inner convection and conduction through the solid domain, especially when it is made of highly conductive material. The three-dimensional geometry of the generic channel is outlined as a plane-symmetrical geometry, as shown in Figure 5.4a, where x_{int} corresponds to half of the channel height. In particular, the only walls having low thickness $s = x_{ext} - x_{int}$ are considered (delimited by red dotted lines in Figure 5.4a).

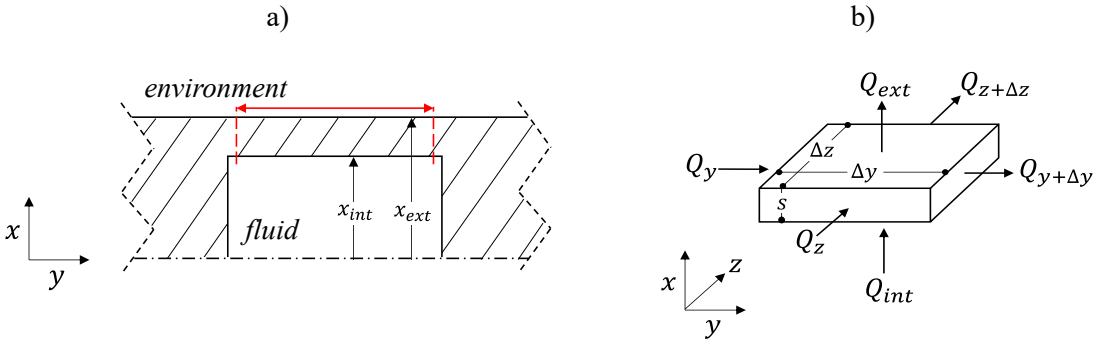

Figure 5.4: Cross-sectional view of a generic FPPHP channel within the adiabatic section (a) and generic wall element (b); red dotted lines delimit the area of interest for the present analysis.

With reference to the wall element of Figure 5.4b, the conduction problem is defined by the following conditions and assumptions:

- Time-dependent heat flux at the inner wall surface;
- Combination of free convection and radiation towards the environment at the outer wall surface;
- Isotropic and constant thermal properties of the material;
- Temperature distribution at the outer wall surface is experimentally measured over N spatial points along y, M spatial points along z and O time instants;
- Thin-wall approximation, such that $T(x = x_{int}, y, z, t) \equiv T(x = x_{ext}, y, z, t)$.

In particular, the latter assumption leads to the fact that the wall temperature distribution is function of the two spatial coordinates y and z, and time.

It is evident that the governing equation for the present problem is the same of Equation (5.6), completed by the same boundary conditions of Equations (5.7) and (5.8). Similarly to Paragraph 5.2.2, the local energy balance equation can be expressed in terms of internal energy variation of the wall element (Figure 5.4b) over time as follows:

$$\rho c_p \frac{\partial T}{\partial t} s \Delta y \Delta z = \left(Q_y - Q_{y+\Delta y}\right) + \left(Q_z - Q_{z+\Delta z}\right) + Q_{int} - Q_{ext} \tag{5.21}$$

The power terms appearing in Equation (5.21) are defined as:

$$\left(Q_y - Q_{y+\Delta y}\right) = \frac{k\partial^2 T}{\partial y^2} s\Delta y\Delta z \tag{5.22}$$

$$\left(Q_z - Q_{z+\Delta z}\right) = \frac{k\partial^2 T}{\partial z^2} s\Delta y\Delta z \tag{5.23}$$

$$Q_{int} = q\Delta y\Delta z \tag{5.24}$$

$$Q_{ext} = h_{env}(T - T_{env})\Delta y\Delta z \quad , \quad h_{env} = \frac{1}{R_{env}} \tag{5.25}$$

By rearranging Equation (5.21), the wall-to-fluid heat flux q reads as:

$$q = s\left(\rho c_p \frac{\partial T}{\partial t} - k\frac{\partial^2 T}{\partial y^2} - k\frac{\partial^2 T}{\partial z^2}\right) + h_{env}(T - T_{env}) \tag{5.26}$$

Here, the filtering approach is again adopted as regularisation method, following the same steps of Paragraph 5.2.2. However, since the here addressed problem depends on a total of three dimensions, the formulations for the Discrete Fourier Transform and the transfer function of the Gaussian filter respectively are:

$$\mathcal{F}(T) = \tilde{T}(u,v,w) = \sum_{g=0}^{M-1}\sum_{h=0}^{N-1}\sum_{i=0}^{O-1} T(g,h,i) e^{-j2\pi\frac{u}{M}g} e^{-j2\pi\frac{v}{N}h} e^{-j2\pi\frac{w}{O}i} \tag{5.27}$$

$$H(u,v,w) = e^{-\left(u^2+v^2\right)/2u_c^2} \cdot e^{-w^2/2w_c^2} \tag{5.28}$$

In Equation (5.28), two cut-off frequencies appear: u_c for the space coordinates and w_c for the time coordinate. Since the physics related to the space coordinates might have a significant weight in the present application, space and time coordinates are, for the sake of the filtering procedure, considered separately (contrarily to the approach of Paragraph 5.2.2). The optimal cut-off frequencies are estimated by means of the discrepancy principle, here formulated, in its bidimensional formulation, as the following minimization problem:

$$\min_{\substack{u_c \in R^+ \\ w_c \in R^+}} fun(u_c, w_c) \quad , \quad fun(u_c, w_c) = \frac{\left\|T_f(u_c, w_c) - T\right\|_2^2}{N \cdot M \cdot O} - \sigma_b \tag{5.29}$$

Since the optimal solution for Equation (5.29) may not be unique, a fixed ratio, *ratio*, between the cut-off frequencies related to space and time dimensions, is introduced to decrease to one the number of degrees of freedom of the objective function *fun*:

$$ratio = \frac{u_{c,opt}}{w_{c,opt}} \tag{5.30}$$

$$u_{c,opt} = \underset{\substack{u_c \in R^+ \\ w_c \to \infty}}{argmin}\, fun(u_c, w_c) \tag{5.31}$$

$$w_{c,opt} = \underset{\substack{u_c \to \infty \\ w_c \in R^+}}{argmin}\, fun(u_c, w_c) \tag{5.32}$$

Hence, the new definition for the transfer function of Equation (5.28) reads as:

$$H^*(u, v, w) = e^{-(u^2+v^2)/2(w_c \cdot ratio)^2} \cdot e^{-w^2/2w_c^2}, \tag{5.33}$$

while Equation (5.29) reduces to $\underset{w_c \in R^+}{min}\, fun(w_c)$, being w_c the only cut-off frequency to be optimized for the final 3D Gaussian filter application.

The estimation error of the wall-to-fluid heat flux for the present approach is discussed through a dedicated validation in Appendix B for the test case of Chapter 8.

5.4 Closure

The IHCP resolution approach for the PHP analysis is presented for tubular and flat plate layouts. While the Tikhonov regularisation method represents a more robust and general approach, valid for different tube materials and, consequently, for different tube thermal properties, its computational burden is extremely high, especially for multidimensional investigations (high number of degrees of freedom). For highly conductive layouts (metallic walls), the reasonable thin-wall approximation allows a reduction in the number of degrees of freedom describing the considered physics. In this case, the more computationally efficient filtering approach can be adopted, allowing analysis on wider datasets and complex geometries without undermining the results accuracy.

Chapter 6 Data reduction methods

6.1 Introduction

In the present Chapter, all the reduction methods adopted for the post-processing of the experimental data collected during the experimental campaigns are described. In particular, all the presented techniques have been mainly applied to the local wall-to-fluid heat fluxes, evaluated by means of the procedures explained in Chapter 5, depending on the geometry under study. This explanation aims at providing the reader with all the necessary tools for the understanding of the main outcomes referred to each studied device. While some of these reduction methods are readily available from the literature, other have been successfully adopted for the first time to PHPs, thus representing an important improvement for such a research field. The adopted methods include statistical techniques, especially useful given the plenty of data provided by the local heat transfer analyses, and techniques based on signal processing tools and algorithms. To enhance the comprehension of the described methods, simple examples are provided along the text.

6.2 Wavelet method and K-means clustering

The understanding of fluid oscillations in PHPs is crucial for a complete evaluation of their heat transfer capability, since oscillations are responsible for heat dissipation at the condenser section. As stated in Chapter 3, such a method has already been employed in the PHP investigation for the fluid oscillation evaluation.

Among all the wavelet functions, the Morlet wavelet, whose shape is defined by Equation (6.1) for dimensionless time η and characteristic parameter ω_0, has been proven to be suitable for the frequency analysis in PHPs [104].

$$\psi(\eta) = \frac{1}{\sqrt{\pi}} e^{-\frac{\eta^2}{2}} e^{i\omega_0 \eta} \tag{6.1}$$

The wavelet transform of a time-dependent signal *g(t)* reads as [123]:

$$W_\psi(a,\tau) = \frac{1}{\sqrt{a}} \int_{-\infty}^{\infty} g(t)\psi^*\left(\frac{t-\tau}{a}\right) dt \tag{6.2}$$

where a and τ are the wavelet scale (dilation of the wavelet function) and time shift, respectively, and the superscript * denotes the complex conjugate. The term $1/\sqrt{a}$ is due to the L1 normalization of the wavelet, used for comparison purposes between different scales.

The wavelet parameters adopted during the experimental investigations of following Chapters are listed in Table 6.1. In particular, such parameters have been chosen to guarantee a good trade-off between frequency and time resolution of the method.

Table 6.1: Parameters used for the wavelet method.

***a* [1/Hz]**	71
ω_0 [rad/s]	2π
f_{min} [Hz]	0.1
f_{max} [Hz]	18

The output of the wavelet analysis is the so-called magnitude scalogram, defined as the absolute value of the wavelet transform, plotted as a function of frequency and time. Specifically, it represents the power related to each frequency over the sample duration. Such a power is strictly linked to the oscillation amplitude of the signal; in fact, high-amplitude oscillations result in high powers in the scalogram. On the other hand, the power spectrum referred to the considered signal is defined as the time integral of the magnitude scalogram, for every frequency. While the scalogram describes the time evolution of the characteristic frequencies underlying the considered oscillatory phenomenon, the power spectrum allows the identification of the dominant frequency f_D related to the considered sample (identified by a peak in the power spectrum). According to their definitions, the measurement units of scalogram and power spectrum are equal to the measurement unit of the analysed signal divided by $Hz^{1/2}$ and $Hz^{3/2}$, respectively, although they are not usually specified in graphs for simplicity.

To provide examples of the wavelet method outputs, four meaningful functions y of time are considered: two sinusoidal functions and two square wave functions with fixed oscillation frequency equal to 1 Hz.

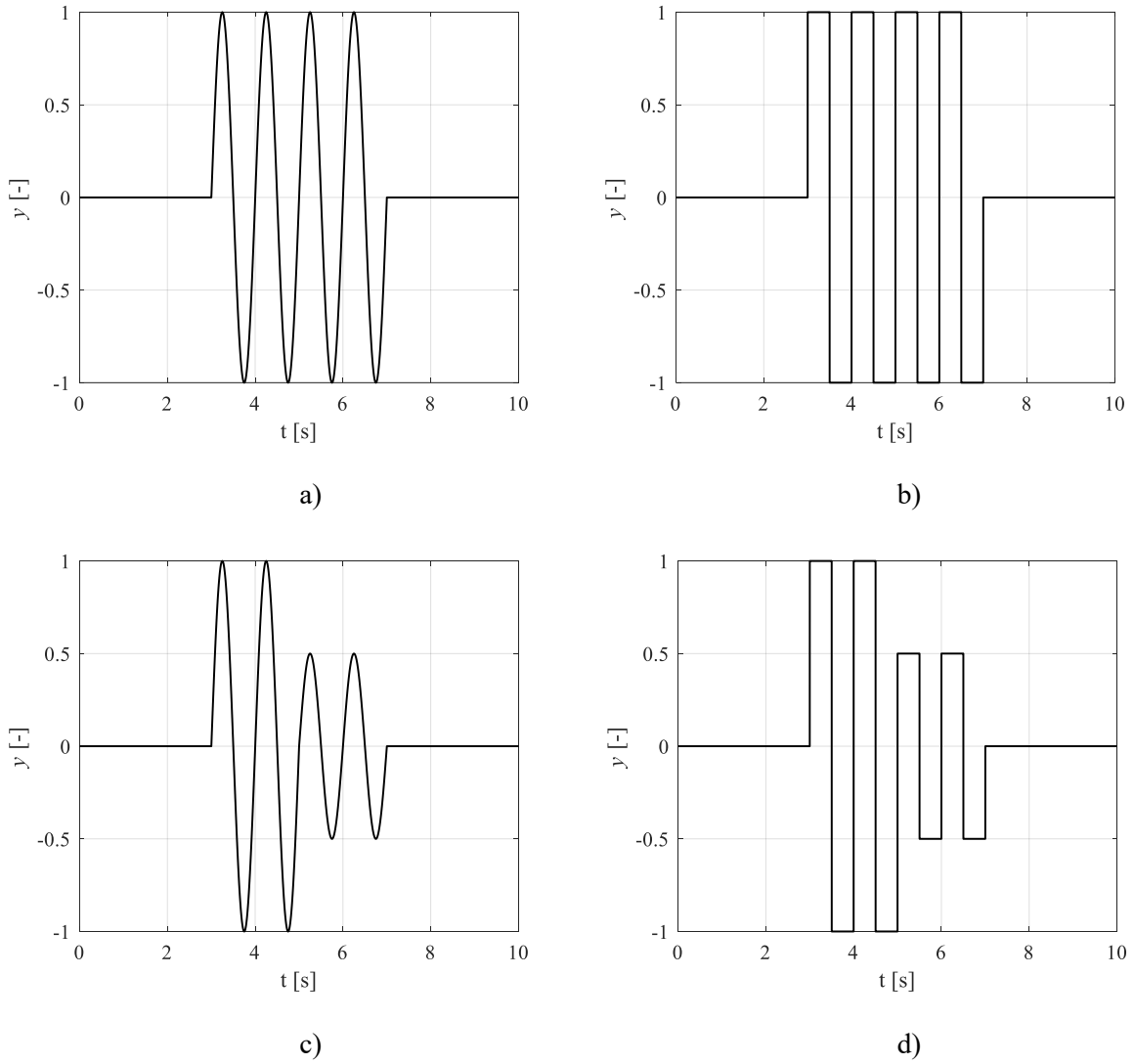

Figure 6.1: Analysed time-dependent signals: sine (a); square wave (b); sine having two different amplitudes (c); square wave having two different amplitudes (d).

The corresponding scalograms and power spectra are reported in Figure 6.2 and Figure 6.3, respectively. It has to be noted that the white dashed lines in scalograms delimit what is known as Cone of Influence (COI) [24]. Specifically, the COI highlights areas (grey-shaded) potentially affected by edge-effects, i.e., where the wavelet extends over the boundaries of the considered time interval, and they might not be representative of an accurate time-frequency description of the considered samples. For this reason, the power spectrum evaluation does not take into account such areas when integrating the power related to each frequency over time. In Figure 6.2a-b, the scalograms exhibit high-amplitude regions around 1 Hz, confirming that the power related to the signals' oscillation, which depends on their amplitude, is concentrated around their characteristic frequency. However, when a wave made up of a number of different oscillating signals with different frequencies (e.g., square waves, Figure 6.2b) is considered, the scalogram exhibits other medium-power regions at varying frequencies. In Figure

6.2c-d, the signals' power fades as soon as the signals' amplitude decreases, confirming instead that the scalogram is capable of giving a reliable time representation of an oscillating signal having time-varying amplitude. On the other hand, power spectra of Figure 6.3 denote peaks at 1 Hz, verifying that the dominant frequency of the signals f_D corresponds to their oscillation frequency. It is interesting to notice that, when the signals' amplitude changes over time (Figure 6.3b-d), the power related to the peaks in the power spectrum decreases since the signals oscillate less vigorously at their characteristic frequency.

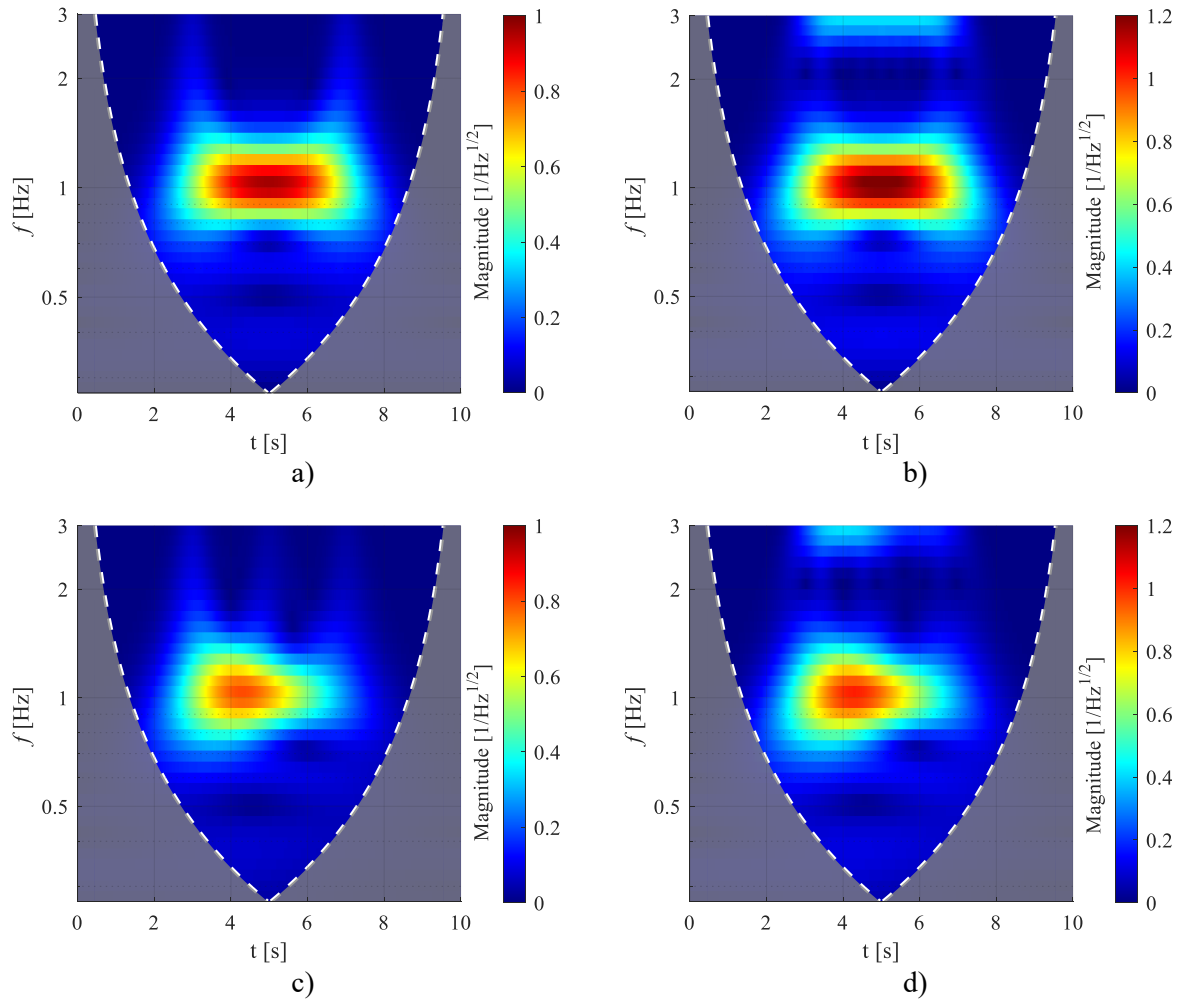

Figure 6.2: Scalograms: sine (a); square wave (b); sine having two different amplitudes (c); square wave having two different amplitudes (d).

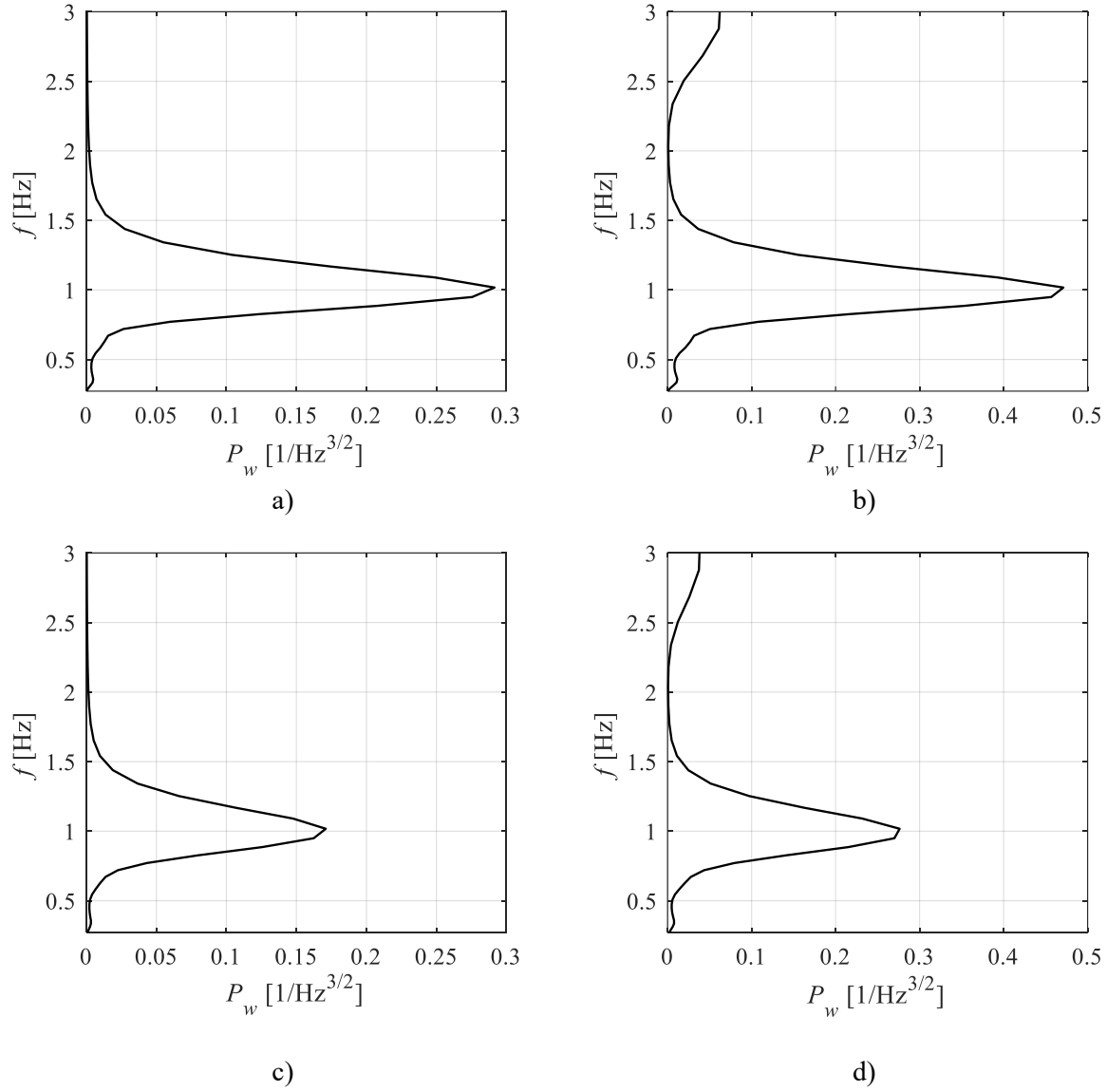

Figure 6.3: Power spectra: sine (a); square wave (b); sine having two different amplitudes (c); square wave having two different amplitudes (d).

To resume, the wavelet method is employed to describe oscillations of a given signal: scalograms depict the time evolution of its oscillatory behaviour, while power spectra are used to identify the main, i.e. dominant, oscillation frequency. When a time analysis on the characteristic oscillation frequencies of real systems is required, i.e., when raw experimental data are processed, the power peaks cannot be always easily identified in scalograms due to the presence of low-power peaks, which might be representative of noisy components rather than actual oscillatory phenomena. Hence, a procedure for scalograms denoising, aimed at discerning meaningful from negligible power peaks, is required. Among other denoising and peak detection techniques, the K-means clustering represents a practical and effective procedure. While this method is employed in different research fields, spanning from computer graphics to medicine, the literature lacks, to the Author's knowledge, of applicative examples

regarding the PHPs investigation. In particular, such a denoising technique relies on an iterative data-partitioning algorithm that assign *N* observations to K separate clusters defined by centroids [124]. K is preliminary chosen, depending on the specific application. The observations assignment depends on within-cluster variance minimizations through the evaluation of squared Euclidean distances from centroids, progressively moved until the minimization condition is satisfied. Given a set of observations $\mathbf{O} = \{\mathbf{O_1}, \mathbf{O_2}, \dots \mathbf{O_n}\}$, the partition into $k \leq K$ subsets $\mathbf{S} = \{\mathbf{S_1}, \mathbf{S_2}, \dots \mathbf{S_k}\}$ is performed according to the following minimization problem:

$$\underset{S}{argmin} \sum_{k=1}^{K} \sum_{s \in S_k} \|s - \mu_k\| \tag{6.3}$$

where μ_k is the mean of the k-th subset. When applied to scalograms, clusters containing residual noise, wavelet artifacts or non-relevant oscillations will present lower k coefficients [125]. Areas including significant oscillatory phenomena will instead present high k coefficients. Consequently, the only partitions defined by k = K are considered as meaningful regions, while other partitions are discarded. For the identification of the optimal K value, which could change depending on the analysed set of data, the Calinski-Harabasz criterion represents a useful reference tool [126]. In addition, since the convergence of the K-means algorithm is affected by the initial position of centroids, their initialization might need several reiterations until an optimal final partition of scalograms, i.e., a partition capable of identifying with good accuracy the high-power regions, is obtained.

6.3 Statistical methods

6.3.1. Coefficient of variation

Coefficients of variation, commonly employed in statistics, are useful coefficients when the studied population contains a significant number of elements to be reduced for the quantification of variations in the analysed samples. In particular, giving a generic 1-D signal α, the general formulation for the coefficient of variation *cv* is defined as [127]:

$$cv = \frac{std(|\alpha|)}{mean(|\alpha|)} \tag{6.4}$$

where *std* and *mean* refer to the standard deviation and the arithmetic mean, respectively. The absolute value of α is here computed to prevent *cv* from providing an undefined solution when the average value of the considered function is equal to 0. Specifically, such statistical quantity defines the irregularity of α in terms of oscillations. As reference for the oscillation regularity evaluated by the

coefficient of variation, three meaningful groups of discrete functions α are taken into account, whose *cv* values are reported in Figure 6.4:

- Sinusoidal functions (maximum oscillation regularity) assume coefficient of variation equal to about 50% (Figure 6.4a);
- Constant functions (no oscillation) assume coefficient of variation equal to 0% (Figure 6.4b);
- Functions having irregular oscillations assume coefficient of variation greater than 50% (Figure 6.4c).

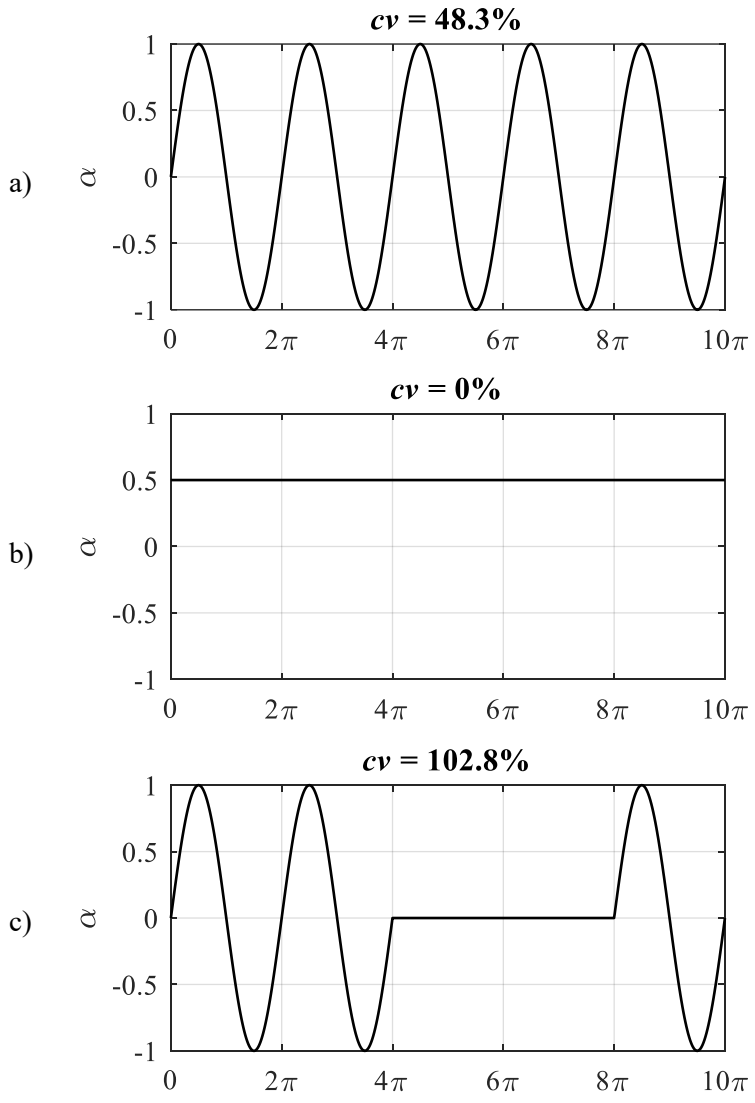

Figure 6.4: Coefficients of variation referred to three meaningful functions; sine (a), constant function (b) and sine with variable amplitude (c).

By extending Equation (6.5) to a generic bidimensional, space-time distribution β having M × N elements, its variation along either dimensions can be quantified by means of a coefficient of variation over time *cvt* and a coefficient of variation along space *cvs*:

$$cvt = \frac{\sum_{i=1}^{M}\left[\frac{std(|\beta(i,\ t=1,\dots,N)|)}{mean(|\beta(i,t=1,\dots,N)|)}\right]}{M} \tag{6.6}$$

$$cvs = \frac{\sum_{t=1}^{N}\left[\frac{std(|\beta(i=1,\dots,M,t)|)}{mean(|\beta(i=1,\dots,M,t)|)}\right]}{N} \tag{6.7}$$

The ratio of the standard deviation to the mean of β is averaged either for every *i*-th space coordinate (Equation 6.8) or for every *t*-th time instant (Equation 6.9) since the employment of a single time-space coordinate, from a statistical point of view, is not representative of the actual variation of the whole time-space distribution.

6.3.2. Cumulative distribution function

The cumulative distribution function Φ is a statistical parameter used for the description of a given population. Specifically, it is defined as the probability that a variable φ will assume a value less than or equal to a generic value φ_0 [127]. Calling $a_0 \in [0,1]$ a value assumed by Φ(φ), the inverse cumulative distribution function $\varphi_0 = \Phi^{-1}(a_0)$ represents the $[a_0 \cdot 100]^{th}$ percentile of the analysed distribution. Consequently, any percentile of the variable φ can be easily identified by means of such distribution function. When φ presents outliers which are far from its average trend, the adoption of percentiles lower than the 100^{th} statistically represents the distribution in a more robust way.

6.4 Cross correlation-and Heat Transfer Delay Method

The Heat Transfer Delay Method (HTDM) is a method based on normalized cross-correlation functions between experimental signals related to the same physical system. Such a post-processing technique is named after its novel application to heat transfer quantities, such as local thermal interactions in adjacent channels of PHPs, but it may be potentially applied to any kind of signals.

In particular, the HTDM is based on the cross-correlation r^* between two finite discrete functions of time *f(t)* and *g(t)* having *N* time samples, defined as [128]:

$$r^* = (f \star g)[\tau] = \sum_{t=0}^{N} f(t)g(t+\tau) \tag{6.10}$$

where τ is the displacement (or lag) between *f* and *g*. Equation (6.10) essentially shifts the function *g(t)* along the time axis, calculating, for each single shift τ, the sum of the product between *f(t)* and *g(t)*. Hence, when a proper overlap of the two functions is reached, r^* is maximized and the time lag between the original signals can be assessed. Other lower-amplitude peaks of *r* depend on the shape of the given functions, and they are not to be considered as representative of the actual time delay. To obtain an accurate and comparable estimation of the cross-correlation, the normalized cross-correlation function r is usually adopted instead of r^*:

$$r(\tau) = \frac{1}{\sqrt{r_{ff}^*(0) r_{gg}^*(0)}} r^*(\tau) \tag{6.11}$$

where $r_{ff}(0)$ and $r_{gg}(0)$ are the autocorrelations of *f* and *g* at zero lag, respectively. According to its very definition, r can assume values in between -1 (perfect negative correlation, also referred as an inverse correlation) and 1 (perfect positive correlation, also referred as a direct correlation).

To provide an example for the interpretation of the *r* function, two arbitrary signals are introduced as follows, and plotted in Figure 6.5a:

$$f(t) = \sum_{i=1}^{4} \frac{1}{i} \cdot \sin\left[2\pi t(0.4 + 0.2i)\right] \tag{6.12}$$

$$g(t) = 1.5 \cdot f(t) \tag{6.13}$$

Their normalized cross-correlation is shown in Figure 6.4b: since the two signals are perfectly in phase, the lag between the two functions equals zero and *r* assumes a maximum peak ($r = 1$) at $\tau = 0$ s. By considering a different case, in which $f(t)$ is shifted of 0.3 seconds with respect to $g(t)$ (Figure 6.4c), the normalized cross-correlation (Figure 6.4d) assumes a peak ($r = 0.98$) at $\tau = 0.3$ s, thus verifying the capability of the function *r* to assess the time lag between two given signals, whether they are in phase or not.

It must be pointed out that τ can assume both positive and negative values: when $\tau > 0$, g is in advance with respect to f. Also, *r* values greater than 0.6 generally suggest a significant correlation between the two considered signals.

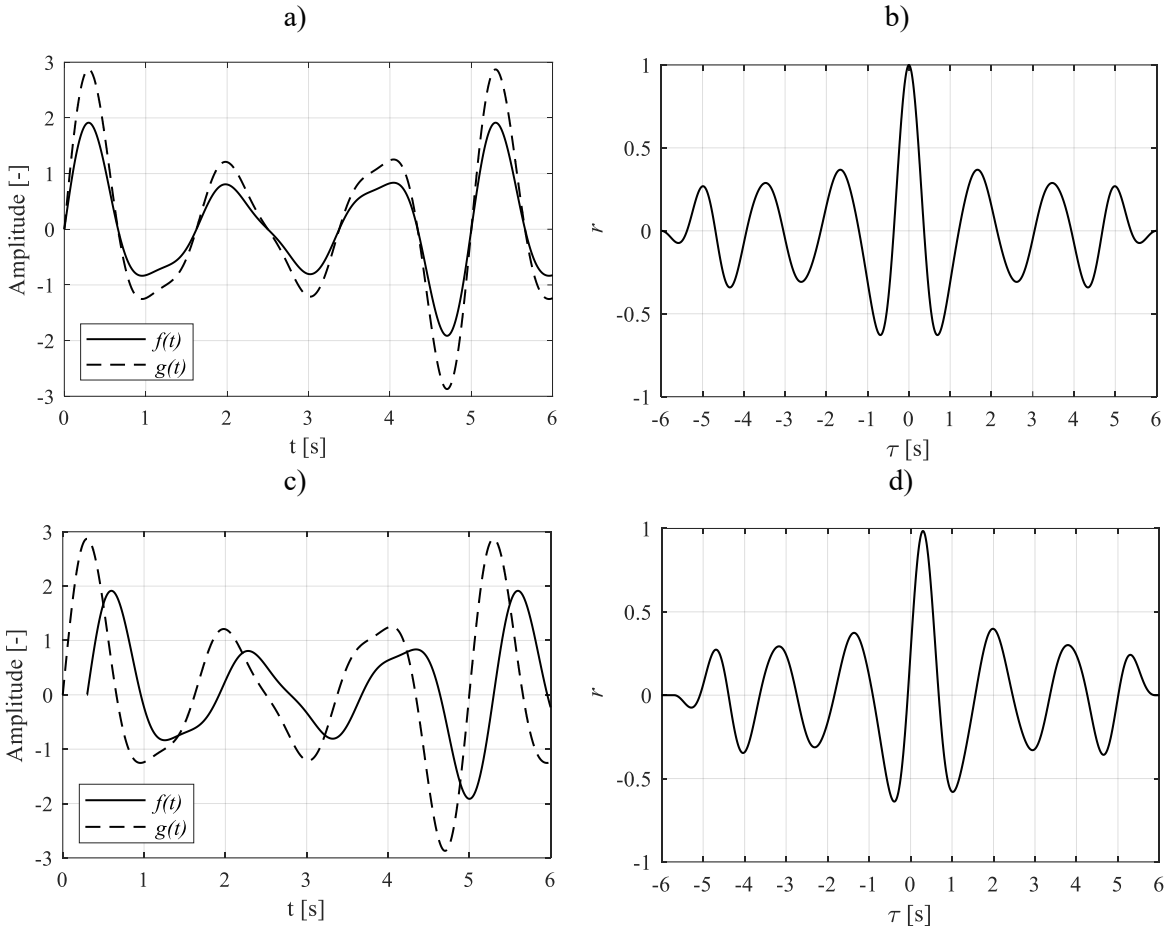

Figure 6.5: Example for the interpretation of the normalized cross-correlation function *r*. Given arbitrary functions *f(t)* and *g(t)* in phase (a) and having a known time lag (c), together with the corresponding *r* functions (b-d, respectively).

When the two analysed signals are due to a common perturbating phenomenon in a given physical system at two different spatial points *a* and *b*, and at a distance $L_{[a\to b]}$, e.g., pressure variations caused by sound waves or temperature variations caused by moving heat sources, the evaluated time lag $\tau_{[a\to b]}$ is related to the travel time of the accounted perturbation. Hence, the velocity $v_{[a\to b]}$ of the perturbating phenomenon can be evaluated as follows:

$$v_{[a\to b]} = \frac{L_{[a\to b]}}{\tau_{[a\to b]}} \tag{6.14}$$

On the other hand, when complex systems presenting several different perturbating phenomena occurring in short periods of time are investigated, the HTDM can be employed to identify which signals referred to generic spatial points are due to the same perturbating phenomenon. To this aim, the two given signals $f(t)$ and $g(t)$ are partitioned into a number of time windows of length t_{win}, and Equations

(6.15) and (6.16) are computed by comparing two subintervals at a time. The new cross-correlation function, based on the partitioning of the investigated functions, is defined as:

$$r^*_{t_1,t_2}(\tau) = \sum_{t_1,t_2=0}^{N-t_{win}} f(t_1 + t_{win}) g(t_2 + t_{win} + \tau) \tag{6.17}$$

6.5 Closure

The data reduction methods adopted for the experimental studies on different PHP layouts consist of either typical methods, such as the wavelet approach, or original methods, based on the definition of statistical parameters or on the evaluation of cross-correlations between the evaluated heat fluxes. The presented methods will be used in Part III as powerful tools for the understanding of the thermo-fluid dynamics underlying the investigated devices.

Part III: Experimental campaigns on different heat pipe geometries and manufacturing materials

Chapter 7 Experimental investigation on a tubular PHP

7.1 Introduction

The present Chapter provides a detailed description of the investigated tubular PHP by means of conventional techniques, e.g., by thermocouples placed on the device outer wall, and novel techniques based on thermography.

The IHCP resolution approach is applied to the outer wall temperature of metallic channels to evaluate the heat flux locally exchanged between the working fluid and the device walls. All the meaningful outcomes of the experimental campaigns are thoroughly presented and discussed, providing quantitative pieces of data for the working regimes interpretation by both global performances and local heat transfer behaviours. Specifically, the aim of such experimental investigations was finding a common interpretative perspective for the evaluated wall-to-fluid heat fluxes among different operation conditions, thus attempting a comprehensive and consistent statistical description of PHPs heat transfer capabilities. In other words, a better insight into the PHPs working principles, which have been, so far, mainly investigated in terms of equivalent resistance, is given.

The listed experimental campaigns and results are referred to the so-called Space PHP, made of aluminium and specifically designed to operate in weightlessness. Experimental tests were performed both on ground and microgravity conditions. The experimental data in weightlessness were collected during the 67th Parabolic Flight Campaign promoted by the European Space Agency.

The studied device is described by following a common approach for both campaigns:

- Description of the experimental apparatus and procedure;
- Quantification of the global performance in pseudo-steady state (where achievable);
- Quantification of the local interactions between the working fluid and the device walls;
- Statistical analysis on the wall-to-fluid heat fluxes.

Additional data regarding the fluid velocity and oscillation frequency might be also provided, depending on the specific working conditions.

7.2 Space pulsating heat pipe: microgravity experiments

Microgravity tests have been performed with the aim of studying the PHP thermal response when the effects of gravity are negligible. However, such a working condition could be usually maintained, due to technical limitations, for short periods of time, thus hampering a characterization of the device in terms of equivalent thermal resistance. Hence, the experimental analysis has focused on the quantitative investigation of the local heat transfer behaviour, which will be proven to give interesting results during the transient operation of the studied device.

7.2.1. Test rig

The studied device (Figure 7.1) is made of an annealed aluminium tube (6060 alloy, I/O diameter = 3/5 mm), shaped in a 3D closed loop layout (overall size: 220x80x25 mm, 14 turns). Such peculiar 3D geometry is specifically designed to fit the limiting constrains of the Heat Transfer Host aboard the International Space Station [109]. The thermal conductivity of the aluminium channels was certified by the manufacturer to be equal to 201 W/mK at 300 K. Two aluminium heat spreaders (100x12x10 mm) are brazed on the tube in the evaporator zone, holding two ceramic ohmic heaters (Innovacera®, electrical resistance 18 Ω ± 10). The evaporator section is insulated by means of a layer (0.01 m) of insulating material. The heating power is provided by a programmable power supply (GW-Instek®, PSH-6006A). The condenser zone is embedded between two aluminium heat spreaders (80x120x10 mm, Figure 6.11b), cooled by means of a Peltier cell system (eight Peltier cells by Adaptive Thermal Management®, ETH-127-14-11-S; control system by Meertstetter Engineering®, TEC 1123) coupled with a cold plate temperature control system loop (Aavid Thermalloy®). Also, a sapphire insert (Precision Sapphire Technologies®, length 140 mm, same OD/ID of the aluminum tube) is present in the adiabatic section to directly inspect the flow regimes and measure the fluid temperature distribution, as explained in previous works [103,109]. The temperature of the evaporator is measured through five T-type thermocouples located between the evaporator spreader and the heater, while the temperature at the condenser is monitored by six T-type thermocouples located between the Peltier cold side and the condenser aluminium heat spreader and two placed on the condenser heat spreader. All the thermocouples were calibrated with a thermal chamber (BINDER®) and a reference four wire Pt-100 (ITS-90 standard, max. error 0.035 K).

a)

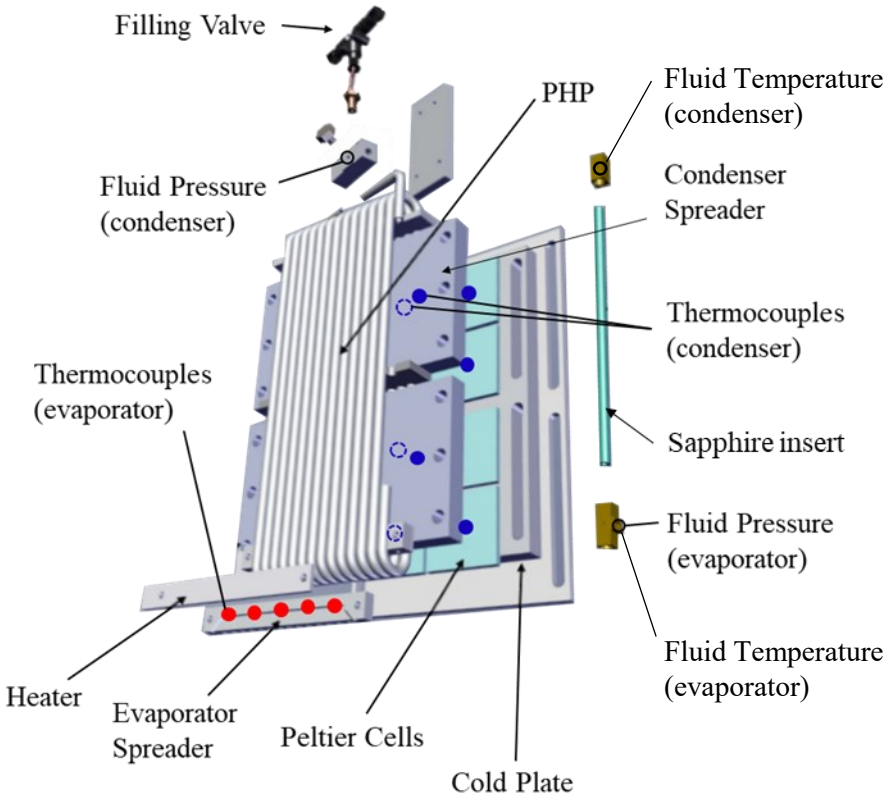

b)

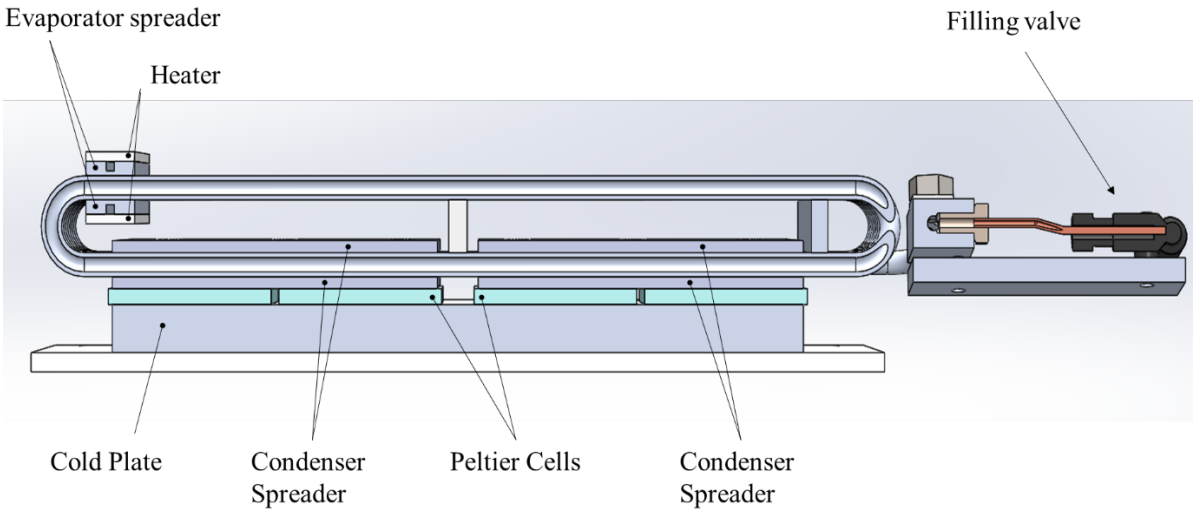

Figure 7.1: Exploded view and measurement tools location (a); sectional view (b).

The fluid pressure at the condenser and evaporator sections was measured by two miniature pressure transducers (Keller® PAA-M5-HB, 1 bar abs, 0.2% FSO accuracy), directly inserted in the fluid stream.

The fluid temperature was instead measured by means of two K-type micro-thermocouples (Omega® KMTSS-IM025E-150, bead diameter 0.25 mm, response time 0.1 s with 95% confidence). All the thermocouples' signals were recorded at 10 Hz, while the pressure measurements were sampled at 18 Hz.

The aluminium channels within the adiabatic section were uniformly coated with a high-emissivity opaque paint (ε = 0.92), and the temperature was acquired by a previously calibrated [129], high-speed and high-resolution InfraRed (IR) camera (AIM® TEC-MMG from ESA/ESTEC, 1280x1024 pixels), with sampling frequency of 50 Hz.

The uncertainty related to each measured parameter [109], as provided by the manufacturers, is listed in Table 7.1.

Table 7.1: Uncertanty of the measurement tools.

Parameter	**Specs**	**Sampling frequency**	**Uncertainty**
Channel wall temperature	T-type Thermocouple (0.5 mm bead diameter)	10 Hz	± 0.1°C
	High-speed Medium Wave Infrared Camera	50 Hz	± 0.2°C
Fluid temperature	Omega® KMTSS-IM025E-150 K-Type thermocouple (0.25 mm bead diameter)	10 Hz	± 0.2°C
Fluid pressure	Keller® PAA-M5-HB, 1 bar abs	18 Hz	± 500 Pa
Power Input	GW-Instek®, PSH-6006A	-	± 2 W

7.2.2. Experimental procedure

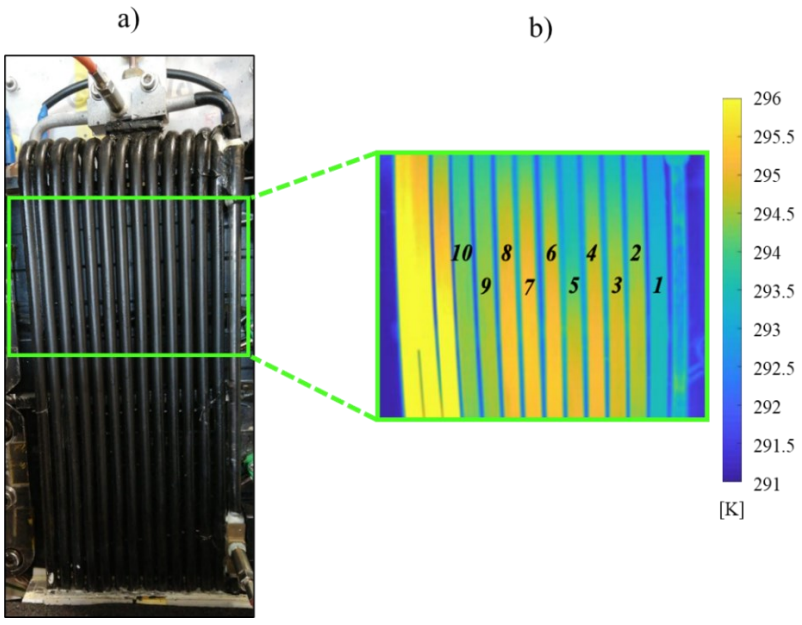

Figure 7.2: Sample of IR acquisition and channel numeration.

The condenser temperature set-point was equal to 20°C. The IR measurements were carried out in between the evaporator and the condenser since the adiabatic section was the only portion directly accessible to the IR camera. Specifically, the camera framed just a portion of the PHP adiabatic section (about 0.084 m long, green box in Figure 7.2). The analysis was carried out on 10 of the 14 PHP, numbered in Figure 7.2.

The device was first vacuumed (down to 10^{-6} mbar) and then partially filled by with degassed FC-72 (filling ratio = 50 ± 1% vol.).

The test rig was then mounted on an Airbus A310 and a total of 93 parabolic trajectories were performed over three days. Every parabola provided about 20 seconds of microgravity conditions between two intervals of about 20 seconds of hyper-gravity each. For further details on parabolic flights and adopted manoeuvres, see [130]. The IR acquisitions were triggered during the microgravity periods. The gravity level was monitored by accelerometers (sampling frequency = 10 Hz) attached to the floor structure of the aircraft. The device was oriented in Bottom Heated Mode (BHM, evaporator below the condenser), and tests were performed varying the heating power from 30 W up to 210 W. Each power input to the evaporator was provided before the microgravity period, thus maintaining the heat load constant for the whole parabolic trajectory.

For every heat load, multiple tests were performed to evaluate the repeatability of the observed phenomena: Table 7.2 reports the power inputs given to the evaporator, together with the number of tests performed for each heat load.

Table 7.2: Number of tests for each power input given to the evaporator.

Power input [W]	Number of tests
34	4
51	10
68	11
100	5
135	4
202	6

7.2.3. Local heat transfer analysis

The thermographic acquisitions were processed by means of the approach explained in Paragraph 5.2.2. Specifically, R_{env} in Equation (5.8) was assumed equal to 0.1 m^2K/W, which is a representative value for air natural convection with radiative heat transfer towards the environment, while the environmental temperature varied in the range 18°C to 22°C. In addition, the standard deviation of the raw data was estimated by measuring the wall temperature distribution while maintaining the system

under isothermal conditions. For the present study case, the standard deviation of the raw data σ_Y was found equal to 0.06 K.

In Figure 7.3, the measured temperature distribution along the axial coordinate over a 20 seconds' observation window is reported for a single test case (power input equal to 100 W, channel 1).

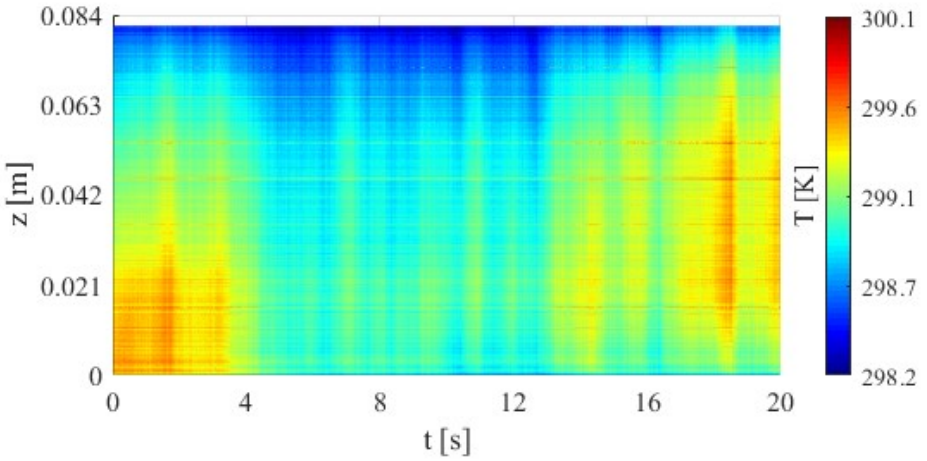

Figure 7.3: Measured wall temperature distribution for power input of 100 W, channel 1.

The corresponding evaluated wall-to-fluid heat flux distribution, obtained by the IHCP resolution approach, is reported in Figure 7.4.

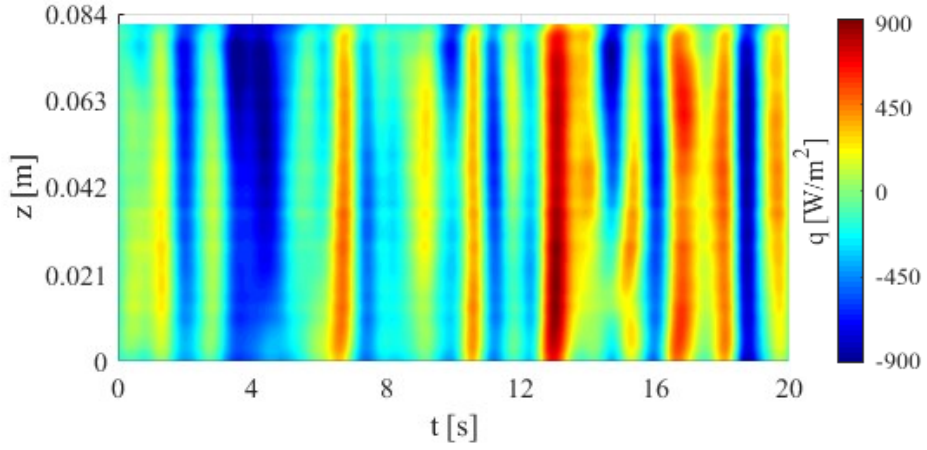

Figure 7.4: Estimated wall-to-fluid heat flux distribution, for power input of 100 W, channel 1.

As already stated in [75], the heat flux distribution over time provides useful information about the fluid dynamics of the device: positive heat fluxes may correspond to the passage of hot vapor plugs and liquid slugs from the evaporator to the condenser. Negative heat fluxes may denote instead flow reversals phenomena, during which cold fluid flows from the condenser to the evaporator at a lower temperature than that of the channel wall, previously heated by hot fluid coming from the evaporator.

Such oscillatory behaviour is evident, in Figure 7.4, from the alternance of positive and negative heat flux peaks.

However, from a phenomenological standpoint, it has to be stressed that the present data are referred to a fully transient response of the device. In fact, the device under study is classified as a hybrid Thermosyphon/Pulsating Heat Pipe: the transition between hyper and microgravity thus results in a transition between the Thermosyphon and the PHP working mode, where the flow pattern undergoes a sudden change due to the rising predominance of capillary forces with respect to buoyancy forces [74]. The experimental data reduction performed by Mangini et al. [131] on a similar PHP system revealed that the transition effects persist for some seconds after the onset of microgravity.

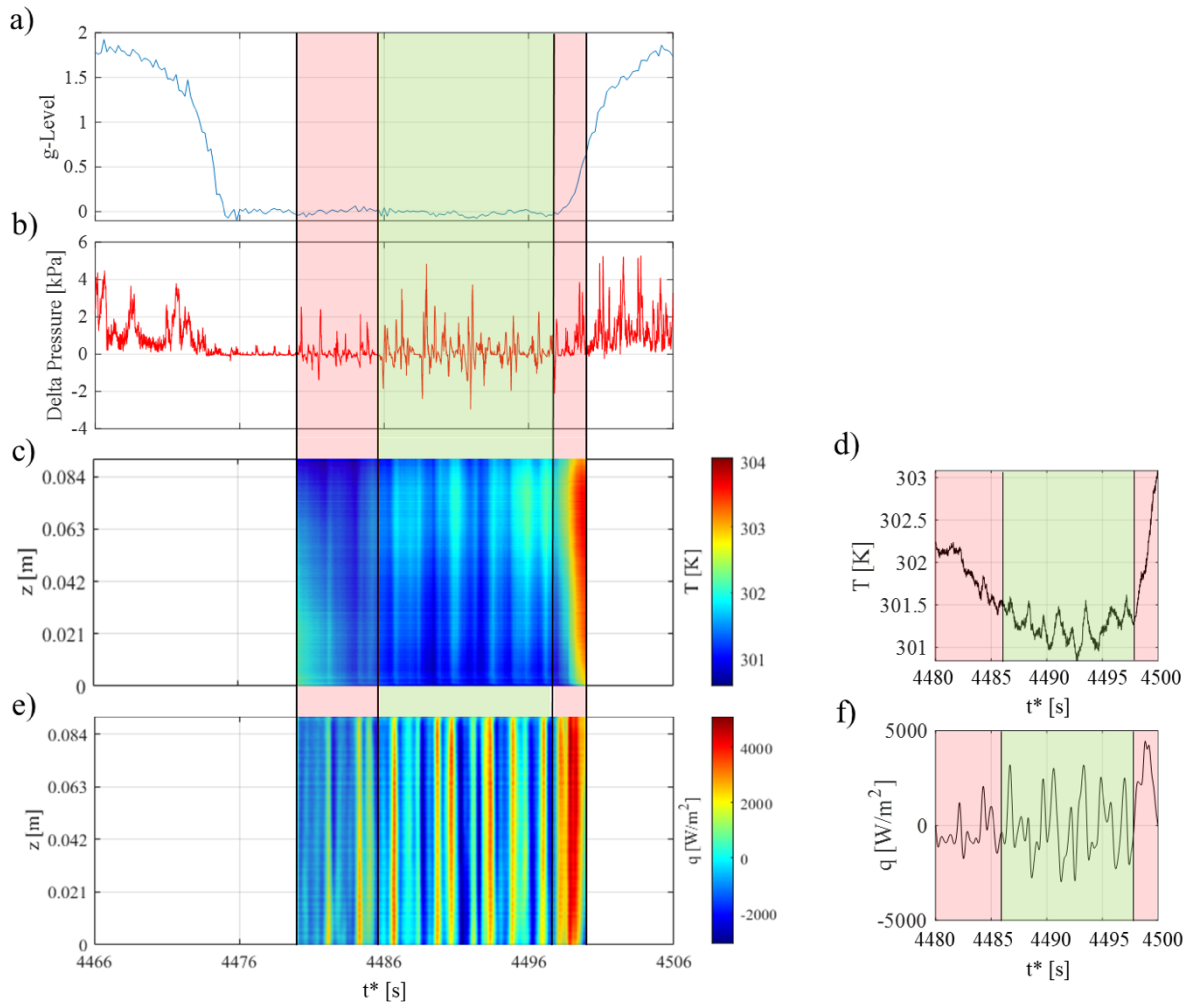

Figure 7.5: Gravity level (a), pressure difference (b), measured wall temperature (c), temperature distribution (axial coordinate = 0.045 m) (d), wall-to-fluid heat flux (e) and heat flux distribution (axial coordinate = 0.045 m) (f) over absolute time t*, referred to channel 1 and power input equal to 202 W.

In Figure 7.5, they are reported the g-level (Figure 7.5a), defined as the measured gravity field divided by 9.81 m/s^2, the fluid pressure difference Δp (Delta Pressure) between the evaporator and the condenser (Figure 7.5b), the IR acquisition (Figure 7.5c) and the corresponding wall-to-fluid heat flux (Figure 7.5e) for power input to the evaporator equal to 202 W. The synchronization between the considered pieces of data was carried out by adopting the absolute time t*, where t* = 0 occurs at the pressure acquisition trigger during the flight.

In the reported example, both the wall temperature and the wall-to-fluid heat flux show appreciable oscillations, as clearly noticeable from the distributions of Figure 7.5c-e. Two zoomed time windows of these distributions are a reported in Figure 7.5d-f to easily catch this behaviour. According to [109], the consecutive variations of Δp from positive to negative values denote the presence of fluid motion between the evaporator and the condenser through those channels in which the fluid pressure measurement is performed. Consequently, the Δp of Figure 7.5b exhibits clear fluid oscillations. Additionally, it must be underlined that, in the present study cases, the Delta Pressure and the IR acquisitions are not referred to the same channel but to two adjacent ones. However, for such high-power input to the evaporator, the fluid motion is simultaneously induced in every PHP channel [101], confirming that adjacent channels experience the same fluid oscillations. These results highlight that the estimated wall-to-fluid heat flux is thus capable of perceiving fluid oscillations likewise the pressure transducers, without the necessity to adopt any intrusive technique on the device layout.

Regarding the gravity field variation, the red-shaded areas of Figure 7.5 are referred to time intervals in which the transition effects between hyper (g-level > 1) and micro-gravity (g-level = 0) are evident, while the green-shaded areas are related to the time intervals in which the flow pattern is in a sort of stable condition, i.e. periodic oscillations with constant amplitude and frequency. In fact, after the hyper-gravity conditions, the wall temperature decreases almost monotonically, even though some fluid oscillations are still appreciable from Figure 7.5f. These remarks confirm the presence of a short settling period after the transition from hyper-gravity to micro-gravity. On the contrary, after such transition, the wall temperature (Figure 7.5d) fluctuates around a constant value, while the heat flux presents almost regular oscillations in terms of amplitude and oscillation frequency, thus denoting that the PHP is working in stable conditions.

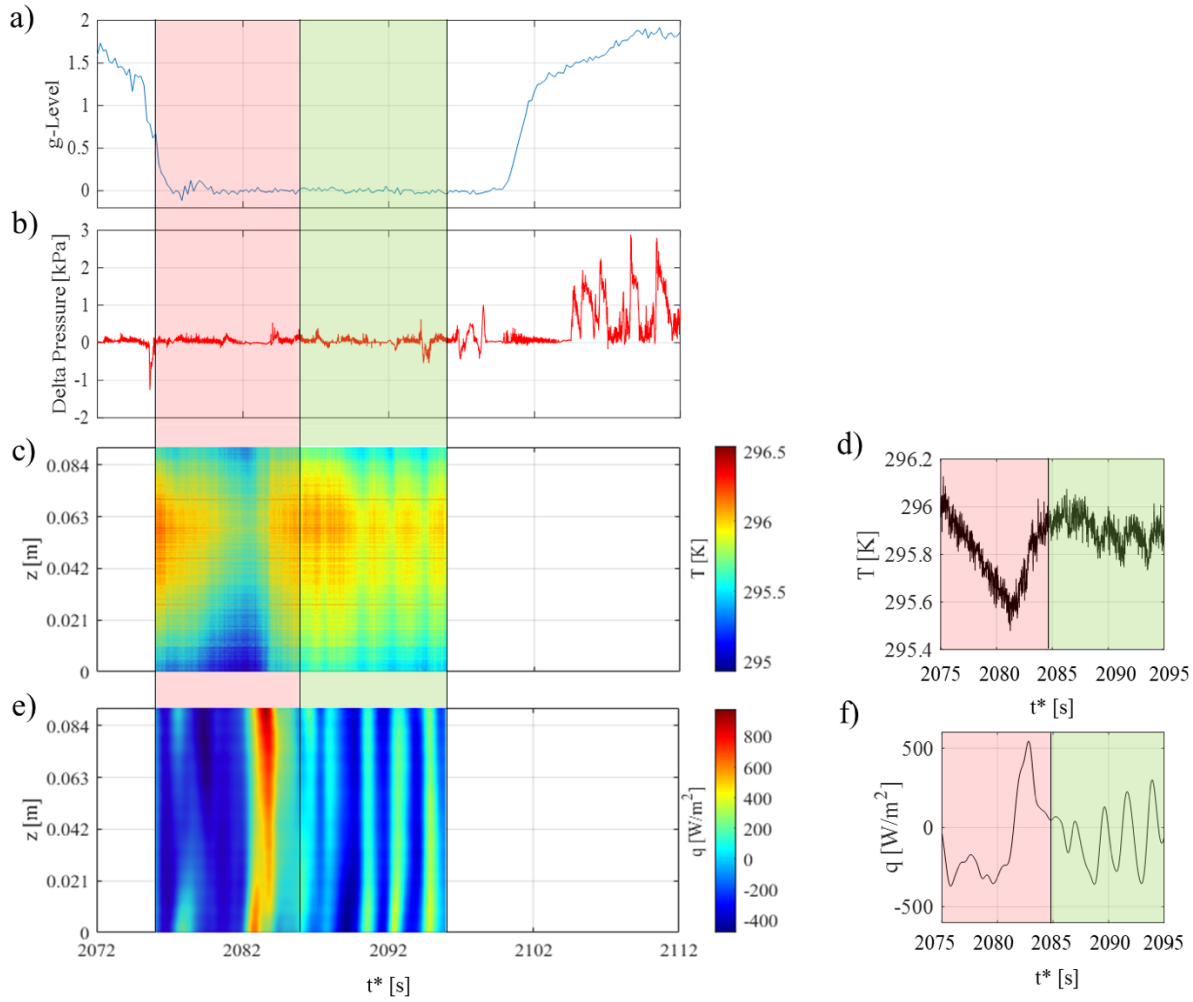

Figure 7.6: Gravity level (a), pressure difference (b), measured wall temperature (c), temperature distribution (axial coordinate = 0.045 m) (d), wall-to-fluid heat flux (e) and heat flux distribution (axial coordinate = 0.045 m) (f) over absolute time t*, referred to channel 1 and power input equal to 34 W.

In Figure 7.6, the same analysis is reported for power input equal to 34 W. Similarly to the case of Figure 7.5, the evaluated heat flux (Figure 7.6e-f) is capable of describing fluid oscillations, although, for low power inputs, the accordance between the wall-to-fluid heat flux and the Delta Pressure (Figure 7.6b) is not always verified. It is probably due to the fact that, for low power inputs, every channel works independently, as also discussed in Paragraph 7.2.4. As observed in the previous example, the transitional phase (red-shaded area) is characterised by differences in terms of wall temperature and wall-to-fluid heat flux trends, with respect to those assessed within the stable PHP working mode (green-shaded area).

7.2.4. Working regimes assessment (stable conditions)

In the following analysis, only the stable working conditions are considered, i.e. the transition period between hyper and microgravity is ignored, thus considering just 10 of the 20 seconds of acquisition in microgravity.In order to highlight the fluid motion characteristics, Figure 7.7 and Figure 7.9 show the measured temperature distributions and the corresponding estimated heat flux distributions of four channels (i.e. 1, 5, 7 and 8), for three different power inputs to the evaporator: low power (34 W), intermediate power (100 W) and high power (202 W).

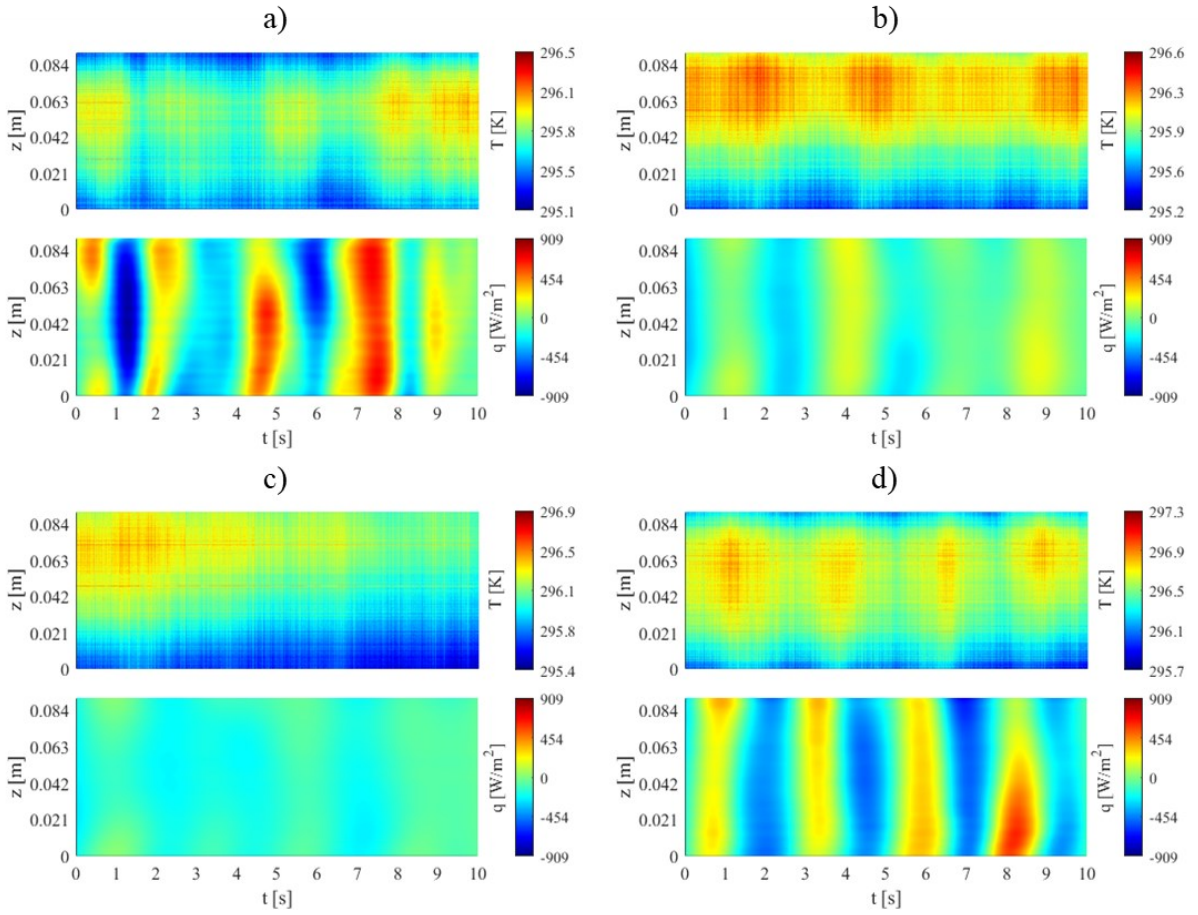

Figure 7.7: Wall temperature distributions and corresponding estimated heat fluxes for channel 1 (a), 5 (b), 7 (c) and 8 (d) for power input equal to 34 W in stable microgravity conditions.

For low power inputs, the device response differs from channel to channel; in fact, some channels present a slight fluid oscillation (Figure 7.7a-b), described by the alternance of weak positive and negative peaks with low oscillation frequency, while other channels (Figure 7.7b-c) are almost inactive, i.e. the heat flux is almost null within the whole distribution, except for some weak oscillations. Such remark highlights that the power input is not able to thermally drive the fluid in the whole device, i.e., the PHP is not fully activated, thus confirming that adjacent channels may have different fluid-dynamics

behaviour, especially for low power inputs to the evaporator. In fact, the full activation of the device occurs when an appreciable fluid motion is present in each PHP branch, with regular oscillations in terms of heat flux amplitude and oscillation frequency.

By increasing the power input up to 100 W, the oscillations become generally stronger, with higher heat flux amplitudes and oscillation frequencies (Figure 7.8), although some small differences of behaviour among the channels are still present. The device is very close to the full activation.

For power input equal to 202 W (Figure 7.9), the fluid oscillation is thermally induced in every channel; the oscillations are stable, with high heat flux amplitudes and oscillation frequencies and no significant variations among the channels' behaviour are observed. Hence, the device is completely activated, and the PHP oscillating behaviour involves all the channels, with similar characteristics.

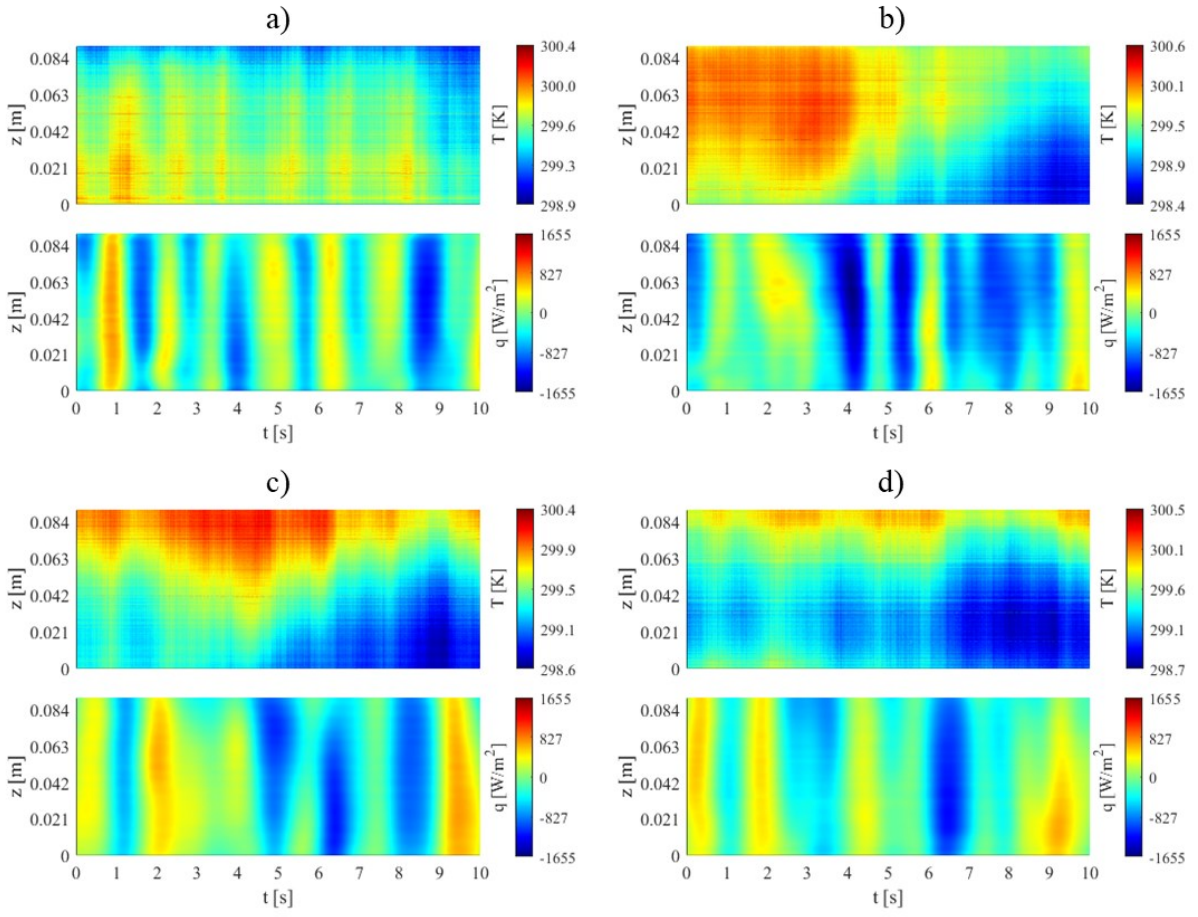

Figure 7.8: Wall temperature distributions and corresponding evaluated heat fluxes for channel 1 (a), 5 (b), 7 (c) and 8 (d), for power input equal to 100 W in stable microgravity conditions.

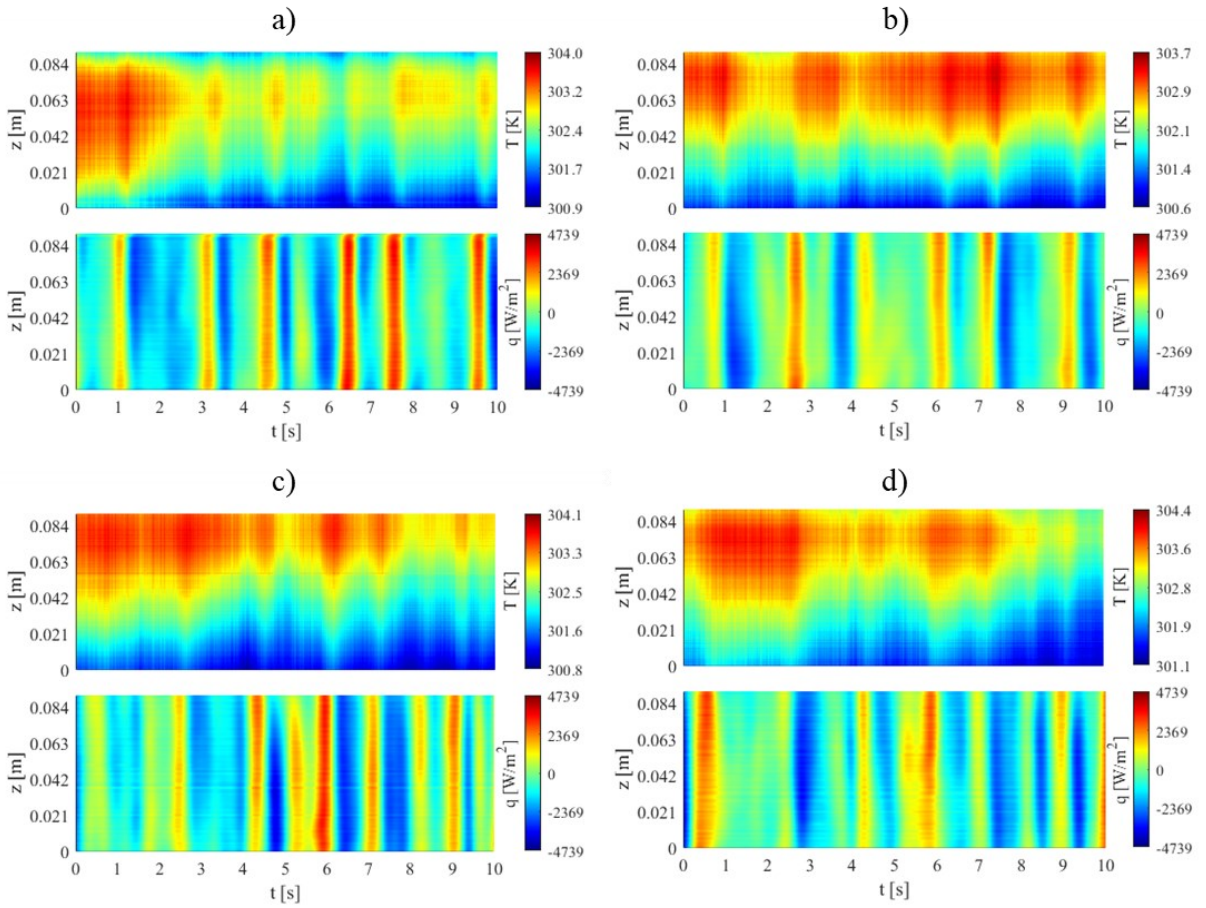

Figure 7.9: Wall temperature distributions and corresponding evaluated heat fluxes for channel 1 (a), 5 (b), 7 (c) and 8 (d), for power input equal to 202 W in stable microgravity conditions.

7.2.5. Statistical approach on the local wall-to-fluid heat fluxes for the working regimes description

Since the adopted inverse heat transfer approach provides a large amount of data about local time-space heat fluxes exchanged at the wall-fluid interface, a robust statistical approach is needed to quantitatively describe the available data population. To this aim, the coefficients of variation of Paragraph 6.3.1 are first employed.

Specifically, by considering local wall-to-fluid heat fluxes exchanged in PHPs branches, the physical meaning of such coefficients can be interpreted as follows:

- when the wall-to-fluid heat flux presents regular oscillations amplitude, *cvt* assumes low values; on the other hand, when the heat flux time oscillations present an irregular trend, *cvt* assumes high values;
- analogously, *cvs* is high when great space variations of the heat flux are appreciable along the channel, while it assumes low values when the whole channel is simultaneously interested by the same thermal phenomena.

Figure 7.10 shows the statistical analysis applied to the present investigation for every power input in stable working mode: time-related *cvt* (red shade) and space-related *cvs* (blue shade) were evaluated for every analysed channel.

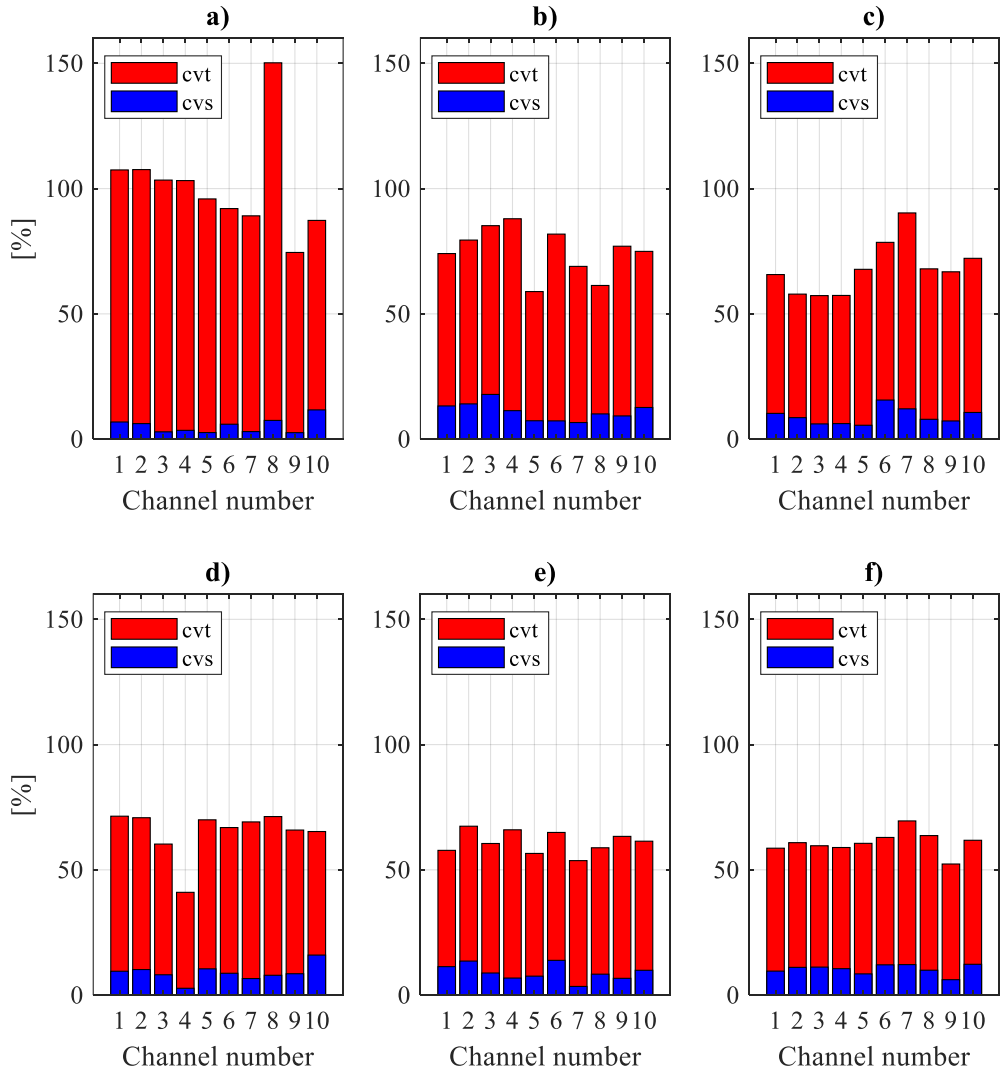

Figure 7.10: Coefficients of variation *cvt* and *cvs*, referred to time (red) and space (blue) variations of the evaluated wall-to-fluid heat flux in each channel, respectively, for power input equal to 34(a), 51(b), 68(c), 100(d), 135 (e) and 202 W (f).

For the lowest power input equal to 34 W (Figure 7.10a), the *cvt* assumes high values (from 75% to 150%) and differs significantly from channel to channel. The variation interval of *cvt*, defined as the difference between the maximum and the minimum value at a specific power input, is 75% at 34 W. These values highlight that the fluid motion has a great variability over the entire device and the heat flux oscillations are not stable, thus highlighting that the PHP is not fully activated.

The coefficient of variation in time decreases as the power input increases, also presenting a lower variability from channel to channel (Figure 7.10b). For higher power inputs (Figure 7.10c-d), the

coefficient of variation is in the range of 50-60% and its variation interval is 10%, confirming that the PHP is fully activated and characterised by regular fluid oscillations.

In the same figure, the blue charts are instead referred to the space regularity coefficient *cvs*, obtained by means of Equation (6.6): for every considered power input given to the evaporator, *cvs* is always in the range 5-15%. These low values, with no great variations from channel to channel even for the lowest examined power input (Figure 7.10a), show that, within the channel, there are no significant variations along the axial coordinate in the local heat flux because the oscillatory phenomenon affects the whole channel simultaneously. It is therefore not possible, for the current experimental configuration, to appreciate the motion of the thermal disturbance inside the single tube due to the high speed of the phenomenon compared to the thermal inertia of the wall.

To achieve a full channel-wise description of the heat transfer phenomena, the average heat flux amplitude A_{av}, here defined as the average of the absolute wall-to-fluid heat flux distributions related to each analysed channel, is reported in Table 7.3 for the considered test cases. The average behaviour of the exchanged wall-to-fluid heat fluxes are promptly observed, highlighting a general increasing trend with the power input to the evaporator.

Table 7.3: Average wall-to-fluid heat flux amplitude for each PHP channel, referred to one test case selected among every analysed case for each power input.

A_{av} [W/m^2]		Power Input [W]					
		34	*51*	*68*	*100*	*135*	*202*
Channel number	*1*	310	282	395	367	689	1295
	2	303	394	236	433	579	1383
	3	355	325	325	490	658	1440
	4	255	262	283	507	564	1092
	5	274	331	341	491	578	933
	6	192	216	379	503	583	1228
	7	232	313	471	402	474	1261
	8	264	282	495	348	462	1269
	9	239	238	405	475	474	1215
	10	171	312	408	340	484	1102

However, due to the presence of outliers in the wall-to-fluid heat fluxes amplitude which may not be representative of the overall heat transfer behaviour within the adiabatic section, a more complete method is furtherly adopted. First, the totality of the time-space heat flux distributions (absolute value) was used as input for the cumulative distribution function Φ, described in Paragraph 6.3.2. Φ(q) is reported in graph of Figure 7.11, for every power input to the evaporator: for power inputs ranging from 34 to 100 W, the cumulative distribution function presents comparable trends, denoting similar

statistical distributions for q, even though the curve related to 34 W undergoes a sharp change in shape for Φ(q) > 0.9 due to the strong and sporadic heat flux peaks occurring during the PHP intermittent working mode. By increasing the heat load, Φ(q) progressively flattens, confirming the variation in the working behaviour (PHP full activation) that results in higher wall-to-fluid heat flux amplitude within the whole statistical distribution.

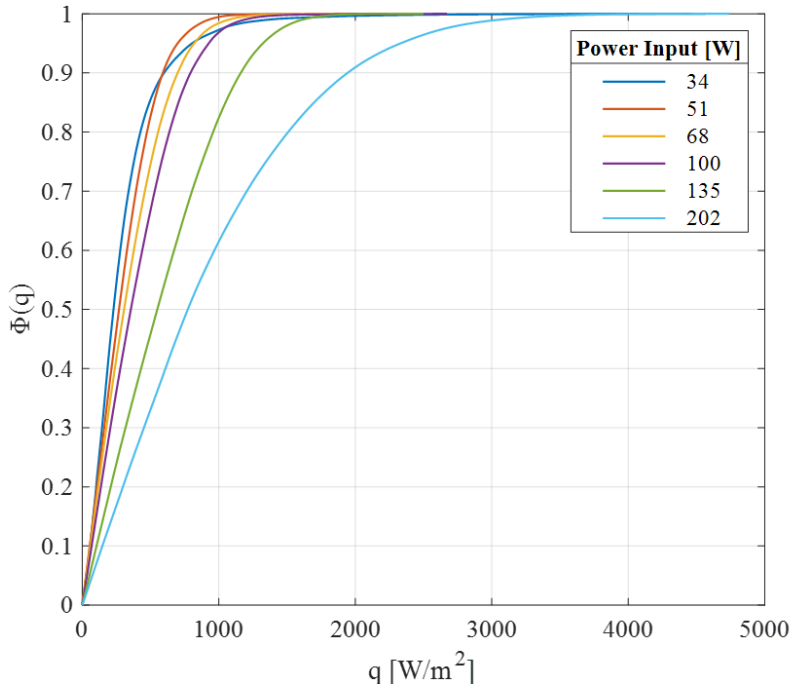

Figure 7.11: Cumulative distribution function Φ of the absolute wall-to-fluid heat flux q, for every power input given to the evaporator.

To quantitatively define the PHP working regimes, the 80th percentile of the heat flux amplitude, q_{80}, corresponding to Φ(q) = 0.8, is therefore evaluated and reported in Figure 7.12 as a function of the power input. Here, the q_{80} is almost constant at low power inputs, verifying the similar wall-to-fluid thermal interactions during the intermittent functioning mode. From 100 W up to the maximum power input, the heat flux amplitude increases almost linearly with the power input, confirming the increasing entity of the wall-to-fluid thermal interactions within the adiabatic section during the full activation functioning mode.

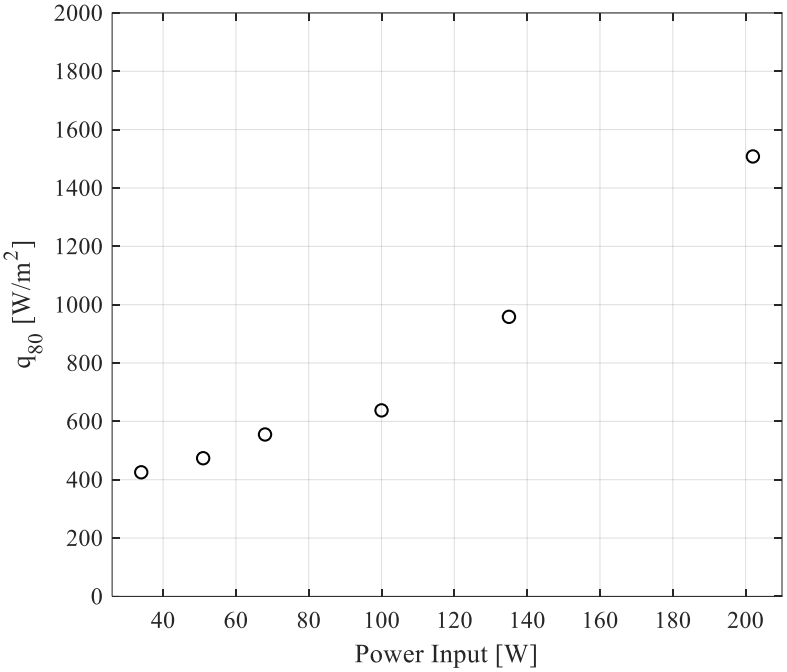

Figure 7.12: 80th percentile of the wall-to-fluid heat flux amplitude, evaluated by considering every test case of Table 2.

7.2.6. Frequency analysis on the local wall-to-fluid heat fluxes

To achieve a better understanding of fluid oscillations during the stable working mode, single axial coordinates of the wall-to-fluid heat fluxes were used as inputs for the wavelet method (Paragraph 6.2) since such quantities were proven to be strictly linked with the fluid oscillatory behaviour. It must be highlighted that the analysis was limited to fluid oscillation frequencies higher than 0.5 Hz, due to the fact that the analysed time window is limited to 10 seconds, thus preventing the possibility to observe a sufficient number of peaks corresponding to dominant frequencies lower than 0.5 Hz. For the present application, the uncertainty related to the evaluated dominant frequency was found to be equal to 0.06 Hz.

In order to test the robustness of this approach, the wavelet analysis was replicated for different axial coordinates of the same heat flux distribution referred to one channel: the resulting f_D did not change along the channel, thus confirming the independency of the oscillation frequency of the axial coordinate.

The wavelet transform analysis was then performed for all the study cases, considering only the stable working conditions. In Figure 7.13-Figure **7.15**, the wavelet transform approach was applied to the wall-to-fluid heat fluxes referred to three different power inputs to the evaporator, for three representative channels, i.e. channel 1, 5 and 8 (z = 0.045 m). For low power input (Figure 7.13), the dominant oscillation frequencies were found to be generally low (around 0.6 Hz). The presence of channels in which a dominant frequency couldn't be appreciated confirms what already observed in the

previous section, where the wall-to-fluid heat flux distributions showed a partial activation of the device.

The dominant fluid oscillation frequency increases with the power input (Figure 7.13 and Figure 7.14), and the fluid oscillations become more and more repeatable within the overall device, thus denoting a full activation of the PHP. However, power spectrum of Figure 7.15c presents different powers related to each dominant frequency, hence the repeatability of the oscillatory phenomenon cannot be fully stated. This is mainly due to the limited observation window, which does not allow a complete characterization of the PHP chaotic behaviour.

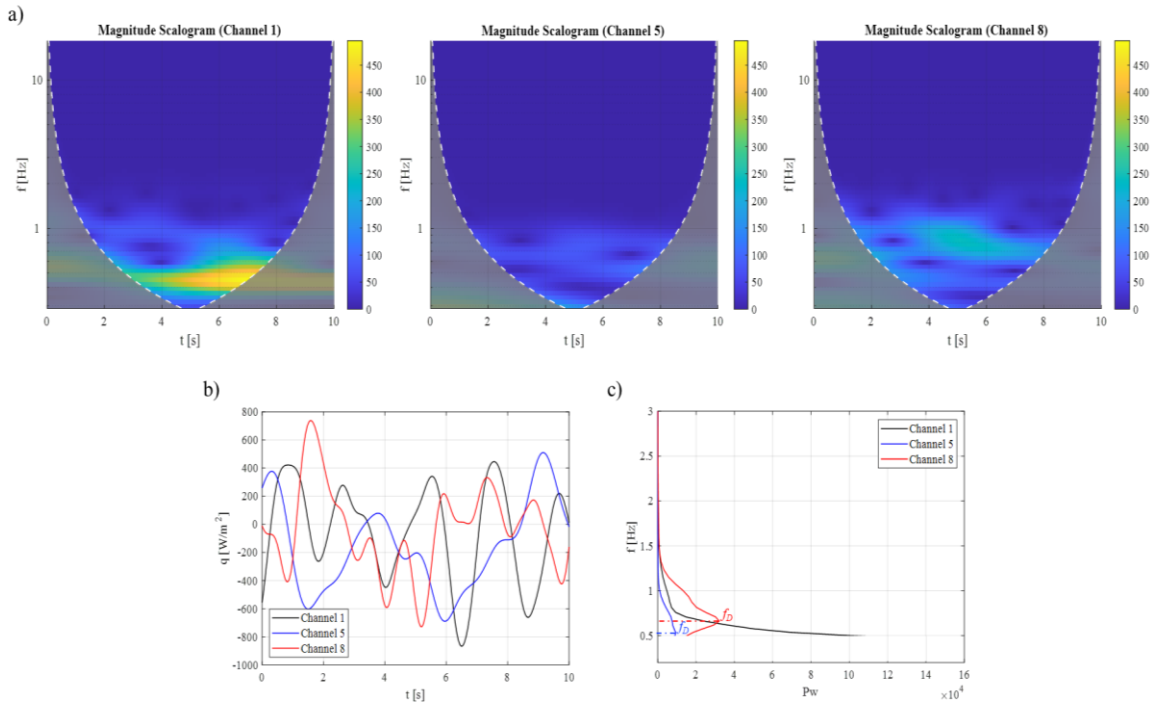

Figure 7.13: Magnitude scalograms (a), wall-to-fluid heat fluxes (single axial coordinate) (b) and power spectrum (c), for power input equal to 34 W, channels 1, 5 and 8.

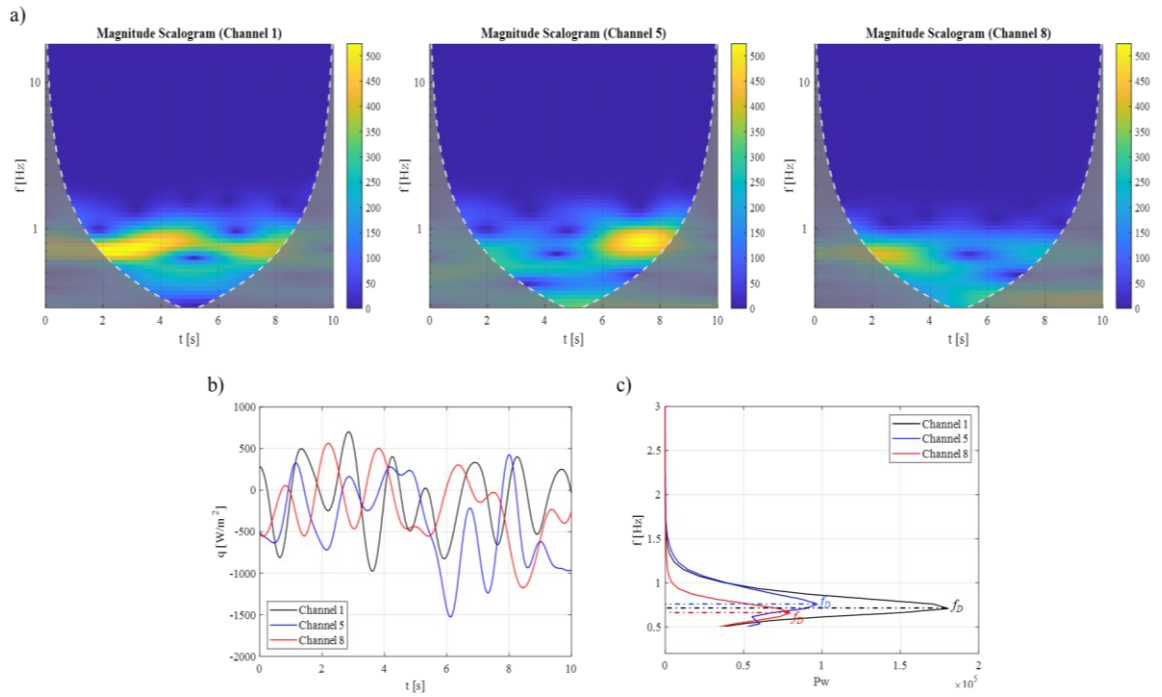

Figure 7.14: Magnitude scalograms (a), wall-to-fluid heat fluxes (single axial coordinate) (b) and power spectrum (c), for power input equal to 100 W, channels 1, 5 and 8.

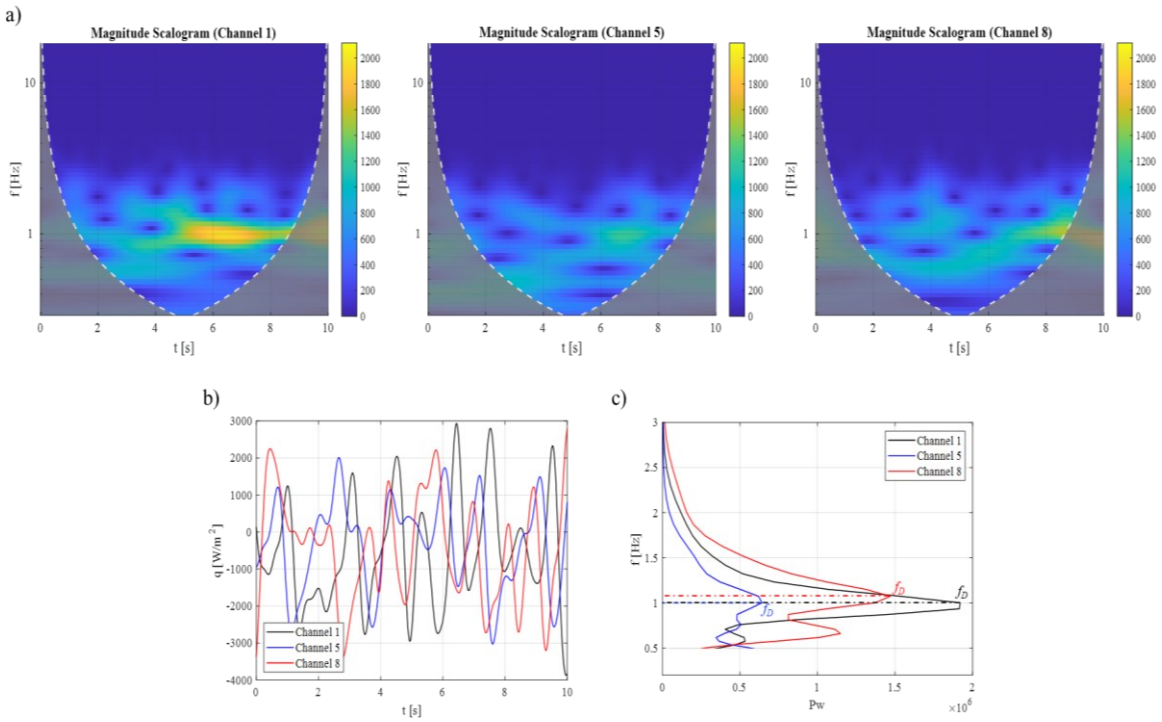

Figure 7.15: Magnitude scalograms (a), wall-to-fluid heat fluxes (single axial coordinate) (b) and power spectrum (c), for power input equal to 202 W, channels 1, 5 and 8.

Table 7.4 provides a sample of the evaluated dominant frequencies related to every channel, considering one test case of Table 7.2 for each power input to the evaporator. Here, the channel-wise oscillatory behaviour can be appreciated, highlighting that some PHP channels are inactive at low power inputs since a dominant frequency could not be evaluated (dashes), while the PHP is fully activated for high power inputs. Again, the dominant frequency has an increasing trend with the power input, although few channels still show a different oscillatory behaviour, i.e., different dominant frequencies, even at elevated power inputs. It has to be highlighted that the dominant frequency does not present any perceivable correlation with the average heat flux amplitude of Table 7.3, thus suggesting that the fluid oscillation frequency is not strictly linked to the heat transfer entity through the adiabatic section, although both quantities averagely increase with the power input in every channel.

Table 7.4: Dominant frequency for each PHP channel, referred to one test case for each power input.

f_D [Hz]		Power Input [W]					
		34	*51*	*68*	*100*	*135*	*202*
Channel number	*1*	-	-	-	0.71	0.81	0.93
	2	-	0.66	-	0.71	0.81	0.93
	3	0.58	-	0.62	0.71	0.81	0.93
	4	-	0.57	0.53	0.53	0.81	0.66
	5	-	0.57	0.61	0.76	0.58	1
	6	-	0.61	0.61	0.58	0.81	1
	7	0.54	0.61	0.57	0.58	0.81	1
	8	0.66	-	0.6	0.66	0.81	1.1
	9	-	0.5	0.57	0.71	0.76	0.9
	10	0.54	-	0.6	0.71	0.71	0.61

The evaluated dominant frequencies of Table 7.4 are furthermore processed by computing the 80th percentile, introduced in Paragraph 6.3.2, of the fluid dominant frequency ($f_{D,80}$), which is reported in Figure 7.16 as a function of the heat load. In the same figure, a comparison between the here found $f_{D,80}$ and the dominant frequencies observed by Perna et al. [104] for the same test conditions is also presented. Specifically, in [104] the dominant frequency was evaluated by processing the fluid pressure acquisitions referred to a single channel. The agreement between both pieces of data is thus assessed, thus confirming the effectiveness of the adopted IR non-intrusive technique. Moreover, during the intermittent flow regime, $f_{D,80}$ does not change substantially, while it increases during the device full activation and seems to settle around constant values for high power inputs to the evaporator (> 135 W).

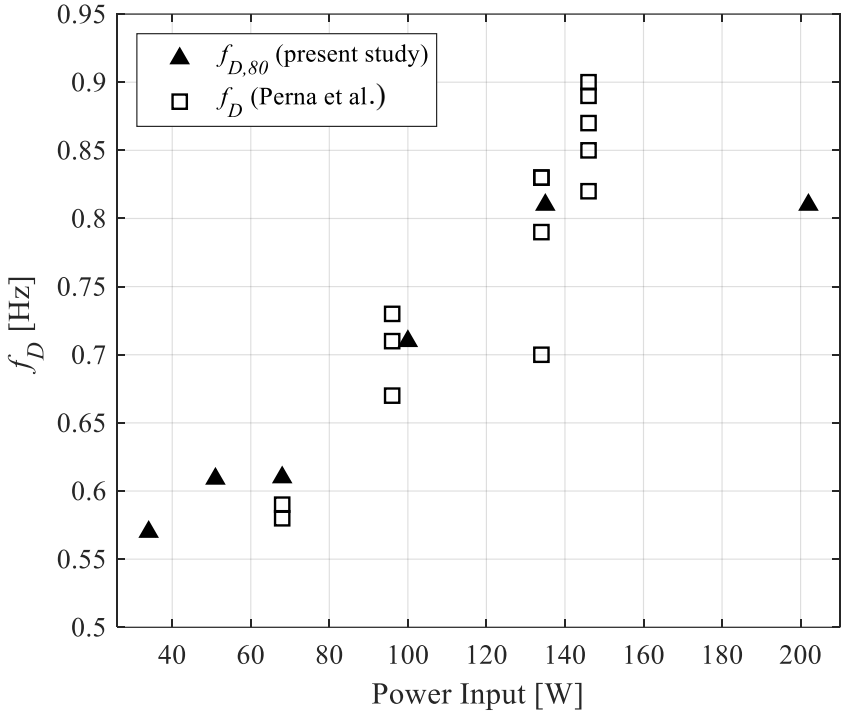

Figure 7.16: Comparison between the 80th percentile of the dominant frequency and the dominant frequencies obtained by Perna et al. [104] for the same study cases by processing the fluid pressure signals referred to one single PHP channel.

The $f_{D,80}$ is finally processed by evaluating its coefficient of variation *cvf*, i.e., its variation with the power input to the evaporator, by means of Equation (7.1).

In Figure 7.17, *cvf* is shown as a function of the power input to the evaporator. The channels in which no fluid oscillation could be perceived were assumed to have $f_{D,80}$ = 0 Hz. Such statistical coefficient quantifies the deviation of f_D from its mean value: when *cvf* is high, the analysed population presents some values which strongly differ from the others. On the contrary, when *cvf* is low, the given population presents similar values. In fact, when *cvf* is equal to 0%, the population is entirely constituted by equal values.

For low power inputs, *cvf* is high, denoting that fluid oscillation occurs in few channels. *cvf* gradually decreases with the power input during the intermittent flow regime since some channels start to exhibit fluid oscillations. From 135 W to the maximum power input, *cvf* is low and almost constant, denoting that the device is working in optimal conditions (full activation) and the dominant oscillation frequencies are similar for each heat load, although a slight variation from channel to channel is still appreciable within every test case, i.e., *cvf* is always greater than 20%.

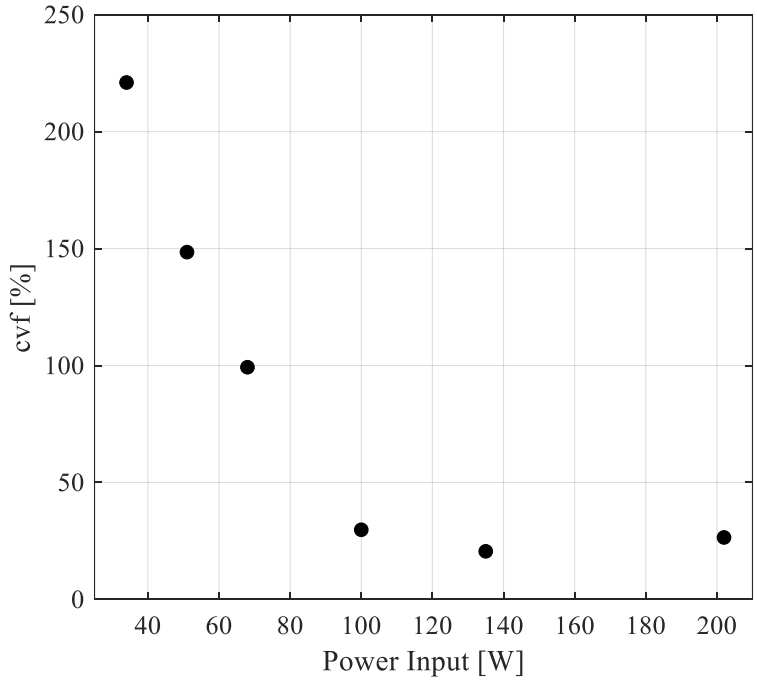

Figure 7.17: *cvf* against power input, obtained by considering the dominant oscillation frequencies related to every PHP channel and all the test cases of Table 7.4; when the channels did not exhibit any fluid oscillation, the dominant frequency was assumed equal to 0 Hz.

7.3 Space pulsating heat pipe: ground experiments

Ground tests were performed with the same experimental apparatus presented in Paragraph 7.2, except for what concerns the IR analysis. In fact, the outer wall temperature of the aluminium channels was acquired by means of a different high-resolution medium wave IR camera (FLIR® SC7600, 18 Hz, 640x512 pixels), with sampling frequency of 18 Hz. Moreover, the sapphire insert was coated on half side with the same high-emissivity paint to allow simultaneous acquisitions of the outer wall and working fluid temperature. Hence, the local analysis is, in the present Paragraph, firstly referred to the aluminium channels, and secondly to the sapphire channel.

The purpose of the conducted ground experimental campaign was to thoroughly characterize the device in pseudo-steady state conditions, not achievable during the few seconds of microgravity in weightlessness experimentations, both in terms of global and local heat transfer performance. The provided results are thus believed to be of great relevance for the long-term operation of the device.

7.3.1. Experimental procedure

The device was first vacuumed (down to 10-6 mbar) and then partially filled by means of a micro-metering valve (IDEX® Upchurch Sc. P- 447) with methanol (filling ratio = 50 ± 1% vol.). Specifically, methanol was used among other fluids due to its relatively low dynamic viscosity and high latent heat, but mostly because it guarantees the presence of a capillary flow inside the device, according to the static criterion, i.e. Bond number less than 4 [48], even if the 3 mm internal diameter is rather big with respect to the values that can be commonly found in the literature. During the experimental campaign's conceptualization, the non-recommended chemical compatibility level of aluminium and methanol for long-terms applications due to the generation of NCGs was considered [132]. However, the relatively short duration of the tests (~ 2 months) resulted in a negligible production of NCGs. Despite the fact that the obtained outcomes may not be fully exploited for an immediate industrial application, they are certainly interesting from a physical point of view, thus improving the understanding of phenomenological aspects, and providing useful references for the validation of numerical models present in the literature.

Before the filling procedure, the working fluid was degassed in a secondary tank by continuous boiling: incondensable gases thus accumulated in the upper part of the tank, and they were therefore sucked from above by means of several vacuuming cycles with the same procedure described by Henry et al. [133].

During the experiments, the device was tested in horizontal orientation, vertical BHM and vertical Top Heated Mode (THM), as shown in Figure 7.18.

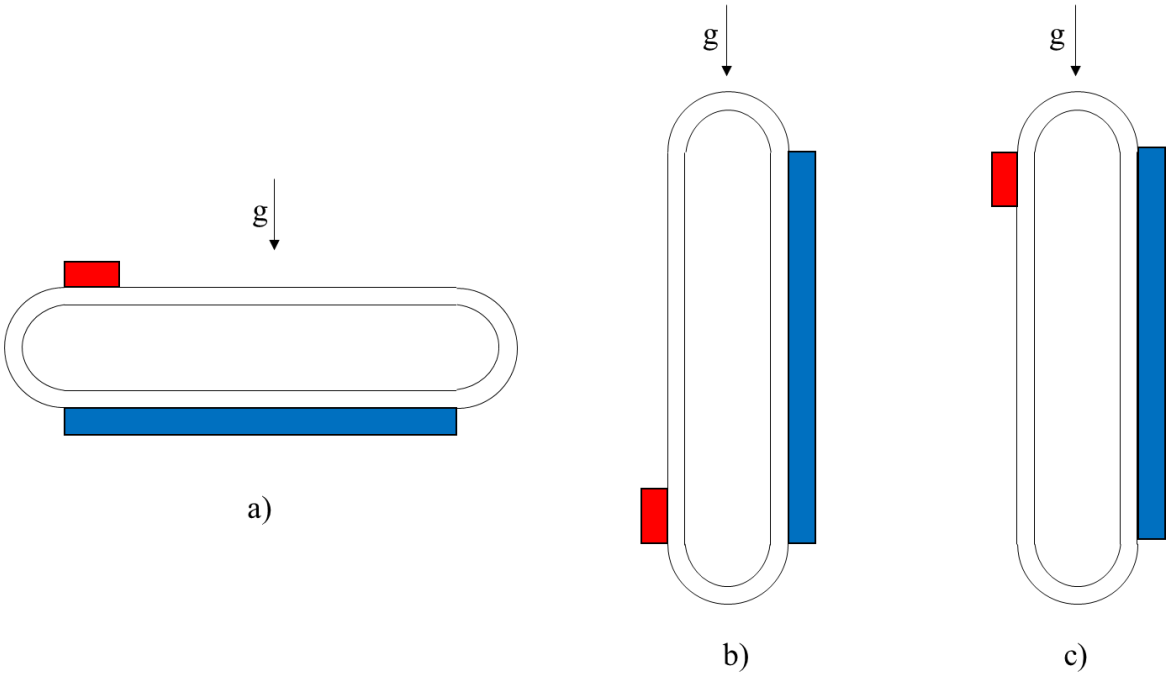

Figure 7.18: Sketch of the considered PHP orientations, depending on the heat source position (red) with respect to the heat sink (blue) and the gravitational field g: horizontal orientation (a), BHM (b) and THM (c).

The condenser temperature T_{cond} was set to 10°C and 20°C for each orientation mode, while the heat load to the evaporator was varied from 10 W up to a maximum of 210 W. For every combination of condenser temperature and device orientation, two IR acquisitions (60 seconds each) were carried out within the pseudo-steady states of the system, i.e. after about 25 minutes from each heat load step to the evaporator. The IR measurements were carried out in between the evaporator and the condenser within a 0.069 meters long section (Figure 7.19) since the adiabatic zone was the only portion directly accessible to the IR camera. The 13 aluminium channels are numbered starting from the one next to the sapphire insert.

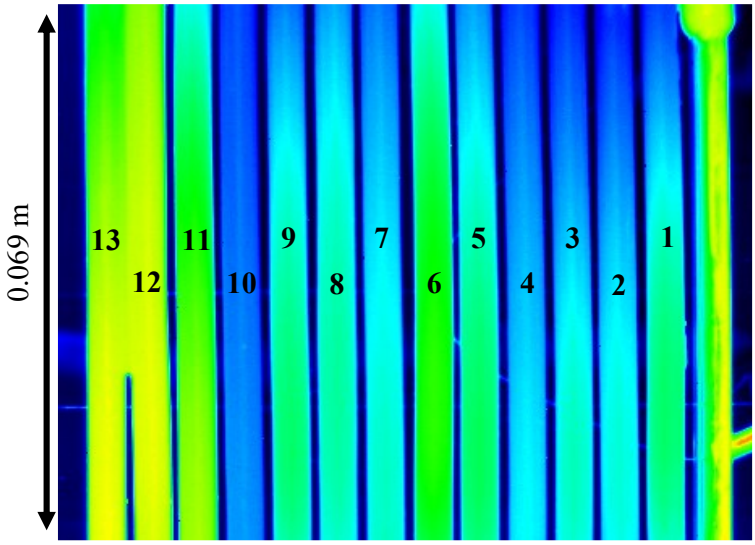

Figure 7.19: Sample of IR acquisition, used as reference for the aluminium channels' numeration.

For safety reasons, the evaporator temperature was limited to a maximum of 105°C by a thermal switch, directly placed on the evaporator heater.

The investigated PHP configurations are summarized in Table 7.5. Specifically, the thermal switch activation was avoided by setting, case by case, different upper limits to the providable power input to the evaporator Q.

Table 7.5: Studied PHP configurations and provided power inputs.

Orientation	T_{cond} **[°C]**	**Range of** Q **[W]**
Horizontal	20	10 up to 190
BHM	20	10 up to 190
THM	20	10 up to 180
Horizontal	10	10 up to 190
BHM	10	10 up to 210
THM	10	10 up to 150

7.3.2. Global performance

For every studied configuration, the PHP thermal characterization was first achieved by evaluating the equivalent thermal resistance R_{eq} by means of Equation (3.1). Considering the thermal conductivity of the insulation layer (0.02 W/mK), the difference between the evaporator and the environmental temperature ($\Delta T \approx 50$ K for the most unfavourable condition), and the total external surface of the evaporator insulation (0.0034 m^2), the heat losses to the environment in the evaporator section are always less than the 0.5% of the heat load provided by the heater and they are consequently neglected in the present study.

For the present study case, both T_{eva} and T_{cond} were evaluated by averaging the wall temperature at the two PHP sections, measured by means of the thermocouples over the last 5 minutes within the pseudo-steady state. By adopting the approach by Kline and McClintock [134], the uncertainty on R_{eq} was assessed to have a maximum of about 15% at very low heat loads and a minimum around 0.6% at high heat loads. Specifically, calling $\delta_{\Delta T}$ the uncertainty related to the temperature difference $\Delta T = T_{eva} - T_{cond}$ and δ_Q the uncertainty related to the provided heat load Q, the uncertainty on the equivalent thermal resistance is computed as $\delta_{R_{eq}} = \sqrt{\left(\frac{1}{\Delta T}\delta_{\Delta T}\right)^2 + \left(\frac{1}{Q}\delta_Q\right)^2}$.

The thermal resistance referred to the empty device was found to be equal to 1.4 K/W; this value is representative of the heat transferred by only conduction through the aluminium tube between the heated and the cooled section. Such resistance was evaluated for power inputs up to 50 W, since higher heat loads brought to the system overheating and to the consequent activation of the thermal switch.

In Figure 7.20, the equivalent thermal resistance is shown, with the corresponding error bars, for every PHP orientation and condenser temperature as a function of Q.

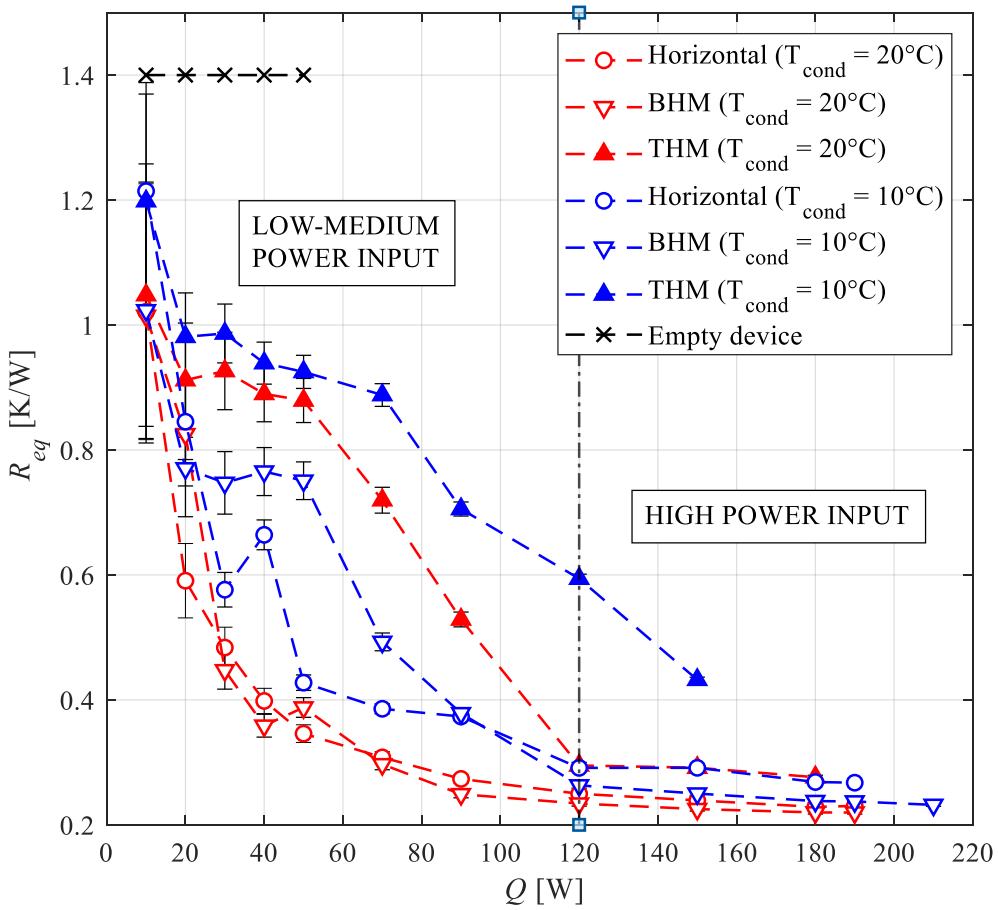

Figure 7.20: Equivalent thermal resistance of the device as a function of the power input Q, evaluated for every considered orientation and condenser temperature.

Here, two main effects are expected to affect the device thermal performance: the viscous effects, related to a lower functioning temperature of the device, and the gravity effects, related to the PHP orientation with respect to the gravitational field.

Since the fluid viscosity is inversely proportional to the fluid temperature, the fluid motion damping increases when the condenser temperature is set to the lowest value T_{cond} = 10°C (blue trends in Figure 7.20). Consequently, R_{eq} assumes higher values with respect to the configurations at T_{cond} = 20°C (red trends in Fig. 5a). In fact, for low fluid temperatures (from 10°C to 20°C), the variation of fluid viscosity μ with respect to temperature $\frac{\partial \mu}{\partial T} \approx -1 \cdot 10^{-5}$ Pa·s/K, while, for high fluid temperatures (higher than 30°C), $\frac{\partial \mu}{\delta T} \approx -7.3 \cdot 10^{-6}$ Pa·s/K. This results in a percent variation of viscosity of about -25% and -6% at low and high temperatures, respectively, thus denoting stronger viscosity effects at lower values of $T_{cond,}$ i.e., lower fluid temperature.

Regarding the effect of the orientation on the device thermal performance, two different zones are defined according to the heat load given to the evaporator: the low/medium power input zone (Q < 120 W), where these effects are more evident and the trends vary in a wider range of thermal resistances, and the high power input zone ($Q \geq$ 120 W), where R_{eq} is less dependent both on the heat load and the orientation. In the low/medium power input zone, the horizontal orientation (circles in Figure 7.20) is characterized by values of thermal resistance which decrease almost monotonically with the increase of the power input given to the evaporator for both condenser temperatures. The BHM (downward triangles in Figure 7.20) presents instead two different trends from one condenser temperature to the other: at T_{cond} = 20°C, R_{eq} is comparable with the thermal resistance trend observed in the horizontal orientation for the same condenser temperature, while, at T_{cond} = 10°C, R_{eq} settles around 0.76 K/W to start decreasing from 50 W. Hence, the BHM configurations, when compared with the horizontal modes, denote similar performances at low heat loads. Although such evidence disagrees with various literature findings related to the planar devices [135], the enhanced PHP thermal response at low power inputs in the horizontal orientation was found to be comparable with the one assessed in [136] for a similar 3D geometry. In fact, in 3D layouts, the presence of small gravity heads, even when they are not favourable, may assist the triggering of the fluid motion.

Regarding the THM (upward triangles in Figure 7.20), the device exhibits a low performance at low power inputs due to the counter-gravity effects, which strongly hamper the fluid motion.

In the high power input zone, the considered geometry may be responsible for the high PHP thermal performances, denoted by R_{eq} values which stabilizes around 0.25 K/W for all the configurations but the THM at T_{cond} = 10°C. The device thus seems not to be significantly affected either by the orientation or by the condenser temperature at high heat loads, confirming the results found in previous works [16,136]. It must be pointed out that such interesting inclination-independent feature is not generally obtained for planar layouts having similar geometry, number of turns and working fluid. Verma et al. [137] studied a 6-turn planar PHP with inner diameter of 1.45 mm, showing that, when the device was

filled with methanol, its equivalent thermal resistance was higher for the horizontal orientation with respect to that for the vertical orientation. Similar outcomes were found by Mameli et al. [61] and Ayel et al. [138].

The thermal behaviour in the THM at T_{cond} = 10 °C leads to the highest global thermal resistance values in the investigated power input range. However, the trend of R_{eq} (Q) is sharply decreasing, and it may reach lower values if power inputs would be higher than 150 W. The test was stopped here not because of a dry-out event, but due to safety issues, since the heater temperature overcame 105 °C and the thermal switch cut off the power supply.

7.3.3. Local heat transfer analysis: metallic channels

To provide a deeper insight into the heat transfer phenomena occurring in the device, a local heat transfer analysis was carried out for every PHP working configuration. To this aim, the IR acquisitions on the adiabatic section were post-processed by means of the procedure presented in Paragraph 5.2.2, resulting in N×M time-space heat flux distributions referred to each of the 13 analysed channels. Since the heat losses to the environment within the whole adiabatic section, for the most unfavourable test condition, i.e. Q = 210 W, were lower than 3 W (average wall temperature ≈ 50°C), the IR measurements were assumed to perceive temperature variations due to the inner thermal interactions between the channel wall and the working fluid rather than between the channel wall and the environment. Such assumption was extended to every study case since heat losses to the environment spanned from about 0.7% of the total provided power input at low heat loads to about 1.5% at high heat loads.

The wall temperature distribution (Figure 7.21a) and the corresponding wall-to-fluid heat flux distribution (Figure 7.21c) are reported for channel 4 (horizontal orientation, T_{cond} = 20°C, Q = 120 W), together with their space distribution for 4 different time instants (Figure 7.21b and Figure 7.21d, respectively).

a)

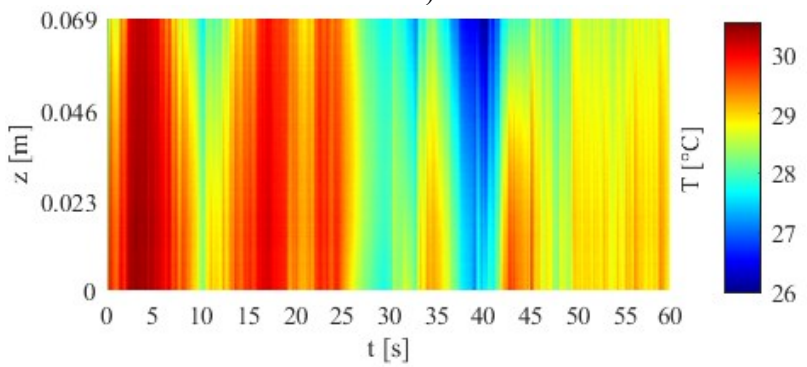

b)

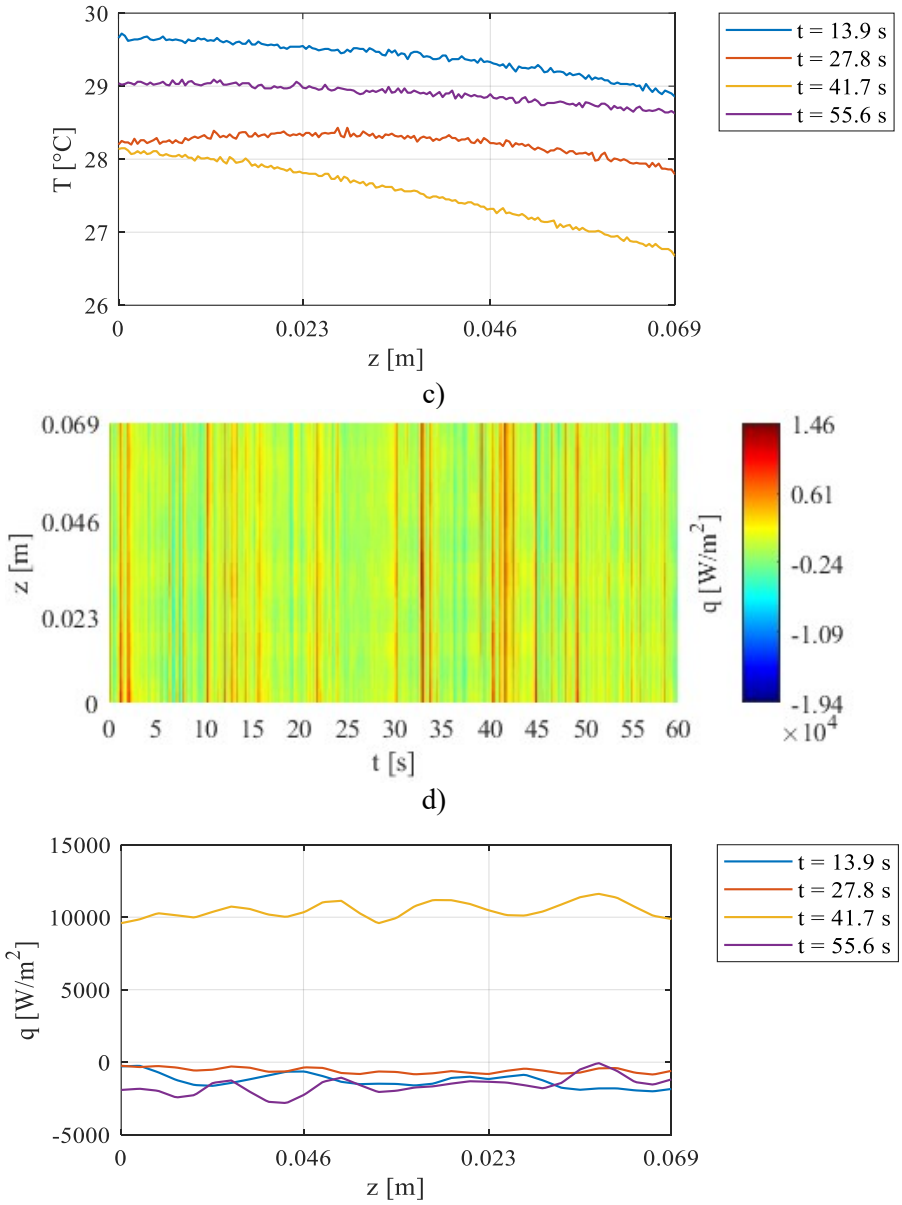

Figure 7.21: Raw IR measurement (a) and its space distribution for 4 different time instants (b); evaluated wall-to-fluid heat flux (c) and its space distribution for 4 time instants (d). Channel 4, horizontal orientation, Q = 120 W, T_{cond} = 20°C.

The interpretative process for the heat flux maps in terms of fluid motion inside the PHP channels follows exactly the same reference of Paragraph 7.2.3. It has to be reminded that fast transient phenomenon, e.g. alternance of liquid slugs and vapour plugs in the fluid flow, could not be fully perceived on the outer surface due to the filtering effect of the aluminium wall, as noticeable from Figure 7.21b-d.

7.3.4. Working regimes assessment

The study of the PHP working modes, coupled with the device global performance evaluation, is crucial for the achievement of a comprehensive description of the device heat transfer capability at varying working conditions. In fact, the different working modes define the heat transfer modes obtained by means of the thermally induced fluid motion between the evaporator and the condenser section. A novel objective detection method for the working regimes identification is adopted, based on the post-processing of the IR measurements on the adiabatic section through analytical (IHCP solution approach) and statistical tools proposed in Paragraph 7.2. Specifically, such method can be performed on opaque tubes in a repeatable and comparable way for any tubular PHP geometry or experimental condition by using the heat flux locally exchanged within the adiabatic section between the working fluid and the PHP walls.

It must be pointed out that the local investigation on the PHP heat transfer behaviour within the adiabatic zone has been proven to perceive fluid motion in the overall device alike direct fluid visualizations, thus providing complementary definitions of the working modes with respect to those presented by means of the only evaporator/condenser temperature measurements:

- when the device is not yet activated, the local wall-to-fluid heat flux is almost null in every PHP channel;
- the device start-up occurs when at least one channel locally presents slight heat flux variations over time;
- during the intermittent flow mode, the heat flux oscillates in multiple PHP branches. From a local point of view, the device stop-overs are to be intended as periodic deactivations of some PHP channels, where the wall-to-fluid heat flux alternates oscillations to almost null values;
- full activation, where every PHP branch presents regular oscillations over time of the wall-to-fluid heat flux.

In the present investigation, the working modes occurring during the device operation were identified by adopting both the evaporator temperature and the wall-to-fluid heat flux fluctuations within the adiabatic section to give an insight into the heat transfer behaviour of the studied PHP. First, the history of the evaporator temperature over the entire duration of the tests was adopted as reference for the identification of the device working modes at different heat loads for every studied configuration, [48]. Figure 7.22 shows the evaporator temperature trends for two configurations, namely the horizontal orientation, T_{cond} = 10°C (Figure 7.22a) and the BHM, T_{cond} = 20°C (Figure 7.22b). In Figure 7.22a, the evaporator temperature starts to present appreciable fluctuations from 20 W, which persist also during the pseudo-steady state of the device, thus denoting the device activation. By increasing the heat load up to 120 W, the evaporator temperature presents, in every measurement point, an alternance of high and low peaks, suggesting the occurrence of several stop-overs typical of the intermittent flow mode

[48]. From 150 W up to the maximum provided power input, the temperature fluctuations are more stable in time, thus denoting the full activation of the device [62]. By carrying out a similar analysis on the data provided in Figure 7.22b, the activation of the device was observed at 30 W, the intermittent flow mode was assessed in the range 40 to 70 W, while the full activation of the device occurred from 90 W up to 190 W.

a)

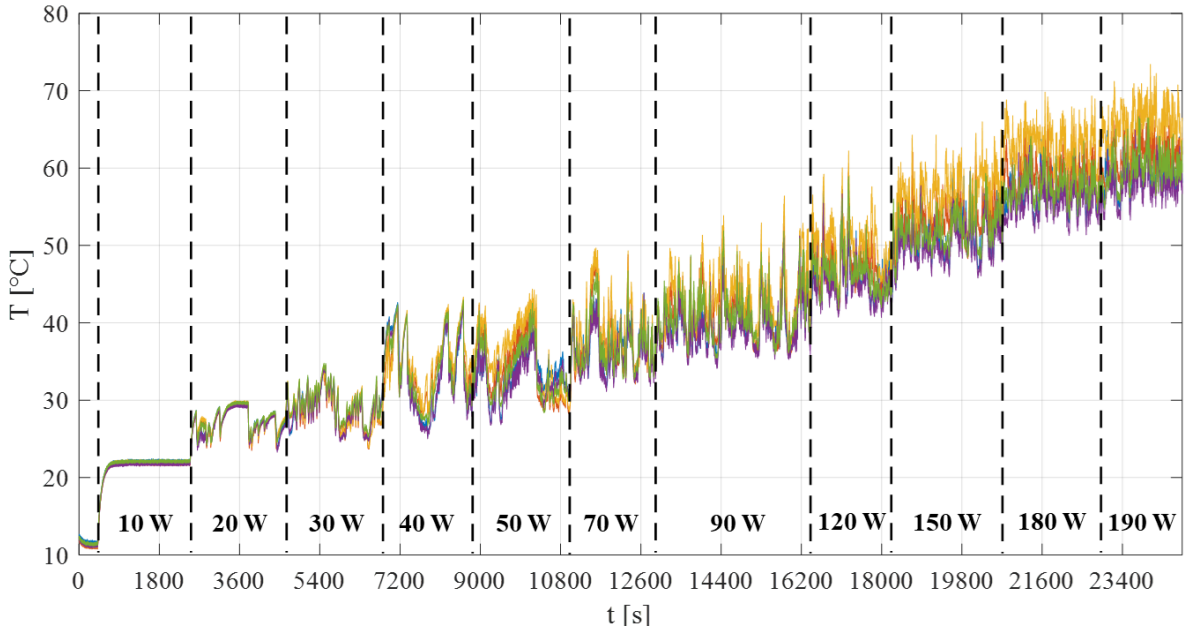

b)

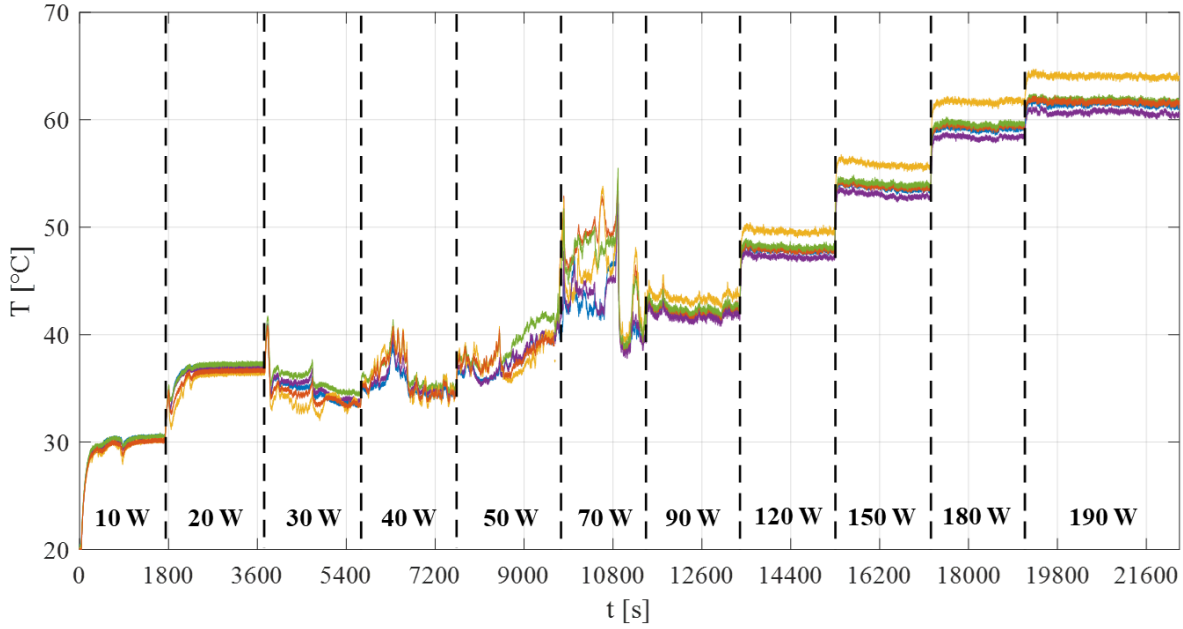

Figure 7.22: History of the evaporator temperature over the entire duration of the tests for the horizontal mode, T_{cond} = 10°C (a) and the BHM, T_{cond} = 20°C (b).

The evaporator temperature variations were therefore compared with the evaluated local wall-to-fluid heat flux within the adiabatic section to provide an additional reference for the identification of the PHP working modes. For every tested configuration, the evaporator temperature, measured at five different locations over 6 minutes within the pseudo-steady state of the system, was compared with the local wall-to-fluid heat flux exchanged through channel 1, 4, 7 and 10 (reference of Figure 7.19) for the axial coordinate z = 0.035 over 1 minute, together with its error bars (black lines, according to the estimation error provided Appendix A).

In Figure 7.23, three different study cases were chosen as representative samples for the mentioned working mode identification procedure. In the THM, for Q = 10 W and T_{cond} = 20°C (Figure 7.23a-b), the device exhibits a pure conduction working mode since the evaporator temperature is greatly stable (Figure 7.23a) and the local heat flux is almost null (Figure 7.23b), thus denoting the absence of fluid motion. In the BHM, for Q = 90 W and T_{cond} = 10°C (Figure 7.23c-d), the evaporator temperature presents instead strong variations due to device stop-overs (Figure 7.23c). Similarly, the wall-to-fluid thermal interactions within the adiabatic section are characterized, in every considered channel, by null local heat fluxes, followed by slight heat flux peaks (Figure 7.23d), suggesting that the device is operating in an intemittent way. Specifically, by comparing Figure 7.23c and Figure 7.23d, while the evaporator temperature is almost stable from t = 300 s to 340 s, it undergoes an overall increase from t = 340 s to 360 s, typical of a fluid motion stop-over phenomenon. Such behaviour is strictly linked to the local wall-to-fluid heat flux. In fact, during the first seconds of the observation window, q presents weak fluctuations in every channel, while, during the last seconds of acquisition, q is almost null in every PHP branch, highlighting that evaporator and the condenser sections are not thermally interacting, i.e. the heat provided to the evaporator is not being effectively dissipated. Finally, in the horizontal orientation, for Q = 180 W and T_{cond} = 10°C, the PHP is fully activated. In fact, the evaporator temperature (Figure 7.23e) presents relatively low deviations with respect to its mean value, while the heat fluxes (Figure 7.23f) denote strong and persistent fluid oscillations between the evaporator and the condenser section in the overall device.

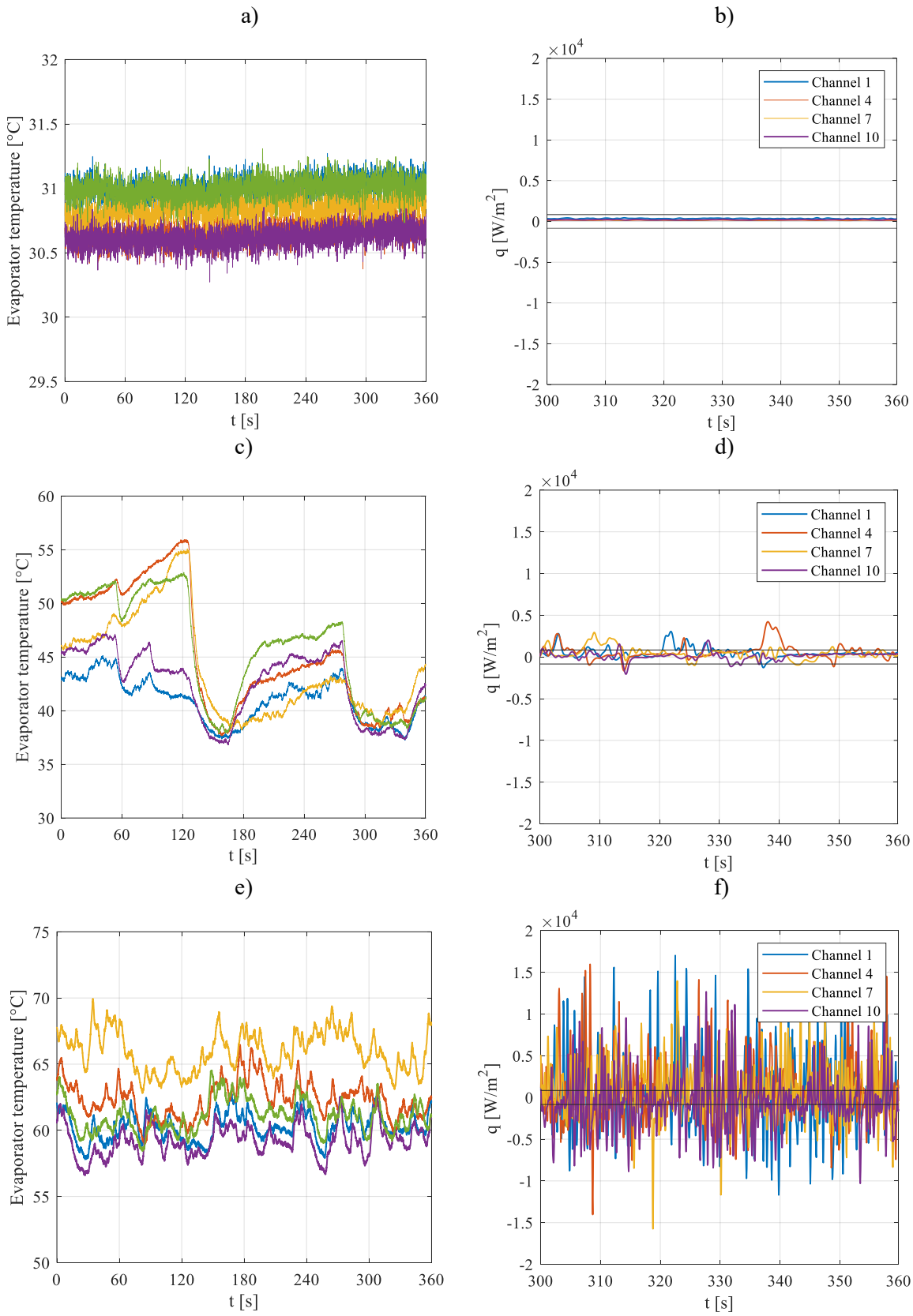

Figure 7.23: Evaporator temperature and local heat flux evaluated on 4 PHP channels together with its error bars (black lines), for the THM, Q = 10 W, T_{cond} = 20°C (a,b), the BHM, Q = 90 W, T_{cond} = 10°C (c,d) and the horizontal orientation, Q = 180 W, T_{cond} = 10°C (e,f).

The PHP working modes, observed by replicating the above evaluation for every studied configuration, are summarized in Table 7.6. Here, the horizontal orientation is characterized by low activation power inputs to the evaporator, and the intermittent flow mode persists for a wider range of power inputs with respect to the BHM. In fact, for such orientation, the gravity tends to promote a stable fluid oscillation in the whole PHP, thus anticipating at lower heat loads the full activation of the device. Within the THM, the device operates instead in a narrow range of heat loads, and it generally does not work in a satisfactorily way, especially at low condenser temperature. Moreover, both the BHM and the THM seem to be strongly influenced by the condenser temperature at low heat loads due to a strong delay of activation from T_{cond} = 20°C to T_{cond} = 10°C.

Table 7.6: Device working modes for different PHP configurations and power inputs to the evaporator Q. "-": device inactivity (pure conduction), "S": start-up, "I": intermittent flow, "FA": device full activation.

	***Q* [W]**											
	10	*20*	*30*	*40*	*50*	*70*	*90*	*120*	*150*	*180*	*190*	*210*
Orientation	***T_{cond} = 20°C***											
Horizontal	-	*S*	*I*	*I*	*I*	*I*	*I*	*FA*	*FA*	*FA*	*FA*	
BHM	-	-	*S*	*I*	*I*	*I*	*FA*	*FA*	*FA*	*FA*	*FA*	
THM	-	-	-	-	*S*	*I*	*I*	*FA*	*FA*	*FA*		
	T_{cond} = 10°C											
Horizontal	-	*S*	*I*	*I*	*I*	*I*	*I*	*I*	*FA*	*FA*	*FA*	
BHM	-	-	-	-	-	*S*	*I*	*FA*	*FA*	*FA*	*FA*	*FA*
THM	-	-	-	-	-	-	*S*	*I*	*I*			

The regime limits in terms of heat input level may slightly vary between the cases where the heat loads are increasing (heat load ramp-up) or decreasing (heat load ramp-down) due to hysteresis phenomena, as also shown by Mameli et al. [139]. Nevertheless, from the start-up point of view, the "heat ramp-up" procedure used here is the most conservative between the two because the fluid activation energy must be provided to trigger the flow motion. Finally, for what concerns the repeatability, the Authors tested the same configurations several times, confirming that each operating regime occurs accordingly to those shown in Table 7.6.

7.3.5. Statistical approach on the local wall-to-fluid heat fluxes

To provide a quantitative and repeatable identification of the working modes at different heat loads in pseudo-steady state conditions, the coefficient of variation over time *cvt* is adopted (Paragraph 6.3.1). It has to be underlined that, in the present investigation, the number of statistically reduced samples was equal to the number of time instants N = 1080 (corresponding to 60 seconds) for both the *std* and the *mean* operators, averaged over the number of axial coordinates M = 195 (corresponding to 0.069 m), thus ensuring the robustness of the adopted statistical approach. *cvt* was evaluated for every n-th analysed channel.

As further step, all the evaluated coefficients of variation referred to each channel were expressed in terms of average value (cvt_{av}) and standard deviation (cvt_{std}) on the overall device, by considering the 13 analysed aluminium channels as follows:

$$cvt_{av} = \frac{\sum_{n=1}^{13} cvt_n}{13} \tag{7.2}$$

$$cvt_{std} = \sqrt{\frac{\sum_{n=1}^{13} (cvt_n - cvt_{av})^2}{13}} \tag{7.3}$$

From a physical point of view, since *cvt* quantifies the variation over time of the heat flux for the n-th channel, cvt_{av}, defined by Equation (7.2), describes how the heat flux varies, on average, over the whole device. Furthermore, cvt_{std}, defined by Equation (7.3), describes the dispersion of *cvt* around its average in the whole PHP, thus quantifying the variations in local thermal behaviour from channel to channel.

cvt_{av} and cvt_{std} are shown in Figure 7.24a and Figure 7.24b, respectively, as a function of Q.

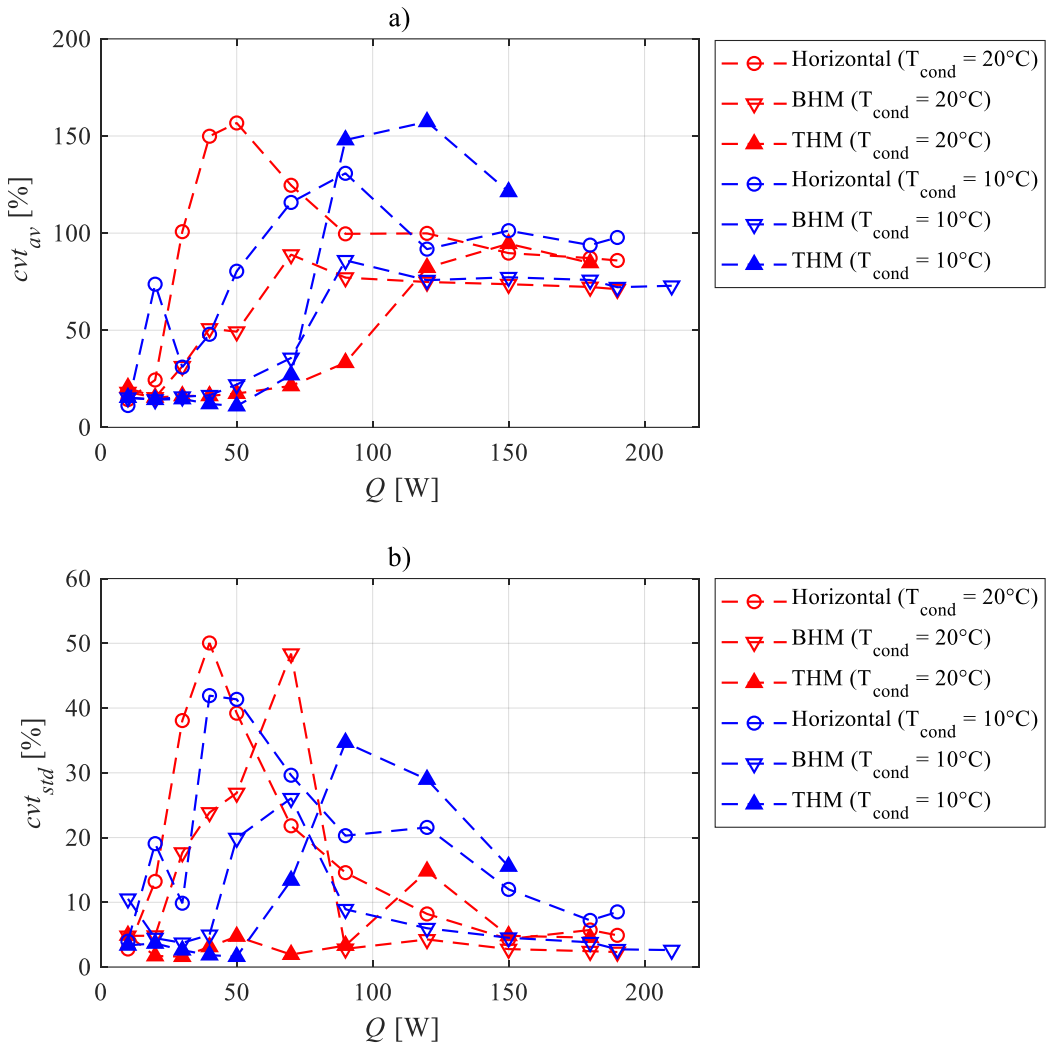

Figure 7.24: cvt_{av} (a) and cvt_{std} (b) against the power input to the evaporator for every PHP configuration.

Hence, the PHP working modes, qualitatively identified in Table 7.6, can be quantified as follows:

- PHP inactivity, described by values of cvt_{av} and cvt_{std} in the range 10 to 20% and 0 to 10%, respectively, due to almost null exchanged heat fluxes within the observation windows;
- PHP start-up, where both cvt_{av} and cvt_{std} exceed the inactivity threshold of 20% and 10%, respectively;
- intermittent flow, described by values of cvt_{av} and cvt_{std} which increase up to about 155% and 50%, respectively, due to significantly different heat transfer phenomena involving each channel;
- full activation, where cvt_{av} stabilizes in the range 70 to 100% and cvt_{std} settles in the range 0 to 15%, denoting that the fluid motion is perceivable in every PHP branch and the fluid oscillations are regular.

In particular, cvt_{av} is in the range 86 to 100% for both the horizontal orientation and the THM, while the BHM is characterized by lower values of such statistical quantity (70 to 78%).

As already highlighted in Paragraph 7.3.2, the device performance is independent of gravity within the high power input zone ($Q \geq 120$ W). For high heat loads, the device is fully activated for almost every considered configuration, thus suggesting that a regular fluid motion in the overall system promotes the independency of the PHP from orientation. Moreover, since the full activation is characterized by both fluid oscillations and circulations depending on the working conditions, as shown in Paragraph 7.3.4, no significant relation between the flow motion type and the PHP performance can be assessed. Although the circulatory flow is preferable in planar geometries to achieve higher heat transfer performances, the present 3D layout seems not to be greatly influenced by the circulatory flow at high power input levels, in accordance with the data provided in [140] for a similar 3D CLPHP geometry. However, the local thermofluidic interactions between the working fluid and the PHP wall may exhibit great variations from the oscillatory to the circulatory flow motion. To investigate such dependency, the 80th percentile of the local wall-to-fluid heat flux distributions is shown in Figure 7.25 as a function of Q for the horizontal and BHM configurations. Here, q_{80} significantly increases with Q in the horizontal configurations up to 6000 W/m^2, denoting strong local thermal interactions during the oscillatory flow at high heat loads to the evaporator. On the contrary, the exchanged wall-to-fluid heat fluxes within the adiabatic section for the BHM configurations settle to an almost constant low value for $Q > 90$ W, probably due to the fact that, when the circulatory flow occurs, the PHP tends to approach the thermal equilibrium in the adiabatic section. This results in weaker local wall-to-fluid thermal interactions, more comparable with the only heat dissipations to the surrounding environment by both natural convection and radiation at the adiabatic section, which are assumed to be, for the present application, lower than 300 W/m^2. This value is furthermore comparable with the q_{80} referred to low power inputs to the evaporator, where the device is not yet activated, and the heat exchanged between the PHP walls and the working fluid is almost equal to that exchanged with the environment.

As already mentioned, despite the higher amplitudes of the local wall-to-fluid heat flux, the thermal performance of the device (Figure 7.20) at high heat loads does not present any significant variations. This suggests that the heat stored or released by the channels wall within the adiabatic section, i.e. the evaluated local wall-to-fluid heat flux, is just a result of stronger interactions between the evaporator and the condenser section in terms of fluid motion, and it only presents a weak link with the total heat dissipated by the condenser. For the evaluation of the 80th percentile of the local wall-to-fluid heat flux q_{80}, the adopted samples were greater than 2 million (N·M·number of aluminium turns) for each heat load, thus providing a significant description of the local wall-to-fluid thermal interactions from a statistical standpoint.

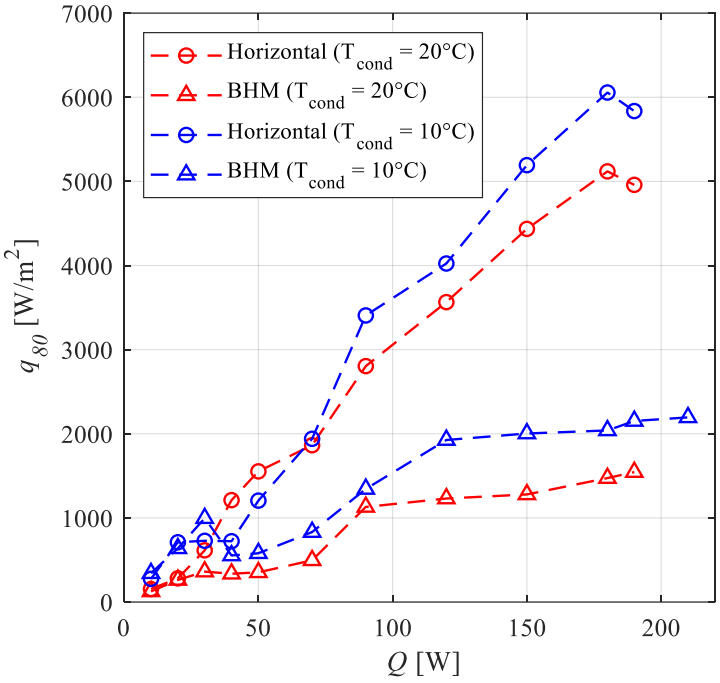

Figure 7.25: q_{80} as a function of the power input given to the evaporator, for every PHP configuration.

7.3.6. Flow modes detection

The PHP heat transfer behaviour is not only defined by the different working modes occurring during the device operation, but also by the different fluid flow modes, namely the fluid oscillation and the fluid net circulation. Specifically, the net fluid circulation, when compared to the oscillatory flow, usually guarantees a lower and more stable evaporator temperature at high power inputs [92], thus improving the device thermal performances.

To achieve a better understanding of the heat transfer modes of the device, different PHP configurations were considered with the aim of assessing the presence of either fluid oscillation or circulation. In graphs of Figure 7.26(a-c-e), the thermocouples signals referred to the evaporator section are plotted for three different test cases, i.e. horizontal mode (Q = 120 W), BHM (Q = 120 W) and THM (Q = 150 W) for the same condenser temperature T_{cond} = 20°C, over one minute within the pseudo-steady state. For the same cases, ΔP, defined as the difference between the fluid pressure measured near the evaporator and the condenser in a single PHP channel (Figure 7.19a), is reported in Figure 7.26(b-d-f), as well as its moving average over time (red line). The window length for the moving average was chosen equal to 2 seconds to remove the high-frequency noisy components from the analysis without having a loss of information regarding the stable oscillations of pressure signals. ΔP represents the driving force for the fluid motion, and it has been already proven to be a useful quantity for the fluid motion assessment within the PHP branch where the pressure transducers are placed [109]. In fact, when ΔP assumes positive values, the fluid flows through the channel from the evaporator to the

condenser, while, for negative ΔP values, flow reversals phenomena occur in the same branch. By comparing graphs of Figure 7.26(a-c-e), the evaporator temperature is clearly more stable within the BHM (Figure 7.26c). Moreover, while the ΔP referred to both the horizontal orientation (Fig. Figure 7.26b) and the THM (Fig. Figure 7.26f) oscillates from positive to negative values, i.e. its moving average varies around zero, the ΔP related to the BHM (Figure 7.26d) is positive over almost the whole observation window, i.e. its moving average assumes only positive values, thus denoting that the fluid circulates from the evaporator to the condenser without any flow reversals. The presented analysis was replicated for every test case, highlighting that the circulatory flow occurs only within the BHM mode, in accordance with previous works [48]. In particular, the heat loads required for the device to operate in a circulatory mode were found to be in the ranges 90 to 190 W and 120 to 210 W for T_{cond} = 20°C and T_{cond} = 10°C, respectively.

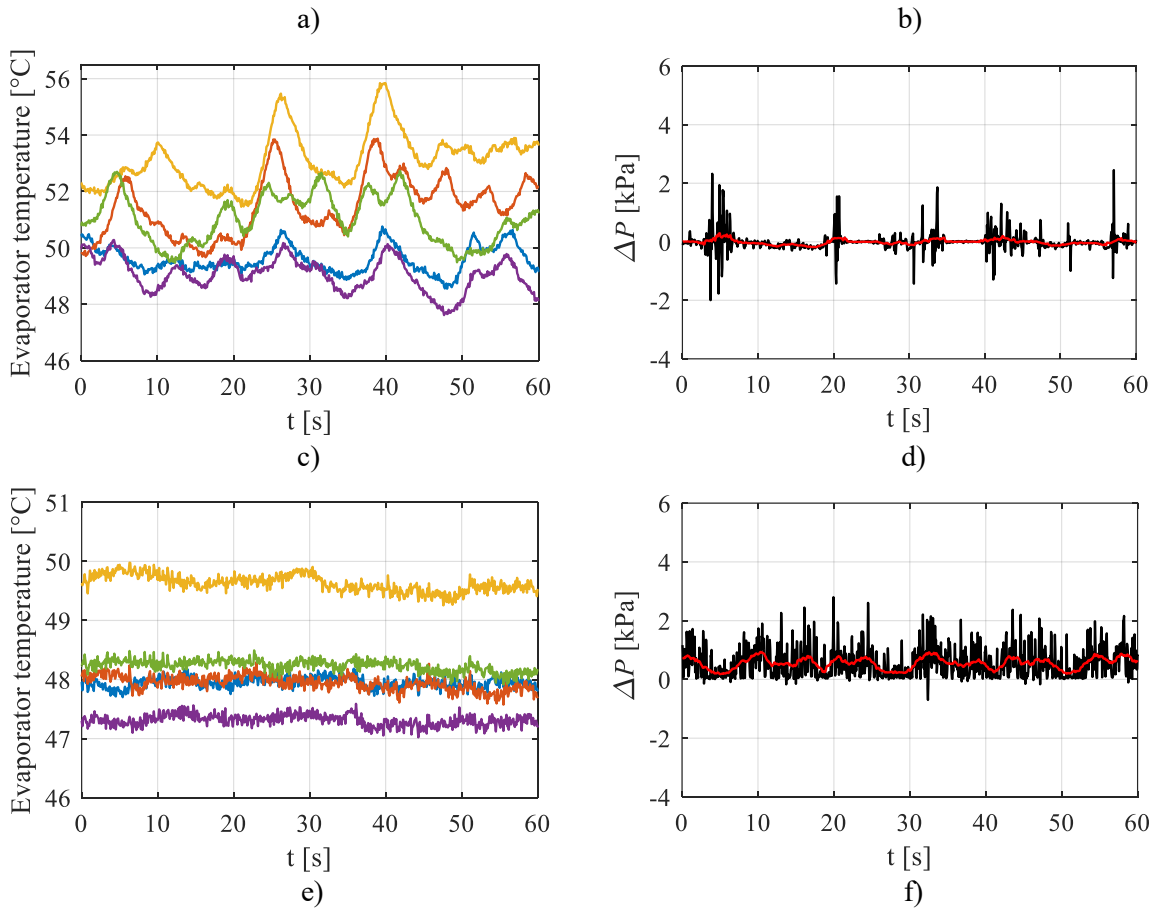

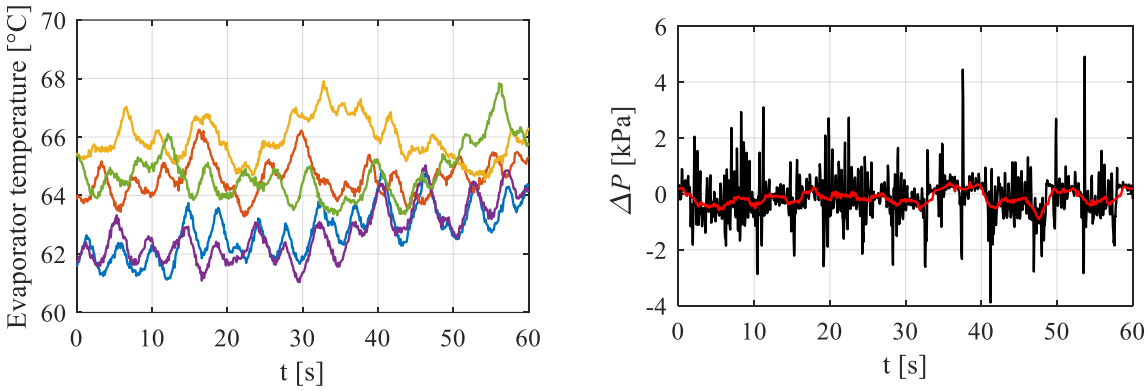

Figure 7.26: Thermocouples signals referred to the evaporator section and corresponding ΔP (red line: moving average over time). Horizontal orientation, Q = 120 W (a, b); BHM, Q = 120 W (c, d); THM, Q = 150 W (e, f), T_{cond} = 20°C.

To provide a further validation of the oscillatory/circulatory flow detection procedure presented above, the local heat transfer properties were therefore investigated. To this aim, the local heat flux distributions over time, referred to each PHP branch, were adopted as inputs for cross-correlations and, consequently, for the HTDM (Paragraph 6.4).

In Figure 7.27, the evaluated normalized cross-correlation (Equations (6.10), (6.11)) between the local heat fluxes for the fixed axial coordinate z = 0.035 m over time, referred to channel 1 and 2, respectively (reference of Figure 7.19), is shown for the same test cases of Figure 7.26(a-b) and Figure 7.26(c-d). In the horizontal orientation (Figure 7.27a), the normalized cross correlation function assumes a peak ($r \approx 0.43$) for $\tau = 0$ s, denoting that the two considered heat fluxes independently oscillate with no time lag, i.e. the fluid is oscillating in parallel in both channels between the evaporator and the condenser. On the contrary, in the BHM (Figure 7.27b), $r(\tau)$ assumes a peak ($r \approx 0.76$) for τ = 1.6 s, denoting that both the positive and negative heat flux peaks exhibit a perceivable delay from one channel to the other. Here, the wall-to-fluid thermofluidic interactions result in either in-series warm-ups or cool-downs of the PHP channels, suggesting that the fluid is circulating along the entire device. Moreover, the positive sign of the time delay highlights that the fluid crosses channel 2 in advance, in accordance whit the fluid flow direction assessed by means of graph of Figure 7.26d. The uncertainty related to the resulting time delays was estimated to be equal to the minimum obtainable time delay, i.e. the reciprocal of the thermographic measurements sampling frequency (= 0.06 s).

a)

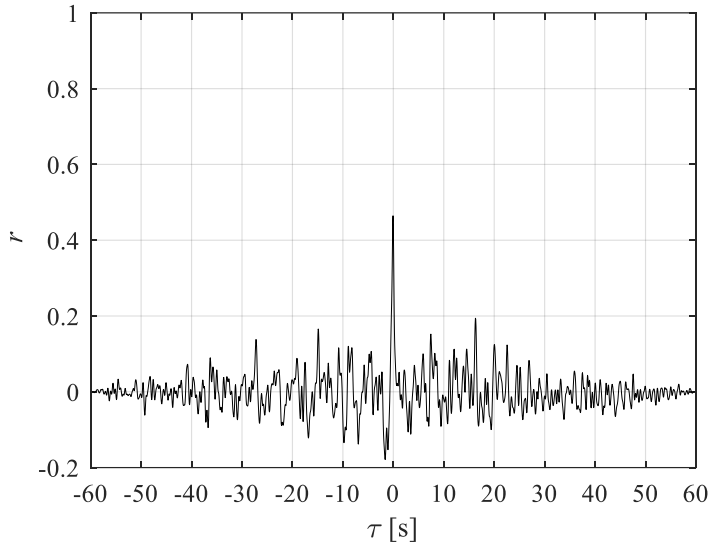

b)

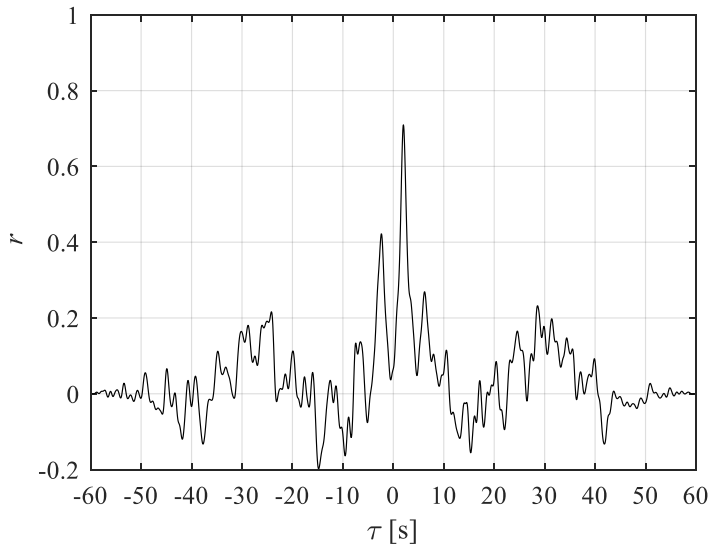

Figure 7.27: Normalized cross correlation function, evaluated by using the local wall-to-fluid heat fluxes referred to channel 1 and 2 for the fixed axial coordinate z = 0.035 m over time. Horizontal orientation, Q = 120 W, T_{cond} = 20°C (a); BHM, Q = 120 W, T_{cond} = 20°C (b).

7.3.7. Circulatory flow: average fluid velocity

Once assessed either fluid oscillation or circulation with preferential direction inside the device for all the considered power inputs to the evaporator, the time delays between heat fluxes occurring in all the adjacent channels of the device were assessed in case of circulatory flows by means of cross-correlations. The evaluated delays τ are listed in Table 7.7 and Table 7.8 for each channels pair, according to the channels numeration of Figure 7.19b.

Table 7.7: Time delays referred to each channel pair; T_{cond} = 20°C.

τ [s]			***Q*** **[W]**		
Paired channels	**90**	**120**	**150**	**180**	**190**
1-2	1.98	1.61	0.71	0.63	1.11
2-3	1.85	1.49	0.84	0.48	0.23
3-4	1.89	1.57	0.88	0.089	0.13
4-5	1.93	1.54	0.44	0.48	-
5-6	1.99	1.63	0.8	1.31	1.11
6-7	2.10	1.63	1.57	1.24	-
7-8	1.90	1.56	1.56	1.17	0.56
8-9	2.19	1.60	1.78	0.47	-
9-10	1.84	1.53	1.54	0.54	1.12
10-11	1.83	1.42	-	-	1.22
11-12	1.78	1.34	-	-	-
12-13	1.67	1.44	-	-	-

Table 7.8: Time delays referred to each channel pair; T_{cond} = 10°C.

τ [s]			***Q*** **[W]**		
Paired channels	**120**	**150**	**180**	**190**	**210**
1-2	2.13	1.80	1.79	2.03	1.57
2-3	2.28	2.03	1.71	1.06	1.27
3-4	2.00	1.80	1.75	0.92	1.56
4-5	1.92	1.98	1.94	1.94	0.80
5-6	2.27	1.88	1.79	1.22	2.09
6-7	2.13	1.88	1.94	1.78	1.59
7-8	2.57	1.88	1.78	1.10	1.53
8-9	2.13	1.93	1.67	1.44	1.61
9-10	2.01	1.85	1.79	1.67	1.71
10-11	1.87	1.73	1.56	1.56	1.44
11-12	1.85	1.49	-	-	-
12-13	1.95	1.50	-	-	-

It has to be noticed that, at high heat loads (from 150 W up to 210 W), the time delay provided by the present procedure could not be evaluated for every channel pair. This is due to the inner fluid dynamics of the studied PHP, which may consistently vary from low to high power inputs to the evaporator. Considering the formation of a stable slug-plug flow, the Bond criterion, which is a static criterion, is satisfied for the present application, but dynamic effects on the working fluid need to be considered, such as the inertial effects, which might significantly increase with the power input given to the evaporator. To this aim, the Weber number was evaluated, and found higher than 4, thus highlighting the possibility for the device to undergo transitions from slug-plug to dispersed flow. This result in highly chaotic wall-to-fluid thermal interactions, which undermine the evaluation of significant cross-correlations between wall-to-fluid heat fluxes locally exchanged in adjacent channels.

The evaluated delays were furtherly processed by means of Equation (6.14) thus evaluating the fluid velocity $v_{[i\rightarrow i+1]}$ from the *i*-th to the *i+1*-th channel. In particular, given that the heat fluxes were considered for the fixed axial coordinate z = 0.035 m, the distance $L_{[i\rightarrow i+1]}$ was equal to 0.439$\pm$ 0.001 m. By averaging $v_{[i\rightarrow i+1]}$ in the overall device, the average fluid velocity v_{av} was finally evaluated.

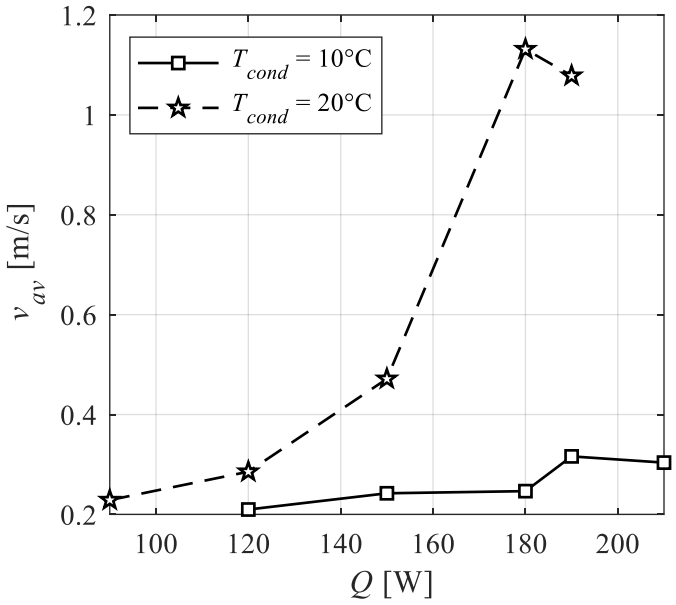

Figure 7.28: Average fluid velocity in the circulatory flow as a function of Q for the two analysed condenser temperatures.

In Figure 7.28, v_{av} is plotted against Q for the two considered condenser temperatures during the oscillatory flow. For T_{cond} = 20°C, the average velocity significantly increases with the power input given to the evaporator, ranging from a minimum of 0.23 m/s at Q = 90 W to a maximum on average equal to about 1.1 m/s at high heat loads, in accordance with previous studies [48]. On the contrary, the average fluid velocity undergoes a slight increase for T_{cond} = 10°C, where v_{av} settles around 0.3 m/s at high heat loads. This is probably due to the fact that, by decreasing the condenser temperature and consequently the fluid temperature in the overall device, the viscosity of the working fluid increases (as stated in Paragraph 7.3.2, thus strongly hampering the fluid motion.

It has to be stressed that, due to the thermal inertia of the PHP wall coupled with high fluid oscillation frequencies, the HTDM cannot be directly applied to two points belonging to the same device channel for the evaluation of the instantaneous fluid velocity during the oscillatory flow.

An experimental validation procedure for the HTDM is provided in Appendix C.

7.3.8. Local heat transfer analysis: sapphire insert

A preliminary local heat transfer analysis was also carried out on the sapphire insert of the device. The temperature distributions acquired by means of thermography on the outer wall of the sapphire insert were used as inputs for the method of Paragraph 5.2.1. It has to be pointed out that, when IR measurements are conducted on confined two-phase flows, the radiative properties of the working fluid in the IR spectrum need to be carefully considered. The main issue concerns the difference in emissivity between the liquid and the vapour phase: for most of fluids (including methanol), the combined effect of low emissivity and high transmissivity of the vapour phase prevents a reliable measurement of its temperature by means of thermography. Secondly, the liquid phase emissivity depends on its thickness: for methanol, a high emissivity is obtained when the liquid thickness exceeds 1 mm [106]. Hence, in the present experimental set-up, a correct measurement of the liquid phase temperature can be reliably obtained when the liquid phase fills the whole channel's section. Other flow patterns, such as vapour bubbles surrounded by liquid film or annular flows, eventually result in a measured temperature which is a combination of either fluid and background temperatures or vapour and liquid temperatures.

In Appendix D, a calibration procedure for thermographic acquisitions in transparent inserts, specifically adopted for FC-72 whereas extendable to other working fluids, is presented.

In Figure 7.29, IR samples are shown for a warm-up phenomenon involving the investigated sapphire channel during the horizontal operation at 90 W. In particular, the high-emissivity coating was placed on the right side of the sapphire channel, while its left part was left uncoated to allow thermographic measurements on the working fluid. From 1.17 s to 1.21 s, the outer wall temperature (right side) is almost constant along the entire branch despite the presence of lower temperature spots due to non-uniformities of the coating, denoting that no significant thermofluidic interactions are interesting the wall. On the other hand, the fluid temperature (left side) is generally low, suggesting that the channel is completely filled with still vapour, and the IR camera is acquiring the background temperature.

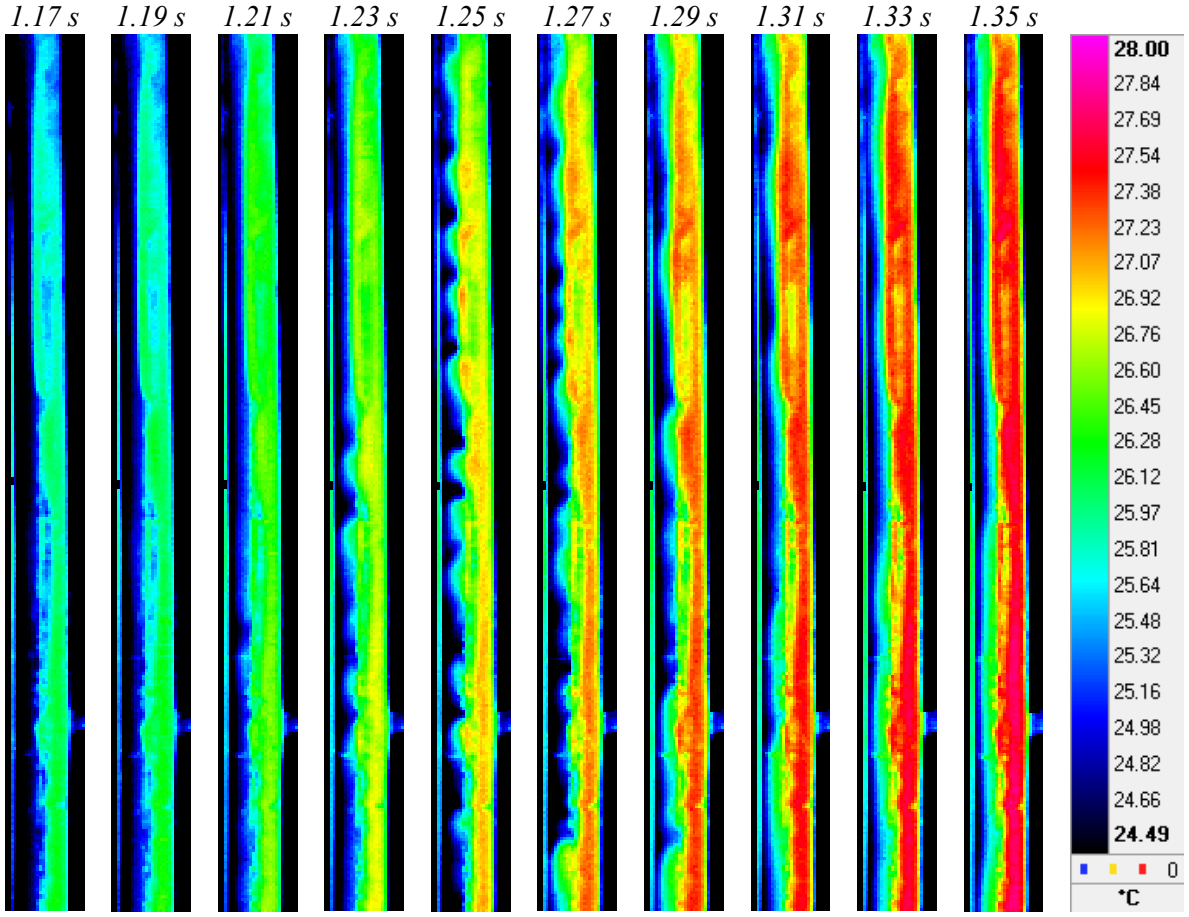

Figure 7.29: IR samples of the sapphire insert during a warm-up event at 90 W, horizontal orientation, over about 0.2 seconds; the evaporator is placed below the channel, while the condenser is above.

From 1.23 s to the end of the observation window, the wall temperature undergoes a sharp increase in temperature, while liquid plugs having higher temperature than the background are visible on the left side of the channel. Such a general behaviour denotes the onset of a warming phenomenon caused by the rising of hot fluid from the evaporator to condenser. This is also confirmed by the direction of the fluid flow: from 1.23 s to 1.25 s, liquid plugs proceed upwards along the channel. The evaluated wall-to-fluid heat flux referred to the same test case is shown in Figure 7.30. In particular, 20 seconds of acquisition were considered over a portion as long as the one investigated for the analysis of Paragraph 7.3.3.

a)

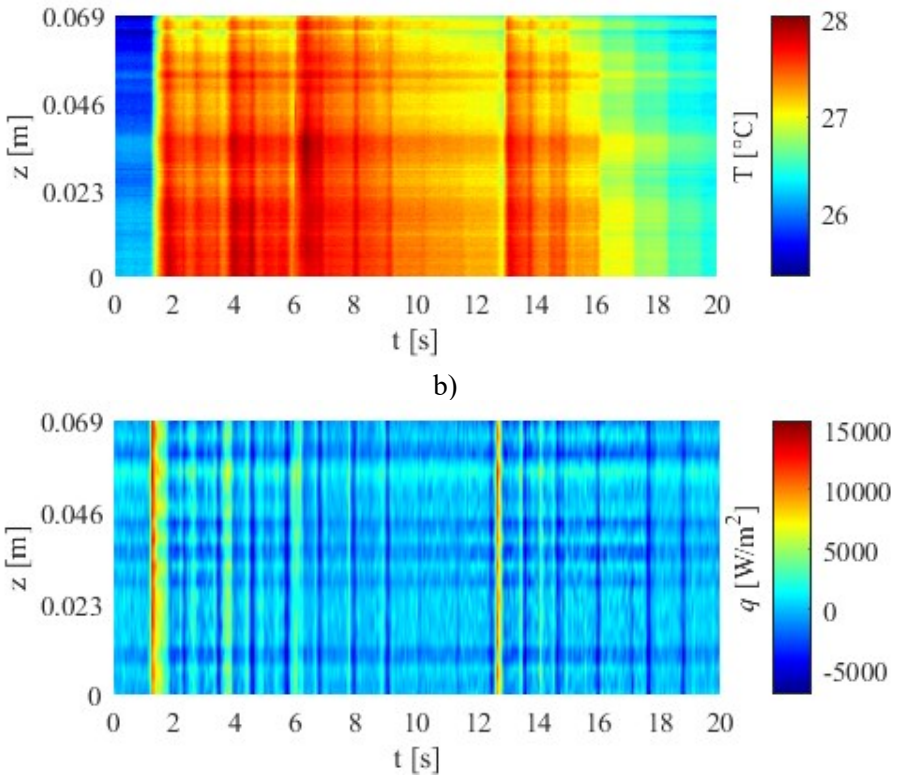

Figure 7.30: Wall temperature distribution (a) and corresponding wall-to-fluid heat flux (b) within the sapphire channel; horizontal orientation, Q = 90 W.

Here, the wall-to-fluid heat flux exhibits mostly positive peaks mainly caused by hot fluid flowing from the evaporator to the condenser in such a branch. The wall cooling is primarily due to heat exchanged by natural convection to the environment during temporary stopovers rather than flowback phenomena from the condenser. Such a remark confirms the intermittent behaviour of the device assessed in Paragraphs 7.3.4 and 7.3.5, thus proving that the local analysis on the sapphire channel gives comparable results with those obtained from a similar investigation on aluminium branches.

To attempt a comprehensive description of the thermal interactions between the working fluid and the device sapphire wall, the wall temperature and the resulting wall-to-fluid heat flux for the fixed coordinate z = 0.035 m over time are reported in Figure 7.31 along with the fluid temperature measured by means of thermocouples inserted in the fluid stream and by thermography.

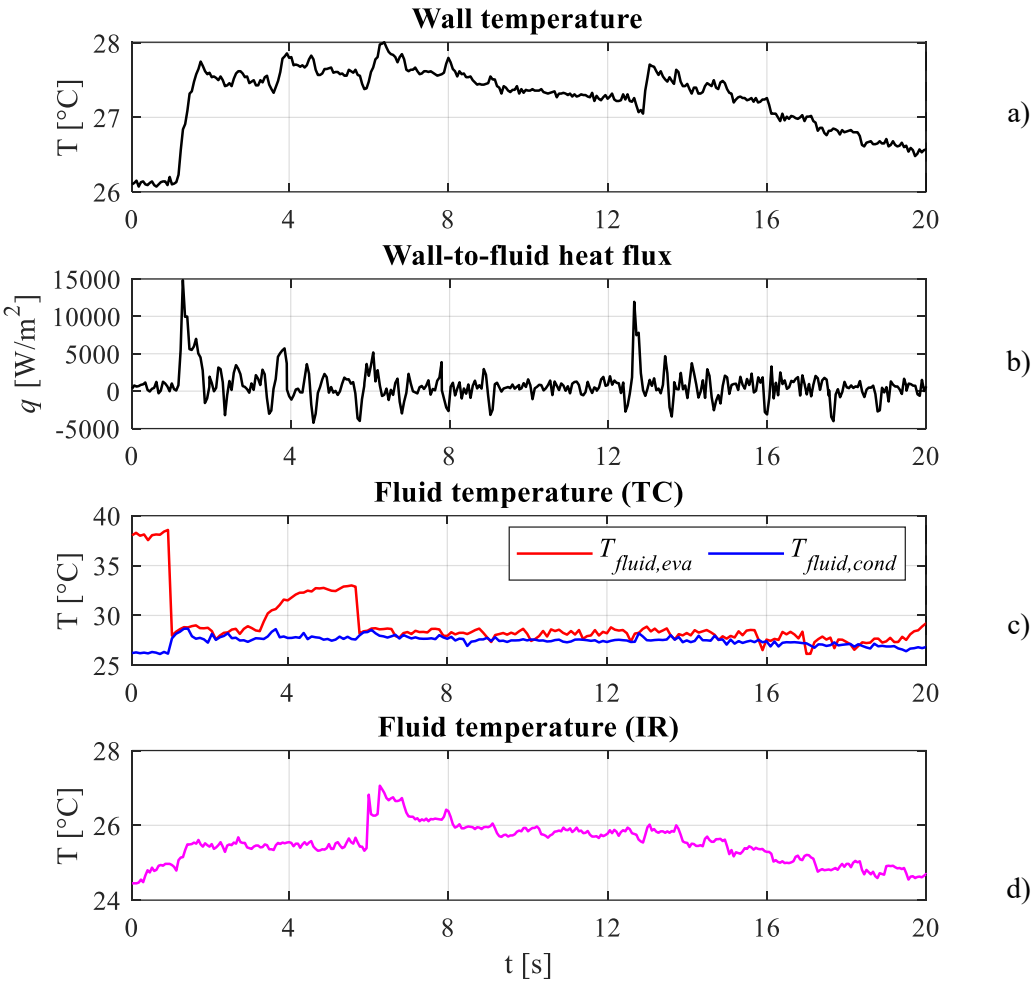

Figure 7.31: Wall temperature (a) and evaluated wall-to-fluid heat flux (b) for the fixed coordinate z = 0.035 m, together with the fluid temperature acquired by thermocouples (c) and thermography (d).

Regarding the fluid temperature acquired by thermocouples (one placed near the evaporator, and one placed near the condenser, Figure 7.31c), it exhibits higher values at the evaporator than at the condenser during the first seconds of acquisition. This is due to the inactivity of the channel, which is also reflected by the almost constant wall temperature (Figure 7.31a) and null heat flux (Figure 7.31b) within the same period. At about 1.4 seconds, when both the wall temperature and the heat flux increase, the two fluid temperature signals get closer, suggesting that the two measurement points are crossed by fluid having similar temperature, i.e., onset of fluid motion. The increase of fluid temperature around 4 seconds, occurring together with oscillations of the wall-to-fluid heat flux, might be due to a temporary overheating of fluid in the evaporator section, coupled with a low-amplitude oscillation of the working fluid. On the other hand, the fluid temperature acquired by thermography (Figure 7.31d) exhibits a different trend with respect to that measured by thermocouples, despite the rather similar temperature values over most of the considered time samples. Since the horizontal orientation hampers the fluid

motion, the occurrence of a semi-annular flow, promoted by low heat dissipation at the evaporator, is likely to occur, thus preventing a correct IR measurement of the fluid temperature.

7.3.9. Local heat transfer overview

To provide a comprehensive description of the PHP heat transfer behaviour under the studied working conditions, the statistical coefficients (cvt_{av} and cvt_{std}) and the flow modes, evaluated in Paragraph 7.3.4, are listed in Table 7.9, together with the working modes presented in Table 7.6 and the average velocities of Figure 7.28 (circulatory flow only).

To deeper investigate the link between the global and the local heat transfer behaviour of the device, the thermal resistance was finally compared with the statistical coefficients cvt_{av} and cvt_{std}, previously adopted in Paragraph 7.3.2 for a quantitatively description of the working modes.

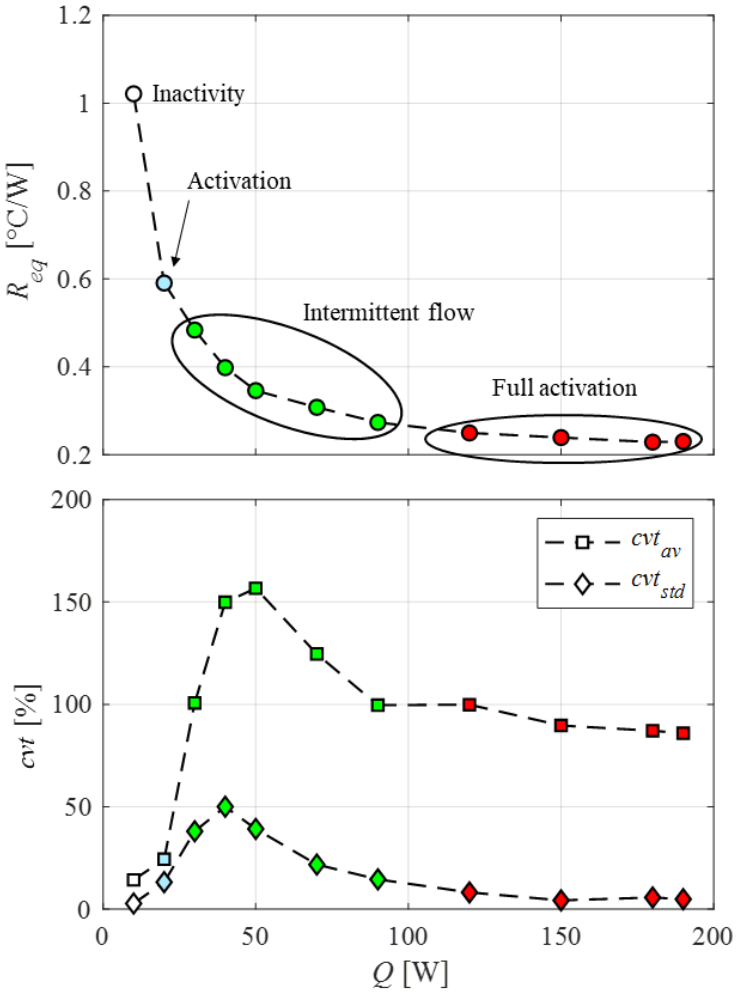

Figure 7.32: Comparison between the device thermal resistance and the statistical coefficients cvt_{av} and cvt_{std}, for the horizontal orientation, T_{cond} = 20°C.

Table 7.9: Evaluated quantities for every analysed configuration. "O": fluid oscillation, "C": fluid circulation.

		Q [W]											
		10	*20*	*30*	*40*	*50*	*70*	*90*	*120*	*150*	*180*	*190*	*210*
Orientation								T_{cond} = 20°C					
Horizontal	*Working mode*	-	*S*	*I*	*I*	*I*	*I*	*I*	*FA*	*FA*	*FA*	*FA*	
	Flow type	-	*O*	*O*	*O*	*O*	*O*	*O*	*O*	*O*	*O*	*O*	
	cvt_{av} [%]	14.3	24.4	100.7	149.9	156.7	124.6	99.6	99.9	89.7	87.1	85.9	
	cvt_{std} [%]	2.8	13.2	38.1	50.1	39.2	21.8	14.6	8.2	4.3	5.7	4.9	
	v_{av} [m/s]	-	-	-	-	-	-	-	-	-	-	-	
BHM	*Working mode*	-	-	*S*	*I*	*I*	*I*	*FA*	*FA*	*FA*	*FA*	*FA*	
	Flow type	-	-	*O*	*O*	*O*	*O*	*C*	*C*	*C*	*C*	*C*	
	cvt_{av} [%]	18.1	15.4	31.4	50.9	49.3	88.9	77.1	74.8	73.7	72.3	71.1	
	cvt_{std} [%]	4.8	4.8	17.7	23.9	26.9	48.4	2.8	4.3	2.8	2.4	2.3	
	v_{av} [m/s]	-	-	-	-	-	-	0.23	0.29	0.47	1.13	1.08	
THM	*Working mode*	-	-	-	-	*S*	*I*	*I*	*FA*	*FA*	*FA*		
	Flow type	-	-	-	-	*O*	*O*	*O*	*O*	*O*	*O*		
	cvt_{av} [%]	20.5	15.4	16.2	16.2	17.4	21.4	33.3	82.2	94.5	84.7		
	cvt_{std} [%]	4.9	1.7	1.6	3.1	4.7	1.9	3.3	14.8	4.8	4.5		
	v_{av} [m/s]	-	-	-	-	-	-	-	-	-	-		
								T_{cond} = 10°C					
Horizontal	*Working mode*	-	*S*	*I*	*I*	*I*	*I*	*I*	*I*	*FA*	*FA*	*FA*	
	Flow type	-	*O*	*O*	*O*	*O*	*O*	*O*	*O*	*O*	*O*	*O*	
	cvt_{av} [%]	11.3	73.7	31.0	47.9	80.4	115.8	130.8	91.8	101.3	93.8	97.8	
	cvt_{std} [%]	4.0	19.1	9.9	41.9	41.3	29.6	20.3	21.6	12.0	7.2	8.5	
	v_{av} [m/s]	-	-	-	-	-	-	-	-	-	-	-	
BHM	*Working mode*	-	-	-	-	-	*S*	*I*	*FA*	*FA*	*FA*	*FA*	*FA*
	Flow type	-	-	-	-	-	*O*	*O*	*C*	*C*	*C*	*C*	*C*
	cvt_{av} [%]	15.3	14.3	15.8	16.5	22.0	35.7	86.0	75.8	77.3	75.9	72.2	72.9
	cvt_{std} [%]	10.5	4.5	3.7	5.0	19.9	26.1	8.9	6.0	4.5	3.8	2.7	2.6
	v_{av} [m/s]	-	-	-	-	-	-	-	0.21	0.24	0.25	0.32	0.30
THM	*Working mode*	-	-	-	-	-	-	*S*	*I*	*I*			
	Flow type	-	-	-	-	-	-	*O*	*O*	*O*			
	cvt_{av} [%]	15.3	14.3	14.6	12.1	11.0	27.0	148	157.3	121.3			
	cvt_{std} [%]	3.6	3.7	2.6	1.8	1.6	13.4	34.7	29.0	15.5			
	v_{av} [m/s]	-	-	-	-	-	-	-	-	-			

In Figure 7.32, such comparison is referred to the horizontal orientation, T_{cond} = 20°C. When the device is inactive (white markers), the thermal resistance assumes a high value since the heat is only transferred by conduction. The device activation (light blue markers), denoted by a sudden increase in both cvt_{av} and cvt_{std} which exceed the activation threshold quantified in Paragraph 7.3.2, is also characterized by an abrupt drop in the thermal resistance. Within the intermittent flow (light green markers), the thermal resistance keeps decreasing with a descending slope, and progressively approaches an asymptotic value. When the device is fully activated (dark green markers), the stable oscillatory flow in the whole device guarantees a low and almost constant thermal resistance. In Figure 7.33, the same comparison is carried out on the BHM, T_{cond} = 20°C. Here, cvt_{av} and cvt_{std} present a sharp increase at Q = 30 W, i.e. such power input to the evaporator promotes the device activation, as also qualitatively observed in Figure 7.22b.

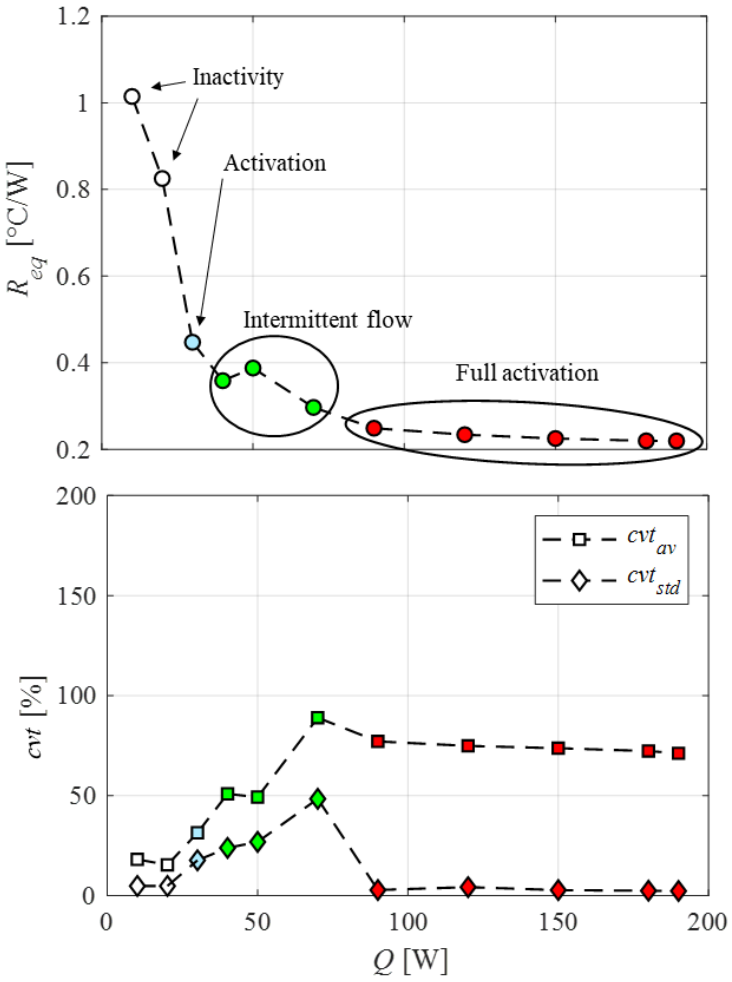

Figure 7.33: Comparison between the device thermal resistance and the statistical coefficients cvt_{av} and cvt_{std}, for the BHM, T_{cond} = 20°C.

During the intermittent flow mode, the BHM presents a lower overshoot of both cvt_{av} and cvt_{std} with respect to the horizontal orientation, suggesting that the gravity forces stabilize the local thermal interactions between the PHP wall and the working fluid. Additionally, during the transition between intermittent flow and full activation, cvt_{std} exhibit a discontinuity in the BHM, denoting that the device thermal behaviour undergoes a sharp change in terms of regularity of the wall-to-fluid thermofluidic interactions in the overall device due to the establishment of the circulatory flow.

7.4 Closure

A multi-turn PHP, tested during the 67th PFC promoted by the ESA (microgravity) and on ground conditions, was thermally characterised by evaluating the local wall-to-fluid heat fluxes with high spatial resolution. Specifically, the IHPC was solved in the wall starting from the IR measurements carried out on the external wall of the PHP adiabatic section. The heat flux amplitudes related to each PHP channel were studied by means of the coefficients of variation. A frequency analysis was additionally carried out on the heat flux. A statistical analysis was therefore performed, thus focusing on the correlation between the heat flux amplitude, the fluid oscillation frequency and the power input given to the evaporator. Finally, a flow modes detection procedure was proposed, and average fluid velocity during the circulatory flow were assessed.

The main research outcomes in microgravity are the following:

- The fluid motion through each PHP channel can be successfully assessed by the wall-to-fluid heat flux conveniently elaborated.
- Two regimes are identified: intermittent flow (sporadic fluid motion, occurring in some channels) and full activation (stable fluid motion within the whole adiabatic section).
- The coefficient of variation over time *cvt* allows the identification of the PHP working regimes: during the intermittent flow regime, *cvt* is high (from 75% to 150%) and varies significantly from channel to channel, while the full activation of the device is outlined by low and almost constant values of *cvt* (from 50 to 60%) within the whole adiabatic section.
- The fluid oscillation frequency investigation confirms the existence of two working regimes, depending on the power input given to the evaporator. During the intermittent flow regime, only some channels present fluid oscillations mainly in the frequency range 0.5–0.6 Hz; on the contrary, for high power inputs to the evaporator, the dominant frequency f_D is generally similar in the whole adiabatic section and it is mostly in the range 0.9–1.0 Hz, even though the oscillatory behaviour may still vary from channel to channel.
- The dominant frequency values are in good agreement with the ones estimated by pressure sensors by Perna et al. [104].
- The 80th percentile of the wall-to-fluid heat flux amplitude q_{80} is almost constant (about 500 W/m^2) at low power inputs. From 100 W up to the maximum power input, the heat flux

amplitude increases almost linearly with the power input, reaching about 1500 W/m^2 at 202 W.

- All the parameters introduced (i.e. *cvt*, q_{80}, f_D and *cvf*) enable to clearly identify in the range 60 ÷ 90 W the transition between the intermittent flow working regime and the full activation working regimes.

On the other hand, the main outcomes regarding the on-ground experimentation are listed below:

- The PHP equivalent thermal resistance at low power inputs to the evaporator is strongly dependent on the chosen device configuration. For high power inputs, the studied three-dimensional layout exhibits instead comparable global performances in almost every considered configuration, with equivalent thermal resistances around 0.25 K/W, thus denoting an independent working behaviour of gravity.
- During the transition from inactivity to full activation, cvt_{av} reaches a maximum peak around 155% for the horizontal mode (T_{cond} = 20°C) and the THM (T_{cond} = 10°C), while it settles in the range 70 to 100% within the full activation for every PHP configuration. Similarly, cvt_{std} denotes a maximum peak around 50% for the horizontal mode (T_{cond} = 20°C) and the BHM (T_{cond} = 20°C) within the intermittent flow, while it approaches an asymptotic trend in the range 3 to 9% within the device full activation.
- The fluid net circulation occurred only during the BHM in the ranges 90 to 190 W and 120 to 210 W for T_{cond} = 20°C and T_{cond} = 10°C, respectively. No significant relation between the circulatory motion and the global performance could be assessed, while the local heat transfer behaviour presents great differences from the oscillatory to the circulatory motion.
- The device performance is independent of the orientation during full activations, i.e. when a regular fluid motion is perceivable in every branch within the adiabatic section.

In conclusion, the adopted approach and the evaluated quantities can describe the device operation in a very complete way, without the adoption of any intrusive technique, e.g., by direct fluid temperature/pressure measurements. This is especially viable in complex experimentations, such as in microgravity conditions during parabolic flights campaigns, where potential leakages due to junctions and inserts are highly undesirable. Moreover, from the on-ground experimentation, the considered three-dimensional geometry presents enhanced thermal performances with respect to the planar layouts even in unfavourable orientations. Such interesting feature is noticeable especially at high power inputs, where the device thermal performance in the BHM, i.e., the generally best orientation for planar geometries, is comparable to that assessed for both the horizontal orientation and the THM which is generally, on the contrary, the most unfavourable condition for planar geometries.

Chapter 8 Experimental investigation on a tubular micro-PHP

8.1 Introduction

The present Chapter deals with the study of a tubular, micro-PHP by both global and local analyses. Its compactness and significant flexibility may be suitable for thermal management applications in the micro-electronics field. Contrarily to the Space PHP set-up, the here studied device exhibits a micro-geometry, and the condenser section is cooled by both natural convection and radiation to the environment rather than by a heat sink having constant temperature. While the former characteristic might result in much higher capillary and viscous forces on the confined fluid flow, the latter boundary condition eventually leads to completely different phase-change phenomena and thermo-fluid dynamics. The combination of both features thus represents an interesting reference study case for the assessment of the device global performance, as well as for the description of local thermofluidic interactions occurring inside the device within the condenser section (accessible to thermography).

8.2 Test rig

The studied 7-turn device, whose geometrical dimensions and layout are shown in Figure 8.1, is made of a stainless-steel (SUS304) tube with inner and outer diameters of 0.32 mm and 0.52 mm, respectively.

a) b)

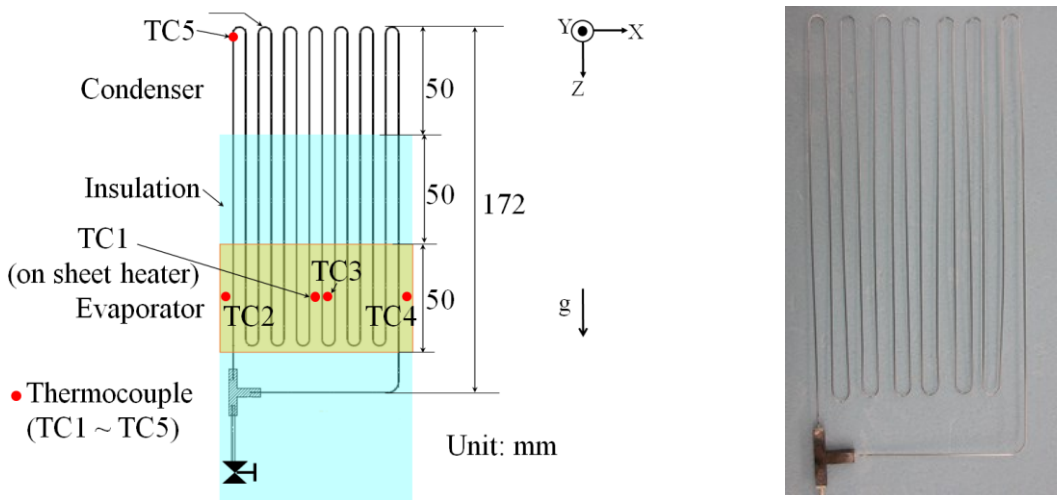

Figure 8.1: Micro-PHP geometrical references (a) and layout (b).

Figure 8.2a outlines the adopted experimental set-up. The evaporator channels were attached to a 3-mm-thick copper spreader (yellow-shaded area in Figure 8.1a) by aluminium tapes to guarantee temperature uniformity, while the heat load was provided by a polyimide sheet heater, placed on the back surface of the spreader. To minimize the heat exchange with the environment, the evaporator, the adiabatic section and the filling valve were insulated by means of 2 cm of expanded polyurethane (light-blue-shaded area in Figure 8.1a).

The condenser tubes were coated with a thin film of high-emissivity paint. The evaporator and adiabatic section were insulated, while the condenser was cooled by natural convection and radiation with the environment. The condenser temperature was monitored by an infrared camera (FLIR® SC7000, space resolution: 640 x 512 pixels accuracy: ±1 K, thermal sensitivity at 303 K: 20 mK). For the present configuration, the infrared spatial resolution at target surface was equal to 0.156 mm/pixel. Moreover, due to the limited viewing angle (less than ± 30°), the channels' surface was considered as a diffuse grey emitter.

Five type-T thermocouples were placed along the test rig: one was placed on the sheet heater, three were placed on the metal plate of the evaporator, and one was directly attached to the tube outer surface within the condenser. In particular, the last was employed to monitor the agreement between thermocouples and IR camera signals. The acquisition frequency of the camera and the thermocouples were 18 Hz and 1 Hz, respectively. The measurement uncertainties of the T-type thermocouple and the voltage and the current of the power supply were ± 0.2 °C, ± (0.03% full scale + 2 mV), and ± (0.2% full scale + 1 mA), respectively. The full scale of the voltage and the current of the power supply is 8 V and 10 A, respectively. The measurement uncertainty of the data acquisition system for the temperature measurement is 1.0 °C.

8.3 Experimental procedure

To verify that the thermal contact resistance at the pipe-heater interface was uniform, a preliminary test with the empty device was performed. Being the temperature acquired by thermocouples at the evaporator section comparable to that acquired at the condenser by thermography, the thermal contact was considered uniform in every turn.

The device is first vacuumed and then partially filled through the valve shown in **Figure 8.1** with 1,1,1,2-Tetrafluoroethane (HFC-134a). To evaluate the influence of the filling on the performance of the micro-PHP, three volumetric FRs in the range 30 ÷ 85% vol. were analysed. Moreover, the purely conductive mode, i.e. empty device, was studied. By adopting the NIST Reference Fluid Thermodynamic and Transport Properties Database [141], the critical diameter for HFC-134a at 280 and 350 K was assessed to be equal to 1.8 mm and 0.99 mm, respectively, thus ensuring the presence of a capillary flow inside the device during its operation.

During the tests, the PHP operated in vertical BHM, i.e. with the evaporator at the bottom. As shown in **Figure 8.1**a, the direction of gravity (i.e., the longitudinal direction of the PHP from the top of the condenser to the evaporator) was considered as positive z direction. A stepwise heat load Q was provided to the evaporator from 0.1 W to 5 W (until the operating limit) by a DC power supply (HEWLETT PACKARD® 6631B), corresponding to a heat flux between $1.6 \cdot 10^2$ W/m^2 and $8 \cdot 10^3$ W/m^2. The experimental data were collected by a data acquisition system (AGILENT® 34970A), for each power input, when the device reached the pseudo-steady state. One IR video of 180 seconds was acquired within the pseudo-steady state for each heat load step. In Figure 8.2b, a sample of IR acquisition within the condenser section is shown, with reference to the analysed channels numeration.

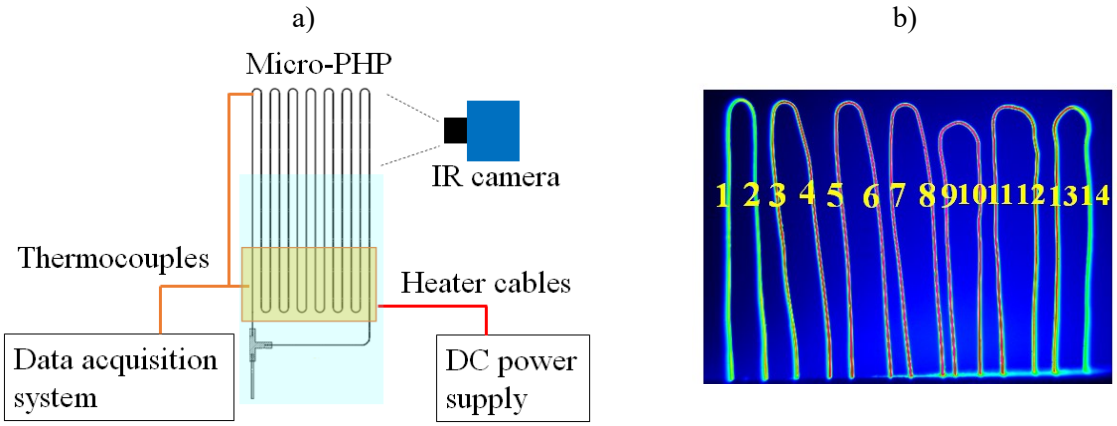

Figure 8.2: Experimental set-up (a) and sample of IR acquisition (b); in yellow, the channel numeration.

In Table 8.1, the considered test cases are listed. Once the evaporator temperature overcome 100°C, the power supply was switched down to prevent a critical pressure increase in the tube.

Table 8.1: Test cases; "x" stands for "acquisition point", "-" stands for "not investigated point".

	Filling ratio [%]		
***Q* [W]**	*30*	*46*	*82*
0.1	x	x	-
0.2	-	x	-
0.3	x	x	-
0.4	-	x	-
0.5	x	x	x
1	x	x	x
1.5	x	x	x
2	x	x	x
2.5	x	x	x
3	-	x	-
3.5	-	x	-
4	-	x	-
4.5	-	x	-
5	-	x	-

8.4 Global performance

For a meaningful description of the device operation in terms of heat loads, the following results are expressed in terms of net power input Q_{net} to the evaporator rather than total electrical power input. Specifically, the heat losses to the surroundings Q_{diss}, evaluated by means of Equation (8.1), varied between the 8% and the 20% of the electrical power input.

$$Q_{diss} = A_p \cdot \frac{\lambda_p}{s_p} \cdot (T_e - T_{env}) \tag{8.1}$$

In Equation (8.1), λ_p and s_p are the thermal conductivity and thickness of the expanded polyurethane layer, respectively, A_p the surface area of the expanded polyurethane layer and T_{env} the environmental temperature.

The influence of filling ratio on the performance of the micro-PHP is presented in Figure 8.3, according to the definition of equivalent thermal resistance Equation (3.1). Specifically, the evaporator temperature was evaluated by averaging the thermocouples' signals on the copper spreader over 3 minutes within the pseudo-steady state, while the condenser temperature was assessed by averaging the thermographic data referred to the whole outer surface of every studied channel for the same duration.

Here, *FR*=46% and *FR*=82% guarantee the best and the worst performance, respectively.

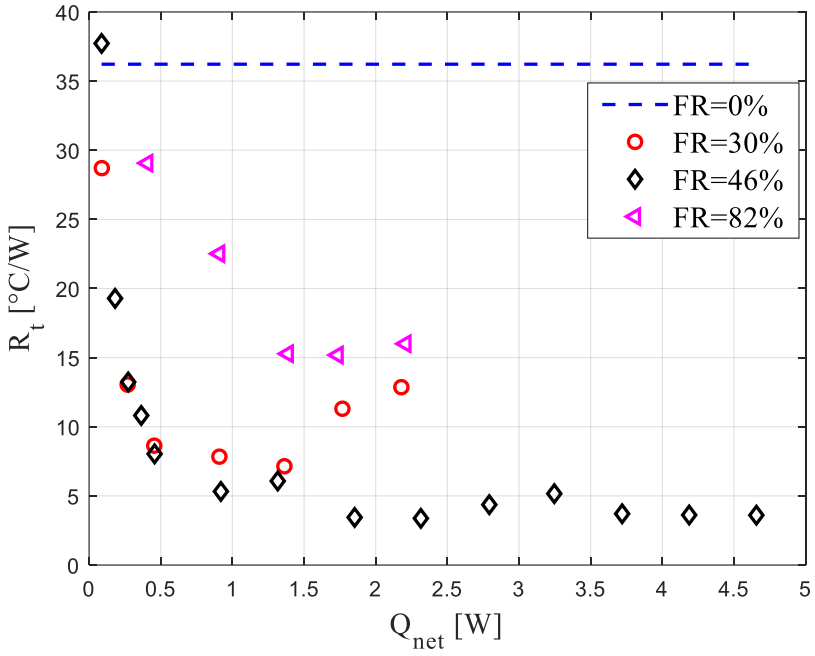

Figure 8.3: Thermal resistance of the micro-PHP as a function of the net heat power for different filling ratios.

Such a remark may be due to the fact that, for the highest filling ratio, the device operates in a quasi-purely conductive mode, since the fluid evaporation is hampered in the evaporator section by the high amount of liquid.

For *FR* = 30%, at heating power higher than 1.5 W, the thermal resistance starts to increase probably due to the occurrence of a dry-out phenomenon, as confirmed by the analysis of IR images presented in Figure 8.4.

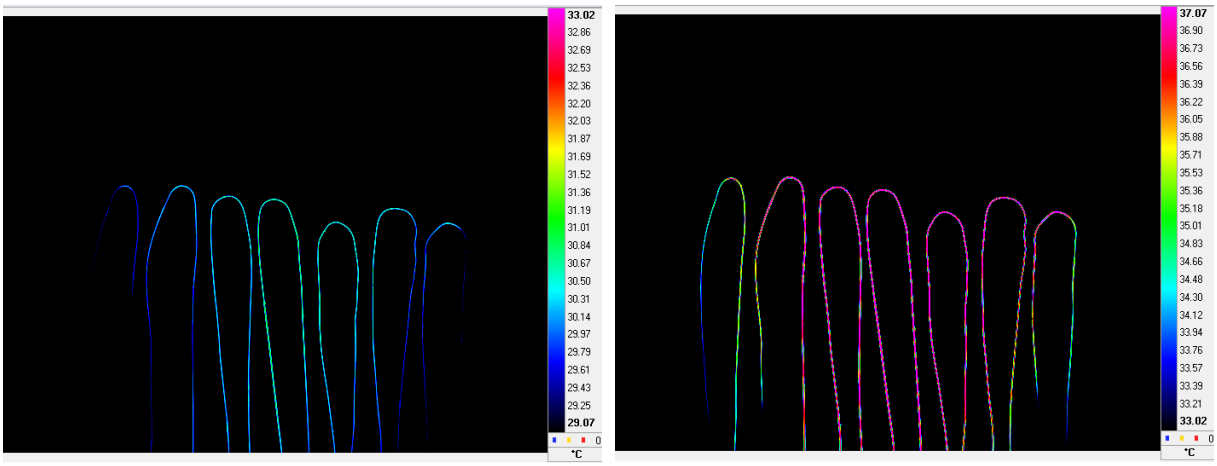

a) b)

Figure 8.4: Condenser temperature maps at different heat inputs (*FR*=30%): Q_{net} =0.9 W (a); Q_{net} = 2.3 W (b).

It can be clearly noted that, for heating power lower than 1.5 W (Figure 8.4a), pulsating phenomena occur, while, for Q_{net} = 2.3 W (Figure 8.4b), most of the turns are at the same, high temperature. Such a thermal behaviour suggests that the condenser, for the considered heat load, is not capable of efficiently dissipating heat, i.e. promoting vapour condensation, thus resulting in a drop in thermal performance of the device.

For *FR* = 0%, the thermal resistance of the micro-PHP was equal to 36.2 °C/W. Despite the value of equivalent thermal resistance obtained in the most favorable working condition (FR = 46%) is high when compared to other PHPs, the beneficial increase in thermal performance between the empty and partially filled device is evident and confirmed by a reduction in terms of thermal resistance of about 80%.

8.5 Local heat transfer analysis

The wall temperature distributions over the first 60 seconds of measurements, referred to each channel in the condenser section and acquired by thermography during the pseudo-steady state, were processed by means of the method described in Paragraph 5.2.2. Figure 8.5 and Figure 8.7 show the one-minute history of the wall temperature maps and evaluated heat fluxes for four meaningful tubes positioned near the edges (channels 1 and 2, according to the reference of Figure 8.2b) and the centre (channels 7 and 8), at *Q* equal to 0.5 W (Figure 8.5), 2.5 W (Figure 8.6), and 4.5 W (Figure 8.7).

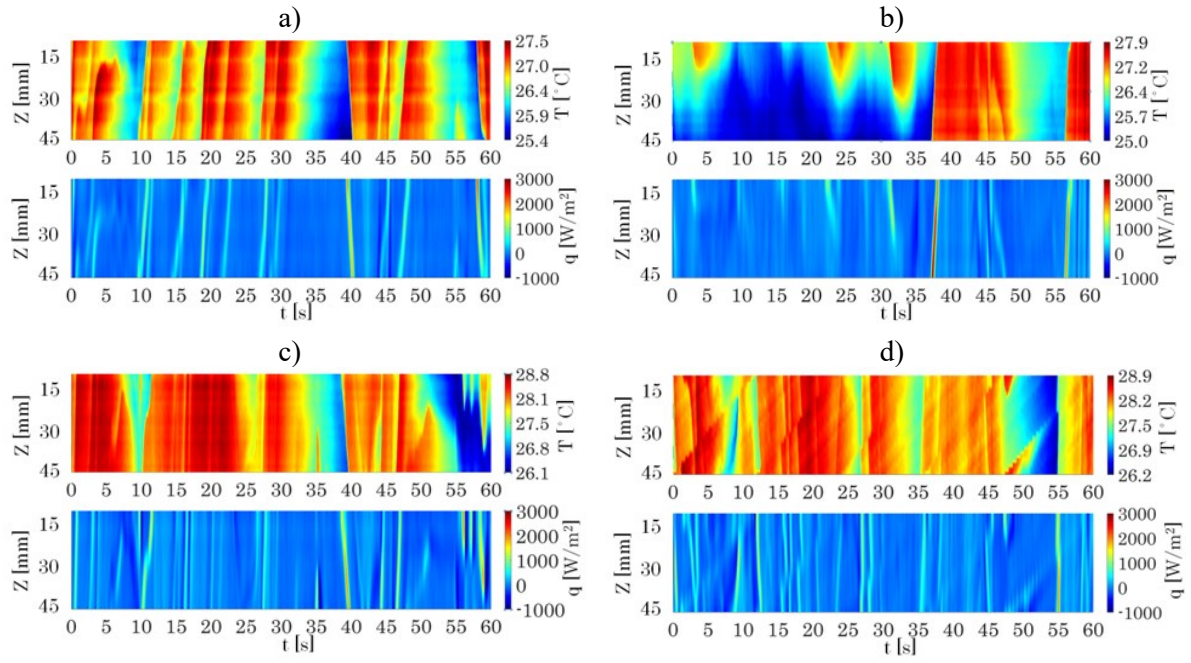

Figure 8.5: Wall temperature distribution and heat fluxes for channel 1 (a), 2 (b),7 (c), and 8 (d) at power input equal to 0.5 W. The vertical axes indicate the distance from the top of the condenser.

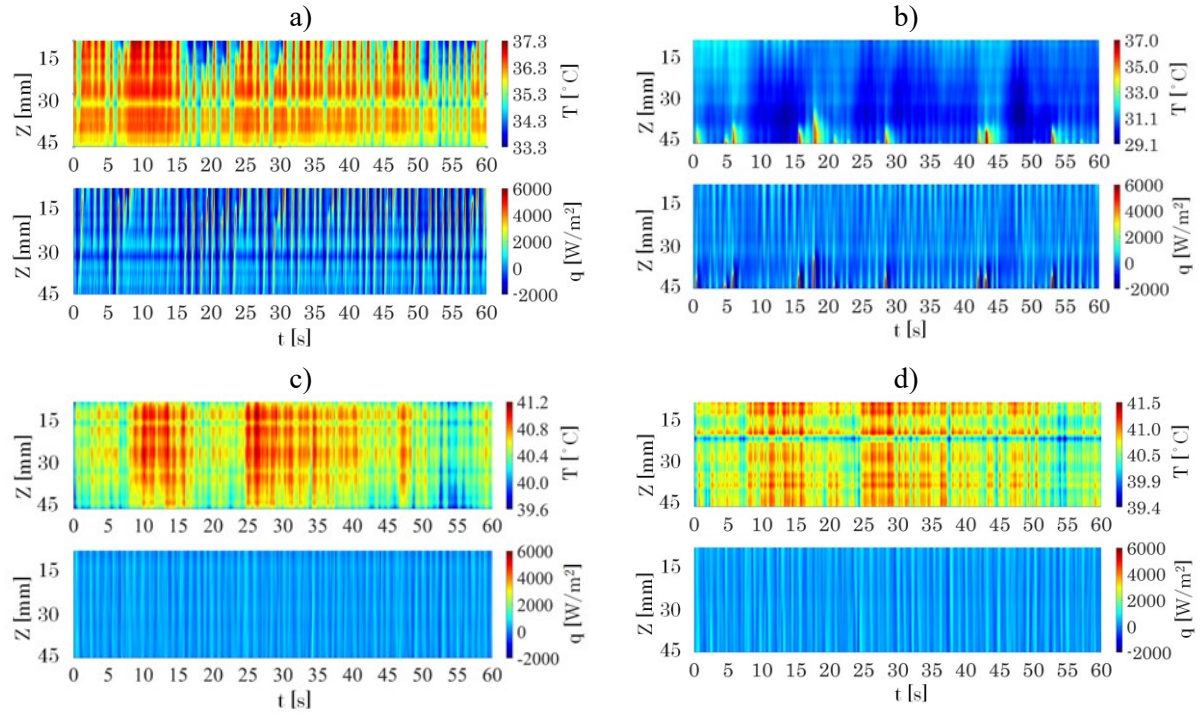

Figure 8.6: Wall temperature distribution and heat fluxes for channel 1 (a), 2 (b),7 (c), and 8 (d) at power input equal to 2.5 W. The vertical axes indicate the distance from the top of the condenser.

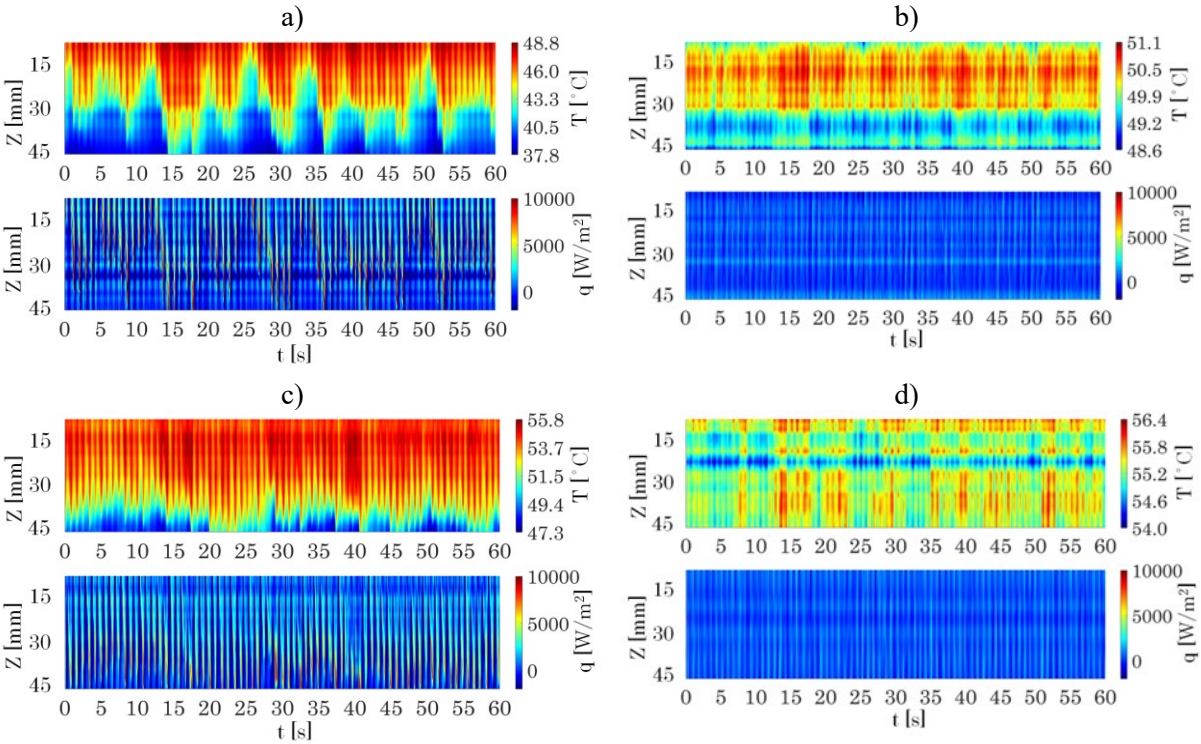

Figure 8.7: Wall temperature distribution and heat fluxes for channel 1 (a), 2 (b),7 (c), and 8 (d) at power input equal to 4.5 W. The vertical axes indicate the distance from the top of the condenser.

With respect to the local behaviour assessed in Paragraph 7.3 for the Space PHP experimental set-up, two main differences can be readily appreciated in the present study case:

- At low power inputs (Figure 8.5), the heat flux peaks are not vertically straight, suggesting that the fluid flows with an appreciable velocity rather than an almost instantaneous one;
- The values assumed by q are, on average, positive.

These remarks are probably due to the fact that, on one hand, the high capillary forces dampen the device motion, resulting in generally lower flow velocities. On the other hand, since the investigated portion belongs to the condenser section, the heat flux is mainly exchanged by hot working fluid, coming from the evaporator, to the device wall, which is constantly cooled down by both radiation and natural convection. It is also interesting to notice that some heat flux peaks exhibit a perceivable variation in amplitude over space due to complex interactions between the working fluid and the device wall in the condenser.

In addition, differences in terms of working regime from power input to power input can be qualitatively assessed. At Q = 0.5 W (Figure 8.5), oscillations are intermittent in all the considered channels. In fact, the oscillatory flow undergoes sporadic and local stopovers, identified by time periods in which the heat flux is almost null. Sometimes, temperature and, consequently, heat flux peaks furtherly stop in the middle of the investigated area, suggesting that the working fluid does not always reach the apex of the condenser section, i.e. it presents low oscillation amplitudes. The left or right-folded slope of heat flux peaks finally suggests that oscillations occur in either a clockwise or counter-clockwise direction.

At higher power inputs (Figure 8.6, Figure 8.7), the stopover periods cease, the fluid velocity increases together with the oscillation frequency, and the oscillatory motion becomes generally more stable. To deeply describe the flow motion at higher heat loads, the temperature history of channels 5, 6, 7, 8, 9 and 10 at z = 40 mm for Q = 2.5 W and Q = 4.5 W is additionally shown in Figure 8.8a and Figure 8.8b, respectively, during the pseudo-steady state.

a)

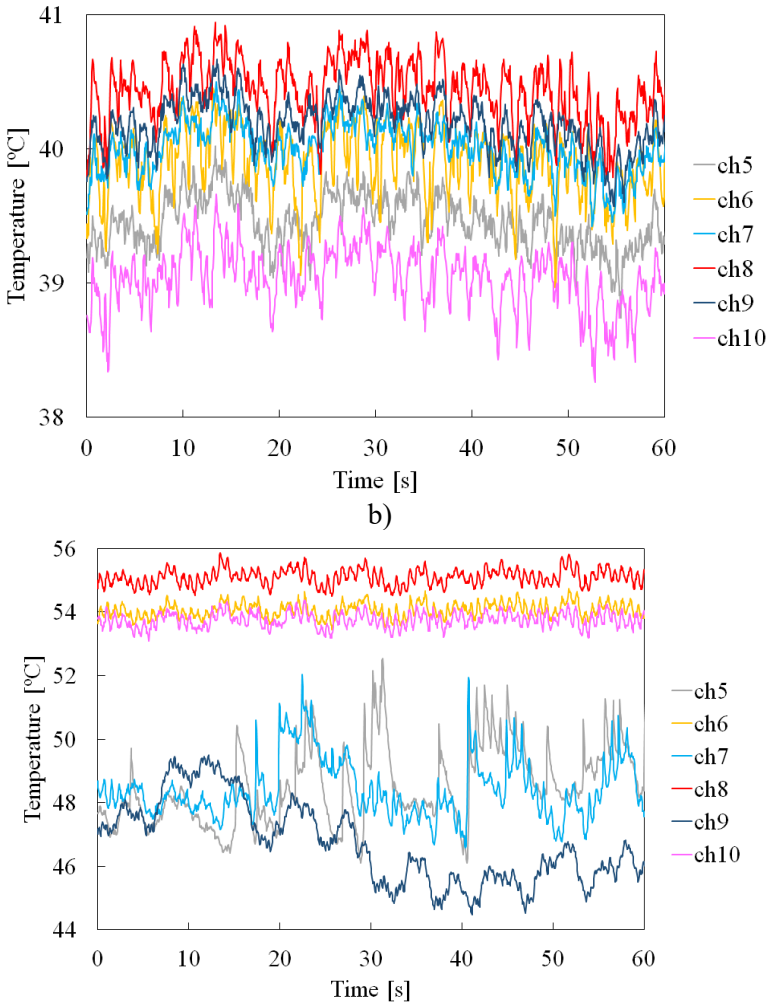

Figure 8.8: Temperature history, acquired by thermography, of representative channels; Q = 2.5 W (a), Q =4.5 W (b).

In particular, in Figure 8.8a, all the temperature profiles exhibit similar values, regardless the considered channel. This highlights that fluid oscillations may occur in a clockwise or counter-clockwise direction indiscriminately. In Figure 8.8b, the temperature referred to odd channels is always higher than that referred to the even ones, suggesting that the working fluid always crosses the condenser in a clockwise direction at high heat loads. In fact, as long as the fluid moves through the condenser, its temperature progressively decreases due to fact that its energy is given to the colder tube. Since it cannot be unquestionably concluded that the fluid circulates, such a particular behaviour has to be conservatively intended as an oscillatory motion with preferential direction.

8.5.1. Statistical approach on the local wall-to-fluid heat fluxes

The wall-to-fluid heat flux distributions evaluated along the condenser section were therefore processed by means of the coefficients of variation (Paragraph 6.3.1). However, in the present analysis,

the ratio between the standard deviation and the mean of q was not averaged neither for every i-th space coordinate (in *cvt*) nor for every t-th time instant (in *cvs*). In fact, the distribution of both *cvt* and *cvs* was considered over 30 mm and 60 seconds, respectively, to assess any significant variations with either the axial or time coordinate.

In Figure 8.9, the *cvt* and *cvs* distributions are shown for six meaningful channels, and power inputs equal to 0.5, 2.5 and 4.5 W.

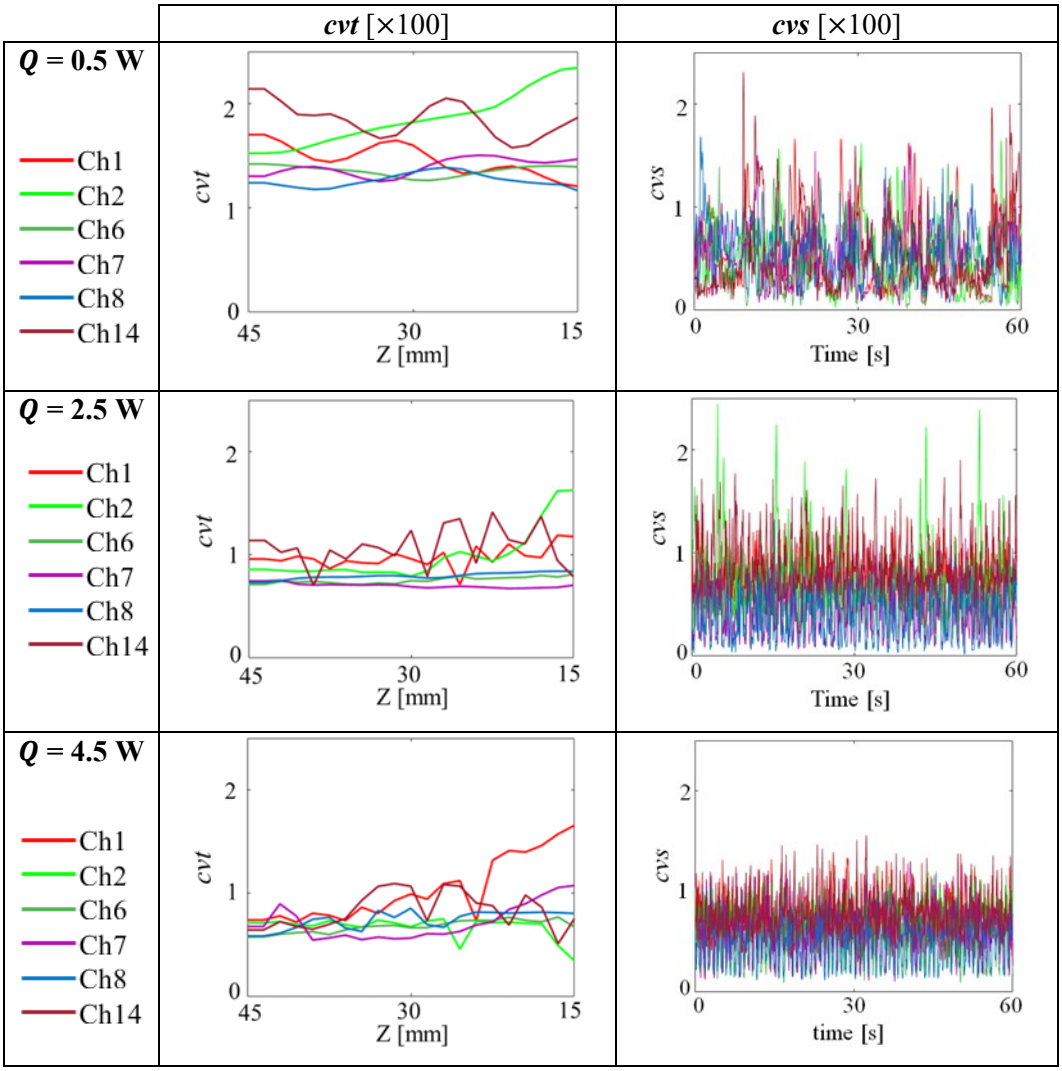

Figure 8.9: *cvt* and *cvs* distributions, evaluated for 6 meaningful channels over 30 mm and 60 seconds, respectively, and at three different heat loads.

Here, the *cvt* distribution exhibits, in every channel, values between 100% and 250% at low power input, suggesting the very high irregularity of fluid oscillations. Also, a maximum variation of about 100% is noticeable among channels, denoting that the oscillatory behaviour strongly changes from branch to branch. As long as the power input increases, the *cvt* values progressively decrease around 100% at Q = 2.5 W and 80% at Q = 4.5 W, highlighting that fluid oscillations become more regular in

the overall device. However, while most of the channels exhibit an almost flat trend in terms of *cvt* over the axial coordinate, the side channels, i.e. channels 1, 2 and 14, show a significant variation from the bottom to the top of the condenser, with values of *cvt* higher, on average, than those of other branches. This might be due to the presence of liquid in the T-joint, the filling valve, and the tube connecting them. In fact, although the mentioned parts are insulated from the environment, their high thermal inertia might promote condensation of vapour inside them. Since their inner volume is equal to about 1/3 of the total one, these parts could potentially act alike liquid reservoirs, eventually damping the fluid motion by absorbing fluid oscillations in the side channels. Regarding the coefficient of variation over space, at Q = 0.5 W, the *cvs* distributions exhibit high peaks around 180%, suggesting that the heat flux strongly varies over space. In fact, the low fluid velocity, coupled with low oscillation amplitudes, results, time instant by time instant, in different thermofluidic interactions between the bottom and top of the condenser. It has to be highlighted that *cvs* presents rather long time periods during which it assumes low values (≈ 0%); this might occur during temporarily stopovers, i.e. when the whole channel interested by same, null local thermofluidic interactions. With the increase of the heat load, *cvs* assumes lower values, averagely equal to 60% at Q = 4.5 W, thus confirming the onset of unidirectional oscillations. In addition, low and high *cvs* peaks quickly alternate over time with regularity due to the presence of stable fluid oscillations, characterized by fluid flowing from the evaporator to the condenser (high *cvs*, i.e. strong differences in terms of heat flux due to the progressively fluid cooling) and backflows (low *cvs*).

8.5.2. Frequency analysis on the local wall-to-fluid heat fluxes

The wavelet analysis was finally performed on the local heat flux. In Figure 8.10, the scalograms at three different power inputs conditions, for an edge tube (ch1) and middle tubes (ch7 and ch8) are shown.

Q [W]	**Ch1**	**Ch7**	**Ch8**
0.5	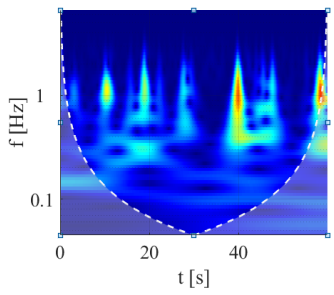	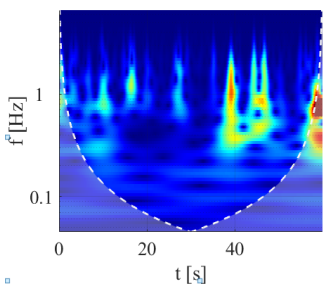	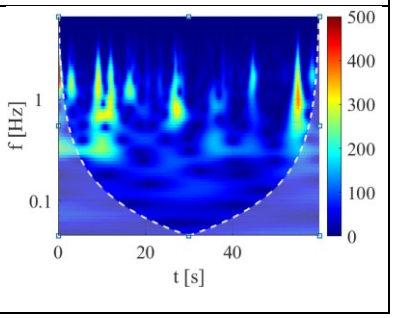

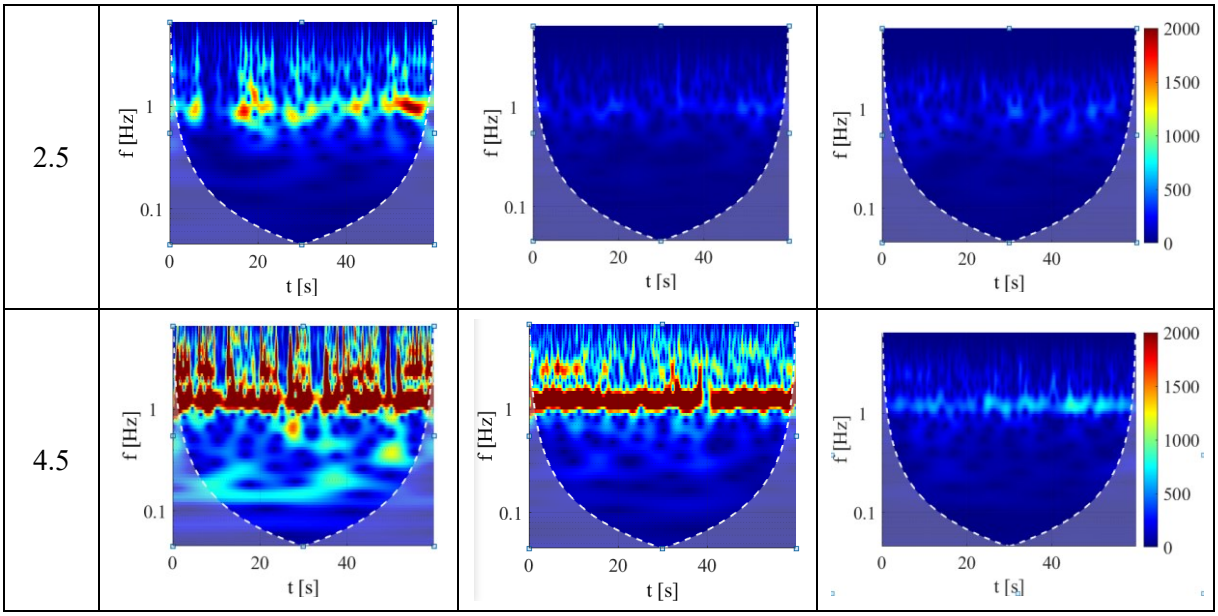

Figure 8.10: Scalograms referred to three channels and three heat loads; wall-to-fluid heat fluxes for the axial position z = 30 mm were used as inputs for the wavelet method.

At Q = 0.5 W, the highly discontinuous operation of the device is noticeable by vertical, high-power areas, resulting from impulsive oscillatory phenomena. At Q = 2.5 W, the fluid oscillations get more regular in terms of oscillation frequency, despite the channels exhibit different oscillatory behaviour. In fact, in channel 1, a high-power area is present around 1 Hz over almost the whole observation window, while, for channels 7 and 8, the signal's power attenuates, suggesting lower oscillation amplitudes of the wall-to-fluid heat flux. At Q = 4.5 W, the straight, horizontal high-power zones in the scalograms highlights strong and highly regular oscillatory behaviour, especially in channels 1 and 7. In addition, the presence of a distinguishable, average-power horizontal area at same frequency in channel 8 confirms that the fluid oscillates in clockwise direction from odd to even channels. To give a complete description of the overall device oscillatory motion, all the channels were investigated in terms of power spectrum by considering heat flux signals referred to three meaningful spatial positions (z = 13, 27, and 44 mm) at the same considered power inputs. The power spectra related to the mentioned signals are shown in Figure 8.11.

z [mm]	***Q*** [W]		
	0.5	2.5	4.5

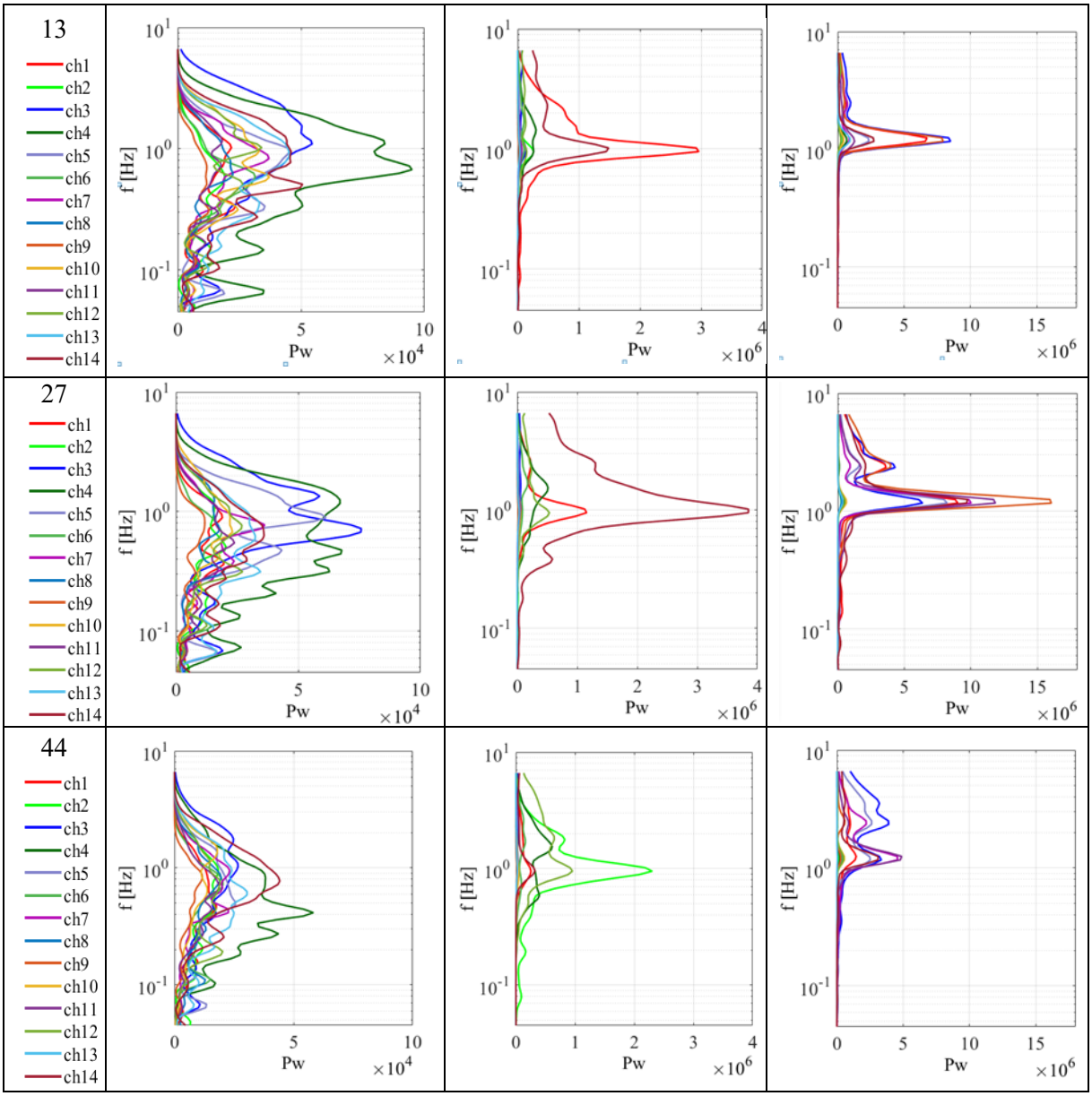

Figure 8.11: Power spectra of estimated heat fluxes at different axial coordinates and power inputs equal to 0.5, 2.5, and 4.5 W.

For low power input (0.5 W), all the channels show multiple peaks. The power increases along the position, especially by getting closer to the top of the condenser (z = 13 mm). Here, the high chaoticity of the system hampers a correct and univocal identification of dominant frequencies. On the contrary, at higher power inputs, dominant frequencies are easier to assess. At 2.5 W, the dominant frequency is around 0.95 Hz for part of the channels. In fact, the oscillation power of the edge tubes is higher than that in other branches due to the relatively high wall-to-fluid heat fluxes induced by the non-penetrative pulsating flow described in the previous Paragraph. At the highest considered power input (4.5 W), most of the channels show a peak in the power spectrum around 1.2 Hz regardless the positions. This

remark suggests that the oscillatory behaviour of the overall device is comparable in every branch, confirming the high operation regularity for such a high power input.

8.6 Flow modes detection

The heat flux signals were therefore processed to understand flow modes in the studied device. Specifically, two heat fluxes referred to points 1b and 7b (reference of Figure 8.12), were considered, for varying power inputs to the evaporator.

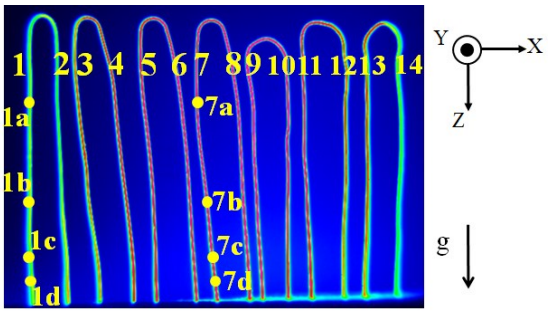

Figure 8.12: Reference points for the flow modes identification.

In Figure 8.13, the heat fluxes referred to the mentioned points are shown for three different heat loads, namely 0.5 W, 2 W and 3.5 W.

a)

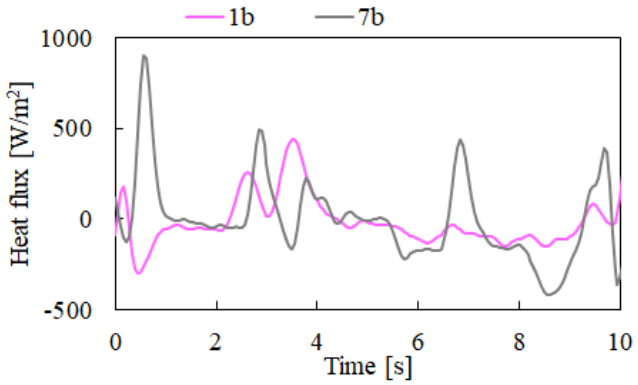

b)

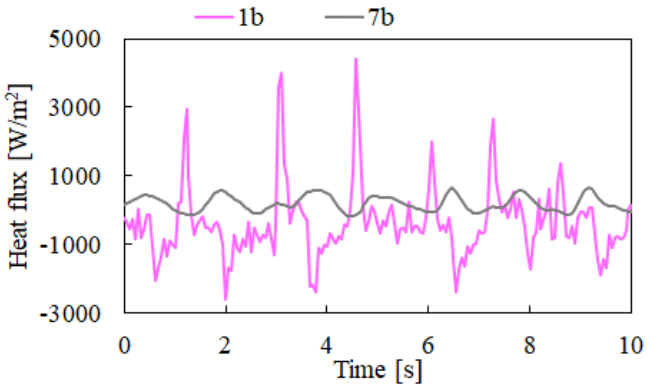

c)

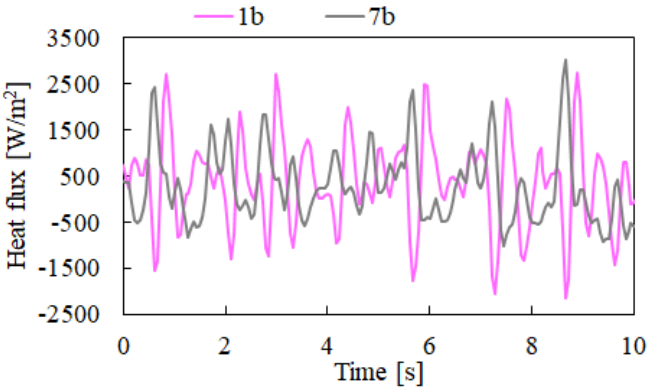

Figure 8.13: Heat fluxes at the 1b and 7b positions; Q = 0.5 W (a), Q = 2 W (b), Q = 3.5 W (c).

At 0.5 W (Figure 8.13a), the heat flux is low and almost null in each channel, despite some peaks. However, the peaks in each channel appeared to occur randomly with respect to each other. It is presumed that the fluid oscillation occurred in each tube, but the oscillation does not propagate throughout, therefore occurring intermittently with stop-over periods in between.

At high heat input, the heat fluxes showed more regular pulsations. However, at 2 W (Figure 8.13b), the waveforms of the two considered heat flux signals still seem unrelated. In fact, the edge tube (channel 1) shows a waveform with periodic sharp peaks at large amplitudes equal to around 4000 W/m^2, whereas waveform related to the central tube (channel 7) exhibits a weaker oscillation. This suggests the existence of two different oscillatory behaviours in the device: stable and continuous oscillations in the central tube and intermittent flow of the hot fluid from the evaporator to the condenser in the edge tube. Compared to the results of 0.5 W and 2 W, the difference in the waveforms between the two considered channels is mitigated at 3.5 W, as shown in Figure 8.13c. The heat fluxes are regularly and stably oscillating regardless the tube location.

The shown signals were therefore used in Equation (6.17) to investigate their correlation by discretizing the observation window into 15-seconds intervals. Such a discretization was employed due to the high chaoticity of the fluid motion patterns from channel to channel.

The results are shown in Figure 8.14. The colour scale in the bidimensional maps highlights the normalized cross-correlation between two time sub-intervals t_1 and t_2 at a time. At 0.5 W (Figure 8.14a), the presence of cross-correlation peaks highly scattered at different combinations of t_1 and t_2 confirm that the two signals are not correlated one to each other. As far as the power input increase to 2 W (Figure 8.14b), the cross-correlation peaks start appearing along the matrix diagonal, i.e., for $t_1 = t_2$. Such a trend suggests that the two signals are somehow correlated over the entire observation window, although their correlation is undermined by the presence of other low-amplitude local phenomena, as shown in Figure 8.13b. At 3.5 W (Figure 8.14c), the cross-correlation peaks mainly fill the matrix diagonal. This suggests that the flows in the middle and edge tubes are always synchronized, i.e., the

heat flux signals replicate with good agreement from channel 1 to channel 7. One of the reasonable interpretations for such a satisfactorily correlation is that the PHP was dominated by a unidirectional flow.

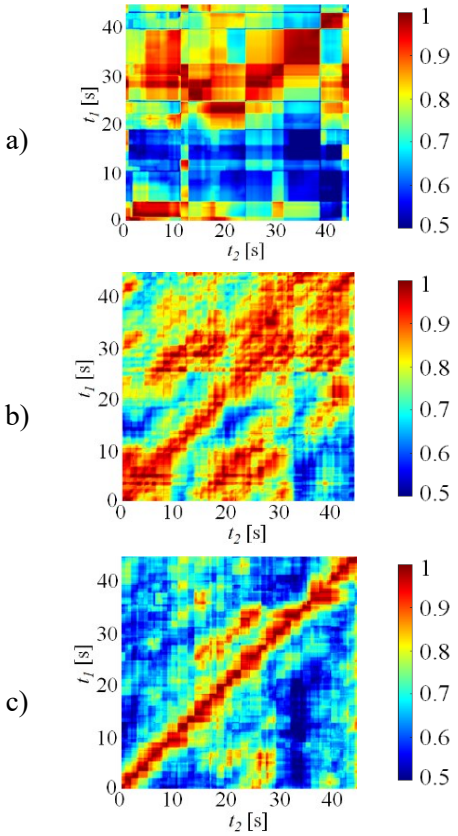

Figure 8.14: Cross-correlation maps of heat fluxes at 1b and 7b positions; Q = 0.5 W (a), Q = 2 W (b), Q = 3.5 W (c).

8.7 Closure

The local wall-to-fluid heat flux distributions were evaluated within the condenser section of a 7-turn micro-PHP to lead to a better understanding of the fundamental governing mechanisms of PHPs, which are, so far, only partially understood. The PHP consisted of stainless-steel tubes with inner diameter of 0.32 mm and HFC-134a was filled with the filling ratio of 46% as the working fluid. The experiments were conducted at the bottom heat condition and the condenser was cooled by the free convection. The time-space temperature maps of the condenser were acquired by high-resolution IR camera. The local heat flux was calculated by solving the IHCP at the tube wall using the temperature maps as the input data. A frequency analysis was performed to clarify the variations of the oscillating motions depending on the positions in the condenser, and the wavelet scalogram and the power spectrum was evaluated. The main outcomes are as follows:

- The best performance was reached for a filling ratio of 46% and for a heat input ranging between 1.9 W and 4.7 W.
- The fluid oscillation started at power input of 0.1 W with low fluid oscillation amplitude.
- Two flow regimes were observed: random-direction flow (from 1.5 W to 3.5 W) and unidirectional flow throughout the PHP, with local oscillation in the tube (from 4 W to 5 W).
- The fluid motion in each tube were reflected to the local fluid-to-wall heat flux.
- The coefficient of variation over space *cvs* allows the identification of the flow regime: in the case of the flow in random direction at relatively low power input (0.5 W and 2.5 W), the *cvs* has high peaks more than 2, whereas during the unidirectional flow in the whole PHP at high power input (4.5 W), the peaks of the *cvs* decreased to less than 1.5.
- At all power inputs, the coefficient of variation over *cvt* referred to the edge tubes is larger than that of the central ones due to the buffer effect caused by the extra fluid in the tube junction and valve.
- The frequency analysis results also highlight the flow regime transition with the increment of the heat input: multiple peaks were observed in each tube at low input, whereas the peaks became more concentrated at high power input and increased to 1.2 Hz.
- Different trends in the cross-correlation were observed, depending on the power input. At the maximum analysed power input (3.5 W), the correlation between heat fluxes in different branches was clear, suggesting a synchronized motion and therefore confirming the onset of a circulatory flow.

The thermographic acquisitions and IHCP resolution approach show a complete picture of working regimes of the tubular micro-PHP, which is difficult to obtain by the direct fluid measurements.

Chapter 9 Experimental investigation on a FPPHP

9.1 Introduction

In the present Chapter, the main outcomes referred to the investigation on a flat plate layout are given. Similarly to the procedures adopted in the previous Chapters, the listed studies are based on both global and local analyses on the mentioned device, despite such a particular geometry imposes a novel reduction approach and results in different local heat transfer interactions.

9.2 Test rig

The examined FPPHP (Figure 9.1) [110] is obtained from a copper plate (width: 80 mm, length: 200 mm, thickness: 3.5 mm) machined with a single square-shaped groove (3 x 3 mm²) forming a series of 8 U-turns in the evaporator zone (see Figure 9.1a-c). This results in a total of 16 channels in the adiabatic section, numbered in Figure 9.1a. The first machined plate is covered with a second copper plate having same dimensions and 0.5 mm of thickness. Both are brazed with tin to guarantee perfect sealing from outside, and the adjacent channels were sealed off from one another. The evaporator zone of the FPPHP is heated by a wire electrical heater (Thermocoax® Type NcAc15, 1 mm external diameter) embedded in a 40 x 80 mm², 2 mm thick copper plate by means of a serpentine groove machined on the back of the plate (Figure 9.1b) and connected to an electrical power supply (ELC® ALR3220, ±10 mV). The condenser section is instead cooled by a single-phase loop circulating an ethylene-glycol/water mixture between a copper cold plate (width: 100 mm, length: 80 mm), directly brazed on the rear side of the FPPHP (Figure 9.1b), and a cryostat (Huber® CC240 wl) controlling the temperature of the cooling mixture. Two connection pipes are brazed on top and bottom of the device, allowing the filling and vacuuming of the system, respectively.

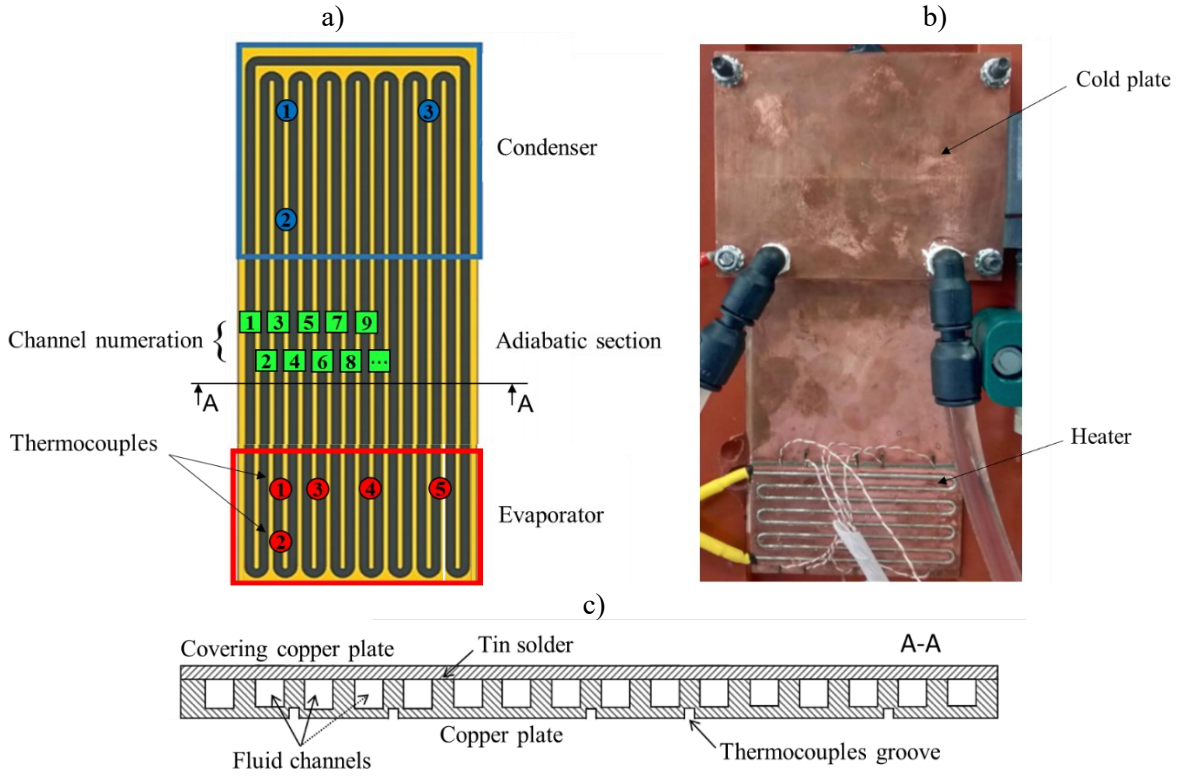

Figure 9.1: Grooved path, with reference to the evaporator, condenser and adiabatic section positions, as well as thermocouples location (circles) and channel numeration (squares) (a); rear side of the FPPHP (b); A-A cross section (c).

The evaporator temperature was monitored by means of five T-type thermocouples (Figure 9.1a) located in the grooves milled in the evaporator zone and directly attached on the FPPHP surface, while the condenser temperature was acquired through three T-type thermocouples on the rear surface of the cold plate. The ambient temperature was measured by one T-type thermocouple. The thermocouples signals were sampled at 1 Hz. In addition, the front side surface of the device was coated with a high-emissivity paint ($\varepsilon = 0.92 \pm 0.01$) to allow measurements of the outer wall temperature within the adiabatic section by a high-speed, medium weave IR camera (FLIR® SC5500, sampling frequency: 50 Hz, pixel resolution: 320 x 256). In particular, the adiabatic section was framed over a 40 mm wide portion, highlighted with a green window in Figure 9.2a. For visualization purposes, no insulation was adopted along the adiabatic section. For the same reason, both the evaporator and the condenser front surfaces were not thermally insulated, while the rear surface of the evaporator was covered with insulating material to reduce heat losses to the environment and obtain an accurate value of the actual heating power.

The uncertainty related to the experimental tools are listed in Table 9.1.

Table 9.1: Uncertainty of the experimental tools.

Sensor	Sampling frequency	Uncertainty	
T-type thermocouple	1 Hz	± 0.1 °C	
MWIR camera	50 Hz	Absolute: ± 1 °C	Sensitivity: < 25 mK
Power supply	-	± 2 W	

9.3 Experimental procedure

The FPPHP was first evacuated, and sealing tested by means of an ultra-high vacuum system (ASM 142, Adixen by Pfeiffer Vacuum®) coupled with a helium detector. The device was therefore partially filled with a water-ethanol mixture (20 wt.% of ethanol, filling ratio: 50% at 20°C), previously degassed by heating-cooling cycles. The FPPHP was positioned in vertical BHM and horizontal orientations, while the condenser temperature was set to 20°C. The power input given to the evaporator ranged from 50 W up to 250 W, where the tests were stopped due to the increase of evaporator temperature over the safety limit for the used materials and sensors. Two IR acquisitions, each lasting 20 seconds, were carried out during the so-called pseudo-steady state of the device, i.e. after about 30 minutes from every heat load step applied to the evaporator. In Figure 9.2b, a sample of IR acquisition is shown (one single frame). The thermocouples signals were instead constantly recorded during the tests.

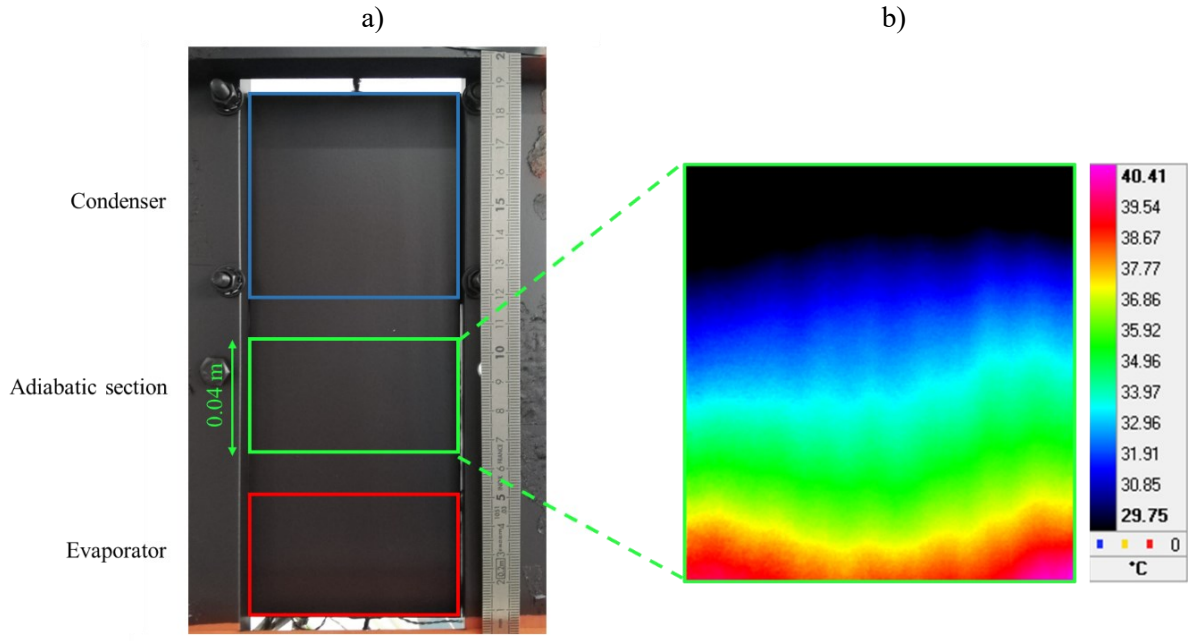

Figure 9.2: Front side of the device, externally coated with a high-emissivity paint, with reference to the section framed by the MWIR camera (green box) (a) and sample of IR acquisition (b).

The cases under test are listed in Table 9.2.

Table 9.2: Test cases; "x" stands for "acquisition point", "-" stands for "not investigated point".

	$\boldsymbol{Q}$ [W]							
Orientation	*50*	*70*	*90*	*100*	*120*	*150*	*200*	*250*
BHM	x	x	x	-	x	x	x	x
Horizontal	x	-	-	x	-	x	x	x

9.4 Global performance

The device was first characterized, for every considered study case, by evaluating its global performance. Hence, the equivalent thermal resistance was quantified by means of Equation (3.1). The evaporator and condenser temperatures were averaged over 5 minutes during the pseudo-steady state of the device. Since part of the evaporator section was not insulated, the net power input Q_{net} was quantified as $Q_{net} = Q - Q_{diss}$, where $Q_{diss} = S'_{eva} \cdot h_{env}(T_{eva} - T_{env})$ is the power dissipated at the evaporator section to the surrounding environment by both natural convection and radiation. The non-insulated evaporator surface S'_{eva} was estimated, according to the FPPHP geometry, equal to 0.0037 m^2, and the maximum dissipated power of about 1.4 W was found for the horizontal orientation, Q = 250 W, with average evaporator temperature of 50°C. During the tests, the environmental temperature T_{env} ranged from about 18°C to 21°C.

The uncertainty $\delta_{R_{eq}}$, referred to each value of R_{eq}, was evaluated by means of $\delta_{R_{eq}} = \sqrt{\left(\frac{1}{Q_{net}}\delta_{\Delta T}\right)^2 + \left(-\frac{\Delta T}{{Q_{net}}^2}\delta_{Q_{net}}\right)^2}$, where $\delta_{\Delta T}$ is the uncertainty related to the temperature difference $\Delta T = (T_{eva} - T_{cond})$ and $\delta_{Q_{net}}$ is the uncertainty on the net heat load, which depends on the uncertainty of the power supply (Table 1).

In Figure 9.3, the resulting R_{eq} evaluated by means of Equation (3.1) is shown for each net heat load, together with the corresponding error bars. The equivalent thermal resistance for the empty device was assessed to be almost equal to 0.7 K/W.

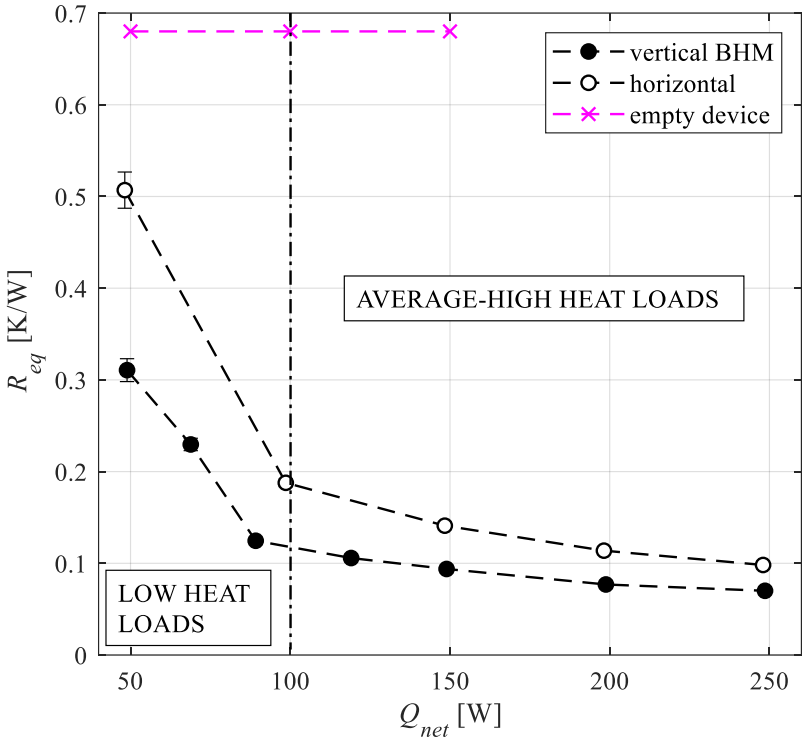

Figure 9.3: Equivalent thermal resistance of the studied FPPHP at varying net heat loads to the evaporator for the two considered device orientations.

For every power input to the evaporator, the vertical BHM presents lower values of R_{eq} with respect to the horizontal orientation, denoting better thermal performances within the gravity-assisted mode in agreement with Ayel et al. [110]. In addition, for both configurations, R_{eq} strongly decreases until about Q_{net} = 100 W, to approach an almost asymptotic value at high power inputs. Such abrupt change in trend could be due to the fact that the device undergoes a significant variation in terms of working behaviour from low power inputs (Q_{net} < 100 W) to higher heat loads. To further investigate such variation, the evaporator temperature, measured by means of thermocouples during the tests, was considered. In fact, such quantity is generally used for a qualitative identification of working modes in PHPs [3]. Specifically, intermittent flows are described by strong fluctuations of the evaporator temperature due to the occurrence of stopovers, while full activations, where the working fluid effectively oscillates in every channel, are described by either abrupt drops in evaporator temperature or weak evaporator temperature fluctuations.

The measured evaporator temperature history $T_{eva,hist}$ referred to both orientations is shown in Figure 9.4, as well as the power input provided to the evaporator during the entire duration of the tests (black lines).

a)

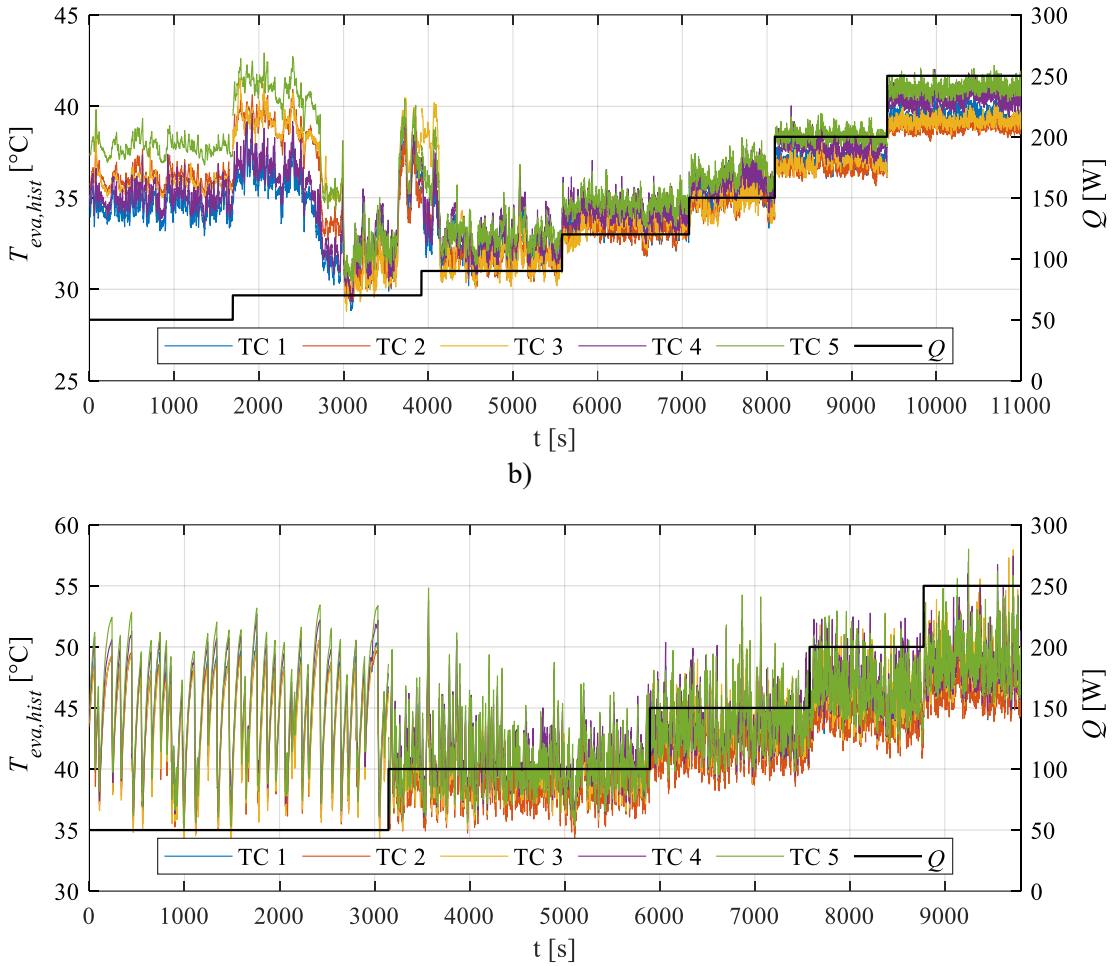

Figure 9.4: Evaporator temperature history for the vertical BHM (a) and the horizontal orientation (b), together with the power input provided to the evaporator over time (black line).

For power inputs lower than 100 W, the vertical BHM orientation exhibits generally high evaporator temperature fluctuations due to stopovers (Figure 9.4a). In addition, a significant variations of $T_{eva,hist}$ from measurement point to measurement point suggests that, in some FPPHP branches, the working fluid properly flows between the evaporator and the condenser, i.e. the evaporator is cooled down, while others channels are not efficiently working. Hence, the device seems to operate under the intermittent flow working regime. A similar conclusion can be obtained from the analysis of the horizontal orientation case (Figure 9.4b), where $T_{eva,hist}$ presents strong stopovers at 50 W highlighted by great temperature fluctuations, in accordance with the higher value of R_{eq} observed in Figure 9.3 with respect to the vertical BHM orientation. By increasing the heat load to the evaporator, $T_{eva,hist}$ fluctuates in a narrower range for both orientations during the pseudo-steady state, suggesting a full activation of the device and therefore explaining the change in slope of the R_{eq} curves in Figure 9.3.

The assessed working regimes are listed in Table 9.3.

Table 9.3: Device working regimes; "I": intermittent flow, "F": full activation.

Orientation	***Q [W]***						
Vertical BHM	*50*	*70*	*90*	*120*	*150*	*200*	*250*
	I	*I*	*F*	*F*	*F*	*F*	*F*
Horizontal	*50*	*100*	*150*	*200*	*250*		

9.5 Local heat transfer analysis

To give a deeper insight into the device heat transfer behaviour, the wall-to-fluid heat flux q, locally exchanged within the whole adiabatic section, was evaluated for every study case by adopting the post-processing procedure described in Paragraph 5.3. The thermal conductivity of copper was certified by the manufacturer to be equal to 401 W/mK at 300 K, and R_{env} was assumed equal to 0.1 m^2K/W. In addition, during the tests, T_{env} varied from 18°C to 21°C. σ_b was evaluated equal to 0.04 K from isothermal acquisitions, while the ratio $ratio_{opt}$ varied in the range 0.8 to 1.1 for high and low power inputs to the evaporator, respectively. It has to be reminded that q is not here referred to the whole wall-fluid interface, but only to the median portion of thin walls in each channel (Figure 5.4a). However, despite such an evaluated thermal quantity is limited to the thermofluidic interactions within a rather small part of the device, it is believed to describe the FPPHP thermal behaviour in terms of fluid oscillations and working regimes. In fact, the low thickness of such a portion guarantees higher wall temperature variations, directly linked to the inner thermo-dynamics.

In Figure 9.5, the raw temperature acquired by means of thermography is shown (Figure 9.5a), together with the corresponding evaluated wall-to-fluid heat flux distribution (Figure 9.5b) for a single test case (horizontal orientation and Q = 100 W) and for channel 8 (central channel, see reference of Figure 9.1a).

a)

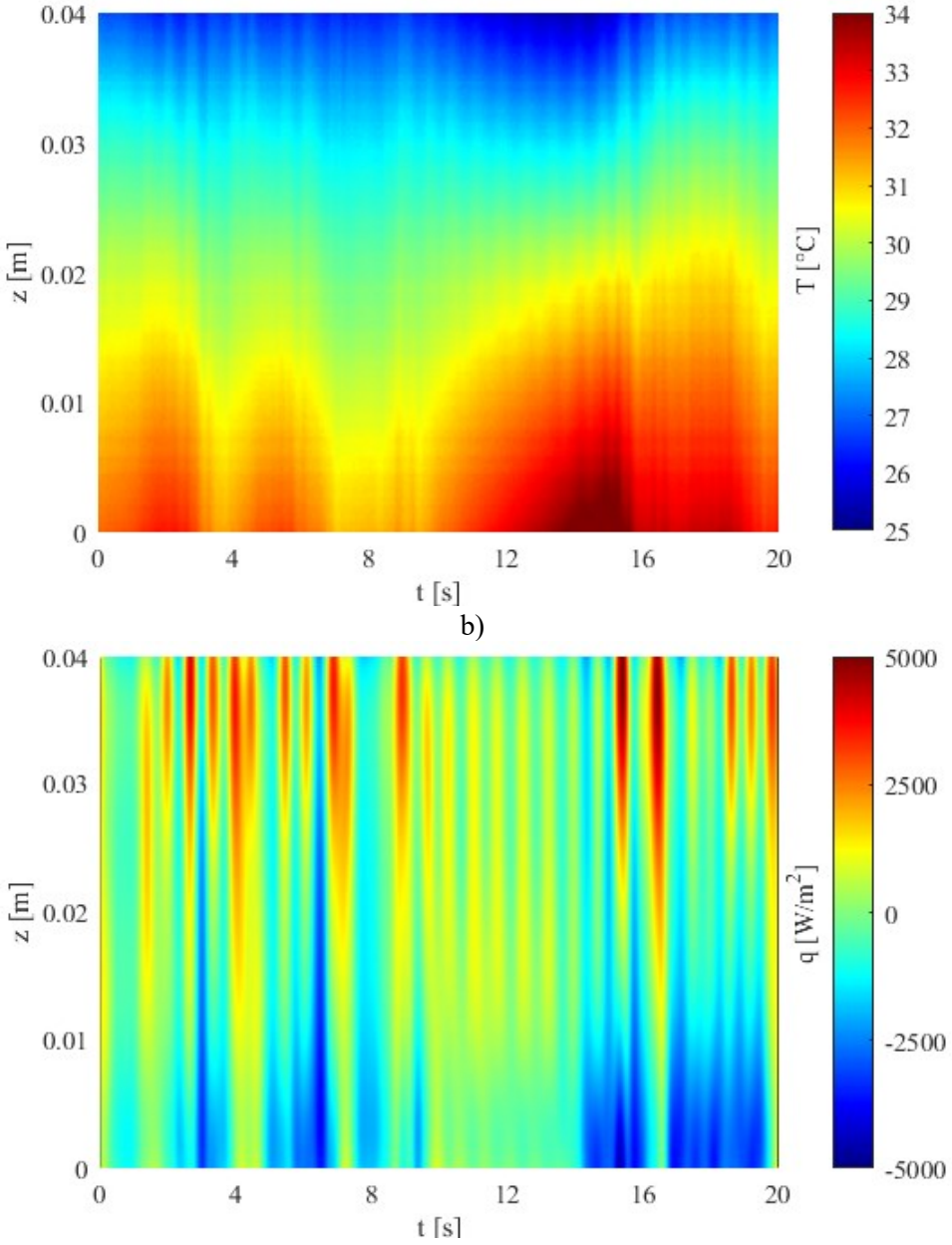

Figure 9.5: Space-time temperature distribution acquired by means of thermography (a) and resulting wall-to-fluid heat flux q (b); (channel 8, horizontal orientation, Q = 100 W).

The interpretation of the present heat flux distribution is the same adopted in Chapter 7 for tubular layouts where the adiabatic section was investigated, although the amplitude of q presents here non-negligible variations along the z coordinate in the analysed channel. In particular, the wall-to-fluid heat flux exhibits an increasing trend from the evaporator ($z < 0$ m), where it seems to assume lower values, to the condenser ($z > 0.04$ m), where it seems to assume higher values instead. Such a characteristic local heat transfer behaviour could be due to the conductive heat transfer through the device section

between the evaporator and the condenser, which propagates to the adiabatic section the effects of both heat transfer areas on the working fluid.

To verify the actual presence of a significant gradient of the wall-to-fluid heat flux along the z coordinate, the investigation was extended to all channels. In Figure 9.6, the average value of q, q_{av}, referred to each axial coordinate over time, is shown for every FPPHP branch. By computing the mean of q_{av} of all channels at every z coordinate (black dotted line), the heat flux trend along z in the whole device can be observed. Here, the wall-to-fluid heat flux exhibits, on average, an increasing trend in every branch of the device, confirming what previously stated for a single channel. The analysis was replicated for every heat load provided to the evaporator, verifying the presence of a significant space variation in the evaluated wall-to-fluid heat flux distributions.

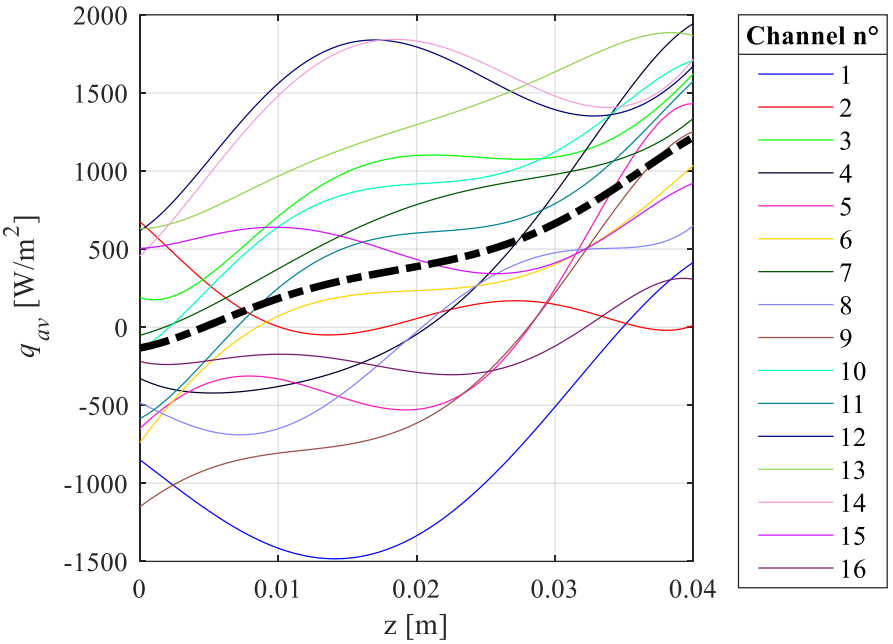

Figure 9.6: Wall-to-fluid heat flux averaged in every FPPHP channel for each axial coordinate over time; the linear interpolation (black, dotted line) of the values assumed by q_{av} outlines the variation of the wall-to-fluid heat flux with z in the overall device (horizontal orientation, Q = 100 W).

It has to be considered that the observed variation of q along the axial coordinate depends on the geometry and the material of the device, which is highly conductive. On the contrary, by considering different kinds of materials, e.g. polymeric materials, or different geometries, e.g. tubular layouts, the wall-to-fluid heat flux distributions could present negligible space variations, as observed in Paragraphs 7.2 and 7.3.

Time variations of the thermofluidic behaviour were instead analysed by comparing the global and local response of the device. To this aim, the values assumed by q over time in every FPPHP branch

for a single axial coordinate, namely z = 0.02 m, were compared with the evaporator temperature acquired by means of thermocouples.

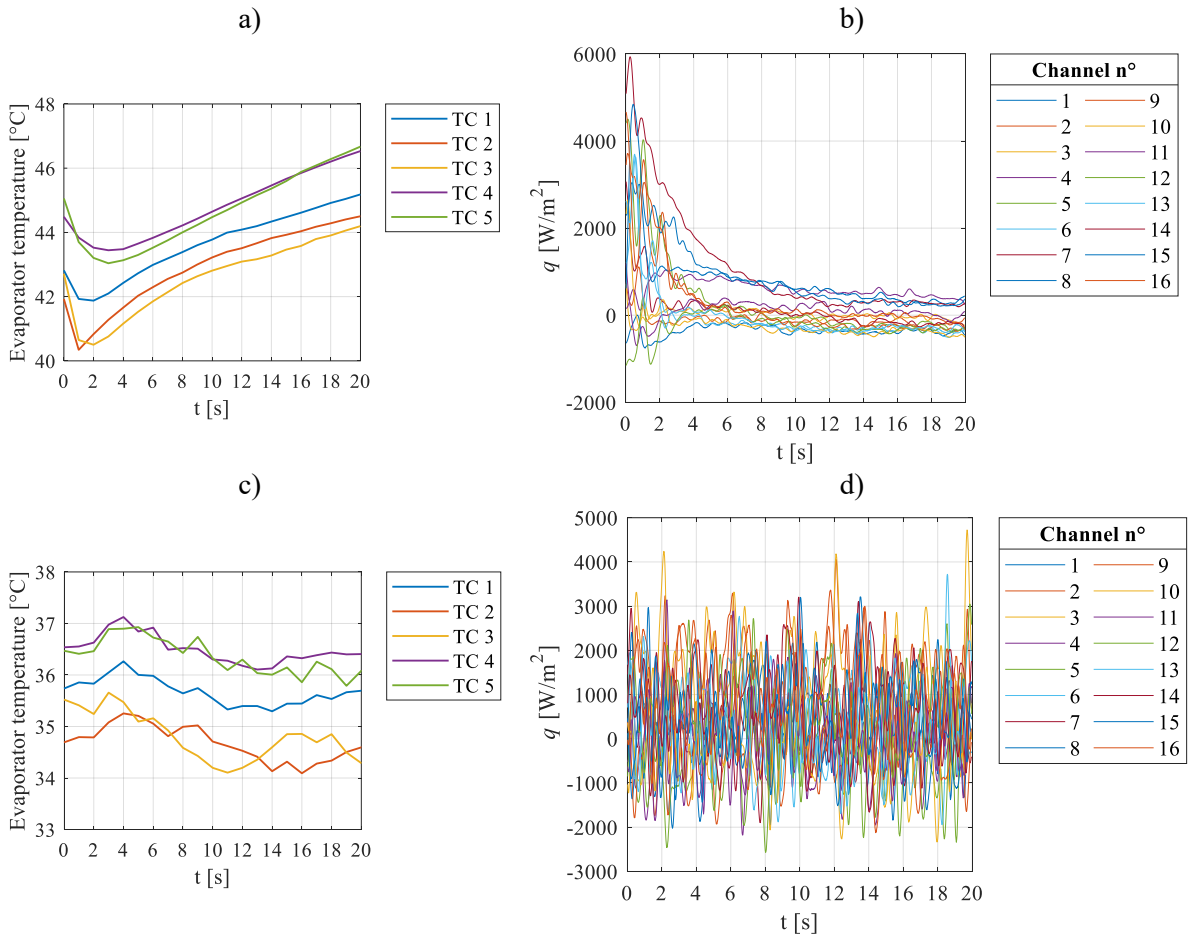

Figure 9.7: Evaporator temperature, acquired by means of thermocouples, and local heat flux referred to every channel for the horizonatl orientation at Q = 50 W (a,b) and for the vertical BHM at Q = 150 W (c,d).

In Figure 9.7, such qualitative comparison is shown for two different operating conditions, i.e. horizontal orientation, Q = 50 W (Figure 9.7a-b), and vertical BHM orientation, Q = 150 W (Figure 9.7c-d). In the horizontal configuration, the evaporator temperature (Figure 9.7a) exhibits an overall decrease during the first 2 seconds of acquisition, suggesting that the device is properly working. After 2 seconds, the evaporator temperature starts increasing until the end of the observation window, denoting the occurrence of a stopover. On the other hand, during the first 2 seconds of acquisition, q oscillates in almost every channel (Figure 9.7b), suggesting fluid motion between the evaporator and the condenser, while it starts approaching null values after 2 seconds without any significant oscillation, denoting instead absence of fluid motion. Regarding the vertical BHM operation, the evaporator temperature (Figure 9.7c) slightly fluctuates over the entire observation window, denoting an efficient

operation of the device, while q (Figure 9.7d) presents regular and persistent oscillations for every PHP branch, i.e. the fluid is regularly flowing in the overall adiabatic section.

The wall-to-fluid heat flux is thus proven to give information about the fluid motion and the device operation similarly to the evaporator temperature fluctuations, although the heat flux interpretation exhibits greater robustness and repeatability in confirming a relation between local and global FPPHP thermal behaviours. In addition, the heat flux variations over time are capable of describing the device working regimes. In fact, from a local point of view, intermittent flow regimes are denoted by an intermittent functioning of each channel, i.e. alternation of heat flux oscillations and null heat fluxes, while full activations are represented by regular and persistent heat flux oscillations over time in every PHP branch.

9.5.1. Statistical approach on the local wall-to-fluid heat flux

To study the variation of heat flux distributions over time and along space, the coefficients of variation of Paragraph 6.3.1 were adopted. The average and standard deviation of such coefficients in the overall device were therefore computed according to the definitions of Equations (7.2) and (7.3) to provide a general description of the wall-to-fluid interactions.

In Figure 9.8, cvt_{av} and cvt_{std} are shown for the two considered orientations as functions of the power input to the evaporator. For heat loads lower than 100 W, cvt_{av} reaches peaks of about 75%, while cvt_{std} decreases to about 10%. At average-high heat loads, cvt_{av} and cvt_{std} stabilize around 70% and 8% for both orientations, thus giving a further reference for the description of the significant change in slope of R_{eq} during the transition from intermittent flow to full activation of the device (Figure 9.3). The provided values and general trends of the statistical coefficients are in good agreement with those found in Paragraph 7.3.5, although the very different geometry analysed in the present work, suggesting the validity of the adopted statistical coefficients for other PHPs layouts.

Besides, the intermittent flow regime in the horizontal orientation, when compared to the vertical BHM orientation, exhibits, at 50 W, higher values of cvt_{av} and cvt_{std}. This suggests stronger variations over time of the heat flux from channel to channel and, consequently, a more intermittent operation of the FPPHP, in accordance with previous works [142–144]. Also, such evidence agrees with the higher value of equivalent thermal resistance observed in Figure 9.3, as well as with the higher temperature fluctuations observed at the evaporator section (Figure 9.4). On the other hand, within the full activation of the system, cvt_{av} and cvt_{std} assume similar values for both orientations, highlighting comparable heat flux variations over time. Such similarity may explain the gradual approaching of equivalent thermal resistance referred to both orientations at high heat loads to the evaporator.

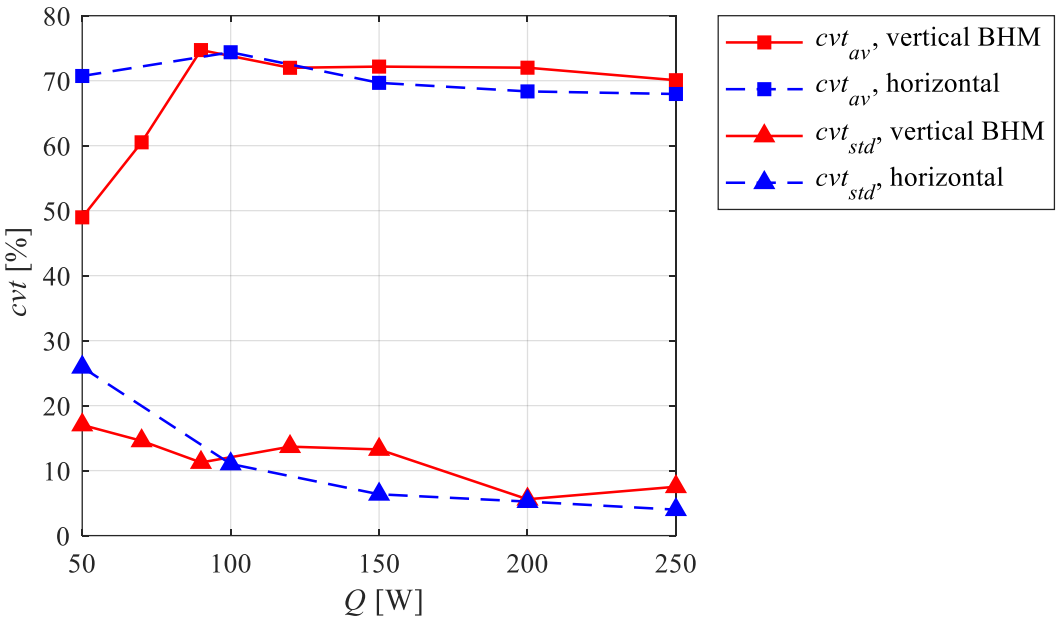

Figure 9.8: cvt_{av} and $cvt_{std,}$ as functions of the power input given to the evaporator, for the two considered orientations.

To also quantify space variations of the heat flux, cvs_{av} and cvs_{std} are shown for the two considered orientations in Figure 9.9.

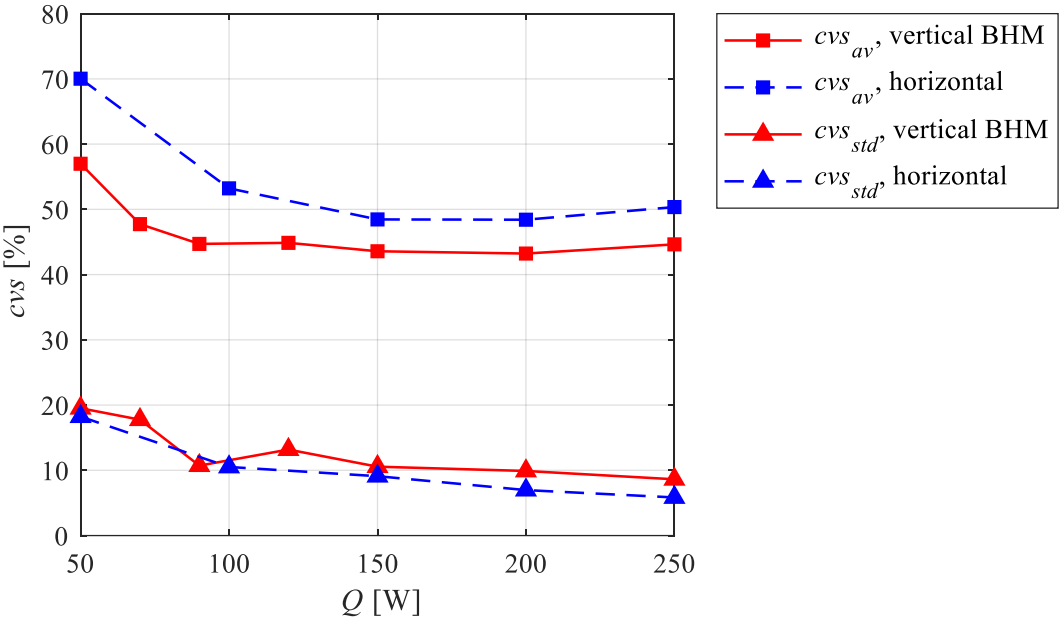

Figure 9.9: cvs_{av} and $cvs_{std,}$ as functions of the power input given to the evaporator, for the two considered orientations.

Here, cvs_{av} referring to both the vertical BHM orientation and the horizontal orientation decreases at low power inputs, to settle around 43% and 50%, respectively, at average-high power inputs. In

addition, cvs_{std} decreases almost monotonically from a maximum of about 20% to a minimum of about 8% for both orientations. Such trends denote that the variations over space tend to gradually decrease during the intermittent flow regime in the overall device unlike time variations of Figure 9.8, while they stabilize during the full activation regime. Such remark suggests that the conduction effects through the metallic section of the present FPPHP are evident in both orientations especially during the intermittent flow regime, where the unregular operation of each FPPHP branch promotes the onset of strong conduction along the z coordinate, as stated in [145]. On the other side, the stabilization of cvs_{av} at lower values during the full activation regime denotes less predominant conduction effects. Moreover, the higher values assumed by cvs_{av} in the horizontal orientation with respect to those assumed in the vertical BHM suggest that the wall-to-fluid interactions are distributed in a less uniform way along the z coordinate, probably due to weaker fluid oscillations. Finally, the values of *cvs* in the present FPPHP assume much higher values with respect to those previously assessed within the adiabatic section in a tubular layout (Paragraph 7.3.5), where the conduction through the adiabatic section was almost negligible, thus confirming the presence of strong conductive phenomena occurring in the studied FPPHP geometry.

To provide a reference for the understanding of conduction between the evaporator and the condenser at varying heat loads in the present FPPHP, the ratio between the power transferred by only conduction $Q_{conduction}$ through the copper plate and the net power input given to the evaporator is shown in Figure 9.10. Specifically, by using the values of evaporator and condenser temperature averaged over 5 minutes during the pseudo-steady state of the device for each given heat load, results:

$$Q_{conduction} = k(T_{eva} - T_{cond}) \cdot S_{copper}/L_{adiab} \tag{9.1}$$

being $S_{copper} = T_{FPPHP} \cdot W_{FPPHP} - l_{channel}^2 \cdot num$ the full metallic cross-section of the device and L_{adiab} the length of the adiabatic section. T_{FPPHP} is the device thickness, W_{FPPHP} is the device total width, $l_{channel}$ is the side dimension of channels and *num* is the total number of channels.

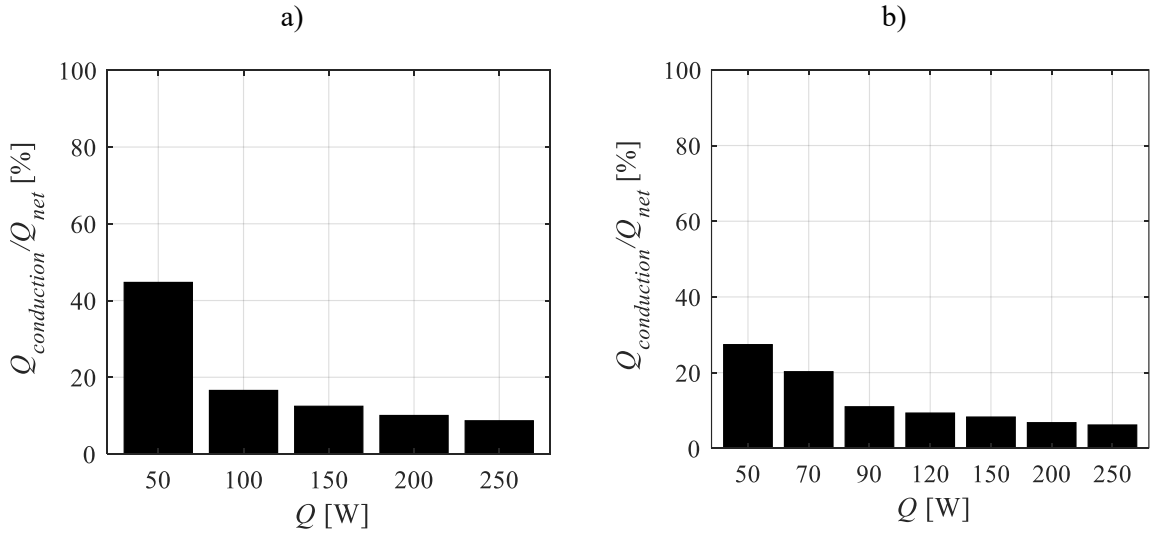

Figure 9.10: Ratio between the power transferred by conduction between the evaporator and the condenser and the net power input to the evaporator as a function of Q for the horizontal orientation (a) and the vertical BHM (b).

For both orientations, $Q_{conduction}$ decreases with respect to the net power input, suggesting that more and more power provided to the evaporator is transferred by the working fluid to the condenser from the intermittent flow to the full activation regime. Hence, this confirms the reduction in terms of heat flux variations over space within the adiabatic section, quantified in Figure 9.9, as well as the different values assumed by cvs_{av} from horizontal orientation to vertical BHM.

Finally, heat flux distributions were statistically reduced by evaluating their 80th percentile (Paragraph 6.3.2) at varying working conditions. In Figure 9.11, q_{80} is plotted as a function of Q: here, strong wall-to-fluid thermal interactions can be noted in the horizontal orientation, where q_{80} increases from 1000 W/m^2 to about 7100 W/m^2. On the contrary, in the vertical BHM orientation, q_{80} slightly increases from 1000 W/m^2 to about only 2200 W/m^2. Such significant difference in terms of wall-to-fluid heat flux amplitude, which was also perceived in Paragraph 7.3.5, is merely due to the effects of the device orientation. In fact, in the vertical BHM operation, the buoyancy forces greatly promote the fluid motion inside the device, resulting in a lower pressure (and, consequently, lower saturation temperature) needed for the working fluid motion and more regular temperature distribution along the channels. Hence, weaker temperature differences between the FPPHP wall and the working fluid are generally perceivable, leading to lower wall-to-fluid heat fluxes.

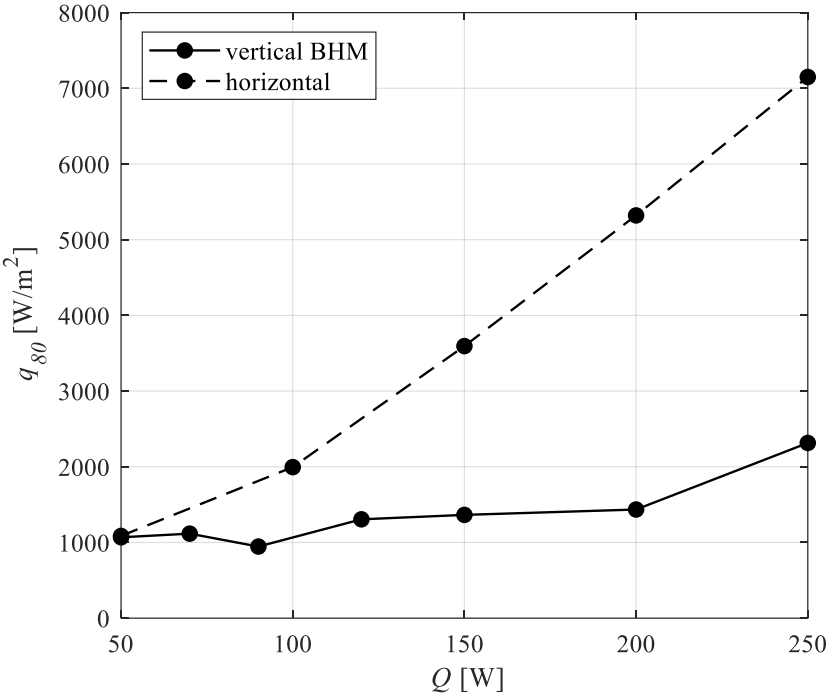

Figure 9.11: 80th percentile of the absolute value of q as a function of the heat load to the evaporator for the two considered orientations.

9.5.2. Frequency analysis on the local wall-to-fluid heat flux

The wall-to-fluid heat fluxes were therefore analysed in terms of oscillation frequency to quantitatively describe the oscillatory behaviour of the working fluid for the device under study. In particular, the wavelet method (Paragraph 6.2) was employed.

It has to be pointed out that, since the heat flux distributions evaluated in the present device significantly vary with space, as shown in the previous Paragraphs, the wavelet method may provide different results depending on the considered axial coordinate. To investigate such dependency, the wall-to-fluid heat flux signals related to a single channel at different z coordinates were used as inputs for the wavelet approach, and the resulting power spectra were therefore compared. In Figure 9.12, such comparison was carried out for channel 9 at z = 0.01 m, z = 0.02 m and z = 0.03 m, and both device orientations at Q = 250 W. Here, despite different amplitudes of the wall-to-fluid heat fluxes of Figure 9.12a-c, their oscillatory trend over time do not present any dissimilarities with respect to different axial points. In fact, all the power spectra of Figure 9.12b-d exhibit absolute peaks in correspondence of the same frequency, thus highlighting same dominant frequency regardless of the considered axial position. For this reason, every processed heat flux was chosen, for the present analysis, at z = 0.02 m, representative of all other z coordinates.

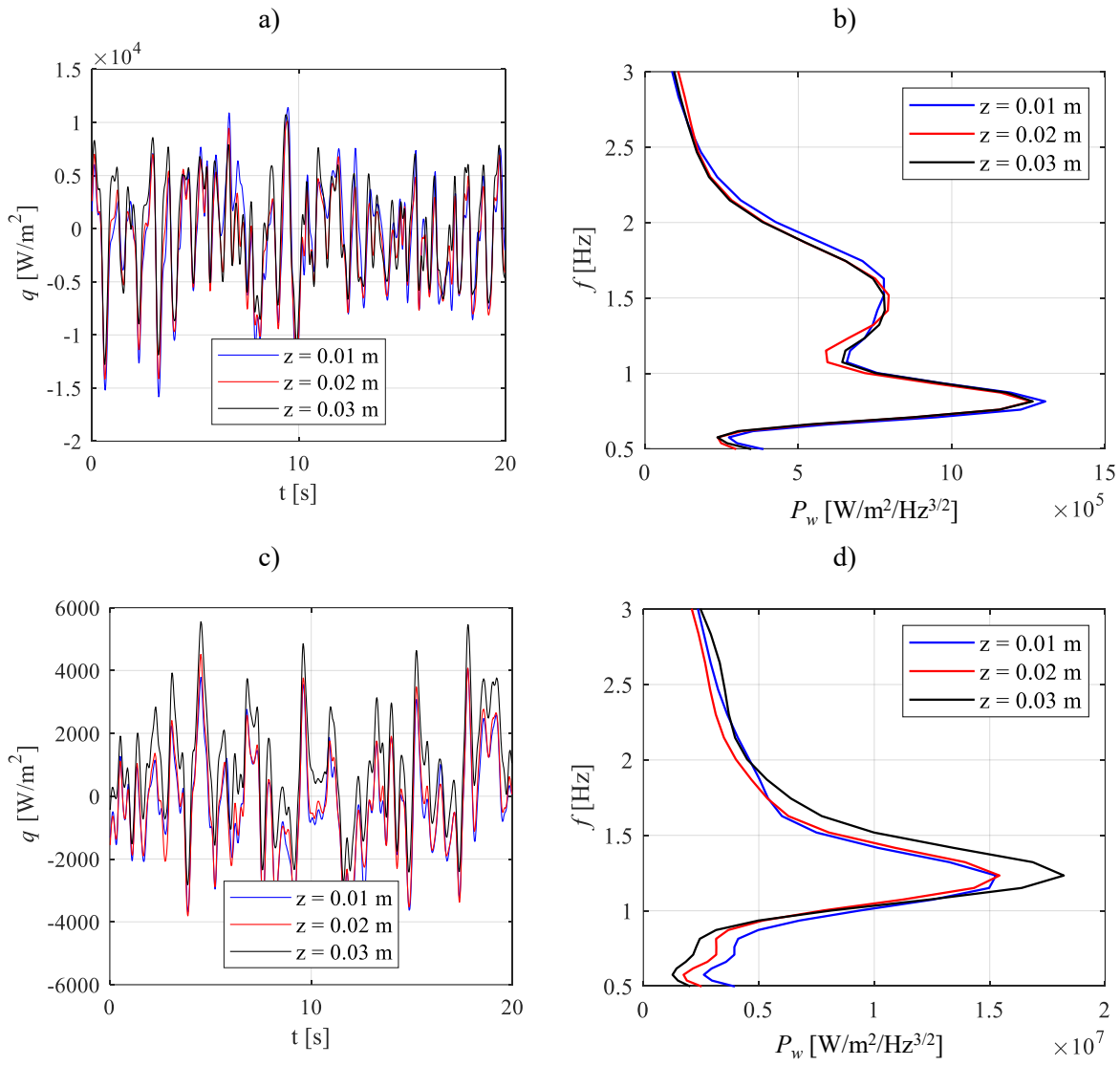

Figure 9.12: Wall-to-fluid heat flux signals over time related to channel 9 and Q = 250 W for three different axial coordinates and corresponding power spectra; vertical BHM (a,b) and horizontal orientation (c,d).

The wavelet method was then extended to the heat flux signals referred to all the FPPHP branches, thus assessing channel-wise fluid oscillation frequencies at varying heat loads and orientations.

In Figure 9.13 and Figure 9.15, the scalograms referred to three channels, namely channels 4, 8 and 12, are shown for the vertical BHM at power inputs equal to 50 W, 150 W and 250 W, respectively. Note that all frequencies, signal powers and power spectrum graphs have the same scales of that of Figure 9.15 for reasons of better comparison. The power spectra related to all the FPPHP channels are furtherly presented for a comprehensive description of the oscillatory behaviour.

In Figure 9.13a (Q = 50 W), the scalogram exhibit a medium-power area during the first seconds of acquisitions, suggesting the presence of weak oscillations. On the contrary, Figure 9.13b-c do not present any significant power spots except for some low-power areas, thus highlighting nearly absence

of fluid motion. Such evidence is confirmed by the power spectra of Fig. 7d, which are flat for most of the channels, i.e. no fluid oscillations can be perceived in almost the whole device. As the power input to the evaporator increases to 150 W (Figure 9.14), the scalograms (Figure 9.14a-b-c) referred to the vertical BHM present more persistent medium-power areas over time; also, all the power spectra of Figure 9.14d exhibit perceivable peaks, suggesting that the fluid oscillates in every branch with dominant frequencies mainly below 1 Hz. For the maximum provided power input (Q = 250 W, Figure 9.15), the scalograms (Figure 9.15a-b-c) highlight many high-power spots, denoting strong fluid oscillations over time. Nevertheless, the power spots are referred to different frequencies, suggesting that the oscillatory behaviour is not stable over the observation window. The presence of strong oscillations described by high-power spots is confirmed by the power spectra (Figure 9.15d), which assume high peaks of P_w. Their absolute maxima are furthermore scattered within a wide range of frequencies in between 0.6 and 1.6 Hz, thus denoting greatly different dominant fluid oscillation frequencies from channel to channel.

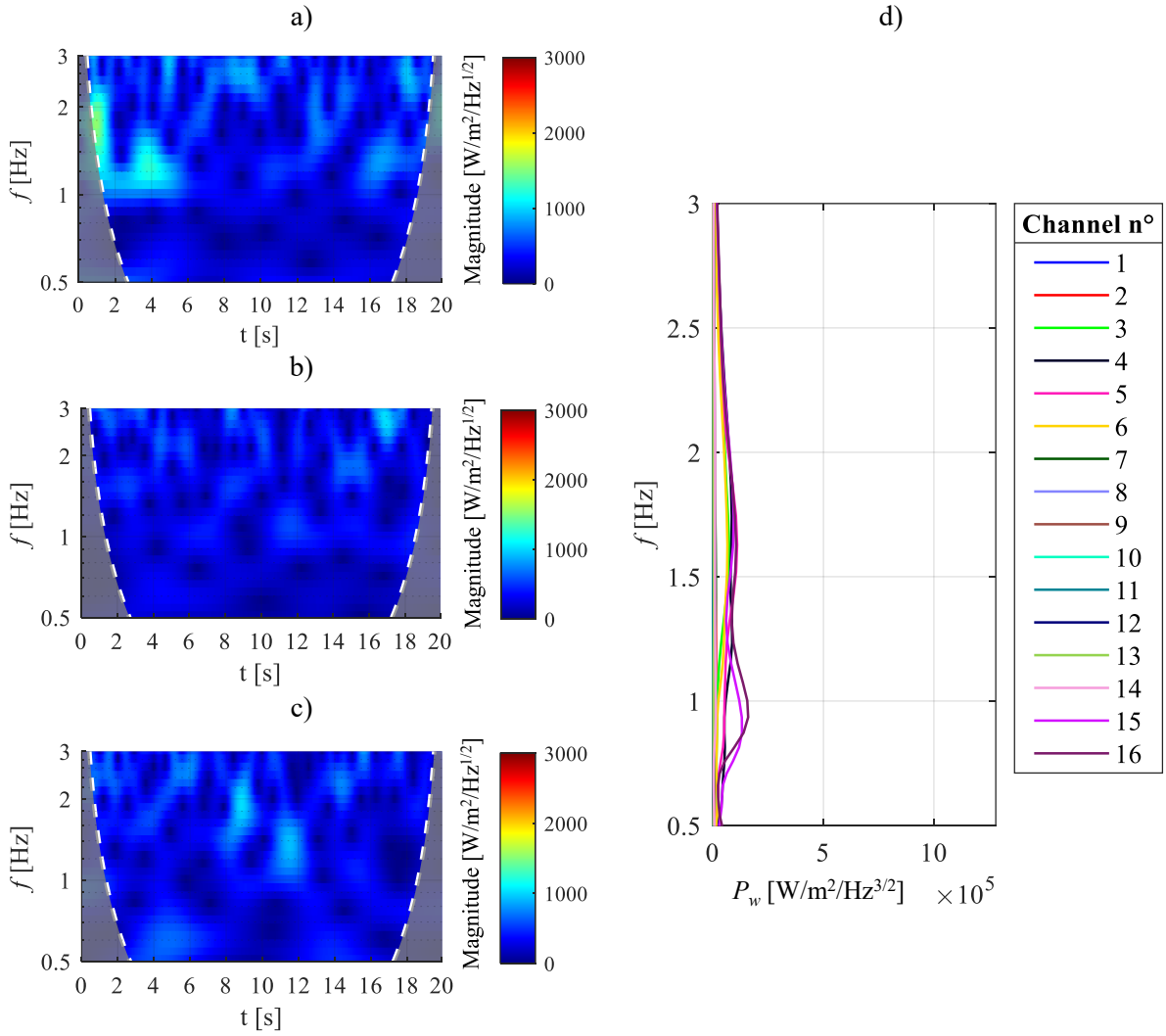

Figure 9.13: Scalograms for channels 4 (a), 8 (b) and 12 (c), and power spectra of the wall-to-fluid heat fluxes for the fixed axial coordinate z = 0.02 m over time related to each FPPHP channel in vertical BHM (d); Q = 50 W.

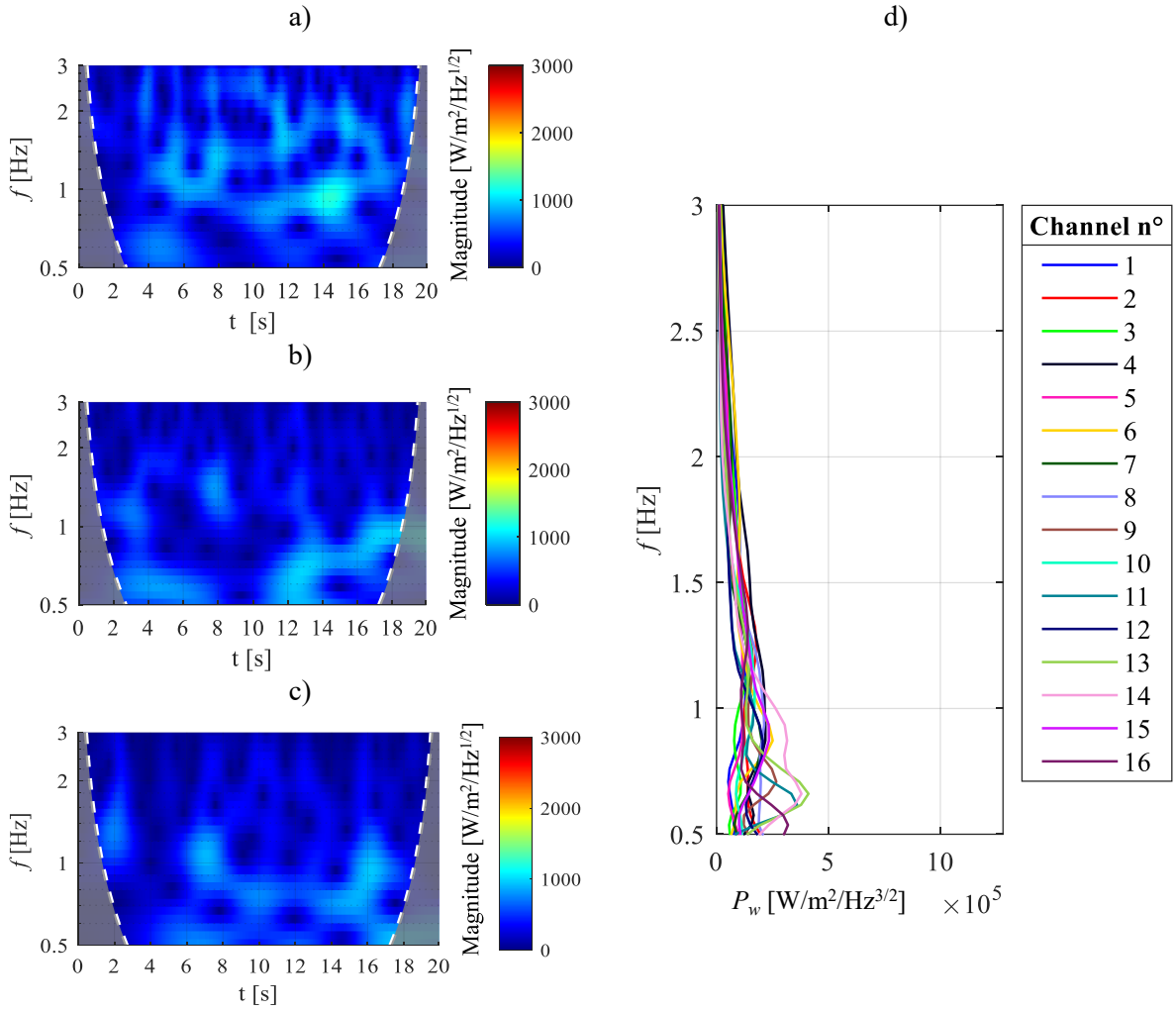

Figure 9.14: Scalograms for channels 4 (a), 8 (b) and 12 (c), and power spectra of the wall-to-fluid heat fluxes for the fixed axial coordinate z = 0.02 m over time related to each FPPHP channel in vertical BHM (d); Q = 150 W.

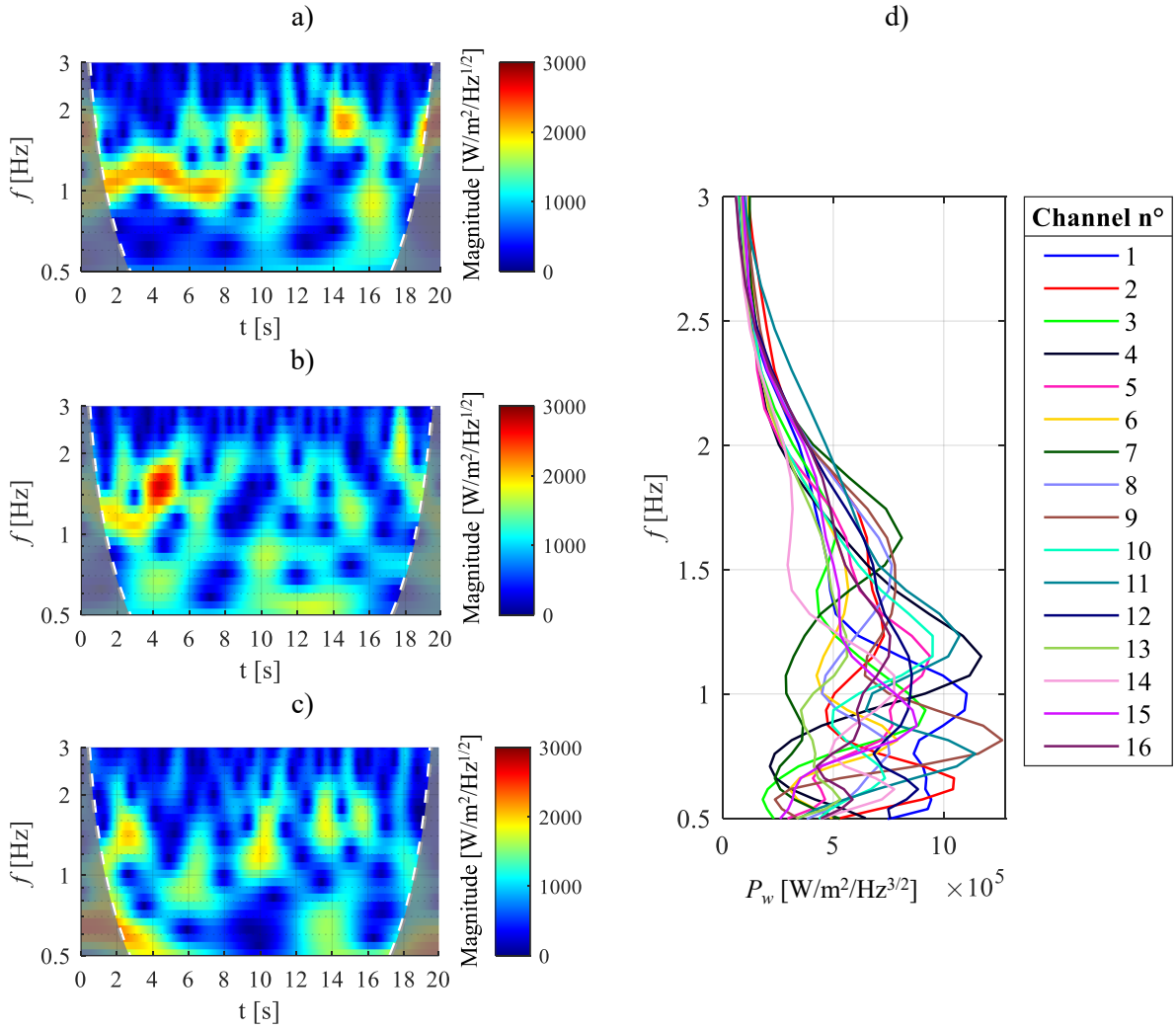

Figure 9.15: Scalograms for channels 4 (a), 8 (b) and 12 (c), and power spectra of the wall-to-fluid heat fluxes for the fixed axial coordinate z = 0.02 m over time related to each FPPHP channel in vertical BHM (d); Q = 250 W.

Similarly, in Figure 9.16 and Figure 9.18, the scalograms and power spectra related to the same channels and power inputs of Figure 9.13 and Figure 9.15 are shown for the horizontal orientation. In Figure 9.16a-b-c (heat load Q = 50 W), scalograms do not present any significant power spots, denoting either absence of fluid motion or very weak and intermittent oscillations. The device inactivity over the observation window is additionally highlighted by a complete absence of peaks in the power spectra of Figure 9.16d. For Q = 150 W (Figure 9.17), the scalograms of Figure 9.17a-b-c exhibit medium-power stripes which persist with continuity during almost the whole acquisition in the considered channels, except for some higher-frequency spots especially evident in Figure 9.17a. High P_w are clearly noticeable from the power spectra of Figure 9.17d, confirming the presence of regular fluid oscillations with dominant frequencies around 0.9 Hz. At 250 W, the scalograms (Figure 9.18a-b-c) show high-power spots which replicate at almost the same frequency over time, denoting the time regularity of the

strong fluid oscillations occurring for such working condition. Such vigorous fluid oscillations in every FPPHP channel are also clear from the power spectra high peaks of Figure 9.18d, with dominant frequencies around 1.2 Hz. It is worth to notice that, contrarily to the vertical BHM orientation, the peaks of P_w span within a much narrower range of frequencies in the horizontal orientation for medium/high power inputs. This might be due to the fact that the buoyancy forces acting on the fluid increase the complexity of the device operation and, consequently, of its oscillatory behaviour. In fact, in the vertical BHM, a transition between slug-plug to semi-annular flow may occur, especially due to the squared section of the present FPPHP channels [146,147], thus increasing the chaoticity of the thermofluidic wall-to-fluid interactions. On the contrary, in the horizontal orientation the flow pattern could probably be slug-plug even for high power inputs to the evaporator, i.e. high inertial forces on the fluid driven by damped oscillations of the vapour bubbles, thus resulting in a similar oscillatory behaviour in each FPPHP branch.

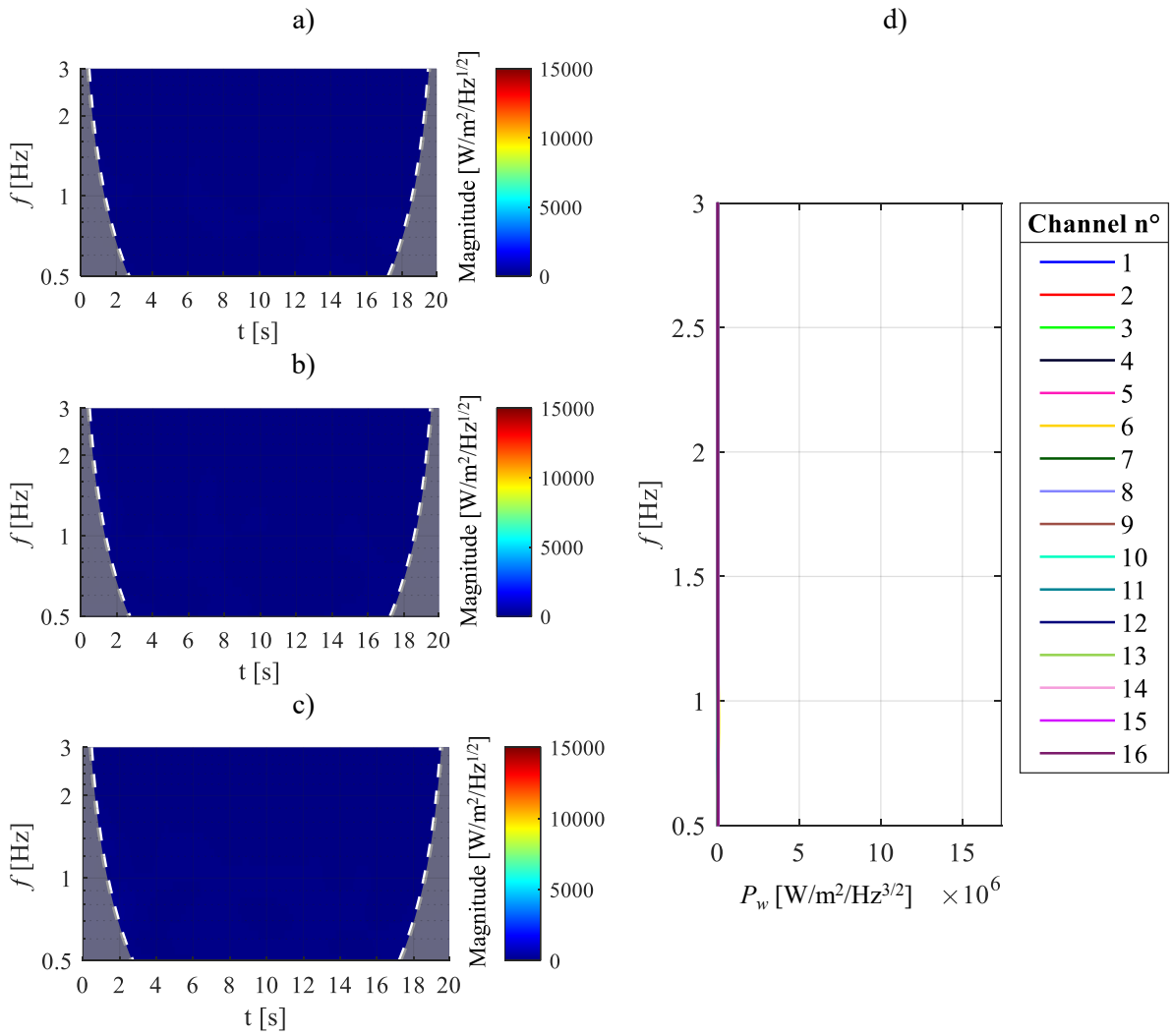

Figure 9.16: Scalograms for channels 4 (a), 8 (b) and 12 (c), and power spectra of the wall-to-fluid heat fluxes for the fixed axial coordinate z = 0.02 m over time related to each FPPHP channel in the horizontal orientation (d); Q = 50 W.

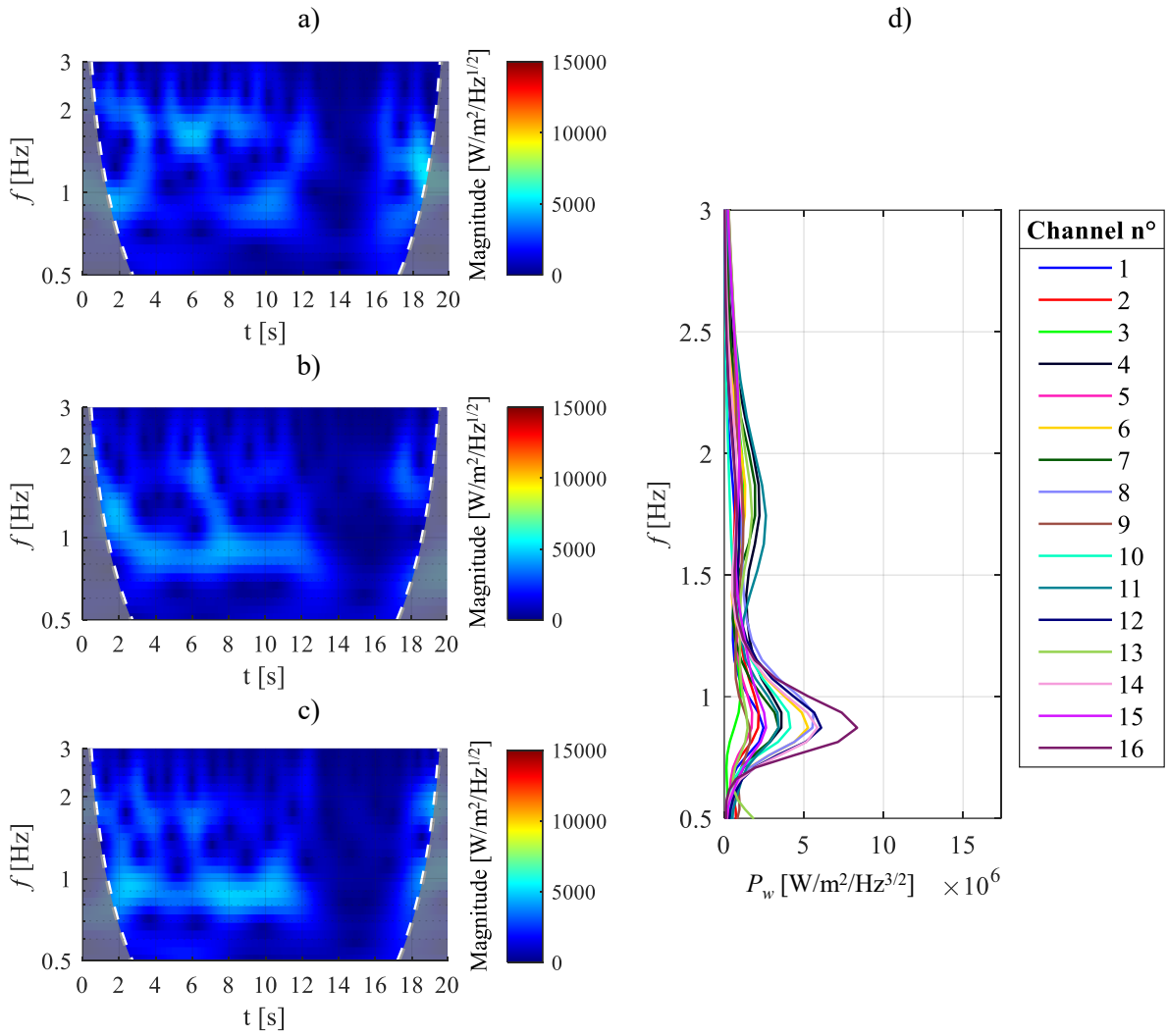

Figure 9.17: Scalograms for channels 4 (a), 8 (b) and 12 (c), and power spectra of the wall-to-fluid heat fluxes for the fixed axial coordinate z = 0.02 m over time related to each FPPHP channel in the horizontal orientation (d); Q = 150 W.

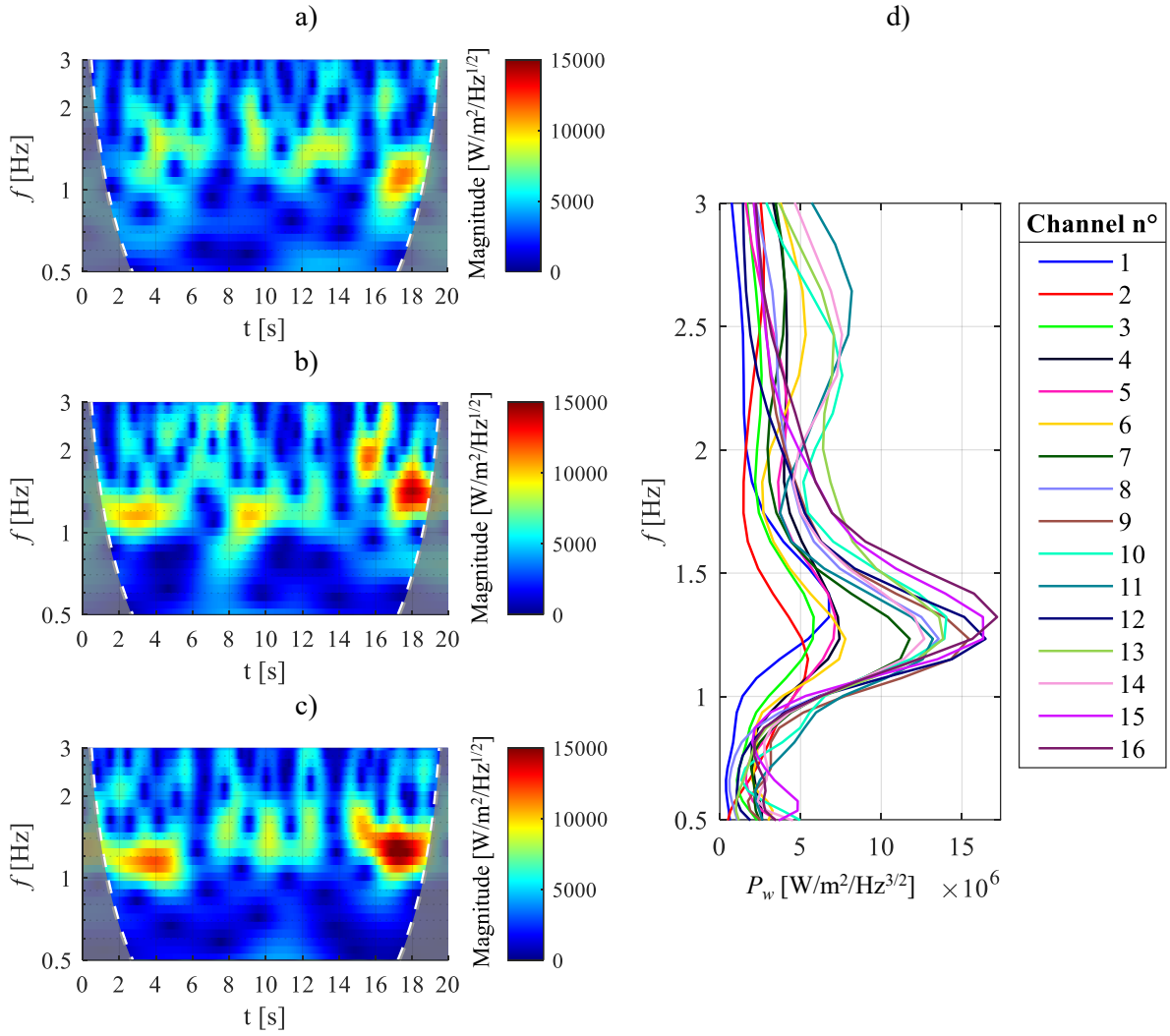

Figure 9.18: Scalograms for channels 4 (a), 8 (b) and 12 (c), and power spectra of the wall-to-fluid heat fluxes for the fixed axial coordinate z = 0.02 m over time related to each FPPHP channel in the horizontal orientation (d); Q = 250 W.

To clearly provide a quantitative description of the channel-wise oscillatory behaviour, all the evaluated dominant oscillation frequencies are listed in Table 9.4 and Table 9.5 for the vertical BHM and horizontal orientations, respectively.

Table 9.4: Dominant oscillation frequencies evaluated in the vertical BHM orientation for every channel at varying heat load. Dots stand for absence of dominant fluid oscillation.

f_d [Hz]	Q [W]						
Channel	*50*	*70*	*90*	*120*	*150*	*200*	*250*
1	-	-	0.81	1.15	1.07	1.32	1
2	1.15	-	0.81	0.58	1.23	1.07	0.66
3	1.63	0.66	0.66	0.71	1.23	0.71	0.93
4	1.23	1.23	0.66	1.42	0.87	1.42	1.15
5	1.63	0.58	1.15	0.93	1.15	0.71	1.15
6	1.52	1.63	0.87	0.93	0.87	1	0.81
7	-	1.42	1	0.81	0.87	1.23	1.63
8	-	1.07	0.93	0.81	0.93	0.87	1.52
9	-	1	1.42	0.58	0.71	0.54	0.81
10	-	1.74	0.62	0.54	1.07	0.54	1.23
11	-	1.16	1.42	0.66	0.61	1.15	0.76
12	-	1.23	1.42	0.62	0.87	1.32	0.62
13	-	-	0.71	0.66	0.66	0.76	1.15
14	-	-	0.93	0.71	0.66	0.93	0.62
15	0.87	-	1.15	0.81	0.87	1.23	0.87
16	0.93	0.66	1.15	0.62	0.54	1.07	1.23

Table 9.5: Dominant oscillation frequencies evaluated in the horizontal orientation for every channel at varying heat load. Dots stand for absence of dominant fluid oscillation.

f_d [Hz]	Q [W]				
Channel	*50*	*100*	*150*	*200*	*250*
1	-	0.66	0.87	1.07	1.32
2	-	0.66	0.93	1.07	1.15
3	-	0.62	1.87	1.07	1.32
4	-	0.71	0.93	1	1.23
5	-	0.71	0.93	1.07	1.32
6	-	1.42	0.87	1	1.23
7	-	1.42	0.87	1.07	1.23
8	-	1.42	0.93	1	1.23
9	-	0.87	0.81	1.07	1.23
10	-	0.76	0.87	1.07	1.32
11	-	0.66	0.87	1.07	1.23
12	-	0.76	0.87	1	1.23
13	-	0.71	1.74	1.07	1.23
14	-	0.71	0.87	1.07	1.23
15	-	0.66	0.87	1.07	1.32
16	-	0.66	0.93	1.07	1.15

In Table 9.4, at low heat loads to the evaporator, the vertical BHM orientation denotes several channels in which the fluid does not present any dominant oscillation within the observation window, thus suggesting that high intermittency of the overall device operation prevents an identification of dominant frequencies. At average-high heat loads, a dominant oscillation frequency can be perceived in every channel, confirming the transition from intermittent flow to full activation of the device. In the

horizontal orientation (Table 9.5), the intense intermittency of the fluid motion hampers a clear identification of a dominant frequency in the overall device at Q = 50 W, while every FPPHP branch denote fluid oscillations from 100 W up to the maximum provided power input, similarly confirming the transition between the two mentioned working regimes. The listed fluid oscillation frequencies agree with those typically found with direct fluid visualizations [145]. In addition, they confirm the working regimes identified in Paragraph 9.4.

The FPPHP oscillatory behaviour over time, which was qualitatively observed in scalograms, was assessed by investigating some of its features, such as continuity and channels activity. Specifically, the continuity t_c is here defined as persistency of fluid oscillations over time around the dominant frequency, i.e. in the range $B_f = f_d \pm 15\% f_d$. It can be conceptually expressed, for a given device channel, as:

$$t_c = \frac{Time\ during\ which\ fluid\ oscillates\ at\ a\ frequency\ close\ to\ the\ dominant\ one}{Total\ acquisition\ time} \tag{9.2}$$

Channels activity t_a is instead referred to presence of fluid oscillations:

$$t_a = \frac{Time\ during\ which\ fluid\ oscillations\ are\ perecevibale}{Total\ acquisition\ time} \tag{9.3}$$

Both properties are believed to complete the fluid oscillations description in terms of time evolution, providing a better quantification of the device heat transfer capabilities. The evaluation of continuity and activity is based on the time-wise determination of main oscillation frequencies, i.e. referred to the power peaks in scalograms. To obtain a reliable and robust identification of such peaks, the K-means clustering technique, described in Paragraph 6.2, was employed.

In Figure 9.19e-f, the time location of frequencies referred to scalogram peaks is shown over time, together with the dominant frequencies (solid lines) and B_f boundaries (dotted lines). As noticeable, time instants which do not present high-power peaks in the threated scalograms are not assigned to any frequencies (gaps in Figure 9.19e-f). In addition, time periods exceeding the COIs limits are not considered. When compared to the vertical BHM (Figure 9.19e), the signal referred to the horizontal orientation (Figure 9.19f) denotes longer periods of oscillation within B_f, suggesting greater continuity over time. In particular, the continuity time t_t, defined as the total time during which oscillations occur around the dominant frequency, was assessed equal to 2.14 s and 8.22 s for the vertical and horizontal orientations, respectively. This confirms the qualitative information provided by the observation of Figure 9.15 and Figure 9.18. On the other hand, the vertical BHM exhibits an overall longer activity since oscillations at given frequencies are present for more time within the observation window. The channel activity time was evaluated equal to 17.32 s and 12.76 for the vertical and horizontal orientations, respectively.

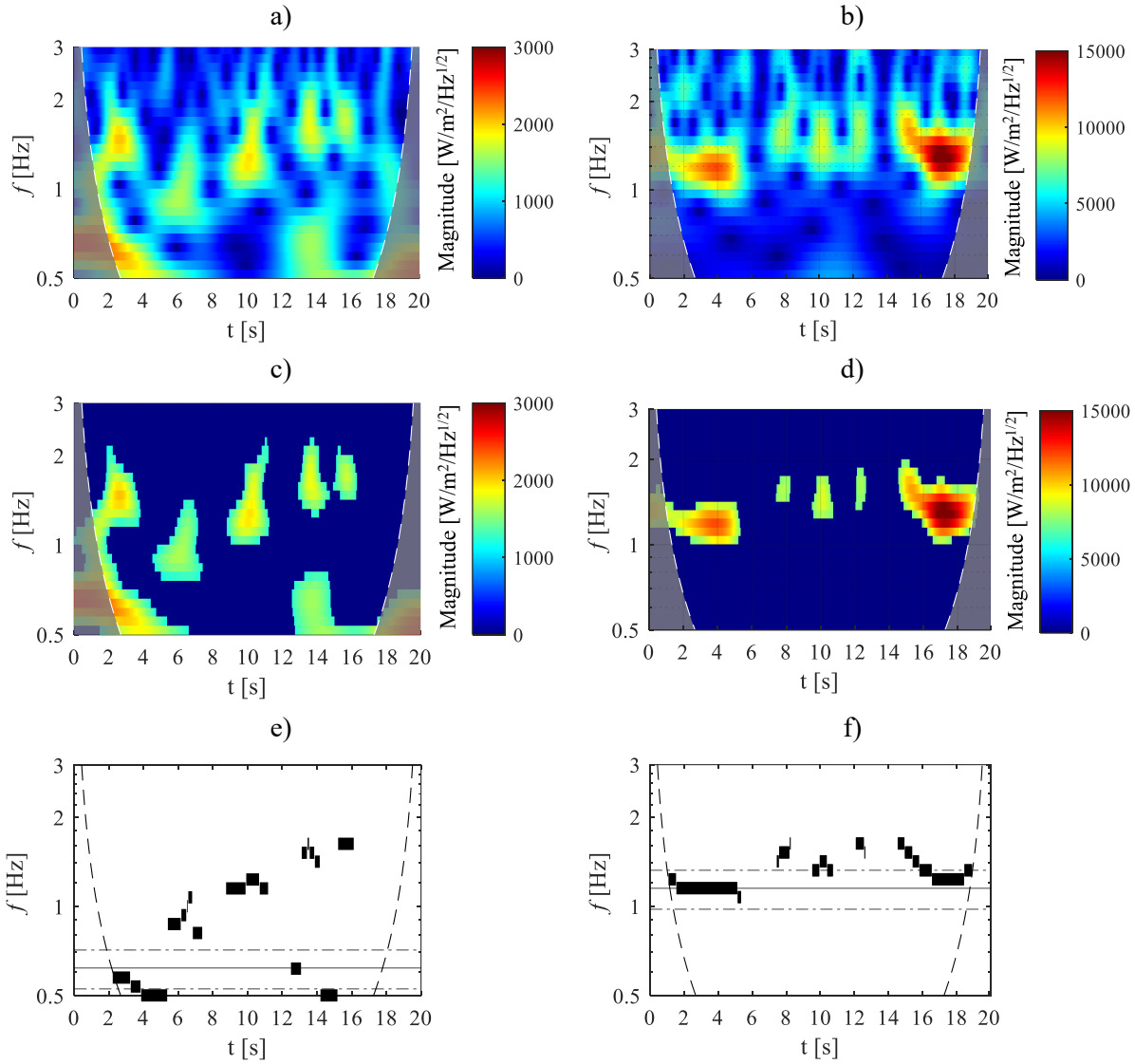

Figure 9.19: Scalograms referred to channel 12 for the vertical BHM (a) and horizontal orientation (b), Q = 250 W; denoised scalograms (c, d) and frequency identification over time (e, f).

The investigation on continuity of fluid oscillations and channels activity was extended to all FPPHP channels for average and high power inputs to the evaporator, namely Q = 150 W and Q = 250 W. Lower heat loads were not considered since either weak or absent fluid oscillations prevented a clear discernment of high-power peaks from low-power backgrounds in scalograms. In Table 9.6 and Table 9.7, t_c and t_a are listed for the mentioned study cases to present a channel-wise description of continuity and activity. For both heat loads in the vertical BHM (Table 9.6), the continuity generally assumes different values from channel to channel with respect to the horizontal orientation (Table 9.7), confirming that the fluid oscillatory motion is more scattered over a wider range of frequencies. For what concerns activity, the vertical BHM denotes more similar t_a values, especially at high heat load, underlining that the fluid oscillations are promoted in every channel by such orientation.

Table 9.6: Continuity and activity, evaluated for the vertical BHM.

Channel	***Q*** [W]			
	150		*250*	
	t_c [%]	t_a [%]	t_c [%]	t_a [%]
1	*17.7*	*52.1*	*28.6*	*89.9*
2	*14*	*88.9*	*30.5*	*91.65*
3	*27.1*	*88.1*	*35.6*	*73.7*
4	*24.2*	*80.1*	*43.4*	*89.9*
5	*5.7*	*47.1*	*31.9*	*79.9*
6	*34.3*	*73.9*	*13.3*	*90.1*
7	*9.6*	*65.1*	*52.9*	*85.7*
8	*11.6*	*87.2*	*25.1*	*93.8*
9	*13.5*	*74.4*	*28.8*	*92.7*
10	*5*	*49.7*	*32.4*	*99.7*
11	*69.5*	*100*	*15.5*	*94.8*
12	*30.2*	*81.8*	*10.7*	*86.6*
13	*36*	*58.4*	*8.7*	*80.5*
14	*46.1*	*80.3*	*21*	*99*
15	*12.5*	*54*	*31.4*	*94.1*
16	*13.2*	*46.8*	*27.8*	*84.7*

Table 9.7: Continuity and activity, evaluated for the horizontal orientation.

Channel	***Q*** [W]			
	150		*250*	
	t_c [%]	t_a [%]	t_c [%]	t_a [%]
1	*46*	*46*	*24.2*	*38.3*
2	*16.9*	*63.1*	*32.4*	*45.8*
3	*15.9*	*56*	*23.2*	*77.5*
4	*18.1*	*83.2*	*26.1*	*72.9*
5	*44.7*	*74.3*	*24.7*	*62.9*
6	*48.8*	*72.8*	*30.1*	*81.6*
7	*34.4*	*65.2*	*36.8*	*85.3*
8	*51.6*	*78.3*	*42.3*	*75.5*
9	*12.6*	*64.8*	*52.5*	*86.2*
10	*52.1*	*81.7*	*23.2*	*75.9*
11	*38.7*	*61*	*27.9*	*73.8*
12	*55.3*	*71.5*	*41.1*	*63.8*
13	*8.7*	*51.3*	*32.6*	*72.2*
14	*47.6*	*71.4*	*30.1*	*86.8*
15	*54.1*	*79.9*	*52.9*	*71.4*
16	*46.6*	*73.4*	*37.6*	*63.8*

Both continuity and activity values were therefore averaged over the entire device, i.e. for all channels, resulting in $t_{c,av}$ and $t_{a,av}$, respectively. In Figure 9.20, $t_{c,av}$ is shown for both considered heat loads and device orientations. The vertical BHM exhibits lower values of $t_{c,av}$ (around 4.5 s and 5.6 s), confirming the greater continuity of oscillations in the horizontal orientation, where $t_{c,av}$ is equal to about 7.5 s and 6.8 s for average and high heat load, respectively. Although, a certain decrease in average

continuity time with the increasing of heat load is perceivable, denoting a reduction in fluid oscillations around the dominant frequency probably due to the onset of higher inertial forces, i.e. less stable oscillatory behaviour [145]. $t_{a,av}$ is instead shown in Figure 9.21 for the same test conditions. Here, the vertical BHM presents generally greater channels activity with respect to the horizontal orientation since the gravity-assisted mode promotes the fluid motion in the overall device without significant stopovers. Also, for such orientation, the activity time increases with the power input, while the horizontal mode presents similar activity times. This remark suggests that, above a certain heat load, channels activity saturates in the horizontal orientation probably due to absence of significant buoyancy forces.

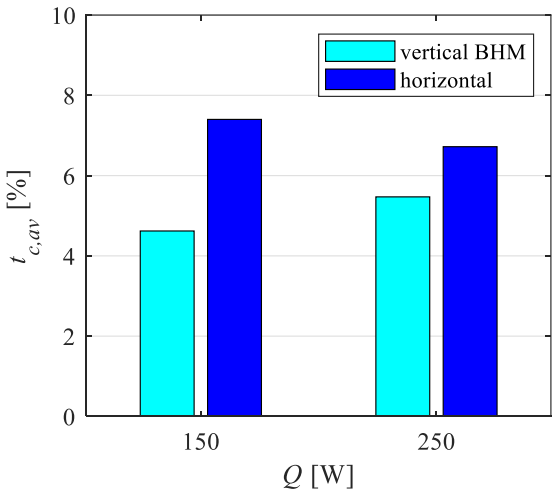

Figure 9.20: Mean continuity time for average and high heat loads and the two considered orientations.

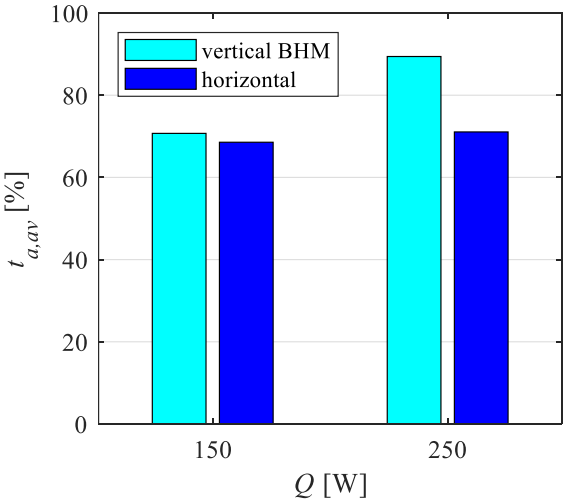

Figure 9.21: Average activity time of channels as percentage of the observation window length.

Higher activity times of the vertical BHM furthermore confirm the better thermal performance assessed in Paragraph 9.4 for such orientation.

After providing a quantification of the main properties defining the oscillatory behaviour in the studied device, the evaluated channel-wise dominant frequencies were statistically reduced for a complete description of fluid oscillations. To this aim, the arithmetic mean ($f_{d,av}$) and the standard deviation ($f_{d,std}$) of f_d were computed by considering every FPPHP channel. In Figure 9.22, $f_{d,av}$ and $f_{d,std}$ are shown for the only power inputs to the evaporator in which f_d could be evaluated in the every channel of the device, i.e. during its full activation. Here, the average dominant oscillation frequency (Figure 9.22a) exhibits a general increasing trend, in accordance with other studies also concerning tubular layouts [11,148,149]. For the vertical BHM orientation, $f_{d,av}$ ranges from about 0.78 Hz to 1 Hz, while the horizontal orientation highlights values of $f_{d,av}$ that increase from a minimum of about 0.84 Hz to a maximum of 1.25 Hz, confirming the typical fluid oscillation frequencies found in the literature [48]. It has to be observed that, while $f_{d,av}$ denotes a linear increment with the power input to the evaporator in the horizontal orientation, it seems to approach an asymptotic value with the increasing of Q in the vertical BHM. This suggest that the semi-annular or annular flow, promoted by the gravity effects on the device at high heat loads, results in different oscillatory behaviour with respect to that in the horizontal orientation (where a slug-plug flow is more likely to occur), probably due to significantly different phase-change phenomena. Also, the standard deviation of f_d (Figure 9.22b) highlights a different behaviour in terms of oscillations from channel to channel in the vertical BHM orientation, which persists even during the full activation of the device. For the horizontal orientation, $f_{d,std}$ seems to decrease instead with the increasing of the power input, suggesting that, during the full activation, every channel approaches the same oscillatory behaviour.

a)

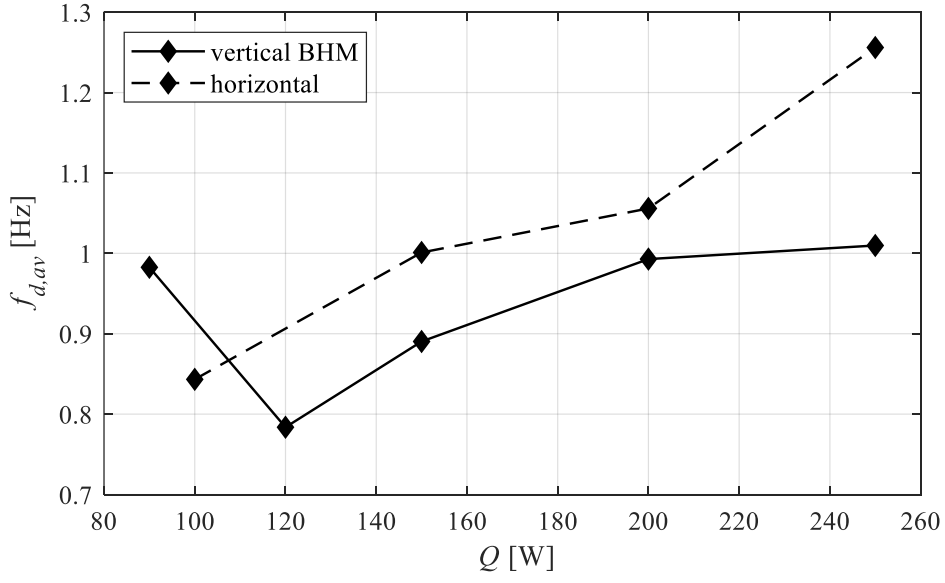

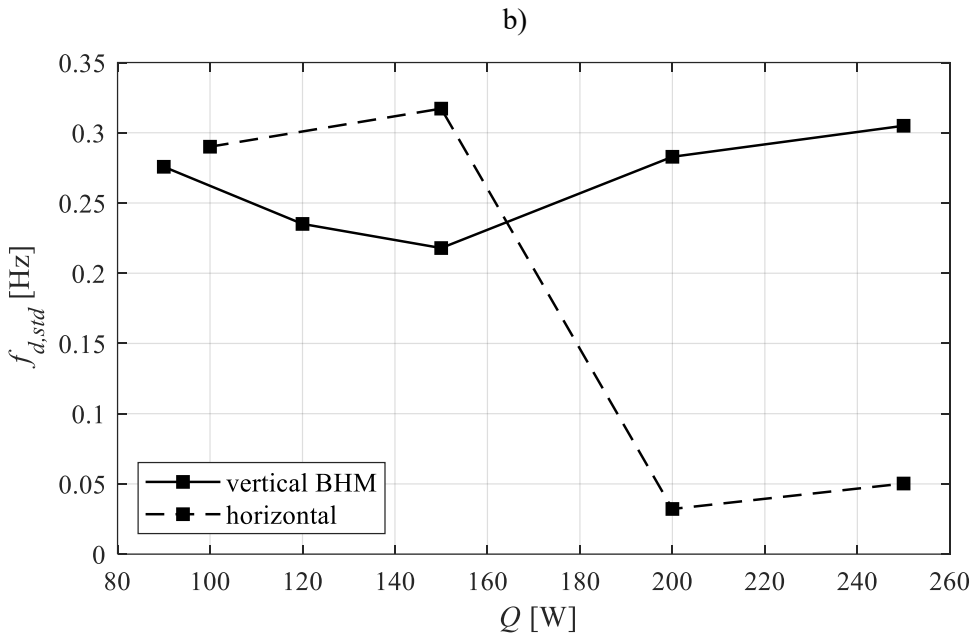

Figure 9.22: Average dominant fluid oscillation frequency in the overall device (a) and channel-wise standard deviation (b) for the two considered FPPHP orientations.

9.5.3. Link between fluid oscillations and transverse interactions

A comprehensive analysis on the local heat transfer quantities evaluated in the previous paragraphs was adopted to attempt a description of conduction between adjacent channels in FPPHPs for the description of transverse interaction in the present layout. To this aim, the temperature distributions acquired by means of thermography and properly regularised as thoroughly explained in Section 5.3 were adopted to provide an estimation of the heat flux exchanged between the *n*-th and (*n+1*)-th channels by conduction $q_{Fou,n\rightarrow n+1}$, according to the Fourier's law:

$$q_{Fou,n\rightarrow n+1}(z,t) = -k\frac{\partial T(y,z,t)}{\partial y} \tag{9.4}$$

In particular, the partial derivative of *T* is evaluated in the median point between adjacent channels for every axial coordinate *z* as a function of time. The values averagely assumed by q_{Fou} over time were therefore adopted to estimate the power transferred by transverse conduction $Q_{tr_{cond}}$ between every adjacent channels pair in the overall device along the adiabatic section (green area in Figure 9.2) as follows:

$$Q_{tr_{cond}} = \frac{\sum_{n=1}^{num-1}\{|\sum_{z=0}^{L_{adiab}} mean[q_{Fou,n\rightarrow n+1}(z,t = 1 \dots N)]\cdot\Delta z\cdot T_{FPPHP}|\}}{num-1} \tag{9.5}$$

where *num* is the total number of FPPHP channels, $mean$ is the arithmetic mean operator, N is the total number of time samples, L_{adiab} is the length of the adiabatic section framed by the IR camera, Δz is the distance between two consecutive pixels in the z direction of the thermographic data, and T_{FPPHP} is the device thickness. Finally, $Q_{tr_{cond}}$ was normalized with respect to the net power input to the evaporator divided by the number of FPPHP channels, resulting in $Q_{ratio} = Q_{tr_{cond}}/(\frac{Q}{num})$. Specifically, Q_{ratio} defines the percentage of transverse conduction with respect to the power potentially transferrable by a single FPPHP branch from the evaporator to the condenser. In Figure 9.23, Q_{ratio} is shown as a function of Q for both considered device orientations. For the vertical BHM, the effects of transverse conduction become more and more negligible as the power input to the evaporator increases. For the horizontal orientation, Q_{ratio} is almost equal to 15% at high power inputs, denoting instead strong conductive effects between adjacent channels in agreement with other literature findings [145].

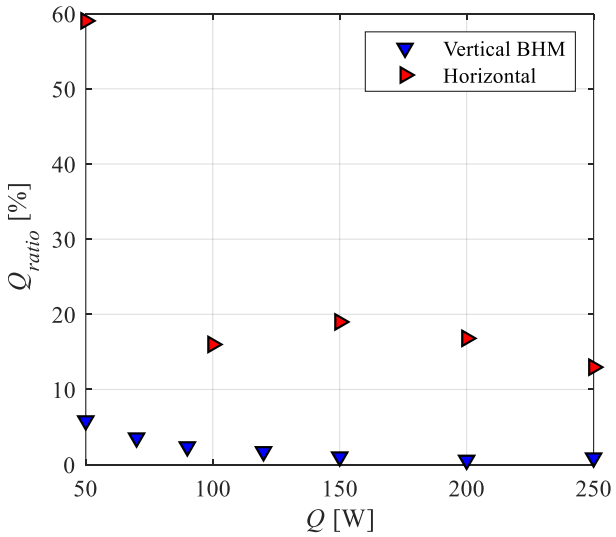

Figure 9.23: Q_{ratio} as a function of the power input to the evaporator for both considered device orientations.

The highlighted variation in terms of transverse conduction from vertical BHM to horizontal orientation may be due to different oscillatory and local heat transfer behaviour of the FPPHP, which is strictly linked to wall-to-fluid heat transfer interactions. To investigate the interplay between local wall-to-fluid heat flux and transverse conduction, q exchanged in two branches, i.e. channel 7 and 8, was compared with the corresponding heat flux $q_{Fou,7\rightarrow8}$ (z = 0.02 m) in terms of oscillation frequency. In Figure 9.24a, all the mentioned heat fluxes related to the vertical BHM are shown for Q = 200 W. In Figure 9.24b, the power spectra resulting from the wavelet method of Paragraph 9.5.2 are instead provided, highlighting no dominant frequency referred to the $q_{Fou,7\rightarrow8}$ signal. The scalograms referred

to the analysed signals were not considered since the only power spectra were believed to be more accurate in underlying differences or similarities between the compared, overall oscillatory behaviours. A similar comparison was carried out in Figure 9.25 for the horizontal orientation, where all considered signals exhibit same dominant frequency. In fact, in such orientation, the fluid similarly oscillates in both FPPHP branches and the regular slug-plug motion results in stronger transverse conduction between adjacent channels. This negative effect is furthermore enhanced by greater amplitudes of q during the horizontal operation, which lead to higher wall temperature variations within the adiabatic section. On the contrary, in the vertical BHM, the greater chaoticity of the fluid motion and different flow pattern, coupled with low-amplitude values of q, seem to prevent the channels from thermally interacting with each other, leading to weaker transverse conduction. The provided analysis adds a further reference for the interpretation of transverse conduction with respect to previous studies [49,146,150]. In fact, such a negative effect on the device thermal performance was here not only linked either to the thermal properties and geometry of the material or the overall fluid oscillation frequency, but also to the similarities in terms of oscillatory behaviour between adjacent channels.

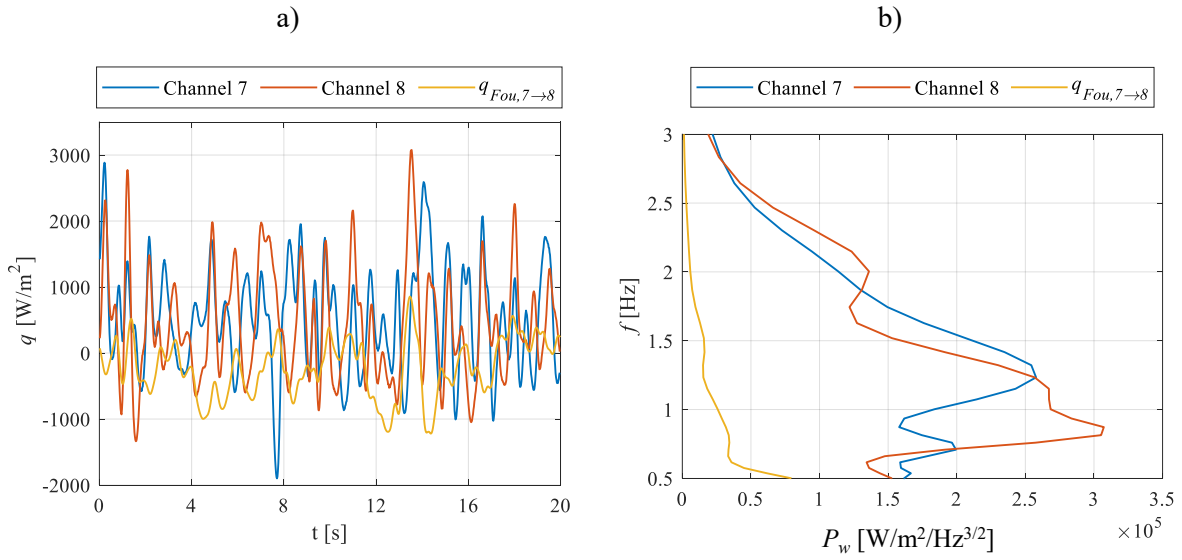

Figure 9.24: Wall-to-fluid heat fluxes referred to channel 7 and 8, heat flux by transverse conduction $q_{Fou,7\to8}$ (a) and corresponding power spectra (b) for the vertical BHM at Q = 200 W and z = 0.02 m.

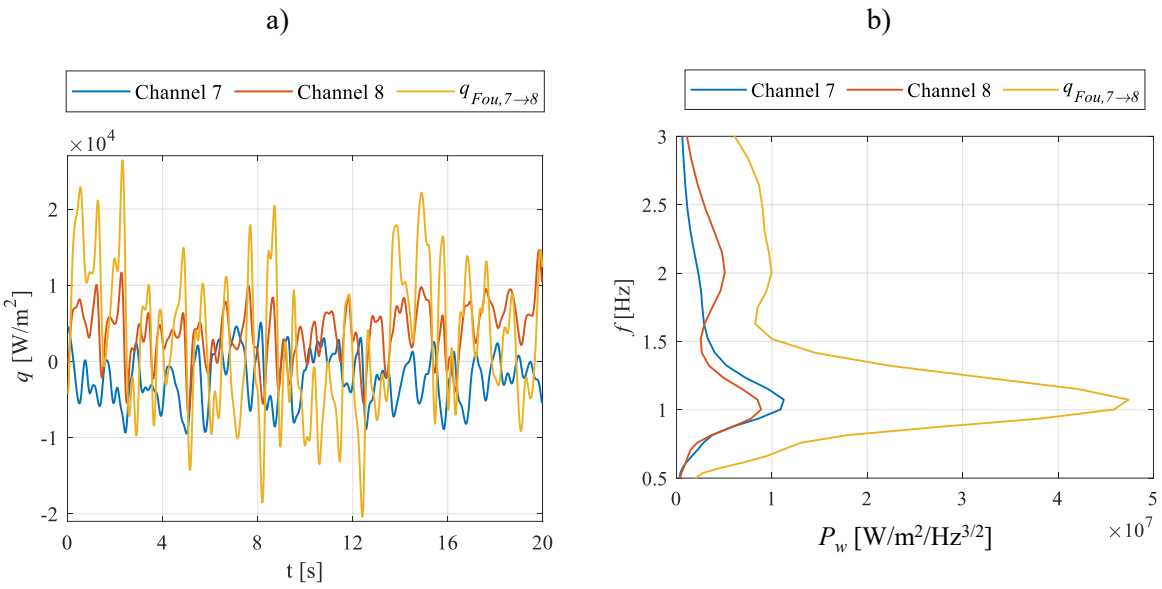

Figure 9.25: Wall-to-fluid heat fluxes referred to channel 7 and 8, heat flux by transverse conduction $q_{Fou,7\to8}$ (a) and corresponding power spectra (b) for the horizontal orientation at Q = 200 W and z = 0.02 m.

9.6 Closure

A metallic FPPHP having a total of 16 channels (8 turns in the evaporator zone) was experimentally studied in vertical BHM and horizontal orientation to assess its local thermal behaviour at heat loads ranging from 50 up to 250 W. The adopted operating fluid was a water-ethanol mixture, with volumetric filling ratio of 50%. The evaporator/condenser temperature was monitored by thermocouples, thus allowing the device characterization by evaluating its equivalent thermal resistance. The external wall temperature referred to the adiabatic zone was acquired by means of an IR camera. The resulting time-space temperature maps, effectively pre-processed by a three-dimensional Gaussian filtered, were used as inputs for the IHCP resolution approach for the evaluation of the heat flux exchanged between the working fluid and the thin walls of the device. The method was validated by adopting synthetic data. The wall-to-fluid heat fluxes were first statistically reduced to quantify, by means of two dedicated coefficients, i.e. cvt and cvs, their time and space variations from channel to channel. The analysis of these coefficients supplied a quantitative tool for the identification and description of the device working regimes. In addition, statistical heat flux amplitudes q80 were presented to achieve a comprehensive overview of the local wall-to-fluid thermal interactions. In general, as expected, the wall-to-fluid heat flux distributions exhibit a significant variation over both time and space in every channel.

The most meaningful and quantitative results of the current study are summarized as follows:

- In the intermittent flow (Q < 100 W), cvt_{av} and cvt_{std} assume values up to around 75% and 30% for both orientations, respectively, denoting a generally discontinuous FPPHP operation. On the contrary, the two coefficients stabilize at about 70% and 8% during the device full activation (Q > 100 W), thus denoting comparable fluid oscillatory behaviours at high heat loads, which result in similar device global performances;
- cvs_{av} decreases for both orientations within the intermittent flow to settle around 43% and 50%, respectively, during the full activation, suggesting that the wall-to-fluid interactions are more uniformly distributed along the device axis with the onset of stable and full fluid oscillations;
- q_{80} reaches a maximum of 7100 W/m^2 in the horizontal orientation at Q = 250 W, while it increases up to 2200 W/m^2 in the vertical BHM.

In conclusion, the presented non-intrusive approach, coupled with a statistical reduction of the available data, has been proven to provide quantitative pieces of information regarding the wall-to-fluid thermal interactions and heat transfer modes of FPPHPs. To notice, the identification of the two-phase flow regimes can be carried out without the need of a transparent insert, a transparent plate or a multilayer sheet for IR analysis, but even from thermographic maps acquired on a metallic, opaque geometry.

Chapter 10 IR analysis on a flexible PHP and a thin LHP

10.1 Introduction

In the present Chapter, the preliminary results of experimental studies on a flexible PHP and a LHP are described. Specifically, assessing the local thermal behaviour of flexible layouts may lead to a better comprehension of their heat transfer modes. In such devices, heat transfer through the walls is suppressed by the poor conductivity of the materials (mainly polymeric), leading to lower thermal performances with respect to metallic PHPs. A relevant part of the overall heat transfer is thus guaranteed by inner fluid convection, making the evaluation of wall-to-fluid heat fluxes of crucial importance. The LHP analysis provides instead a significant reference case for clearly understanding the countless potentialities of the IHCP resolution approach in terms of passive two-phase heat transfer devices investigations, which could go largely beyond the PHP field.

10.2 Fluid temperature measurements and local heat transfer analysis in polymeric pulsating heat pipes

Polymeric PHPs belong to the class of flexible PHPs. The high degree of foldability of such devices, coupled with their low weight, represents an interesting feature from the applicative standpoint. In the present Paragraph, the conceptualization and preliminary data regarding the thermographic investigation of a polymeric PHP are presented. The given insight will be of interest for the post-processing of available data and future experimentations.

The thermodynamic study on the device focuses on the achievement of two main goals:

- Accurate fluid temperature measurements;
- Wall-to-fluid heat fluxes evaluation.

10.2.1. Device specifics

The studied device, whose appearance and cooling/heating sections are shown for a similar layout in Figure 10.1a, is a 6-turn PHP made of polypropylene and having 3 x 0.7 mm rectangular channels. In particular, polypropylene is chosen for fabrication to guarantee high degree of foldability (Figure 10.1b).

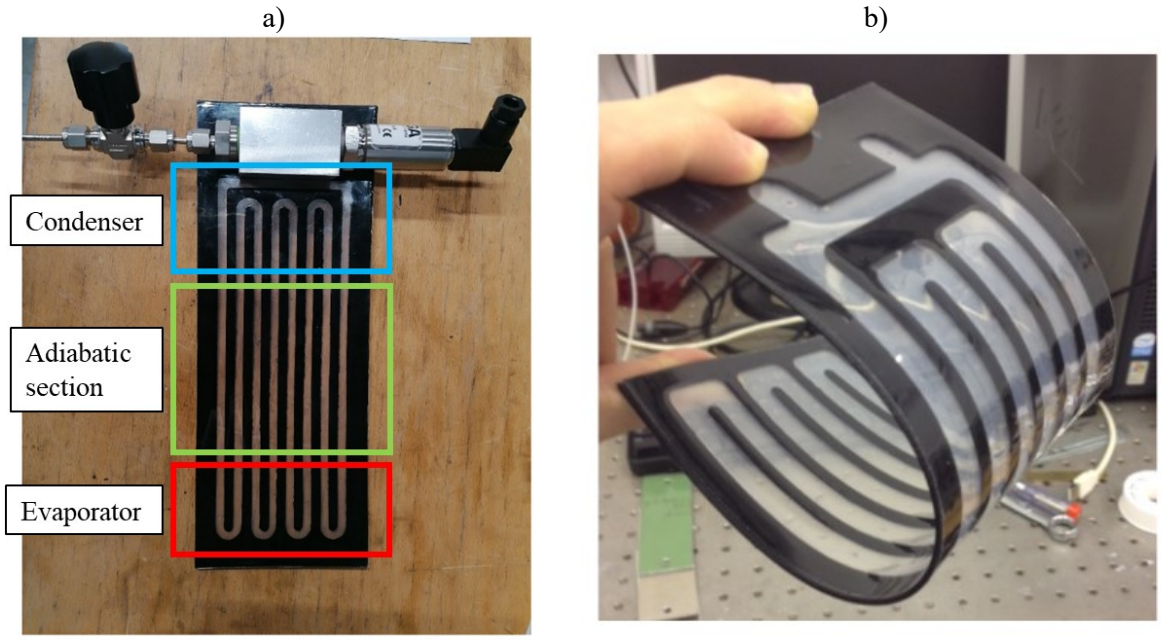

Figure 10.1: Appearance of the studied device (a) and its potential foldability (b).

The serpentine channel is cut-out in a black sheet (0.7 mm thickness) using a commercial laser cutter (HPC® Laser LS1290 Pro). Then, the channel is sandwiched between two transparent sheets (0.4 mm thickness each), which were tightly bonded to the black sheet by selective transmission laser welding using a nanosecond pulsed fibre (SPI® Lasers G4 HS-L 20 W). A micro-metering valve, which is connected to a T-junction directly glued on top of the device in correspondence of a hole machined in one of its channels, is used for the filling/vacuuming procedure. For further details on the experimental apparatus and manufacturing processes, see [112].

A calibrated IR camera (AIM® TEC-MMG from ESA/ESTEC, 1280x1024 pixels) is used to monitor the adiabatic section of the device. Before the preliminary tests, the PHP was filled with pure ethanol (FR = 50% vol.), previously degassed by means of iteratively warming/cooling under vacuum conditions.

10.2.2. Fluid temperature measurements: estimation of the radiative properties

For the fluid temperature measurements by means of thermography, the following radiative properties of the system needed to be estimated since practically unknown for the given application (i.e., for the PHP walls and fluid thicknesses):

- Transmissivity and emissivity of the polypropylene walls;
- Emissivity and transmissivity of ethanol (liquid phase), when confined inside the device channels.

Specifically, to achieve a good characterization of the PHP radiative behaviour in the IR spectrum, the effects of the background and of the emissive elements constituting the PHP, such as the polypropylene walls and the working fluid, must be separately taken into consideration. Hence, the background emissivity and temperature must be known, together with the temperature of the emissive elements.

To this aim, a copper heat exchanger, whose surface was coated with a high-emissivity paint (ε = 0.92), and whose temperature was controlled by a thermal bath, was placed behind the device. The set-up was therefore introduced inside a thermostatic chamber (accuracy = ± 1°C), as shown in Figure 10.2; this guaranteed that, at steady-state conditions, the temperature of all the emissive elements but the background was equal to the set-point temperature of the chamber.

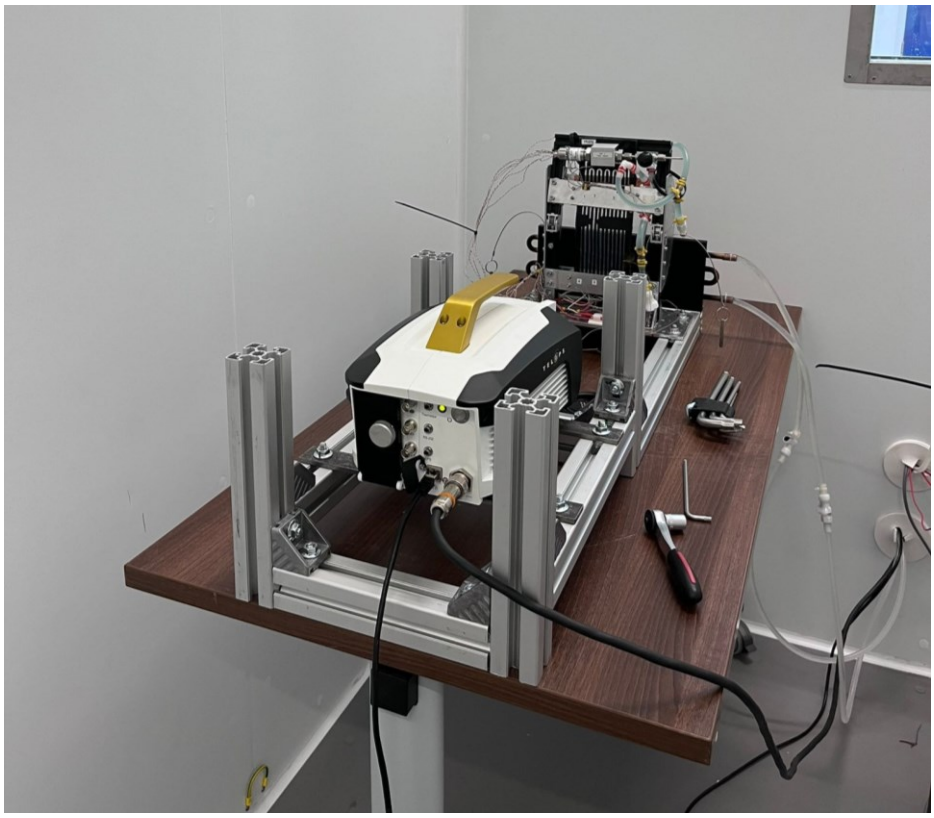

Figure 10.2: Test bench, located inside the thermostatic chamber.

The PHP was tested without triggering its activation by means of any heat load at the evaporator, and IR acquisitions were performed when thermal equilibrium with the chamber environment was reached. In Table 10.1, the pairs of background and thermal chamber temperature set-points imposed over a total of 7 different tests are listed.

Table 10.1: Temperature set-points imposed during the tests.

Test number	Background temperature set-point [°C]	Thermal chamber temperature set-point [°C]
1	55	20
2	19	25
3	21	25
4	18	30
5	22	30
6	19	35
7	22	35

Two T-type thermocouples were placed on the background surface and on the PHP wall, respectively, to assess the accuracy of the given set-point temperatures.

The adopted radiation model is described by the energy flow diagram of Figure 10.3. Specifically, the IR radiation acquired by the IR camera sensors Q_{IR} is a combination of radiations emitted by the background Q_{BG}, the PHP walls Q_w' and Q_w'', and the working fluid Q_f, net of losses through the device elements (walls and fluid) due to their non-unitary transmissivity in the IR spectrum.

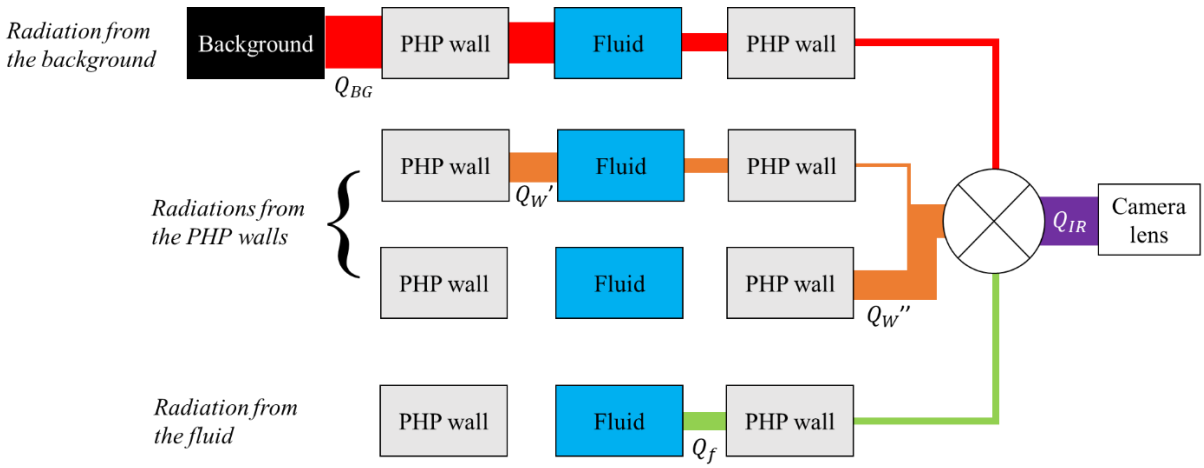

Figure 10.3: Radiation model.

Such a radiation model can be formalized by Equation (10.1), where the subscript *net* stands for net IR radiation reaching the camera lens.

$$Q_{IR} = Q_{BG,net} + (Q_{w,net}{}' + Q_w{}'') + Q_{f,net} \tag{10.1}$$

By furtherly considering the temperature and radiative properties of each emissive element, Equation (10.1) reads as:

$$\sigma\varepsilon_{cam}T_{cam}^4 = \sigma\varepsilon_{BG}\tau_{PHP}\tau_f T_{BG}^4 + \left[\left(1+\tau_{PHP}^{1/2}\right)\tau_f\right]\varepsilon_w T_w^4 + \varepsilon_f\tau_{PHP}^{1/2}T_f^4 \tag{10.2}$$

where σ is the Stefan-Boltzmann constant, ε_{cam} is the emissivity set within the camera parameters (= 1), T_{cam} is the temperature estimated by the camera software, ε_{BG} is the emissivity of the background, τ_{PHP} is the transmissivity of both PHP walls ($\tau_{PHP}^{1/2}$ for the single wall), T_{BG} is the background temperature, τ_f is the transmissivity of the fluid, ε_w is the emissivity of the single PHP wall, T_w is the wall temperature, and ε_f is the fluid emissivity.

The first step of the estimation procedure consisted in evaluating the radiative properties of the PHP walls. It has to be pointed out that, since the device was not fully filled with the working fluid, the liquid phase tended to stratify due to gravity and vibrations at the bottom of the channels, as noticeable from the IR sample of Figure 10.4.

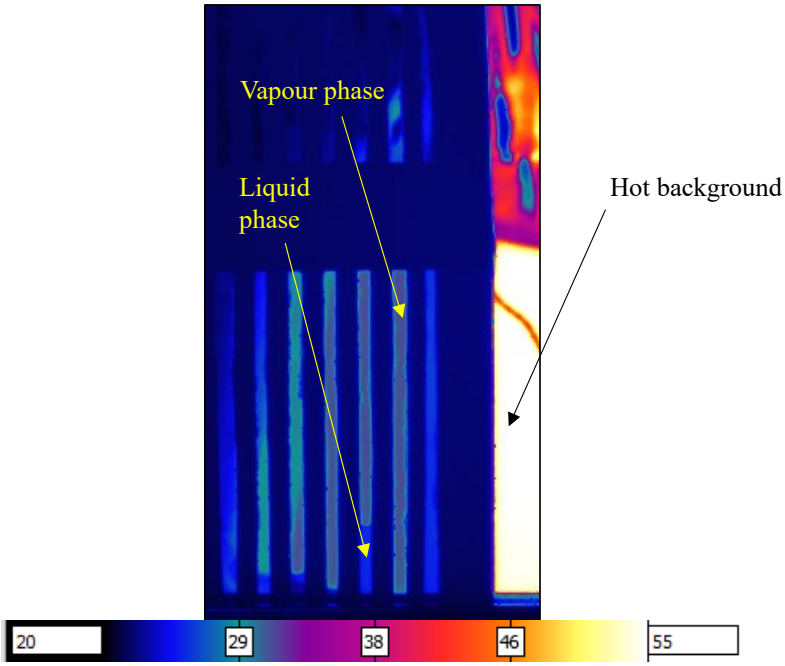

Figure 10.4: IR acquisition sample for the PHP walls transmissivity evaluation; PHP at 20°C, hot background at 55°C.

Hence, by considering the only spots in which the branches were filled with vapour, Equation (10.2) reduces to:

$$\sigma\varepsilon_{cam}T_{cam}^4 = \sigma\varepsilon_{BG}\tau_{PHP}T_{BG}^4 + \left(1+\tau_{PHP}^{1/2}\right)\varepsilon_w T_w^4 \tag{10.3}$$

In fact, the vapour transmissivity was assumed equal to 1, leading to the further assumption of null emissivity. τ_{PHP} and ε_w therefore resulted from the resolution of the following minimization problem, by inputting every temperature combination obtained during the tests:

$$\min_{\substack{\tau_{PHP}\in R^+\\ \varepsilon_{PHP}\in R^+}} \left[\sigma\varepsilon_{cam}T_{cam}^4 - \sigma\varepsilon_{BG}\tau_{PHP}T_{BG}^4 - \left(1+\tau_{PHP}^{1/2}\right)\varepsilon_{PHP}T_w^4\right] \quad ; \quad \begin{matrix}\tau_{PHP}<1\\ \varepsilon_{PHP}<1\end{matrix} \tag{10.4}$$

The fluid radiative properties were instead evaluated by considering areas containing both vapour and liquid phases. To discern the two phases, a coefficient *c* was introduced in (10.1):

$$\sigma\varepsilon_{cam}T_{cam}^4 = \sigma\varepsilon_{BG}\tau_{PHP}\tau_f^c T_{BG}^4 + \left[\left(1+\tau_{PHP}^{1/2}\right)\tau_f^c\right]\varepsilon_w T_w^4 + c\varepsilon_f\tau_{PHP}^{1/2}T_f^4 \tag{10.5}$$

Such a coefficient was set to 0 when the vapour phase was observed, and to 1 when the liquid phase was instead investigated. Hence, by adopting τ_{PHP} and ε_w, estimated by means of Equation (10.4), τ_f (liquid phase) and ε_f were assessed through the resolution of a second minimization problem:

$$\min_{\substack{\tau_f\in R^+\\ \varepsilon_f\in R^+}} \left[\sigma\varepsilon_{cam}T_{cam}^4 - \sigma\varepsilon_{BG}\tau_{PHP}\tau_f^c T_{BG}^4 - \left[\left(1+\tau_{PHP}^{1/2}\right)\tau_f^c\right]\varepsilon_w T_w^4 - c\varepsilon_f\tau_{PHP}^{1/2}T_f^4\right] \quad ; \quad \begin{matrix}\tau_f<1\\ \varepsilon_f<1\end{matrix} \tag{10.6}$$

All the estimated radiative properties are shown in Figure 10.5, along with the 95% confidence intervals. The values are in good agreement with [106], for what concerns the ethanol emissivity, and with [151], regarding the polypropylene wall transmissivity.

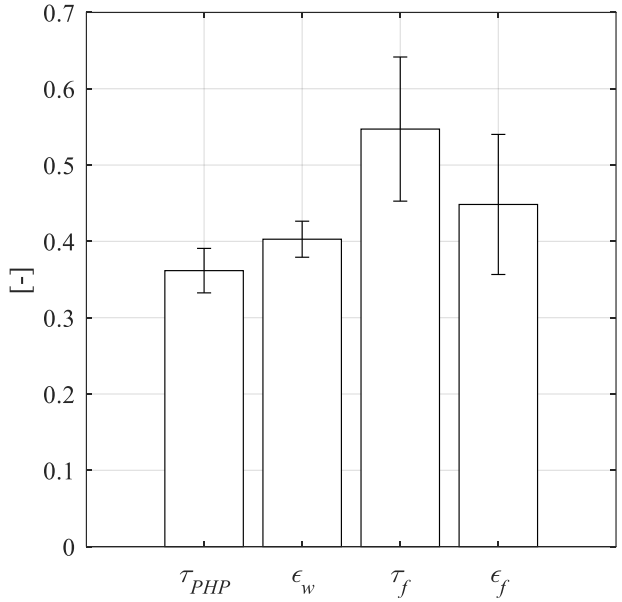

Figure 10.5: Evaluated radiative thermal properties of the PHP elements.

The estimation of the radiative properties of the system will be used, in future studies, for the evaluation of the fluid temperature during its operation in microgravity and standard-gravity conditions.

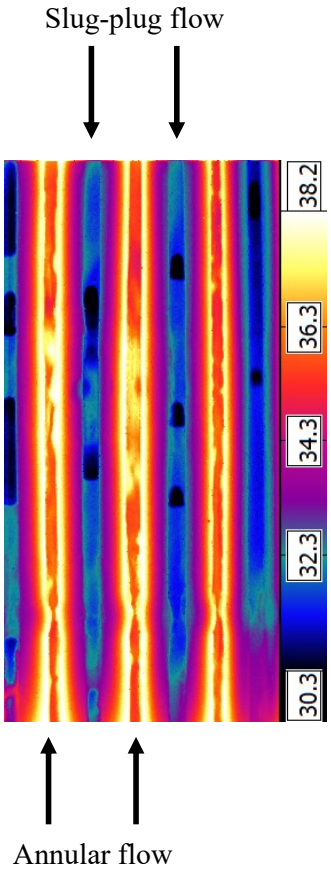

Figure 10.6: IR sample (microgravity experiment, heat load equal to 30 W).

Regarding the former working condition, thermographic data are already available and acquired during the 77th parabolic flight campaign promoted by the European Space Agency. An IR acquisition sample is shown in Figure 10.6, for heat load to the evaporator equal to about 30 W. Coupled with acquisitions in the visible spectrum, the estimation of the fluid temperature is believed to provide a better insight into the thermofluidic behaviour of the system, thus setting the basis for thorough explanations about the observed flow patterns (slug-plug and annular flows).

10.2.3. Local wall-to-fluid heat flux evaluation: feasibility

For the present device, the last point to be accounted for is the feasibility of a local heat transfer investigation. Such a feasibility study can be performed by ensuring that the outer wall temperature exhibits a perceivable variation in temperature due to inner convection in the device. To this aim, part of the outer wall surface in the adiabatic section was coated with a highly emissive paint to perform direct outer wall temperature measurements by means of thermography. Moreover, for the sake of this preliminary investigation, the device properly operated by applying a heat load to the evaporator. In Figure 10.8, the coated portion is shown.

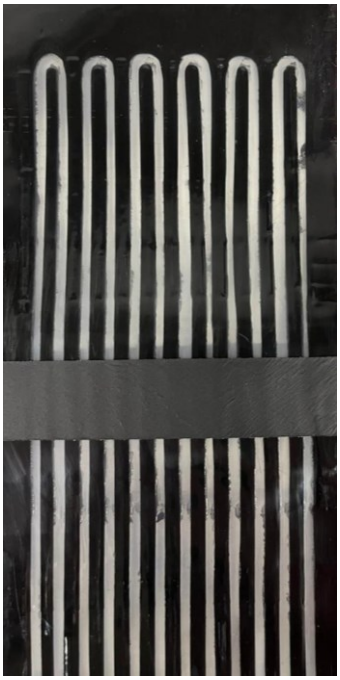

Figure 10.7: Part coated within the adiabatic section for IR acquisitions of the outer wall temperature.

Figure 10.8a reports instead an IR sample, acquired during the device operation (the coated portion is here visible as a horizontal, high-temperature stripe), with reference to the considered measurement location (green point) and corresponding temperature profile (Figure 10.8b). As noticeable, the outer wall temperature of the analysed channel undergoes significant variations due to fluid oscillations in

the device. Such a remark suggests that the conductive properties of the device walls provide, in transient conditions, a meaningful insight into the thermofluidic interactions occurring at the wall-fluid interface, at least when thin walls are taken into account. Considering these preliminary results, the present device is suitable for a future, more complete investigation of its local heat transfer behaviour through the evaluation of wall-to-fluid heat fluxes, possibly achievable by the IHCP resolution approach.

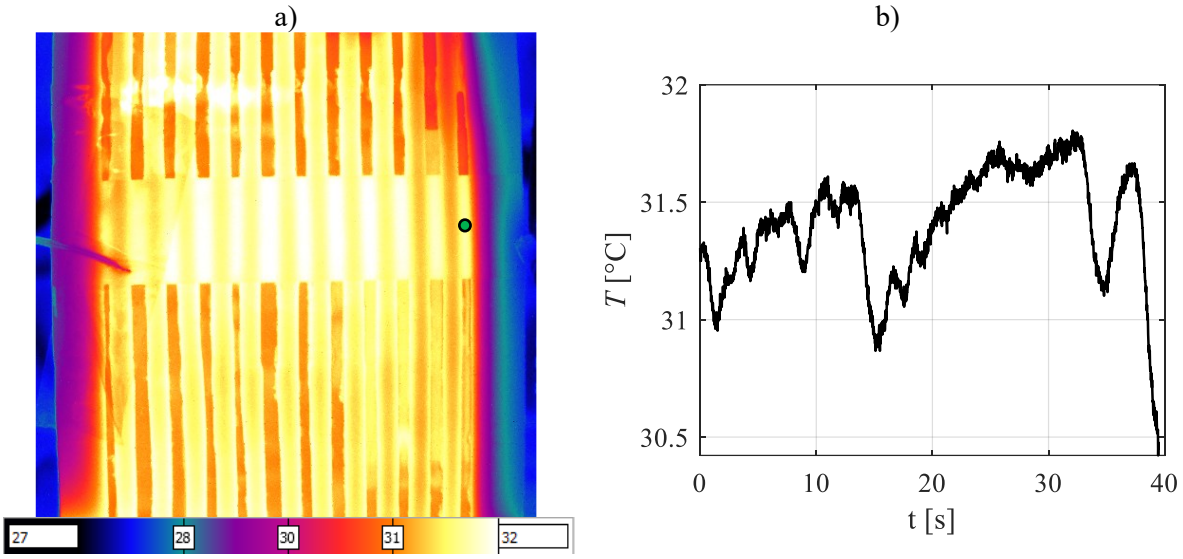

Figure 10.8: Sample of IR acquisition (a) and temperature profile on the outer wall surface of a PHP channel (b); the temperature profile is referred to the green point of picture (a).

10.3 Local heat transfer investigation on the loop heat pipes start-up

The present Paragraph deals with the preliminary results of the experimental campaign carried out on a thin LHP. The physics underling the LHPs operation is greatly different from the one governing PHPs: the local heat transfer behaviour of such devices is thus not comparable with the ones observed during the previously reported experimental campaigns. However, the present investigation opens to a wide range of new applications, with the main aim of providing quantitative results for the validation of existing numerical models.

10.3.1. Test rig

The studied device (Figure 10.9) is a diffusion bonded LHP made of copper with overall dimensions of 76 x 60 x 1.6 mm. Both the vapor and liquid lines have a cross-section of 3 x 1 mm^2. Two sintered copper powder wicks, one in the evaporator and one in the liquid line, provide the needed capillary pressure to promote the working fluid flow inside the LHP. Both porous media have a porosity of 53.46

± 3.87% and 1 mm of thickness. For more details about the LHP manufacturing process and wick structure, see [152].

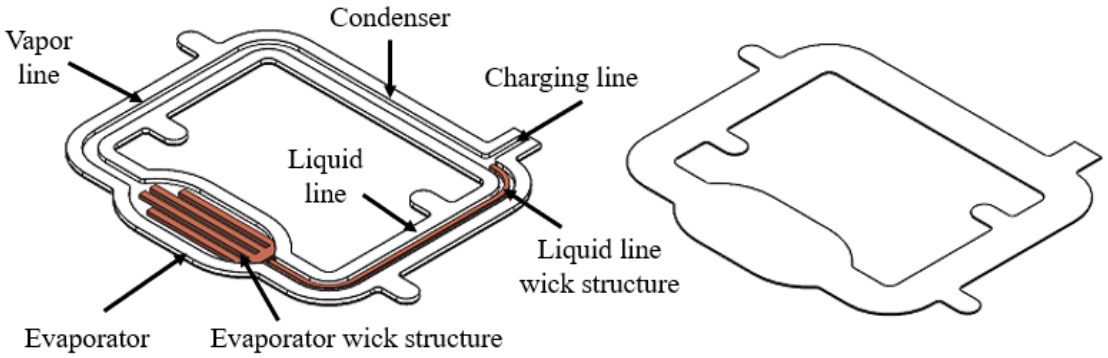

Figure 10.9: Schematic design of the LHP.

The evaporator is heated by a copper block (heating area of 1 mm²) with one cartridge electrical resistance (3.2 mm of diameter and 25 mm of length) and thermally insulated with a layer of polytetrafluoroethylene, while the condenser dissipates heat to the environment by natural convection. The external surface of the device is coated with black, high-emissivity paint (emissivity $\varepsilon \approx 0.92$) to allow IR measurements of the outer wall temperature by means of a medium-weave IR camera (FLIR® ThermaCAM S65) with a pixel resolution of 320 x 240, thermal sensitivity of 0.08 °C in a range from -40 °C to 2000 °C and a sampling frequency of 15 Hz.

The LHP was charged with degassed ethanol (filling ratio = 40% vol., 0.32 ± 0.01 ml) and positioned in horizontal orientation. During the test, 4 W heat load Q was provided to the evaporator. A thermographic acquisition lasting 300 seconds was recorded starting from thermal equilibrium conditions with the environment, i.e. just before supplying power to the heated section, to collect data regarding both the start-up and the pseudo-steady state of the device.

10.3.2. Wall-to-fluid heat flux estimation method

IR acquisitions were used as inputs for the IHCP resolution approach to evaluate the heat fluxes locally exchanged between the working fluid and the LHP wall within the condenser section, as shown in Figure 10.10.

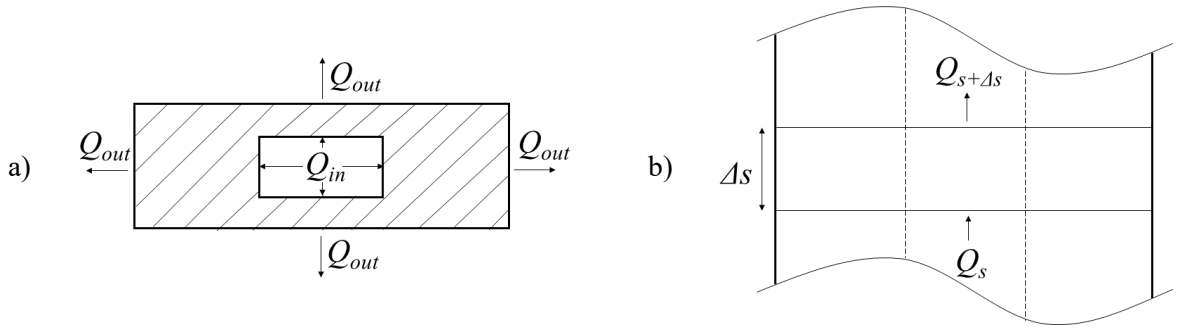

Figure 10.10: Cross-sectional view (a) and overhead view (b) of the generic wall element.

The adopted method is based on the one described in Paragraph 5.2.2. However, due to the different geometry, the new formulation for the conduction problem is here explained. With reference to the generic wall element of length Δs (Figure 10.10), whose temperature is assumed uniform in space, given the great device compactness and the high thermal diffusivity of copper, the energy balance equation in transient conditions is defined as:

$$\frac{dU}{dt} = Q_s - Q_{s+\Delta s} + Q_{in} - Q_{out} \tag{10.7}$$

where U is the internal energy, t is time, Q_s and $Q_{s+\Delta s}$ are the power terms referred to the spatial coordinate s, while Q_{in} and Q_{out} are the power terms exchanged at the fluid-to-wall and the wall-to-environment interfaces, respectively. By substituting all the power terms in Equation (10.7) and rearranging, the wall-to-fluid heat flux reads as:

$$q(s,t) = \frac{\left(\rho c_p \frac{\partial T(s,t)}{\partial t} - k \frac{\partial^2 T(s,t)}{\partial s^2}\right) \cdot S_{cross} + h_{env}(T(s,t) - T_{env}) \cdot S_{out}}{S_{in}} \tag{10.8}$$

Similarly to previous approaches, h_{env} was assumed to be equal to 10 W/m^{2}K [9]. S_{cross} is the cross-sectional surface, while S_{in} and S_{out} are the inner wall and outer wall surfaces of the element, respectively. The second order derivative of temperature comes from the difference Q_s - $Q_{s+\Delta s}$, where the Laplacian operator appears. Equation (10.8) was solved by means of the finite difference method, by adopting the filtering approach as regularisation method together with the discrepancy principle.

For the present application, σ_b was found equal to 0.04 K from isothermal IR acquisitions on the studied layout. In the present analysis, six wall sections were considered (dotted lines in Fig. 3), and their temperature was assessed by averaging IR acquisitions over 10 x 10 pixels areas (blue squares in Figure 10.11).

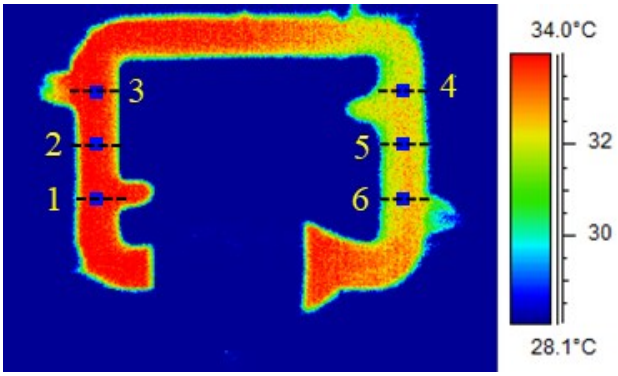

Figure 10.11: Sample of IR acquisition and sections of interest for the present study.

The six resulting temperature distributions were first processed by means of a one-dimensional Gaussian filter, and then used in Equation (10.8) to estimate the wall-to-fluid heat flux exchanged in sections 2 (vapor line) and 5 (liquid line).

10.3.3. Local heat transfer behaviour in the liquid and vapour lines

To give an overview of the raw measurements referred to the considered wall sections, the temperature signals acquired during the overall test are shown in Figure 10.12a. Figure 10.12b shows instead a magnification of the first transient, i.e. when the heat load is supplied to the evaporator.

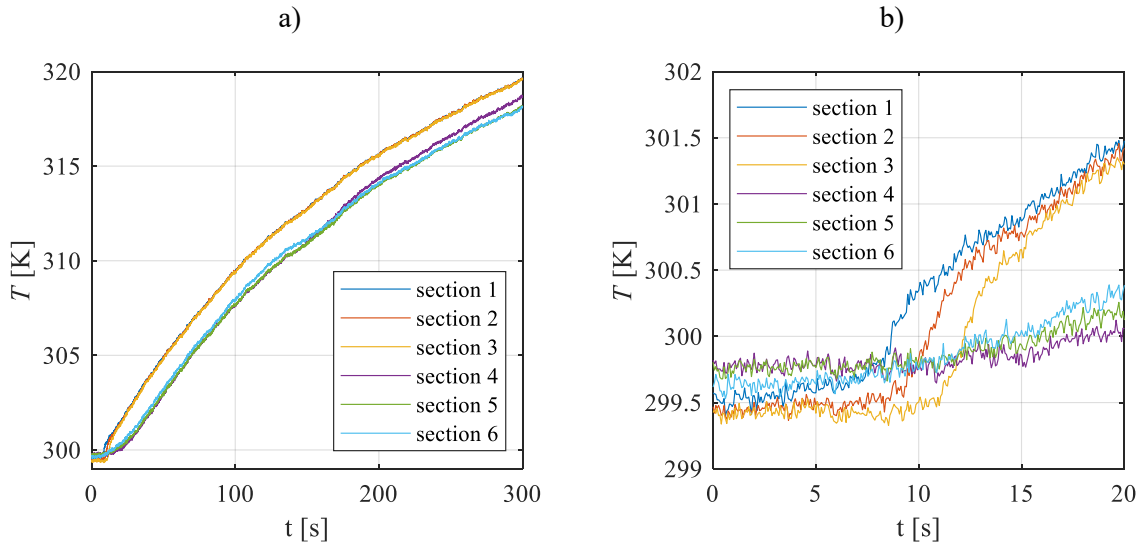

Figure 10.12: Temperature acquired during the overall test (a) and magnification of the first transient (b).

During the first seconds of acquisition, the overall device is in thermal equilibrium with the environment and all the temperature trends are almost flat. At about 10 seconds, the vapor line temperature, represented by section 1, 2 and 3 of Figure 10.11, undergoes a sharp increase. After the

evaporator was successfully activated, vapor starts flowing in the condenser section, eventually exchanging heat with the LHP wall.

The unidirectional vapor motion from the evaporator towards the condenser is furthermore confirmed by the fact that the temperature increment of section 1 is followed by a consequent heating of section 2 and 3. On the other hand, the temperature of the liquid line, i.e. of section 4, 5 and 6, does not exhibit any significant variations during the first transient, while it starts increasing as soon as the vapor reaches the condenser.

The acquired temperature signals were therefore processed by means of the method described in Section 3 for the wall-to-fluid heat fluxes evaluation in both vapor and liquid lines. It has to be highlighted that, according to the reference system of Figure 10.10, positive heat fluxes occur when the device wall warms up.

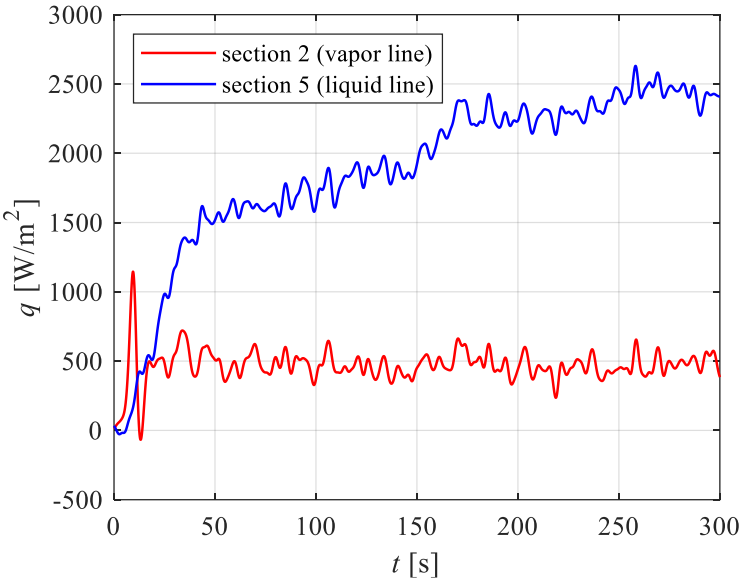

Figure 10.13: Evaluated wall-to-fluid heat fluxes.

In Figure 10.13, the wall-to-fluid heat fluxes exchanged in the vapor and liquid lines of the device for the considered power input are shown (see Figure 10.11 for reference). In the vapor line, q exhibits a peak of 1100 W/m^2 at about 10 seconds, i.e., when the device starts-up, and it settles at around 450 W/m^2, suggesting that the LHP is approaching a pseudo-steady state operation. In the liquid line, q denotes instead a slow ascending trend during the start-up, while it keeps increasing with time up to 2500 W/m^2 possibly due, at least in part, to the presence of the wick structure enhancing local wall-to-fluid interactions.

10.4 Closure

The presented investigations are few of the potential applications of IR-based post-processing on different PHP geometries and materials (flexible PHPs), or different types of HPs (thin, metallic LHPs).

In particular, the presence of transparent walls in flexible PHPs allows, given a proper calibration of the procedure, a simultaneous and consistent estimation of working fluid temperature and exchanged wall-to-fluid heat flux by means of the IHCP resolution approach. This underlines the possibility of extending the procedure carried out for tubular layouts with transparent inserts made of sapphire to the analysis of flat plate layouts. Moreover, due to the manufacturing process concerning flexible PHPs, all the channels are transparent to infrared radiations. When compared to tubular layouts having few transparent inserts, such an additional advantage leads to a complete description of the local heat transfer behaviour in all the channels.

The extension of the IHCP resolution approach to other devices, such as LHPs, will furtherly open to a number of investigation frontiers and interesting remarks, with the aim of enhancing the phenomenological understanding by means of non-intrusive and easily employable experimental techniques.

Chapter 11 Conclusions and future developments

The main purpose of the here reported research activities was to describe the investigated devices from a novel point of view, i.e., by providing comprehensive results in terms of local thermofluidic interactions between the working fluid and the devices walls. To this aim, four different layouts were studied:

- Tubular PHP (named Space PHP);
- Tubular micro-PHP;
- FPPHP;
- Thin LHP.

The outer wall temperature of the devices was acquired by means of high-speed, high-resolution IR cameras. The resulting space-time temperature maps were post-processed by means of the IHCP resolution approach, thus evaluating local wall-to-fluid heat fluxes. The estimated heat fluxes were proven to be inherently linked to the fluid motion, even though no information could be obtained in terms of liquid-vapour displacement due to the thermal inertia and overall thermal properties of the walls. All the evaluated heat fluxes were therefore threated by means of different techniques:

- Statistical reductions. Two different coefficients, *cvt* and *cvs*, were proposed to quantify heat flux variations over time and along space, respectively. While *cvt* granted a quantitative and repeatable identification of the device working regimes, *cvs* was used to assess thermal interactions along the axial coordinate, i.e., between the evaporator and the condenser. The heat flux amplitude was furthermore statistically reduced by computing the 80th percentile (q_{80}).
- Wavelet method. Dominant fluid oscillation frequencies were extensively assessed in every analysed channel.

- Cross-correlations. Flow modes (oscillatory and circulatory flows) were identified by evaluating the time delays between heat fluxes signals referred to adjacent channels. In addition, the average fluid velocity in the circulatory flow was estimated through the HTDM.

To achieve a complete description of the thermal behaviour of the studied devices, the thermal performance was estimated by typical and already established means, i.e., by acquiring evaporator and condenser temperatures through thermocouples. Comparisons between global and local thermal behaviours were thus carried out.

The test conditions and key quantified physical phenomena are listed in Table 11.1.

Table 11.1: Test conditions and quantified phenomena.

Studied device	Cooling method	Section of interest	Quantified phenomena
Space PHP	Prescribed temperature (Peltier cells array)	Adiabatic section	• Thermal performance • Heat flux amplitude against power input • Working regimes • Flow modes • Average fluid velocity (circulatory flow on ground) • Oscillation frequency (microgravity)
Micro-PHP	Free convection	Condenser	• Thermal performance • Working regimes • Oscillation frequency • Flow modes
FPPHP	Prescribed temperature (copper heat exchanger)	Adiabatic section	• Thermal performance • Heat flux amplitude against power input • Working regimes • Oscillation frequency and transverse conduction
Flexible PHP	Device inactivity and prescribed temperature (copper heat exchanger)	Adiabatic section	• Fluid temperature • Outer wall temperature variations (feasibility study)

Thin LHP	Free convection	Condenser (liquid and vapour lines)	• Heat flux variation during activation

Hence, the adopted post-processing methods provided quantitative results not only about the local heat transfer behaviour of the studied devices, which could be employed for the validation of existing numerical methods, but also about other thermal and hydrodynamic quantities of interest.

11.1 Comparison between different PHPs in terms of wall-to-fluid heat transfer

While significant remarks regarding the experimental campaigns are reported in each Chapter, the main outcomes coming from a comparison between different PHPs layouts are resumed below:

- In metallic flat plate layouts, the local heat transfer behaviour within the adiabatic section is strongly influenced by conduction occurring between the evaporator and the condenser, contrarily to tubular layouts. On the other hand, when the condenser section is investigated, strong variations of the wall-to-fluid heat flux are perceivable both over time and along space, confirming the onset of complex thermofluidic interactions in such a device section.
- Heat flux exchanged between the working fluid and the device wall is mainly positive along the condenser section (free convection), whereas it similarly varies from positive to negative values in the adiabatic section. In fact, the condenser mainly experiences hot fluid coming to the evaporator, while the adiabatic section warms up or cools down depending on the fluid oscillatory or circulatory motion between the two heat transfer sections.
- Despite the considered geometry, orientation plays a significant role in terms of wall-to-fluid heat flux amplitude. The vertical BHM presents lower values of heat flux peaks, especially during the circulatory flow, while the horizontal orientation exhibits higher peaks and steeper slopes with the increasing of the heat load.
- A strong link between global performance and local heat transfer behaviour exists for all the observed configurations. A decrease in equivalent thermal resistance leads to a stabilization of heat flux variations over time.
- The frequency analysis on local heat fluxes provides comparable results with those evaluated by means of other techniques (e.g., by considering fluid pressure signals). Fluid oscillation frequencies are strongly discontinuous during the intermittent flow, while full activations always guarantee stable fluid oscillations in most of the branches of the studied devices.

More quantitative results are discussed in the next Paragraphs.

11.1.1. Repeatable working regimes detection by means of cvt

One of the leading results is linked to the reduction of the evaluated wall-to-fluid heat fluxes by means of statistical quantities. In particular, the *cvt* value was proven to give quantitative perspectives for the working regime identification in PHPs. To underline the strength and validity of such a coefficient for all the tested devices, the values of cvt_{av} are shown for the Space PHP, the micro-PHP and the FPPHP in Figure 11.1. For the sake of comparison, the only vertical BHM orientation was considered for all the PHPs, while the power input given to the evaporator was normalized with respect to the maximum provided heat load (safety threshold above which each device experienced a dangerous increase in evaporator temperature, although far from the operational limit). Also, the data about the Space PHP are referred to the condenser temperature equal to 20°C (same set-point temperature given during the FPPHP investigation).

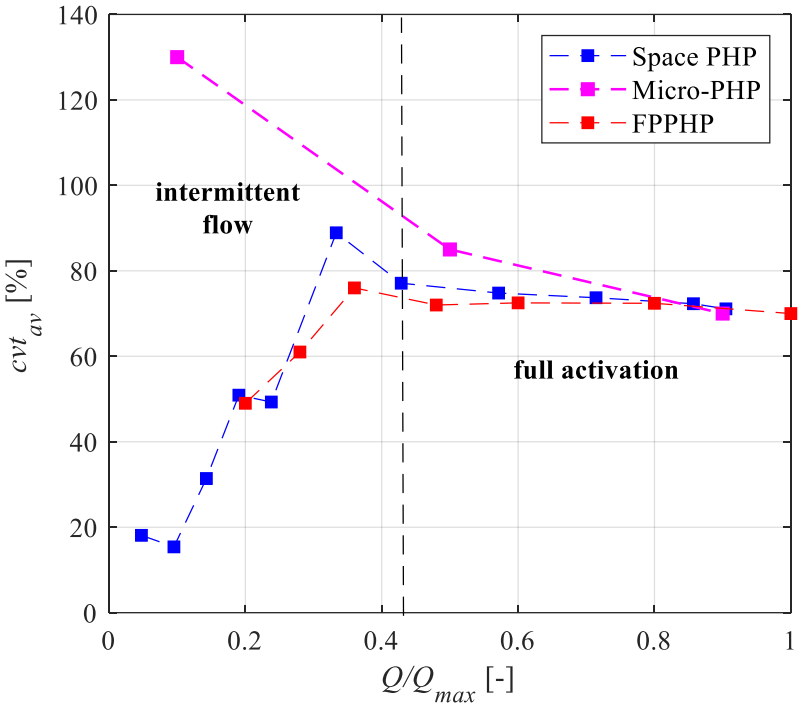

Figure 11.1: Comparison between different devices in terms of cvt_{av} of the wall-to-fluid heat flux (vertical BHM orientation).

Here, it is interesting to notice that, despite the analysed device, the intermittent flow is characterised by higher peaks in the cvt_{av}, i.e., by stronger heat flux variations over time in the overall device when the heat load promotes highest intermittency of the fluid motion. For what concerns the Space PHP and the FPPHP, cvt_{av} increases up to a peak value at almost same normalized power input to the evaporator. The values assumed by the peaks differ of about 10%. In the micro-PHP, cvt_{av} presents instead a higher peak value at a lower normalized power input. This may be due to two main factors:

different observation section (condenser), which could result in different observed heat flux variations; different intermittent flow pattern in micro-devices (the extremely low inner diameters result in high viscous forces on the fluid stream). Nonetheless, during the full activation, all the devices exhibit a stabilization of the cvt_{av} around 73%, suggesting that such a value could be a significant reference for the full activation identification in every PHP geometry, regardless the observation window and the cooling method.

11.1.2. Trends in the q_{80} values

Another useful remark was achieved by comparing the values assumed by q_{80} in the Space PHP and the FPPHP, i.e., where the adiabatic section was investigated during pseudo-steady state conditions. Such a comparison is shown in Figure 11.2. Here, the vertical BHM orientation was not considered since it promoted net fluid circulation inside the only Space PHP, with consequently different thermofluidic interactions between the working fluid and the device wall.

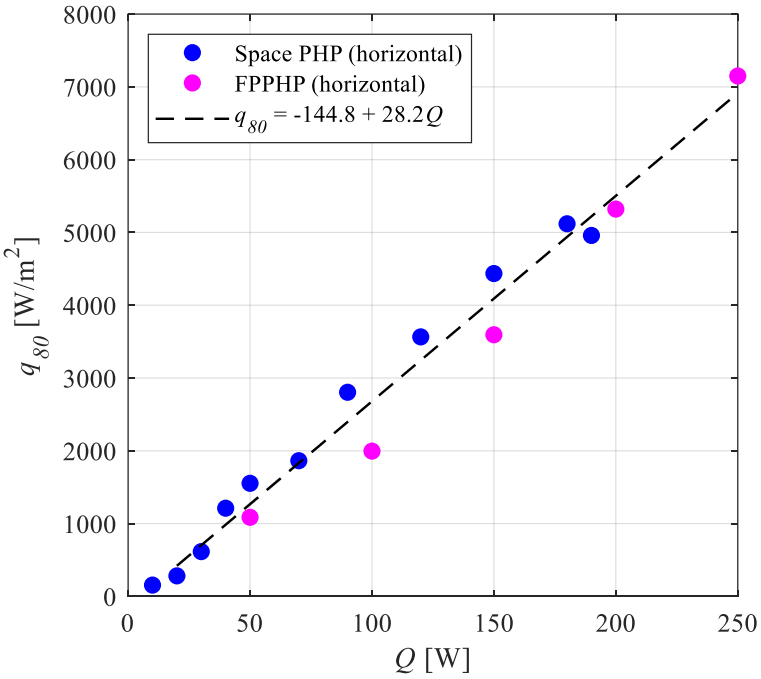

Figure 11.2: q_{80} against the heat load to the evaporator for the Space PHP and the FPPHP.

Trends referred to both devices show an increase in q_{80} both during the intermittent flow (from 20 W up to about 100 W) and the full activation regions. Such an increase with the heat load was therefore modelled by means of a linear fit of the data. Specifically, the curve which best fitted (in a least-squares sense) the data is defined by q_{80}=-144.8+28.3Q, with R^2 = 0.97. The provided correlation can accurately describe the local wall-to-fluid interactions over the entire PHPs operation, suggesting that, in the

horizontal orientation, the amplitude of heat flux peaks does not depend either on the considered geometry or on the considered working regime. The q_{80} values and the provided model as a function of the heat load could lead to a proper validation of the existing numerical models of PHPs in terms of local heat transfer quantities.

11.1.3. Stabilization of the dominant fluid oscillation frequency

Finally, the dominant fluid oscillation frequencies evaluated in the micro-PHP and in the FPPHP during the full activation were compared in vertical BHM orientation. The Space PHP was not here taken into account due to the onset of circulatory rather than oscillatory flows.

The $f_{D,av}$ values are shown in Figure 11.3 as a function of the normalized heat load. Here, it is clear that, as long as the heat load increases, the fluid oscillation frequency tends to stabilize, regardless the operating conditions, the geometry or the working fluid. Such a common trend opens to an interesting observation about the PHP flow pattern transition. Specifically, at high heat loads, a stabilization of the dominant fluid oscillation frequency could result in a saturation of heat transferrable to the condenser, thus enabling local dry-out phenomena at the evaporator. The formation of dry spots could therefore promote the onset of annular flows, at least in some channels.

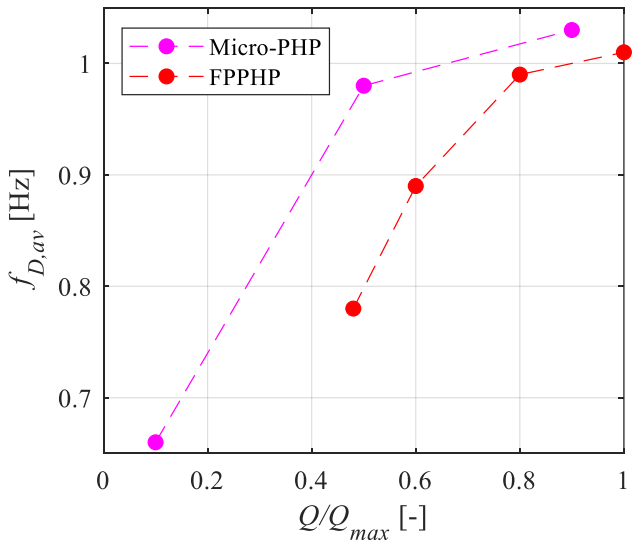

Figure 11.3: $f_{D,av}$ as a function of dimensionless heat load (full activation of the devices).

11.2 Future perspectives

The proposed approaches provide useful data for the quantitative description of two-phase passive heat transfer devices, and they open to a wide yet significantly unexplored phenomenological insight.

As confirmed by the presented results, the potentialities linked to the IHCP resolution approach applied to thermal management devices are massive, especially for non-intrusive investigations.

Anyway, some of the possible future developments are listed below:

- Study on the effects of the adiabatic section thermal inertia on the PHPs thermal behaviour. This is a controversial point, since the influence of the adiabatic section on the fluid flow is typically assumed as negligible. However, higher thermal inertias could lead to stronger heat fluxes from the walls to the working fluid. A thermalisation of the working fluid will be promoted, with consequent reduction of the pressure difference between the evaporator and the condenser and a delay of the device full activation. A possible solution of experimental implementation would be realizing different PHPs having heat transfer sections made of same conductive material (boundary conditions unchanged) and adiabatic sections made of more or less conductive materials. Such a configuration would require the employment of junctions between the adiabatic section and the heat transfer areas. A more straightforward possibility would be progressively adding solid material to the adiabatic section of a PHP, thus stepwise increasing its thermal inertia.
- Evaluation of the wall-to-fluid heat flux in the evaporator section in FPPHPs and tubular PHPs. Such an estimation would be of great interest for numerical simulations. However, evaluating wall-to-fluid heat fluxes by means of the IHCP resolution approach in the evaporator is extremely complex. This is due to the usual presence of a thermal spreader, which undermines the observation of wall temperature variations through thermography. Moreover, since part of the evaporator must be accessible to IR cameras, the heat load would be unevenly provided on only one side of the heating section, leading to different heat transfer conditions at the evaporator boundaries. One possible experimental solution is represented by the realization of a metallic evaporator section, with electrical breaks (plastic or glass junctions) at the evaporator-adiabatic section interface. In this way, heat could be directly generated inside the metallic walls by Joule effect, while maintaining electrically insulated the heating area from the rest of the device. Further considerations about the feasibility of such approach from a manufacturing standpoint are left to the reader.
- Weightlessness analysis. Collection of microgravity data on the operation of different PHPs is crucial for fully establishing the effectiveness of such heat transfer devices, and their reliability for application in the space industry. The IHCP resolution approach will be adopted for a systematic evaluation of wall-to-fluid heat fluxes and consequent data reduction in such conditions. In the near future, the data collected in collaboration with the University of Brighton (United Kingdom), the Polytechnic University of Milan (Italy) and the University of Pisa (Italy) during the 78th Parabolic Flight Campaign promoted by the European Space Agency (spring 2022) will be post-processed to provide complementary

outcomes on the local heat transfer phenomena. The new results, along with the ones already available on ground and short microgravity conditions, will also be of great importance for the implementation of future long-term tests, especially for what concerns the Space PHP, whose experimental investigation on the International Space Station is scheduled in 2024.

- Simultaneous evaluation of local wall-to-fluid heat flux and fluid temperature (liquid phase) in flat, transparent layouts. Such an estimation will be carried out on flexible PHPs, together with metallic FPPHPs with sapphire windows (on-going fabrication).
- Robust improvement and validation of numerical models. This is one of the key points regarding the near future developments, since local wall-to-fluid heat flux data, estimated in a wide portion of the devices, could be adopted for the tuning of parameters defining the models outputs.
- Application to other devices. The high flexibility of the heat flux estimation approach could lead to its application not only in the field of PHPs or LHPs, but also to other heat transfer devices governed by strongly transient operations, presenting complex geometries or low accessibility by intrusive means.

Appendix A

To validate the procedure presented in Section 5.2.2 and applied to the case of Chapter 7 (aluminium channels), synthetic temperature data were generated by solving the direct problem with a known distribution of the heat flux $\mathrm{q}(z,t)$ at the internal wall surface. The numerical model for the direct problem was implemented within the COMSOL Multiphysics® environment.

The resulting temperature distributions were then spoiled by Gaussian noise levels, characterized by a standard deviation σ ranging from 0.01 to 0.1 K, and used as input data for the IHCP solution approach. According to the expected results in the real cases, the convective heat flux q was assumed as a sinusoidal function characterized by time-space variations, where L is the length of the considered channel portion:

$$\mathrm{q}(z,t) = A \cdot cos\ (p\pi t) \cdot \left(1 + \frac{z}{8} \cdot L\right) \tag{A.1}$$

The effectiveness of the proposed approach at different heat flux amplitudes and frequencies was quantified by taking A equal to 2000 and 4000 W/m^2, while the p parameter was varied among 1.2, 1.6, 2 and 2.4, corresponding to frequencies of 0.6, 0.8, 1 and 1.2 Hz, respectively. The adopted values of amplitude and frequency are representative of the oscillatory phenomena that characterise the studied device.

From the direct problem, solved by using the wall-to-fluid heat fluxes of Equation (A.1), the maximum residual between the internal and external wall temperatures was found to be about equal to 0.02 K. The thin-wall approximation of Equation (5.5) is thus validated since the maximum residual is much lower than the noise level assumed in Section 7.2.3 for the experimental setup (0.06 K).

It has to be underlined that the inverse approach in transient conditions is affected by the thermal inertia of the PHP channels that makes difficult to catch high-frequency phenomena. The effects of the

aluminium wall on the wall-to-fluid heat flux restoration were thus studied by solving the direct problem, using heat fluxes of Equation (A.1) with p ranging from 2.5 to 8 and A equal to 2000 W/m^2. For oscillation frequencies of the wall-to-fluid heat flux greater than 3 Hz (p = 6), the maximum variation of the external wall temperature was found to be lower than the noise level of the experimental setup. Hence, in this case, the thermographic measurements on the tube outer surface are able to catch transient phenomena that occur inside the PHP tube in a time higher than 0.3 s, while every other significantly faster transient phenomenon cannot be fully perceived on the outer surface due to the filtering effect of the aluminium wall.

To quantify the efficiency of the applied approach at different signal-to-noise levels, an error analysis was performed by evaluating the estimation error, defined as follows:

$$E_q = \frac{\|q_{restored} - q_{exact}\|_2}{A\sqrt{M \cdot N}} \tag{A.2}$$

In Figure A.1, the estimation error, evaluated for every combination of heat flux frequency and amplitude, is plotted against the noise level. For A equal to 4000 W/m^2, the estimation procedure is able to restore the heat flux distribution with good accuracy (7% < E_q < 20%), while, for A = *2000 W/m^2,* the heat flux restoration procedure is affected by higher though acceptable restoration errors (8% < E_q < 25%). Moreover, the estimation error was observed to increase with the oscillation frequency. For noise level equal to 0.06 K (experimental setup), the estimation error was found to range from 9% to 21%.

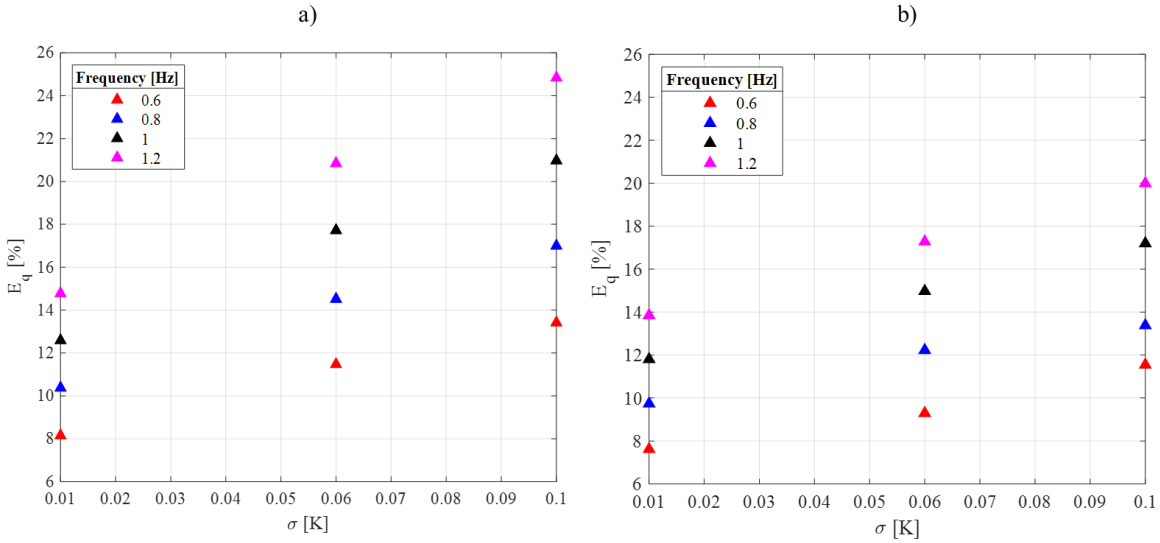

Figure A.1: Estimation error for A = 2000 W/m^2 (a) and A = 4000 W/m^2 (b), considering oscillation frequencies between 0.6 and 1.2 Hz.

The validation was replicated for the case of Chapter 8, where micro-channels made of stainless-steel were studied. Similarly to aluminium channels, the thermal properties of the stainless-steel walls could not allow the identification of liquid slugs or vapour plugs by the only IR acquisitions. The results of the procedure are reported in Table A.1 for different amplitudes and frequencies of the exact heat flux, and noise level equal to 0.06 K.

Table A.1: Estimation error evaluated for the case of Chapter 8.

A [W/m^2]	Frequency [Hz]	E_q [%]
2000	0.5	10
2000	1	16.1
4000	0.5	7.4
4000	1	14.2

Here, the estimation error increases with the frequency, while it decreases with the increase of A, in accordance with the analysis of Figure A.1. The maximum estimation error within the analysed application ranges was found to be equal to 16.1% of q_{exact}.

Appendix B

A dedicated validation of the estimation method by means of synthetic temperature data has been performed. The validation of the inverse procedure for the wall-to-fluid heat flux evaluation is based on four different steps, similarly to the one performed in Appendix A:

1) **Direct problem implementation**. The heat transfer by conduction through the studied solid domain is simulated on a CFD environment by providing a known heat flux distribution q_{exact} as boundary condition at the wall-fluid interfaces;
2) **Simulation of experimental data acquisition**. The resulting synthetic temperature distribution is randomly spoiled with gaussian noise levels σ;
3) **Inverse problem implementation**. The noisy temperature is filtered by means of Equation (5.33) and used as input for Equation (5.26), thus attempting to evaluate back the given wall-to-fluid heat flux q_{exact};
4) **Evaluation of the estimation error**. q_{exact} is finally compared with the heat flux evaluated in step (3), $q_{restored}$, thus assessing the goodness of the estimation procedure for the given heat flux distribution and noise levels.

Step (1) was performed through the Comsol Multiphysics© software by finite elements method. More than 150 000 elements were found to guarantee the grid-independency of the model. To ensure the reliability of the method validation, q_{exact} given in step (1) has to be as much similar as possible to the thermofluidic interactions occurring in the real device. Hence, according to the expected physical behaviour in experimental cases, the convective heat flux is assumed to exhibit a sinusoidal shape described by time-space variations, representative of the working fluid oscillations through the adiabatic section:

$$q_{exact,A} = Amp \cdot cos(2\pi t \cdot f - \varphi) + \frac{Amp}{2} - \frac{z}{H} \cdot Amp \tag{B.1}$$

where H is the length of the considered portion of the adiabatic section and z is the axial coordinate. Here, variations over the z coordinate are expressed by the term $\frac{z}{H} \cdot Amp$, while variations over y are introduced by means of the phase φ. Adjacent channels are assumed to exhibit a phase shift equal to π. In addition, the wall-to-fluid heat flux is expected to vary between the thin walls and side walls surfaces A and B, respectively, highlighted in Fig. 4 for a generic channel, thus leading to the following definition of $q_{exac,B}$:

$$q_{exact,B} = 2q_{exact,A} \tag{B.2}$$

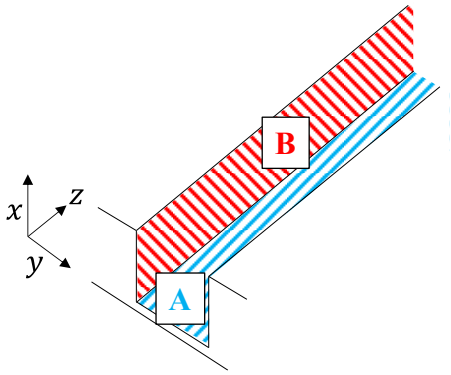

Figure B.1: Two surfaces at which q_{exact} is defined for the generic device channel. A: thin wall; B: side wall.

Specifically, the heat flux exchanged over surface B is believed to present greater heat flux amplitudes due to the higher thermal inertia of the side walls; a validation of this assumption by preliminary experimental data will be provided along the text. The capability of the inverse procedure of effectively evaluating the wall-to-fluid heat flux was quantified by adopting different amplitudes and oscillation frequencies of q_{exact}. In particular, Amp was considered equal to 2000, 4000 and 8000 W/m^{2}K, while f was considered equal to 0.5, 0.8 and 1.2 Hz. From the direct problem simulation, the maximum residual between the inner and outer wall temperatures, i.e. for $T(x = x_{int})$ and $T(x = x_{ext})$ according to Figure 5.4, was found to be less than 0.02 K. Since such a value was lower than the noise level evaluated in Section 9.5 for the present experimental set-up (0.04 K), the thin-wall approximation was consequently verified.

a) b)

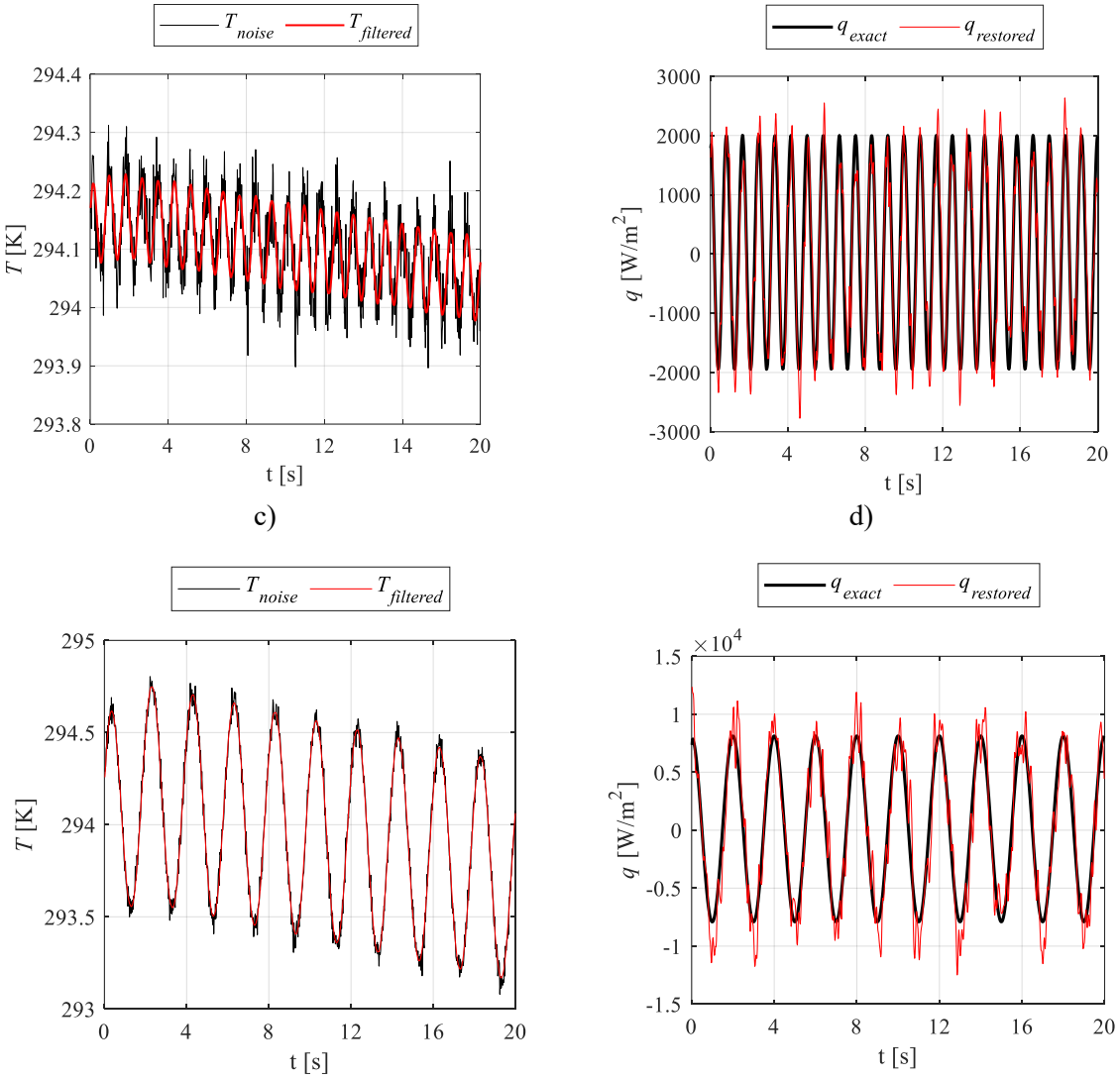

Figure B.2: Noisy and filtered temperature signals (σ = 0.04 K, z = 0.02 m) for Amp = 2000 W/m^2, f = 1.2 Hz (a), and Amp = 8000 W/m^2, f = 0.5 Hz (b), and corresponding exact and restored heat fluxes (c and d, respectively). The fixed axial coordinate z = 0.02 m is considered.

For step (2) of the validation procedure, three different noise levels σ were adopted, namely 0.01, 0.04 and 0.08 K. To provide references for the restoration procedure of the given exact wall-to-fluid heat flux distributions, the validation data referred to two different q_{exact} cases for a single channel (φ = 0) are shown in Figure B.2 by considering σ = 0.04 K and the axial coordinate z = 0.02 m.

In Figure B.2a-c, the noisy temperature T_{noise}, resulting from step (2), and the filtered temperature $T_{filtered}$, resulting from step (3), are reported for Amp = 2000 W/m^2, f = 1.2 Hz and Amp = 8000 W/m^2, f = 0.5 Hz, respectively. In Figure B.2b-d, the exact and restored heat fluxes are additionally shown for the same test cases. In Fig. 5a, the lower amplitude of the considered q_{exact} results in lower temperature variations and lower signal-to-noise ratio, leading to a hard restoration of the exact heat flux peaks (Figure B.2). On the contrary, the heat flux of Figure B.2d is restored with slightly greater accuracy

thanks to the higher signal-to-noise ratio of T_{noise} (Figure B.2c), even though some variations from the exact value are still appreciable due to residual noise in the $T_{filtered}$ signal.

Moreover, the goodness of the assumption of Equation (B.2) was verified by comparing preliminary experimental data with numerical data obtained by the heat flux restoration procedure on synthetic distributions. In Figure B.3, all the terms appearing in Equation (5.26) are plotted as a function of time for a generic PHP channel and a median axial coordinate. Specifically, $q_z = -sk\frac{\partial^2 T}{\partial z^2}$, $q_y = -sk\frac{\partial^2 T}{\partial y^2}$, $q_t = s\rho c_p \frac{\partial T}{\partial t}$ and $q_{env} = h_{env}(T - T_{env})$. Figure B.3a is referred to the numerical data, while Figure B.3b is referred to the preliminary experimental data. From the restoration procedure on synthetic data (Figure B.3a), obtained by adopting Equation (B.2), the q_t peaks assume values about half, in module, of those assumed by q_y, while q_z approaches the positive peaks of q_t. A comparable behaviour can be perceived from the heat flux evaluation on the preliminary data (Figure B.3b), at least when stable (nearly sinusoidal) oscillations occur (until 12 seconds), thus confirming the assumption of Equation (B.2).

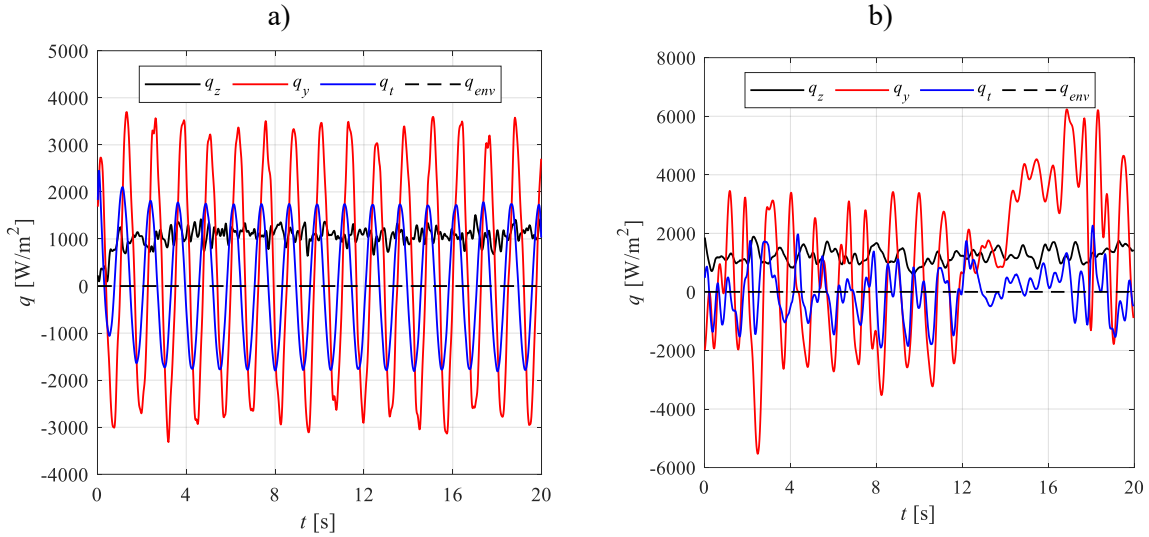

Figure B.3: Comparison between numerical (a) and experimental (b) data for the validation of the assumption adopted in Equation (B.2).

Finally, the restoration error for step (4) was defined as:

$$E = \frac{\|q_{restored} - q_{exact}\|_2}{max\,(q_{exact}) \cdot \sqrt{N \cdot M \cdot O}} \tag{B.3}$$

Since the effectiveness of the Gaussian kernel is dependent on the randomly generated noise distribution of step (2), steps (2-4) were repeated for 100 different random sequences of noise to the numerical data and an averaged value of E was evaluated for each considered noise level.

a)

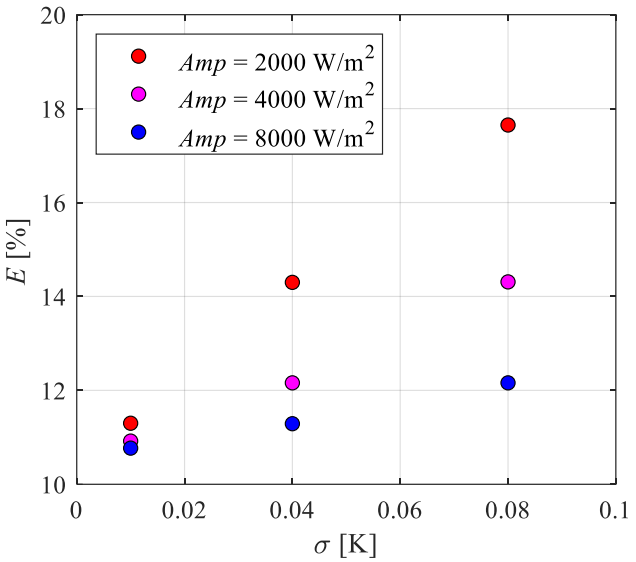

b)

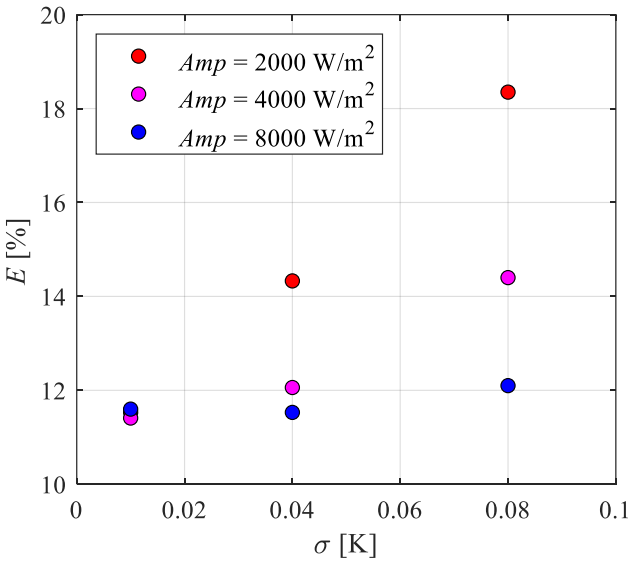

c)

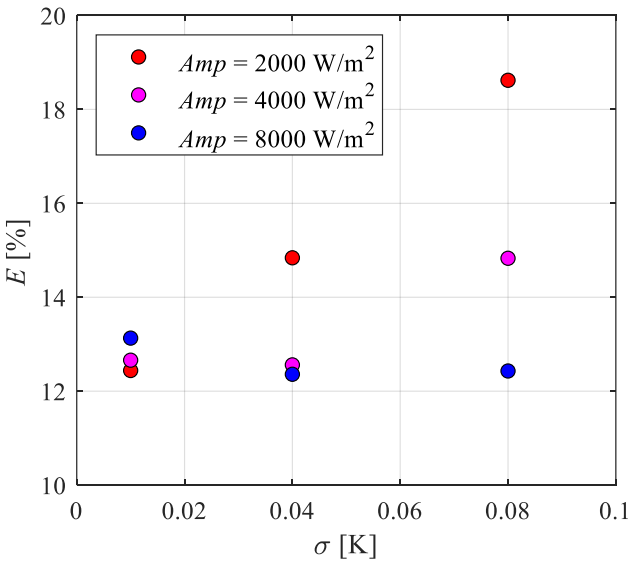

Figure B.4: Restoration error E as a function of noise level σ for different amplitudes of q_{exact} and frequencies equal to 0.5 Hz (a), 0.8 Hz (b) and 1.2 Hz (c).

The estimation error, evaluated for every combination of frequency and amplitude of q_{exact}, is plotted against the noise level in Figure B.4. Here, the restoration error E generally decreases with the increase of Amp, while it increases with f, as already highlighted for bidimensional approaches. For noise level equal to 0.04 K (present experimental set-up), the estimation error was found in the range 11% to 15% of q_{exact}, thus validating the rather good accuracy of the wall-to-fluid heat flux evaluation procedure of Paragraph 5.3.

Appendix C

To validate the HTDM by means of an experimental approach, i.e. providing an estimation error for the average fluid velocity evaluation, a dedicated test rig was employed (Figure C.1). Specifically, it consists of a loop made up of a thermal bath (HAAKE® DC5 circulator) filled with pure water and an aluminium tube having same inner/outer diameter of that used for the PHP manufacturing. Connections between the thermal bath and the aluminium channel are obtained by plastic tubes and LEGRIS® junctions. The aluminium tube is externally coated with a highly emissive paint to monitor the outer wall temperature over a 0.23 m long tube section by means of the same IR camera adopted for the PHP experimental analysis, acquiring thermograms at the same sampling frequency (18 Hz).

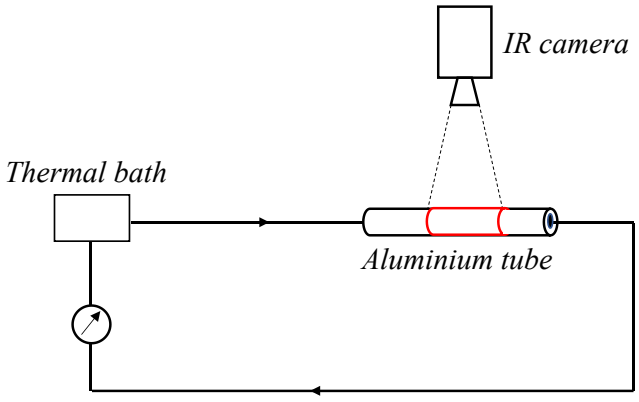

Figure C.1: Test rig for the HTDM validation.

Before the test, the loop was at isothermal conditions with the environment, i.e. at 31°C, and entirely filled with ambient air. Moreover, the water temperature was increased up to 70°C by internally circulating the liquid inside the thermal bath. Once the set-point temperature was reached, the external circulation was switched on, thus letting the hot water flowing inside the loop. The volumetric flow rate

guaranteed by the circulation pump is assessed by measuring the time required for filling a graduated cylinder at the thermal bath inlet, i.e. at the end of the loop. Such a measurement procedure was replicated 10 times to reduce errors introduced by the operator, thus having a significant number of data to be averaged. The fluid velocity was therefore assessed by dividing the measured flow rate by the tube inner diameter. Given the uncertainty of volume measurements equal to 1 ml, the final uncertainty referred to the fluid velocity is estimated equal to about 0.02 m/s. The fluid velocity assessment was successfully reproduced during the pump operation to prove that the provided flow rate was constant over time.

Three different velocities were tested, namely 0.2, 0.4 and 1 m/s. The transient thermal interaction between the hot water and the aluminium tube, initially in thermal equilibrium with the environment, was caught, for every considered test condition, by means of thermography. In Figure C.2, the progressive increase of outer wall temperature due to inner convection is depicted by means of three IR acquisition samples (t = 0: start of the IR acquisition, before activating the circulation pump) for fluid velocity equal to 0.4 m/s (the fluid flows from left to right).

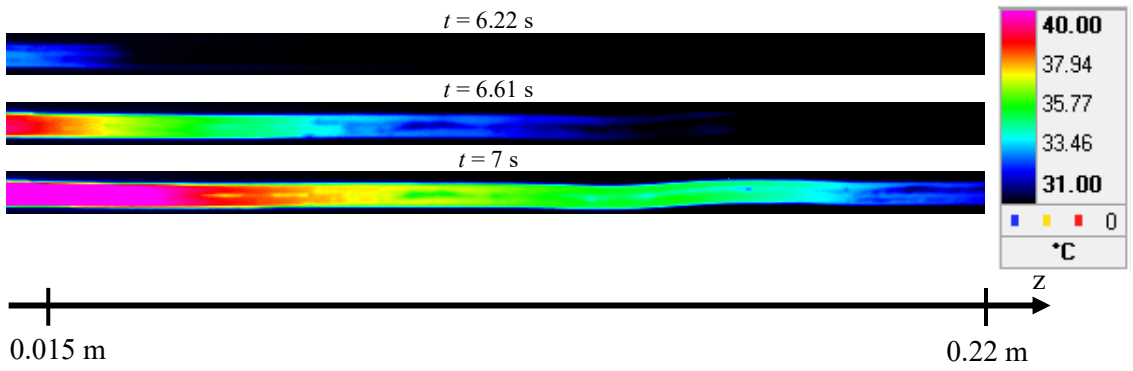

Figure C.2: Acquired thermographic samples of the transient thermal interaction between the hot fluid and aluminium tube at three different times t, for fluid velocity equal to 0.4 m/s.

The measured outer wall temperature is used as input for the IHCP resolution approach, thus evaluating the wall-to-fluid locally exchanged. Figure C.3a reports the wall temperature referred to the two fixed axial coordinates, namely z = 0.015 m and z = 0.22 m, while the corresponding evaluated wall-to-fluid heat fluxes are shown in Figure C.3b. Until about 6 seconds, the wall temperature is constant in both considered points (isothermal conditions, before water circulation in the loop). For this reason, the wall-to-fluid heat flux is almost null within the same considered observation window. When hot water starts flowing inside the tube, the temperature trends undergo a sharp increase, resulting in high peaks in the evaluated heat fluxes.

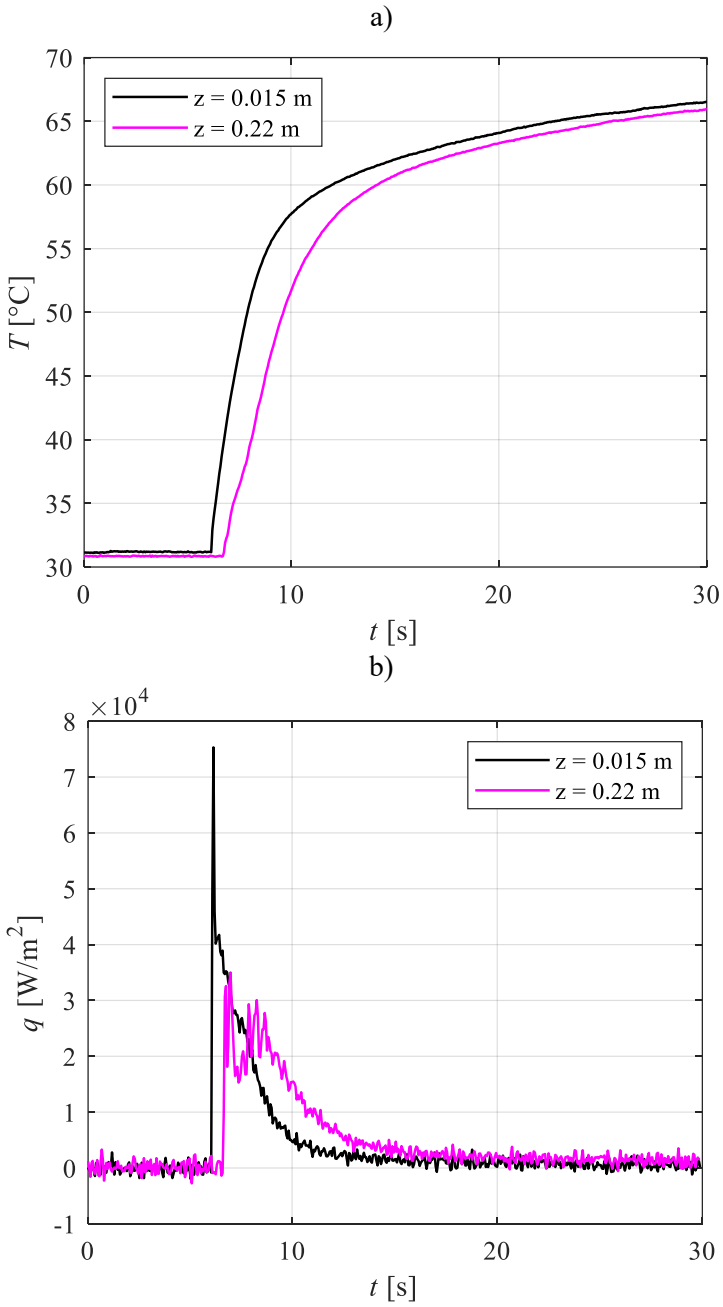

Figure C.3: Wall temperature acquired at two axial coordinates (a) and corresponding wall-to-fluid heat fluxes (b).

In addition, a certain time delay between the heat fluxes is clearly perceivable over the entire transient, suggesting that the thermal interactions occur in sequence; such a behaviour is noticeable for every considered fluid velocity. To quantify the time delay between the thermal interactions occurring at the two points of interest, the heat fluxes are adopted in Equation (6.11) by using the heat flux referred to $z = 0.015$ m as f and the one referred to $z = 0.22$ m as g. The resulting normalized cross-correlation functions are shown in Figure C.4. Here, the peaks are all at negative lags. According to its formulation,

negative lags in the cross-correlation mean that the function *f* is in advance with respect to *g*, thus confirming the given flow direction along the tube axis.

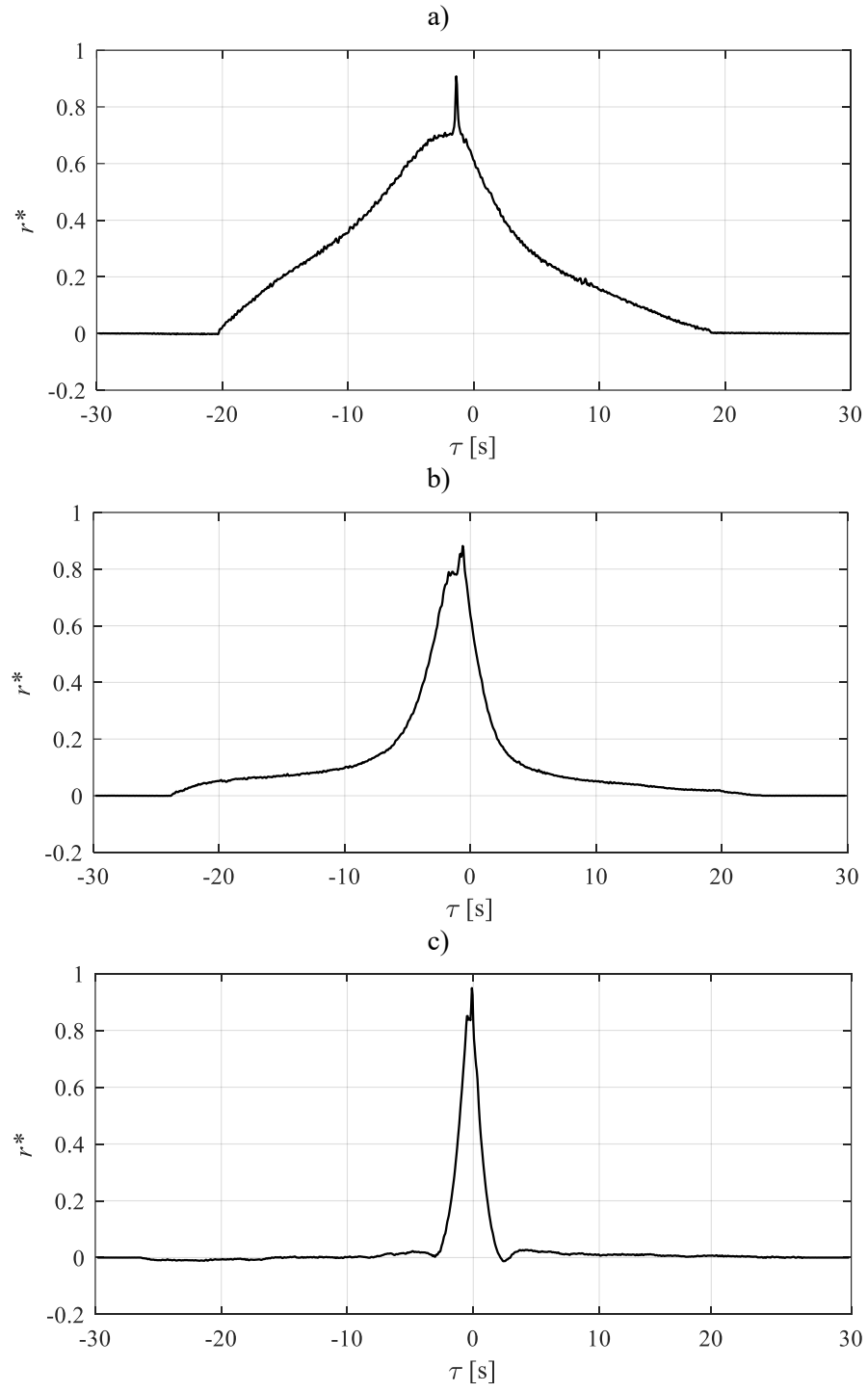

Figure C.4: Normalized cross-correlation functions, resulting from the post-processing of the heat fluxes referred to the two different axial coordinates for fluid velocity equal to 0.2 (a), 0.4 (b) and 1 m/s (c).

The delays evaluated for each fluid velocity are reported in Table C.1. As expected, the time between the two consecutive thermal interactions decreases with the increase of the fluid velocity.

Table C.1: Evaluated time lags for each considered fluid velocity.

Measured fluid velocity [m/s]	τ [s]
0.2	-1.39
0.4	-0.61
1	-0.22

The estimation error for τ is here equal to the reciprocal of the IR camera sampling rate, i.e. 0.06 s. By adopting the distance between the two axial coordinates L = 0.22-0.015 m and the estimated τ, the fluid velocities are finally evaluated by means of Equation (6.14). For comparison, the measured velocities are listed, along with the evaluated ones, in Table 2.

Table C.2: Comparison between measured and estimated fluid velocities.

Measured fluid velocity [m/s]	Evaluated fluid velocity [m/s]
0.2	0.15
0.4	0.34
1	0.92

A good agreement between the two quantities is perceived over the whole range of considered velocities, despite a non-negligible discrepancy probably due to the time discretization of the wall-to-fluid heat flux signals (i.e., discretization of the IR acquisitions).

It has to be pointed out that, even though the present validation case is not perfectly reflecting the two-phase, chaotic flow inside the studied PHP, the thermal interactions between the working fluid and the aluminium walls have been proven to allow a reliable and consistent evaluation of the fluid velocity by means of techniques based on thermography. The method can be extended to any tubular PHP having conductive walls, without the need of designing a complex experimental apparatus with transparent inserts or pressure transducers.

Appendix D

In the present Appendix, the adopted calibration procedure for the fluid temperature measurement through sapphire windows is described. Such an operative technique allows a rather accurate calibration for IR acquisitions, especially useful when the radiative properties of the working fluid and the background are unknown.

The experimental set-up is constituted by two separate loops (Figure D.1): one for the background temperature control (first loop) and one for the working fluid temperature control (second loop). In the first loop, water circulates from a thermal bath (TB1, Huber® CC240 wl) through a plate heat exchanger (BG) made of copper and coated with a black, high-emissivity paint. In the second loop, liquid FC-72 is pushed by a peristaltic pump (PP, Masterflex L/S® Economy Variable-Speed Drive), and it flows, in sequence, inside a sapphire tube (ST, Precision Sapphire Technologies®, length 140 mm, OD/ID = 5/3 mm) and a copper, coiled heat exchanger immersed in a second thermal bath (TB2, Huber® CC240 wl). All the connection pipes are made of plastic, and they are thermally insulated from the environment.

The fluid temperature at the inlet and outlet of the sapphire tube is monitored by two RTDs sensors (uncertainty = 0.1°C), while the background temperature is measured by two T-type thermocouples placed on top of its front surface (uncertainty = 0.2°C). The sapphire channel is instead framed over 9.8 cm by an IR camera (FLIR® SC5500, pixel resolution: 320 x 256), positioned at a distance of 23 cm, to perform direct fluid temperature measurements by means of thermography.

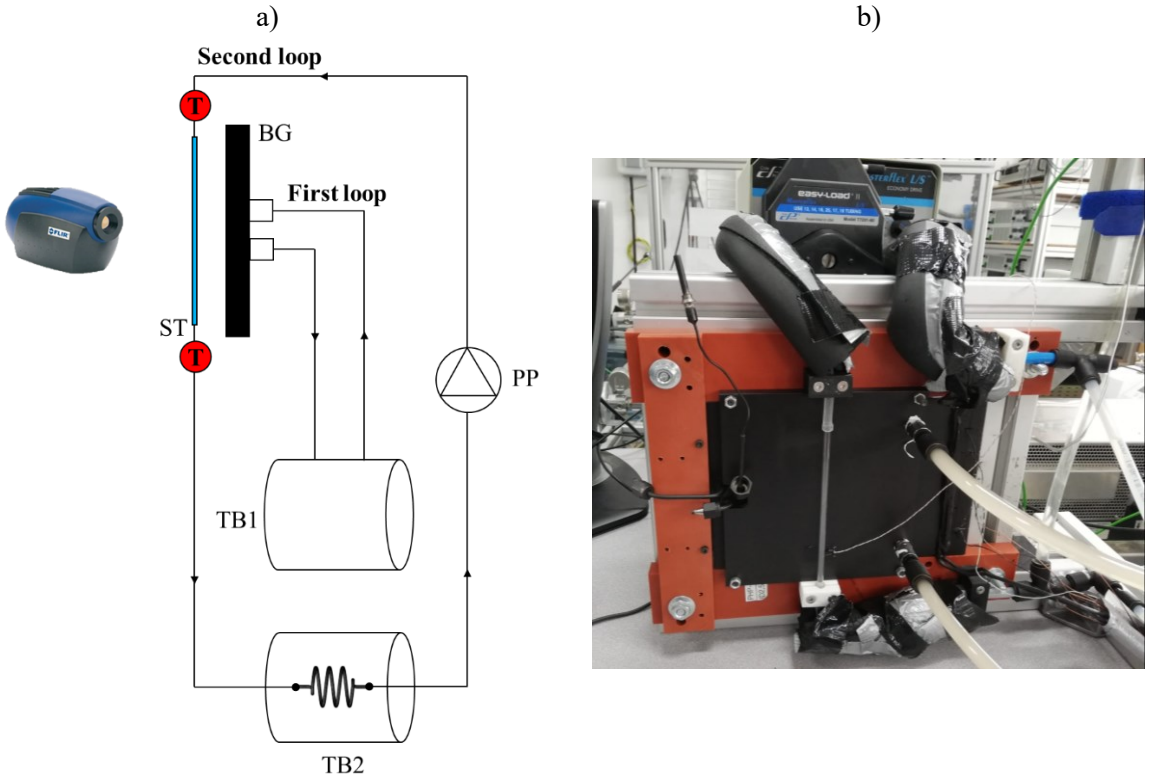

Figure D.1: Sketch of the experimental apparatus (a) and picture of the test section (b); BG: background, ST: sapphire tube, PP: peristaltic pump, TB1: thermal bath (first loop), TB2: thermal bath (second loop).

During the tests, both the background and working fluid temperatures were varied according to the experimental matrix reported in Table D.1, for a total of 8 experimental conditions. The environmental temperature was instead kept constant at 20 ± 1°C.

Table D.1: Experimental matrix.

TEST N°	T_{BG} **(TB1 set-point)** [°C]	T_f **(TB2 set-point)** [°C]
1	18	20
2	18	40
3	18	60
4	18	80
5	24	20
6	24	40
7	24	60
8	24	80

Specifically, listed background and fluid temperatures were chosen to cover the range of temperatures usually noticeable in PHPs, thus providing calibration values useful for experimental investigations on such devices.

The thermographic signals, acquired once the system reached a steady-state operation, were therefore used for tuning the calibration method, thus obtaining a calibration curve for a reliable fluid temperature measurement. In particular, by considering the sapphire walls mainly transmissive and the reflections from the environment negligible, the overall energy Q_{IR} acquired by the camera lens is defined as the sum of the energy emitted by the backscreen Q_{BG} and the ones emitted by the fluid Q_f, net of losses Q_{loss} through the sapphire tube:

$$Q_{IR} = Q_b + Q_f - Q_{loss} = \sigma\varepsilon_b\tau_w^2\tau_f T_b^4 + \sigma\varepsilon_f\tau_w T_f^4 \tag{D.1}$$

where σ is the Stefan-Boltzmann constant, ε_{BG} and ε_f are the background and fluid emissivity, respectively, τ_w and τ_f are the transmission coefficients of the sapphire wall and the liquid phase, while T_{BG} and T_f are the background and fluid temperatures. In Figure D.2, the adopted radiation model is depicted.

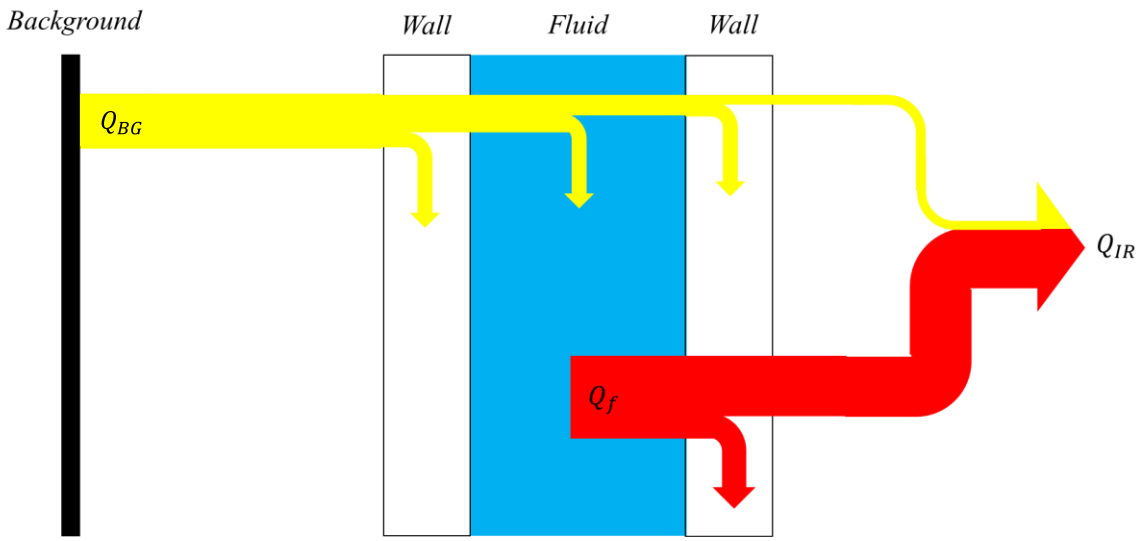

Figure D.2: Schematic of the adopted radiation model.

By introducing two different coefficients c_1 and c_2, which include the radiative properties of interest, Equation (D.1) reads as:

$$Q_{IR} = c_1 T_{BG}^4 + c_2 T_f^4 \tag{D.2}$$

It has to be stressed that, while the background and the liquid temperatures are measured, the other radiative quantities, included in the c_1 and c_2 coefficients, are, in the present case, practically unknown. An auxiliary definition for Q_{IR} is thus needed:

$$Q_{IR}{}' = \sigma \varepsilon_{set} T_{cam}^4 \tag{D.3}$$

being ε_{set} the emissivity value set within the camera parameters (here chosen equal to 1) and T_{cam} the temperature output provided by the thermographic measurements. Hence, c_1 and c_2 can be evaluated by solving the following minimization problem:

$$\min_{c_1, c_2 \in R^+} f(c_1, c_2) ; f(c_1, c_2) = c_1 T_{BG}^4 + c_2 T_f^4 - \sigma \varepsilon_{set} T_{cam}^4 \tag{D.4}$$

By rearranging Equation (D.2), the formulation for the fluid temperature finally reads as:

$$T_f = \sqrt[4]{\frac{Q_{IR}{}' - c_1 T_b^4}{c_2}} \tag{D.5}$$

In Figure D.3, a sample of IR acquisition is shown. The value of T_{cam} was assessed, for every test condition, by averaging the temperature over the blue-box area, located in the middle portion of the tube.

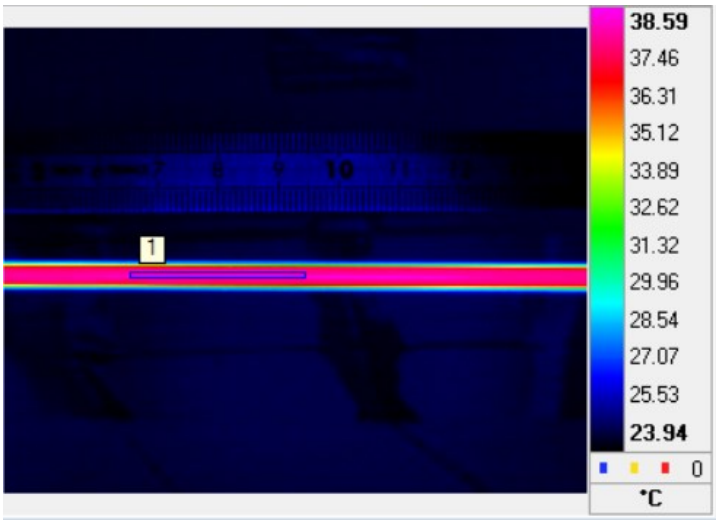

Figure D.3: Sample of IR acquisition, with reference to the area used for the T_{cam} evaluation.

T_f and T_{BG} were instead evaluated by averaging, over a 1-minute-long window, the signals referred to both the RTDs and the thermocouples, respectively, for every test case. Both the measured vectors, having 8 elements each (one for every test case), were adopted in Equation (D.4), resulting in c_1 = 2.68E-9 and c_2 = 5.43E-8.

The measured radiative heat fluxes per square meter Q_{IR}, obtained by Equation (D.3), and the one resulting from Equation (D.4) are compared in Figure D.4. Here, the points lay on the bisection, confirming the validity of the proposed coefficients.

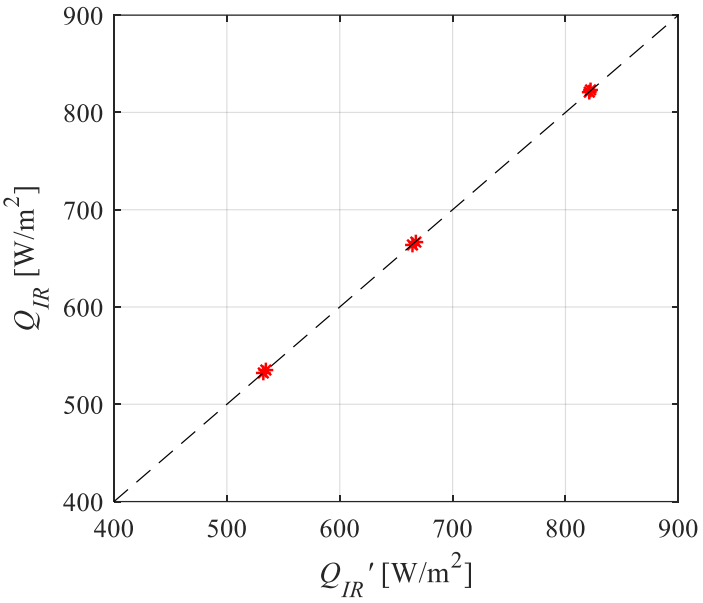

Figure D.4: Radiative heat flux resulting from the minimization problem versus measured radiative heat flux.

Starting from the IR measurements, the fluid temperature (liquid phase) is finally evaluated as:

$$T_f = \sqrt[4]{\frac{Q_{IR} - 2.68E-9 * T_{BG}^4}{5.43E-8}} \tag{D.6}$$

An error analysis on the proposed technique is furthermore performed by evaluating the residual E between the measured fluid temperature (thermal bath set-point) and the one evaluated by means of Equation (D.6). E is plotted in graph of Figure D.5 as a function of T_f imposed by TB2 in the range 40 - 80°C. The maximum error of about 0.1°C was obtained for background temperature equal to 24°C and fluid temperature equal to 60°C.

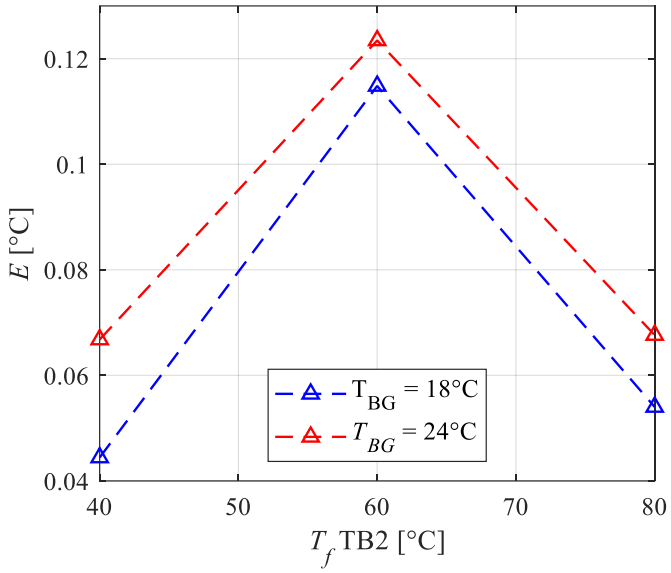

Figure D.5: Estimation error for the fluid temperature evaluation, as a function of the imposed fluid temperature for the two considered background temperatures.

To conclude, it has to be pointed out that the present calibration is sensitive to several factors:

- Properties of the IR camera sensor;
- Distance between IR camera and sapphire channel;
- Distance between sapphire channel and background;
- Radiative properties of the background;
- Radiative properties of the working fluid.

Hence, despite its simplicity and general feasibility, the here proposed experimental procedure needs to be repeated when extended to other layouts or operating conditions, since its outcomes depend on the specific application and experimental equipment used for tests on real devices.

List of tables

List of figures

List of publications

International Journals

- Pagliarini L., Cattani L., Bozzoli F., Mameli M., Filippeschi S., Rainieri S., Marengo M., "Thermal characterization of a multi-turn pulsating heat pipe in microgravity conditions: Statistical approach to the local wall-to-fluid heat flux", International Journal of Heat and Mass Transfer, 195, 117144 (2021).
- Pagliarini L, Cattani L., Mameli M., Filippeschi S., Bozzoli F., Rainieri S., "Global and local heat transfer behaviour of a three-dimensional Pulsating Heat Pipe: combined effect of the heat load, orientation and condenser temperature", Applied Thermal Engineering, 195, 117144 (2021).
- Cattani L, Vocale P, Bozzoli F, Malavasi M, Pagliarini L, Iwata N, "Global and local performances of a tubular micro-pulsating heat pipe: experimental investigation." Heat and Mass Transfer 1-19 (2022).
- Iwata N, Bozzoli F, Pagliarini L, Cattani L, Vocale P, Malavasi M, Rainieri S, "Characterization of thermal behavior of a micro pulsating heat pipe by local heat transfer investigation", International Journal of Heat and Mass Transfer, 1;196:123203 (2022).

Conference Papers

- Pagliarini L, Spiga M, Vocale P, "An analytical approach to the cooling of a flat plate", Journal of Physics: Conference Series Vol. 1868, No. 1, p. 012003 (2021).

- Vocale P, Pagliarini L, Spiga M, “Transient free convection in open-ended vertical channels”, Journal of Physics: Conference Series, Vol. 1868, No. 1, p. 012006 (2021).
- Pagliarini L, Cattani L, Bozzoli F, Slobodeniuk M, Ayel V, Romestant C, Bertin Y, Rainieri S, “Study on the local heat transfer behaviour in a flat plate pulsating heat pipe”, Journal of Physics: Conference Series, Vol. 2177, No. 1, p. 012038 (2022).
- Iwata N, Bozzoli F, Cattani L, Pagliarini L, Vocale P, “Effect of Different Cooling Methods on Thermal Performance of Single Loop Pulsating Heat Pipe”, Journal of Physics: Conference Series Vol. 2177, No. 1, p. 012035 (2022).

Conference Proceedings

- L. Pagliarini, P. Vocale, M. Spiga, An analytical approach to the cooling of a flat plate, 2020 UIT Seminar on Heat Transfer, Gaeta, Italy, September 28, 2020.
- L. Pagliarini, L. Cattani, F. Bozzoli, M. Slobodeniuk, V. Ayel, C. Romestant, Y. Bertin, S. Rainieri, Study on the local heat transfer behaviour in a flat plate pulsating heat pipe, XXXVIII UIT Heat Transfer Conference, Gaeta, Italy, June 21-22, 2021.
- L. Pagliarini, L. Cattani, M. Mameli, S. Filippeschi, F. Bozzoli, Heat Transfer Delay Method for the average fluid velocity evaluation in a multi-turn pulsating heat pipe, Joint 20th International Heat Pipe Conference and 14th International Heat Pipe Symposium, Gelendzhik, Russia, September 7-10, 2021.
- L. Pagliarini, K. G. Domiciano, L. Krambeck, F. Bozzoli, M. Mantelli, Local heat flux analysis of a thin Loop Heat Pipe, 7th AIGE/IIETA International conference and 16th AIGE Conference, Parma, Italy, June 8-9, 2022

Bibliography

[1] S.M. Sohel Murshed, C.A. Nieto de Castro, A critical review of traditional and emerging techniques and fluids for electronics cooling, Renewable and Sustainable Energy Reviews. 78 (2017) 821–833. https://doi.org/10.1016/J.RSER.2017.04.112.

[2] A.J. Hanford, L.M. Engineering, S. Services, M.K. Ewert, L.B.J.S. Center, N. Aeronautics, Advanced Active Thermal Control Systems Architecture Study, Control. (1996).

[3] D. Patil Aniket, B. Yarasu Ravindra, Factors affecting the thermal performance of two phase closed thermosyphon: a review, Int. J. of Emerging Technology and Advanced Engineering. 2 (2012) 202–206.

[4] S. Filippeschi, On periodic two-phase thermosyphons operating against gravity, International Journal of Thermal Sciences. 45 (2006) 124–137. https://doi.org/10.1016/j.ijthermalsci.2005.06.008.

[5] H.N. Chaudhry, B.R. Hughes, S.A. Ghani, A review of heat pipe systems for heat recovery and renewable energy applications, Renewable and Sustainable Energy Reviews. 16 (2012) 2249–2259. https://doi.org/https://doi.org/10.1016/j.rser.2012.01.038.

[6] P. Nemec, A. Čaja, M. Malcho, Mathematical model for heat transfer limitations of heat pipe, Math Comput Model. 57 (2013) 126–136. https://doi.org/https://doi.org/10.1016/j.mcm.2011.06.047.

[7] X. Yang, Y.Y. Yan, D. Mullen, Recent developments of lightweight, high performance heat pipes, Appl Therm Eng. 33–34 (2012) 1–14. https://doi.org/https://doi.org/10.1016/j.applthermaleng.2011.09.006.

[8] S. Launay, V. Sartre, J. Bonjour, Parametric analysis of loop heat pipe operation: a literature review, International Journal of Thermal Sciences. 46 (2007) 621–636. https://doi.org/https://doi.org/10.1016/j.ijthermalsci.2006.11.007.

[9] H. Akachi, Structure of a Heat Pipe, US Patent. 14 (1990) 595–599. https://doi.org/10.1016/0375-6505(85)90011-2.

[10] H. Yang, S. Khandekar, M. Groll, Operational limit of closed loop pulsating heat pipes, Appl Therm Eng. 28 (2008) 49–59. https://doi.org/https://doi.org/10.1016/j.applthermaleng.2007.01.033.

[11] Y. Zhang, A. Faghri, Advances and unsolved issues in pulsating heat pipes, Heat Transfer Engineering. 29 (2008) 20–44. https://doi.org/10.1080/01457630701677114.

[12] A. Faghri, Heat pipes: review, opportunities and challenges, Frontiers in Heat Pipes (FHP). 5 (2014).

[13] V. Patel, N. Mehta, K. Mehta, A. Badgujar, S. Mehta, N. Bora, Experimental Investigation of Flat Plate Cryogenic Oscillating Heat Pipe, J Low Temp Phys. 198 (2020) 41–55. https://doi.org/10.1007/s10909-019-02243-1.

[14] A. Yoon, S.J. Kim, Characteristics of oscillating flow in a micro pulsating heat pipe: Fundamental-mode oscillation, Int J Heat Mass Transf. 109 (2017) 242–253. https://doi.org/https://doi.org/10.1016/j.ijheatmasstransfer.2017.02.003.

[15] Y.-Z. Ling, X.-H. She, X.-S. Zhang, T.-T. Chen, X.-R. Lin, J.-K. Feng, A PCM-based thermal management system combining three-dimensional pulsating heat pipe with forced-air cooling, Appl Therm Eng. 213 (2022) 118732. https://doi.org/https://doi.org/10.1016/j.applthermaleng.2022.118732.

[16] C.-Y. Tseng, K.-S. Yang, C.-C. Wang, Non-Uniform Three-Dimensional Pulsating Heat Pipe for Anti-Gravity High-Flux Applications, Energies (Basel). 13 (2020). https://doi.org/10.3390/en13123068.

[17] G. Karimi, J.R. Culham, Review and assessment of Pulsating Heat Pipe mechanism for high heat flux electronic cooling, in: The Ninth Intersociety Conference on Thermal and Thermomechanical Phenomena In Electronic Systems (IEEE Cat. No.04CH37543), 2004: pp. 52-59 Vol.2. https://doi.org/10.1109/ITHERM.2004.1318252.

[18] S. Khandekar, P.K. Panigrahi, F. Lefèvre, J. Bonjour, LOCAL HYDRODYNAMICS OF FLOW IN A PULSATING HEAT PIPE: A REVIEW, in: 2010.

[19] P.A. Kew, K. Cornwell, Correlations for the prediction of boiling heat transfer in small-diameter channels, Appl Therm Eng. 17 (1997) 705–715. https://doi.org/https://doi.org/10.1016/S1359-4311(96)00071-3.

[20] L. Pietrasanta, M. Mameli, D. Mangini, A. Georgoulas, N. Michè, S. Filippeschi, M. Marengo, Developing flow pattern maps for accelerated two-phase capillary flows, Exp Therm Fluid Sci. 112 (2020) 109981. https://doi.org/https://doi.org/10.1016/j.expthermflusci.2019.109981.

[21] L.D. Fonseca, F. Miller, J. Pfotenhauer, Experimental heat transfer analysis of a cryogenic nitrogen pulsating heat Pipe at various liquid fill ratios, Appl Therm Eng. 130 (2018) 343–353. https://doi.org/https://doi.org/10.1016/j.applthermaleng.2017.11.029.

[22] B.S. Taft, A.D. Williams, B.L. Drolen, Review of Pulsating Heat Pipe Working Fluid Selection, J Thermophys Heat Trans. 26 (2012) 651–656. https://doi.org/10.2514/1.T3768.

[23] J. Gu, M. Kawaji, R. Futamata, Effects of Gravity on the Performance of Pulsating Heat Pipes, J Thermophys Heat Trans. 18 (2004) 370–378. https://doi.org/10.2514/1.3067.

[24] T. Harirchian, S. v Garimella, A comprehensive flow regime map for microchannel flow boiling with quantitative transition criteria, Int J Heat Mass Transf. 53 (2010) 2694–2702. https://doi.org/https://doi.org/10.1016/j.ijheatmasstransfer.2010.02.039.

[25] S. Khandekar, Thermo-hydrodynamics of closed loop pulsating heat pipes, (2004).

[26] H. Han, X. Cui, Y. Zhu, T. Xu, Y. Sui, S. Sun, Experimental study on a closed-loop pulsating heat pipe (CLPHP) charged with water-based binary zeotropes and the corresponding pure fluids, Energy. 109 (2016) 724–736. https://doi.org/https://doi.org/10.1016/j.energy.2016.05.061.

[27] M. Alhuyi Nazari, M.H. Ahmadi, R. Ghasempour, M.B. Shafii, How to improve the thermal performance of pulsating heat pipes: A review on working fluid, Renewable and Sustainable Energy Reviews. 91 (2018) 630–638. https://doi.org/https://doi.org/10.1016/j.rser.2018.04.042.

[28] P. Charoensawan, P. Terdtoon, Thermal performance of horizontal closed-loop oscillating heat pipes, Appl Therm Eng. 28 (2008) 460–466. https://doi.org/https://doi.org/10.1016/j.applthermaleng.2007.05.007.

[29] P. Charoensawan, S. Khandekar, M. Groll, P. Terdtoon, Closed loop pulsating heat pipes - Part A: Parametric experimental investigations, Appl Therm Eng. 23 (2003) 2009–2020. https://doi.org/10.1016/S1359-4311(03)00159-5.

[30] X. Liu, X. Han, Z. Wang, G. Hao, Z. Zhang, Y. Chen, Application of an anti-gravity oscillating heat pipe on enhancement of waste heat recovery, Energy Convers Manag. 205 (2020) 112404. https://doi.org/https://doi.org/10.1016/j.enconman.2019.112404.

[31] J. Qu, Q. Wang, Experimental study on the thermal performance of vertical closed-loop oscillating heat pipes and correlation modeling, Appl Energy. 112 (2013) 1154–1160. https://doi.org/10.1016/j.apenergy.2013.02.030.

[32] T. Daimaru, H. Nagai, Operational Characteristics of the Oscillating Heat Pipe with Noncondensable Gas, J Thermophys Heat Trans. 29 (2015) 563–571. https://doi.org/10.2514/1.T4461.

[33] C.-H. Sun, C.-Y. Tseng, K.-S. Yang, S.-K. Wu, C.-C. Wang, Investigation of the evacuation pressure on the performance of pulsating heat pipe, International Communications in Heat and Mass Transfer. 85 (2017) 23–28. https://doi.org/https://doi.org/10.1016/j.icheatmasstransfer.2017.04.005.

[34] M. Alhuyi Nazari, M.H. Ahmadi, R. Ghasempour, M.B. Shafii, O. Mahian, S. Kalogirou, S. Wongwises, A review on pulsating heat pipes: From solar to cryogenic applications, Appl Energy. 222 (2018) 475–484. https://doi.org/https://doi.org/10.1016/j.apenergy.2018.04.020.

[35] J. Lim, S.J. Kim, Fabrication and experimental evaluation of a polymer-based flexible pulsating heat pipe, Energy Convers Manag. 156 (2018) 358–364. https://doi.org/https://doi.org/10.1016/j.enconman.2017.11.022.

[36] R.-G. Chi, W.-S. Chung, S.-H. Rhi, Thermal Characteristics of an Oscillating Heat Pipe Cooling System for Electric Vehicle Li-Ion Batteries, Energies (Basel). 11 (2018). https://doi.org/10.3390/en11030655.

[37] S. Rittidech, A. Boonyaem, P. Tipnet, CPU Cooling of Desktop PC by Closed-end Oscillating Heat-pipe (CEOHP), Am J Appl Sci. 2 (2005). https://doi.org/10.3844/ajassp.2005.1574.1577.

[38] L. Pietrasanta, G. Postorino, R. Perna, M. Mameli, S. Filippeschi, A pulsating heat pipe embedded radiator: Thermal-vacuum characterisation in the pre-cryogenic temperature range for space applications, Thermal Science and Engineering Progress. 19 (2020) 100622. https://doi.org/https://doi.org/10.1016/j.tsep.2020.100622.

[39] L. Aref, R. Fallahzadeh, S.R. Shabanian, M. Hosseinzadeh, A novel dual-diameter closed-loop pulsating heat pipe for a flat plate solar collector, Energy. 230 (2021) 120751. https://doi.org/https://doi.org/10.1016/j.energy.2021.120751.

[40] A.S. Barrak, A.A.M. Saleh, Z.H. Naji, A Heat Recovery Device using Oscillating Heat Pipe with Circular and Elliptical Tubes, International Journal of Automotive and Mechanical Engineering. 18 (2021) 8442–8453.

[41] D. Bastakoti, H. Zhang, D. Li, W. Cai, F. Li, An overview on the developing trend of pulsating heat pipe and its performance, Appl Therm Eng. 141 (2018) 305–332. https://doi.org/10.1016/J.APPLTHERMALENG.2018.05.121.

[42] S. Rittidech, P. Terdtoon, M. Murakami, P. Kamonpet, W. Jompakdee, Correlation to predict heat transfer characteristics of a closed-end oscillating heat pipe at normal operating condition, Appl Therm Eng. 23 (2003) 497–510. https://doi.org/https://doi.org/10.1016/S1359-4311(02)00215-6.

[43] T. Katpradit, T. Wongratanaphisan, P. Terdtoon, P. Kamonpet, A. Polchai, A. Akbarzadeh, Correlation to predict heat transfer characteristics of a closed end oscillating heat pipe at critical state, Appl Therm Eng. 25 (2005) 2138–2151. https://doi.org/https://doi.org/10.1016/j.applthermaleng.2005.01.009.

[44] M. Ebrahimi Dehshali, M.A. Nazari, M.B. Shafii, Thermal performance of rotating closed-loop pulsating heat pipes: Experimental investigation and semi-empirical correlation, International Journal of Thermal Sciences. 123 (2018) 14–26. https://doi.org/https://doi.org/10.1016/j.ijthermalsci.2017.09.009.

[45] S. Khandekar, P. Charoensawan, M. Groll, P. Terdtoon, Closed loop pulsating heat pipes Part B: visualization and semi-empirical modeling, Appl Therm Eng. 23 (2003) 2021–2033. https://doi.org/https://doi.org/10.1016/S1359-4311(03)00168-6.

[46] M.H. Ahmadi, A. Tatar, M. Alhuyi Nazari, R. Ghasempour, A.J. Chamkha, W.-M. Yan, Applicability of connectionist methods to predict thermal resistance of pulsating heat pipes with ethanol by using neural networks, Int J Heat Mass Transf. 126 (2018) 1079–1086. https://doi.org/https://doi.org/10.1016/j.ijheatmasstransfer.2018.06.085.

[47] X. Wang, Y. Yan, X. Meng, G. Chen, A general method to predict the performance of closed pulsating heat pipe by artificial neural network, Appl Therm Eng. 157 (2019) 113761. https://doi.org/10.1016/j.applthermaleng.2019.113761.

[48] M. Marengo, V.S. Nikolayev, Pulsating Heat Pipes: Experimental Analysis, Design and Applications, (2018) 1–62. https://doi.org/10.1142/9789813234406_0001.

[49] A. Takawale, S. Abraham, A. Sielaff, P.S. Mahapatra, A. Pattamatta, P. Stephan, A comparative study of flow regimes and thermal performance between flat plate pulsating heat pipe and capillary tube pulsating heat pipe, Appl Therm Eng. 149 (2019) 613–624. https://doi.org/https://doi.org/10.1016/j.applthermaleng.2018.11.119.

[50] V.K. Karthikeyan, S. Khandekar, B.C. Pillai, P.K. Sharma, Infrared thermography of a pulsating heat pipe: Flow regimes and multiple steady states, Appl Therm Eng. 62 (2014) 470–480. https://doi.org/https://doi.org/10.1016/j.applthermaleng.2013.09.041.

[51] M. Mameli, M. Marengo, S. Khandekar, Local heat transfer measurement and thermo-fluid characterization of a pulsating heat pipe, International Journal of Thermal Sciences. 75 (2014) 140–152. https://doi.org/10.1016/j.ijthermalsci.2013.07.025.

[52] N. Qian, Y. Fu, Y. Zhang, J. Chen, J. Xu, Experimental investigation of thermal performance of the oscillating heat pipe for the grinding wheel, Int J Heat Mass Transf. 136 (2019) 911–923. https://doi.org/https://doi.org/10.1016/j.ijheatmasstransfer.2019.03.065.

[53] X. Cui, Z. Qiu, J. Weng, Z. Li, Heat transfer performance of closed loop pulsating heat pipes with methanol-based binary mixtures, Exp Therm Fluid Sci. 76 (2016) 253–263. https://doi.org/https://doi.org/10.1016/j.expthermflusci.2016.04.005.

[54] Z. Deng, Y. Zheng, X. Liu, B. Zhu, Y. Chen, Experimental study on thermal performance of an anti-gravity pulsating heat pipe and its application on heat recovery utilization, Appl Therm Eng. 125 (2017) 1368–1378. https://doi.org/https://doi.org/10.1016/j.applthermaleng.2017.07.107.

[55] D. Bastakoti, H. Zhang, W. Cai, F. Li, An experimental investigation of thermal performance of pulsating heat pipe with alcohols and surfactant solutions, Int J Heat Mass Transf. 117 (2018) 1032–1040. https://doi.org/https://doi.org/10.1016/j.ijheatmasstransfer.2017.10.075.

[56] T.-M. Liou, S.W. Chang, W.L. Cai, I.-A. Lan, Thermal fluid characteristics of pulsating heat pipe in radially rotating thin pad, Int J Heat Mass Transf. 131 (2019) 273–290. https://doi.org/https://doi.org/10.1016/j.ijheatmasstransfer.2018.10.132.

[57] K. On-ai, N. Kammuang-lue, P. Terdtoon, P. Sakulchangsatjatai, Implied physical phenomena of rotating closed-loop pulsating heat pipe from working fluid temperature, Appl Therm Eng. 148 (2019) 1303–1309. https://doi.org/https://doi.org/10.1016/j.applthermaleng.2018.11.030.

[58] M. Zufar, P. Gunnasegaran, H.M. Kumar, K.C. Ng, Numerical and experimental investigations of hybrid nanofluids on pulsating heat pipe performance, Int J Heat Mass Transf. 146 (2020) 118887. https://doi.org/https://doi.org/10.1016/j.ijheatmasstransfer.2019.118887.

[59] H. Ahmad, S.Y. Jung, Effect of active and passive cooling on the thermo-hydrodynamic behaviors of the closed-loop pulsating heat pipes, Int J Heat Mass Transf. 156 (2020) 119814. https://doi.org/https://doi.org/10.1016/j.ijheatmasstransfer.2020.119814.

[60] Y. Zhou, X. Cui, J. Weng, S. Shi, H. Han, C. Chen, Experimental investigation of the heat transfer performance of an oscillating heat pipe with graphene nanofluids, Powder Technol. 332 (2018) 371–380. https://doi.org/https://doi.org/10.1016/j.powtec.2018.02.048.

[61] M. Mameli, V. Manno, S. Filippeschi, M. Marengo, Thermal instability of a Closed Loop Pulsating Heat Pipe: Combined effect of orientation and filling ratio, Exp Therm Fluid Sci. 59 (2014) 222–229. https://doi.org/https://doi.org/10.1016/j.expthermflusci.2014.04.009.

[62] X. Cui, Y. Zhu, Z. Li, S. Shun, Combination study of operation characteristics and heat transfer mechanism for pulsating heat pipe, Appl Therm Eng. 65 (2014) 394–402. https://doi.org/10.1016/j.applthermaleng.2014.01.030.

[63] N. Zhao, H. Ma, X. Pan, Wavelet Analysis of Oscillating Motions in an Oscillating Heat Pipe, in: 2011: pp. 545–549. https://doi.org/10.1115/IMECE2011-63632.

[64] J.G. Monroe, Z.S. Aspin, J.D. Fairley, S.M. Thompson, Analysis and comparison of internal and external temperature measurements of a tubular oscillating heat pipe, Exp Therm Fluid Sci. 84 (2017) 165–178. https://doi.org/https://doi.org/10.1016/j.expthermflusci.2017.01.020.

[65] J.L. Xu, X.M. Zhang, Start-up and steady thermal oscillation of a pulsating heat pipe, Heat and Mass Transfer. 41 (2005) 685–694. https://doi.org/10.1007/s00231-004-0535-3.

[66] J.L. Xu, Y.X. Li, T.N. Wong, High speed flow visualization of a closed loop pulsating heat pipe, Int J Heat Mass Transf. 48 (2005) 3338–3351. https://doi.org/https://doi.org/10.1016/j.ijheatmasstransfer.2005.02.034.

[67] Q. Sun, J. Qu, X. Li, J. Yuan, Experimental investigation of thermo-hydrodynamic behavior in a closed loop oscillating heat pipe, Exp Therm Fluid Sci. 82 (2017) 450–458. https://doi.org/https://doi.org/10.1016/j.expthermflusci.2016.11.040.

[68] Z.H. Xue, W. Qu, Experimental and theoretical research on a ammonia pulsating heat pipe: New full visualization of flow pattern and operating mechanism study, Int J Heat Mass Transf. 106 (2017) 149–166. https://doi.org/https://doi.org/10.1016/j.ijheatmasstransfer.2016.09.042.

[69] D. Zhang, J. Guan, Z. He, C. Shen, H. Cao, Experimental investigation on heat transfer and flow patterns of pulsating heat pipe assisted by ultrasonic cavitation, Int J Heat Mass Transf. 183 (2022) 122187. https://doi.org/https://doi.org/10.1016/j.ijheatmasstransfer.2021.122187.

[70] V.M. Patel, H.B. Mehta, Channel wise displacement-velocity-frequency analysis in acetone charged multi-turn Closed Loop Pulsating Heat Pipe, Energy Convers Manag. 195 (2019) 367–383. https://doi.org/10.1016/j.enconman.2019.05.014.

[71] M. Ando, A. Okamoto, H. Nagai, Start-up and heat transfer characteristics of oscillating heat pipe with different check valve layouts, Appl Therm Eng. 196 (2021) 117286. https://doi.org/https://doi.org/10.1016/j.applthermaleng.2021.117286.

[72] A. Gandomkar, M.H. Saidi, M.B. Shafii, M. Vandadi, K. Kalan, Visualization and comparative investigations of pulsating ferro-fluid heat pipe, Appl Therm Eng. 116 (2017) 56–65. https://doi.org/https://doi.org/10.1016/j.applthermaleng.2017.01.068.

[73] A. Gandomkar, K. Kalan, M. Vandadi, M.B. Shafii, M.H. Saidi, Investigation and visualization of surfactant effect on flow pattern and performance of pulsating heat pipe, J Therm Anal Calorim. 139 (2020) 2099–2107. https://doi.org/10.1007/s10973-019-08649-z.

[74] D. Mangini, M. Mameli, A. Georgoulas, L. Araneo, S. Filippeschi, M. Marengo, A pulsating heat pipe for space applications: Ground and microgravity experiments, International Journal of Thermal Sciences. 95 (2015) 53–63. https://doi.org/https://doi.org/10.1016/j.ijthermalsci.2015.04.001.

[75] L. Cattani, D. Mangini, F. Bozzoli, L. Pietrasanta, N. Miche', M. Mameli, S. Filippeschi, S. Rainieri, M. Marengo, An original look into pulsating heat pipes: Inverse heat conduction approach for assessing the thermal behaviour, Thermal Science and Engineering Progress. 10 (2019) 317–326. https://doi.org/https://doi.org/10.1016/j.tsep.2019.02.007.

[76] L.K. Malla, P. Dhanalakota, P.S. Mahapatra, A. Pattamatta, Thermal and flow characteristics in a flat plate pulsating heat pipe with ethanol-water mixtures: From slug-plug to droplet oscillations, Int J Heat Mass Transf. 194 (2022) 123066. https://doi.org/https://doi.org/10.1016/j.ijheatmasstransfer.2022.123066.

[77] R. Xu, X. Li, T. Lei, Q. Wu, R. Wang, Operation characteristics of a gravity pulsating heat pipe under different heat inputs, Int J Heat Mass Transf. 189 (2022) 122731. https://doi.org/https://doi.org/10.1016/j.ijheatmasstransfer.2022.122731.

[78] B. Markal, A.C. Candere, M. Avci, O. Aydin, Effect of double cross sectional ratio on performance characteristics of pulsating heat pipes, International Communications in Heat and Mass Transfer. 127 (2021) 105583. https://doi.org/https://doi.org/10.1016/j.icheatmasstransfer.2021.105583.

[79] M. Slobodeniuk, R. Bertossi, V. Ayel, R. Ravichandran, K. Thyagarajan, C. Romestant, Y. Bertin, Experimental study of the flat plate pulsating heat pipe operation during dry-out and flow re-activation periods under microgravity conditions, International Journal of Multiphase Flow. 147 (2022) 103888. https://doi.org/https://doi.org/10.1016/j.ijmultiphaseflow.2021.103888.

[80] R. Xu, C. Zhang, H. Chen, Q. Wu, R. Wang, Heat transfer performance of pulsating heat pipe with zeotropic immiscible binary mixtures, Int J Heat Mass Transf. 137 (2019) 31–41. https://doi.org/https://doi.org/10.1016/j.ijheatmasstransfer.2019.03.070.

[81] B. Markal, R. Varol, Experimental investigation and force analysis of flat-plate type pulsating heat pipes having ternary mixtures, International Communications in Heat and Mass Transfer. 121 (2021) 105084. https://doi.org/https://doi.org/10.1016/j.icheatmasstransfer.2020.105084.

[82] T. Arai, M. Kawaji, Thermal performance and flow characteristics in additive manufactured polycarbonate pulsating heat pipes with Novec 7000, Appl Therm Eng. 197 (2021) 117273. https://doi.org/https://doi.org/10.1016/j.applthermaleng.2021.117273.

[83] B.Y. Tong, T.N. Wong, K.T. Ooi, Closed-loop pulsating heat pipe, Appl Therm Eng. 21 (2001) 1845–1862. https://doi.org/https://doi.org/10.1016/S1359-4311(01)00063-1.

[84] S. Khandekar, M. Groll, P. Charoensawan, P. Terdtoon, Pulsating heat pipes: thermo-fluidic characteristics and comparative study with single phase thermosyphon, in: International Heat Transfer Conference Digital Library, 2002.

[85] S. Liu, J. Li, X. Dong, H. Chen, Experimental study of flow patterns and improved configurations for pulsating heat pipes, Journal of Thermal Science. 16 (2007) 56–62. https://doi.org/10.1007/s11630-007-0056-8.

[86] S. Khandekar, A.P. Gautam, P.K. Sharma, Multiple quasi-steady states in a closed loop pulsating heat pipe, International Journal of Thermal Sciences. 48 (2009) 535–546. https://doi.org/https://doi.org/10.1016/j.ijthermalsci.2008.04.004.

[87] V.G. Pastukhov, Yu.F. Maydanik, Development of a pulsating heat pipe with a directional circulation of a working fluid, Appl Therm Eng. 109 (2016) 155–161. https://doi.org/https://doi.org/10.1016/j.applthermaleng.2016.08.076.

[88] E. Sedighi, A. Amarloo, B. Shafii, Numerical and experimental investigation of flat-plate pulsating heat pipes with extra branches in the evaporator section, Int J Heat Mass Transf. 126 (2018) 431–441. https://doi.org/https://doi.org/10.1016/j.ijheatmasstransfer.2018.05.047.

[89] Z. Wan, X. Wang, C. Feng, Heat transfer performances of the capillary loop pulsating heat pipes with spring-loaded check valve, Appl Therm Eng. 167 (2020) 114803. https://doi.org/https://doi.org/10.1016/j.applthermaleng.2019.114803.

[90] M. Ebrahimi, M.B. Shafii, M.A. Bijarchi, Experimental investigation of the thermal management of flat-plate closed-loop pulsating heat pipes with interconnecting channels, Appl Therm Eng. 90 (2015) 838–847. https://doi.org/https://doi.org/10.1016/j.applthermaleng.2015.07.040.

[91] Y.B. Kim, H. Kim, J. Sung, Investigation of thermal enhancement factor in micro pulsating heat exchanger using LIF visualization technique, Int J Heat Mass Transf. 159 (2020) 120121. https://doi.org/https://doi.org/10.1016/j.ijheatmasstransfer.2020.120121.

[92] K. Ishii, K. Fumoto, Temperature visualization and investigation inside evaporator of pulsating heat pipe using temperature-sensitive paint, Appl Therm Eng. 155 (2019) 575–583. https://doi.org/https://doi.org/10.1016/j.applthermaleng.2019.04.026.

[93] M. Francom, J. Kim, Experimental Investigation Into the Heat Transfer Mechanism of Oscillating Heat Pipes Using Temperature Sensitive Paint, J Heat Transfer. 143 (2021). https://doi.org/10.1115/1.4049512.

[94] B. Borgmeyer, C. Wilson, R.A. Winholtz, H.B. Ma, D. Jacobson, D. Hussey, Heat transport capability and fluid flow neutron radiography of three-dimensional oscillating heat pipes, J Heat Transfer. 132 (2010).

[95] S.M. Thompson, H.B. Ma, C. Wilson, Investigation of a flat-plate oscillating heat pipe with Tesla-type check valves, Exp Therm Fluid Sci. 35 (2011) 1265–1273. https://doi.org/https://doi.org/10.1016/j.expthermflusci.2011.04.014.

[96] C. Wilson, B. Borgmeyer, R.A. Winholtz, H.B. Ma, D.L. Jacobson, D.S. Hussey, M. Arif, Visual Observation of Oscillating Heat Pipes Using Neutron Radiography, J Thermophys Heat Trans. 22 (2008) 366–372. https://doi.org/10.2514/1.33758.

[97] I. Yoon, C. Wilson, B. Borgmeyer, R.A. Winholtz, H.B. Ma, D.L. Jacobson, D.S. Hussey, Neutron phase volumetry and temperature observations in an oscillating heat pipe, International Journal of Thermal Sciences. 60 (2012) 52–60. https://doi.org/https://doi.org/10.1016/j.ijthermalsci.2012.05.004.

[98] A. Hathaway, C. Wilson, H. Ma, An Experimental Investigation of Uneven Turn Water and Acetone Oscillating Heat Pipes, in: 49th AIAA Aerospace Sciences Meeting Including the New Horizons Forum and Aerospace Exposition, n.d. https://doi.org/10.2514/6.2011-810.

[99] Daniel, D. Duewer, H. Ma, R. Winholtz, C. Wilson, C. Borgmeyer, Thermal And Visual Observation Of Water And Acetone Oscillating Heat Pipes, (2021). https://tsapps.nist.gov/publication/get_pdf.cfm?pub_id=905006.

[100] L. Cattani, D. Mangini, F. Bozzoli, M. Mameli, L. Pietrasanta, N. Miche, S. Filippeschi, M. Marengo, S. Rainieri, An original look into Pulsating Heat Pipes: Inverse heat transfer approach for assessing the thermal behavior, Joint 19th IHPC and 13th IHPS. (2018).

[101] J. Jo, J. Kim, S.J. Kim, Experimental investigations of heat transfer mechanisms of a pulsating heat pipe, Energy Convers Manag. 181 (2019) 331–341. https://doi.org/10.1016/j.enconman.2018.12.027.

[102] D. Mangini, M. Marengo, L. Araneo, M. Mameli, D. Fioriti, S. Filippeschi, Infrared analysis of the two phase flow in a single closed loop pulsating heat pipe, Exp Therm Fluid Sci. 97 (2018) 304–312. https://doi.org/https://doi.org/10.1016/j.expthermflusci.2018.04.018.

[103] D. Mangini, M. Pozzoni, M. Mameli, L. Pietrasanta, M. Marengo, Infrared analysis and pressure measurements on a single loop pulsating heat pipe at different gravity levels, Joint 19th IHPC and 13th IHPS. (2018) 0–10.

[104] R. Perna, M. Abela, M. Mameli, A. Mariotti, L. Pietrasanta, M. Marengo, S. Filippeschi, Flow characterization of a pulsating heat pipe through the wavelet analysis of pressure signals, Appl

Therm Eng. 171 (2020) 115128. https://doi.org/https://doi.org/10.1016/j.applthermaleng.2020.115128.

[105] C. Jung, S.J. Kim, Effects of oscillation amplitudes on heat transfer mechanisms of pulsating heat pipes, Int J Heat Mass Transf. 165 (2021) 120642. https://doi.org/https://doi.org/10.1016/j.ijheatmasstransfer.2020.120642.

[106] D. Brutin, B. Sobac, F. Rigollet, C. le Niliot, Infrared visualization of thermal motion inside a sessile drop deposited onto a heated surface, Exp Therm Fluid Sci. 35 (2011) 521–530. https://doi.org/https://doi.org/10.1016/j.expthermflusci.2010.12.004.

[107] D.S. Jang, H.J. Chung, Y. Jeon, Y. Kim, Thermal performance characteristics of a pulsating heat pipe at various nonuniform heating conditions, Int J Heat Mass Transf. 126 (2018) 855–863. https://doi.org/https://doi.org/10.1016/j.ijheatmasstransfer.2018.05.160.

[108] H.Y. Noh, S.J. Kim, Thermal characterization and optimization of pulsating heat pipes operating in a circulation mode, Int J Heat Mass Transf. 115 (2017) 1234–1246. https://doi.org/https://doi.org/10.1016/j.ijheatmasstransfer.2017.09.004.

[109] M. Mameli, A. Catarsi, D. Mangini, L. Pietrasanta, N. Michè, M. Marengo, P. di Marco, S. Filippeschi, Start-up in microgravity and local thermodynamic states of a hybrid loop thermosyphon/pulsating heat pipe, Appl Therm Eng. 158 (2019) 113771. https://doi.org/10.1016/j.applthermaleng.2019.113771.

[110] V. Ayel, M. Slobodeniuk, R. Bertossi, A. Karmakar, F. Martineau, C. Romestant, Y. Bertin, S. Khandekar, Thermal performances of a flat-plate pulsating heat pipe tested with water, aqueous mixtures and surfactants, International Journal of Thermal Sciences. 178 (2022) 107599. https://doi.org/https://doi.org/10.1016/j.ijthermalsci.2022.107599.

[111] V. Ayel, L. Araneo, P. Marzorati, C. Romestant, Y. Bertin, M. Marengo, Visualization of Flow Patterns in Closed Loop Flat Plate Pulsating Heat Pipe Acting as Hybrid Thermosyphons under Various Gravity Levels, Heat Transfer Engineering. 40 (2019) 227–237. https://doi.org/10.1080/01457632.2018.1426244.

[112] O. Der, A.A. Alqahtani, M. Marengo, V. Bertola, Characterization of polypropylene pulsating heat stripes: Effects of orientation, heat transfer fluid, and loop geometry, Appl Therm Eng. 184 (2021) 116304. https://doi.org/https://doi.org/10.1016/j.applthermaleng.2020.116304.

[113] V.K. Karthikeyan, K. Ramachandran, B.C. Pillai, A. Brusly Solomon, Understanding thermo-fluidic characteristics of a glass tube closed loop pulsating heat pipe: flow patterns and fluid oscillations, Heat and Mass Transfer. 51 (2015) 1669–1680. https://doi.org/10.1007/s00231-015-1525-3.

[114] P.C. Hansen, Discrete inverse problems: insight and algorithms, SIAM, 2010.

[115] R.C. Aster, B. Borchers, C.H. Thurber, Parameter estimation and inverse problems, Elsevier, 2018.

[116] M.N. Özisik, H.R.B. Orlande, Inverse heat transfer: fundamentals and applications, CRC press, 2021.

[117] J. Hadamard, Lectures on Cauchy's problem in linear partial differential equations, Courier Corporation, 2003.

[118] K.G.E.-V.S. Vikhrenko, Inverse Heat Conduction Problems, in: IntechOpen, Rijeka, 2011: p. Ch. 1. https://doi.org/10.5772/26575.

[119] A. Tikhonov, Solutions of ill-posed problems, n.d.

[120] L.G. Shapiro, G. Stockman, Computer vision prentice hall, Inc., New Jersey. (2001).

[121] C. Rowley, A. González, E.J. O'brien, A. Žnidari\vc, Comparison of conventional and regularized bridge weigh-in-motion algorithms, in: 2013.

[122] V.A. Morozov, Methods for solving incorrectly posed problems, Springer Science \& Business Media, 2012.

[123] J.M. Lilly, Element analysis: a wavelet-based method for analysing time-localized events in noisy time series, Proceedings of the Royal Society A: Mathematical, Physical and Engineering Sciences. 473 (2017) 20160776.

[124] I.E. Frank, R. Todeschini, The data analysis handbook, Elsevier, 1994.

[125] Z. Milanović, N. Saulig, I. Marasović, D. Seršić, Spectrogram-based assessment of small SNR variations, with application to medical electrodes, EURASIP J Adv Signal Process. 2019 (2019) 38. https://doi.org/10.1186/s13634-019-0634-4.

[126] T. Caliński, J. Harabasz, A dendrite method for cluster analysis, Communications in Statistics. 3 (1974) 1–27. https://doi.org/10.1080/03610927408827101.

[127] B.S. Everitt, A. Skrondal, The Cambridge dictionary of statistics, (2010).

[128] P. Stoica, R.L. Moses, Spectral Analysis of Signals, Upper Saddle River, N.J. : Pearson/Prentice Hall., 2008. https://doi.org/10.1109/msp.2007.273066.

[129] D. Mangini, M. Marengo, L. Araneo, M. Mameli, D. Fioriti, S. Filippeschi, Infrared analysis of the two phase flow in a single closed loop pulsating heat pipe, Exp Therm Fluid Sci. 97 (2018) 304–312. https://doi.org/10.1016/j.expthermflusci.2018.04.018.

[130] V. Pletser, European aircraft parabolic flights for microgravity research, applications and exploration: A review, REACH. (2016). https://doi.org/10.1016/j.reach.2016.05.002.

[131] D. Mangini, M. Mameli, D. Fioriti, S. Filippeschi, L. Araneo, M. Marengo, Hybrid Pulsating Heat Pipe for space applications with non-uniform heating patterns: Ground and microgravity experiments, Appl Therm Eng. 126 (2017) 1029–1043. https://doi.org/https://doi.org/10.1016/j.applthermaleng.2017.01.035.

[132] R.R. Riehl, S.M.S. Murshed, Life Time Expectancy Prediction and Ageing Process of Heat Pipes Using Nanofluids, Heat Transfer Engineering. 42 (2021) 1755–1764. https://doi.org/10.1080/01457632.2020.1818423.

[133] C.D. Henry, J. Kim, B. Chamberlain, T.G. Hartman, Heater size and heater aspect ratio effects on subcooled pool boiling heat transfer in low-g, Exp Therm Fluid Sci. 29 (2005) 773–782.

[134] S.J. Kline, Describing Uncertainties in Single-Sample Experiments, Mechanical Engineering. 75 (1953) 3–8.

[135] X. Han, X. Wang, H. Zheng, X. Xu, G. Chen, Review of the development of pulsating heat pipe for heat dissipation, Renewable and Sustainable Energy Reviews. 59 (2016) 692–709. https://doi.org/10.1016/J.RSER.2015.12.350.

[136] J. Qu, J. Zhao, Z. Rao, Experimental investigation on the thermal performance of three-dimensional oscillating heat pipe, Int J Heat Mass Transf. 109 (2017) 589–600. https://doi.org/https://doi.org/10.1016/j.ijheatmasstransfer.2017.02.040.

[137] B. Verma, V.L. Yadav, K.K. Srivastava, Experimental study on thermal performance of pulsating heat pipe with al2o3-deionizedwater nanofluid at different orientations, Journal of Enhanced Heat Transfer. 20 (2013) 153–163. https://doi.org/10.1615/JEnhHeatTransf.2013006540.

[138] V. Ayel, L. Araneo, A. Scalambra, M. Mameli, C. Romestant, A. Piteau, M. Marengo, S. Filippeschi, Y. Bertin, Experimental study of a closed loop flat plate pulsating heat pipe under a varying gravity force, International Journal of Thermal Sciences. 96 (2015) 23–34. https://doi.org/https://doi.org/10.1016/j.ijthermalsci.2015.04.010.

[139] M. Mameli, L. Araneo, S. Filippeschi, L. Marelli, R. Testa, M. Marengo, Thermal response of a closed loop pulsating heat pipe under a varying gravity force, International Journal of Thermal Sciences. 80 (2014) 11–22. https://doi.org/https://doi.org/10.1016/j.ijthermalsci.2014.01.023.

[140] C. Feng, Z. Wan, H. Mo, H. Tang, L. Lu, Y. Tang, Heat transfer characteristics of a novel closed-loop pulsating heat pipe with a check valve, Appl Therm Eng. 141 (2018) 558–564. https://doi.org/https://doi.org/10.1016/j.applthermaleng.2018.06.010.

[141] M.L. Huber, E.W. Lemmon, I.H. Bell, M.O. McLinden, The NIST REFPROP Database for Highly Accurate Properties of Industrially Important Fluids, Ind Eng Chem Res. 0 (n.d.) null. https://doi.org/10.1021/acs.iecr.2c01427.

[142] S. Jun, S.J. Kim, Comparison of the thermal performances and flow characteristics between closed-loop and closed-end micro pulsating heat pipes, Int J Heat Mass Transf. 95 (2016) 890–901. https://doi.org/https://doi.org/10.1016/j.ijheatmasstransfer.2015.12.064.

[143] J. Qu, H. Wu, P. Cheng, Start-up, heat transfer and flow characteristics of silicon-based micro pulsating heat pipes, Int J Heat Mass Transf. 55 (2012) 6109–6120. https://doi.org/https://doi.org/10.1016/j.ijheatmasstransfer.2012.06.024.

[144] K.-H. Chien, Y.-T. Lin, Y.-R. Chen, K.-S. Yang, C.-C. Wang, A novel design of pulsating heat pipe with fewer turns applicable to all orientations, Int J Heat Mass Transf. 55 (2012) 5722–5728. https://doi.org/https://doi.org/10.1016/j.ijheatmasstransfer.2012.05.068.

[145] V. Ayel, M. Slobodeniuk, R. Bertossi, C. Romestant, Y. Bertin, Flat plate pulsating heat pipes: A review on the thermohydraulic principles, thermal performances and open issues, Appl Therm Eng. 197 (2021) 117200. https://doi.org/https://doi.org/10.1016/j.applthermaleng.2021.117200.

[146] S. Khandekar, THERMOFLUID DYNAMIC STUDY OF FLAT-PLATE CLOSED-LOOP PULSATING HEAT PIPES, Microscale Thermophysical Engineering. 6 (2003) 303–317. https://doi.org/10.1080/10893950290098340.

[147] D.J. Kearney, O. Suleman, J. Griffin, G. Mavrakis, Thermal performance of a PCB embedded pulsating heat pipe for power electronics applications, Appl Therm Eng. 98 (2016) 798–809. https://doi.org/https://doi.org/10.1016/j.applthermaleng.2015.11.123.

[148] B. Borgmeyer, H.B. Ma, Experimental Investigation of Oscillating Motions in a Flat Plate Pulsating Heat Pipe, J Thermophys Heat Trans. 21 (2007) 405–409. https://doi.org/10.2514/1.23263.

[149] Y. Yasuda, F. Nabeshima, K. Horiuchi, H. Nagai, Visualization of the working fluid in a flat-plate pulsating heat pipe by neutron radiography, Int J Heat Mass Transf. 185 (2022) 122336. https://doi.org/https://doi.org/10.1016/j.ijheatmasstransfer.2021.122336.

[150] H.Y. Noh, A. Yoon, S.J. Kim, Investigation into the effect of transverse condudction on the thermal performance of a flat-plate pulsating heat pipe, Int J Heat Mass Transf. 181 (2021) 121842. https://doi.org/https://doi.org/10.1016/j.ijheatmasstransfer.2021.121842.

[151] P.T. Tsilingiris, Comparative evaluation of the infrared transmission of polymer films, Energy Convers Manag. 44 (2003) 2839–2856. https://doi.org/https://doi.org/10.1016/S0196-8904(03)00066-9.

[152] K.G. Domiciano, L. Krambeck, J.P.M. Flórez, M.B.H. Mantelli, Thin diffusion bonded flat loop heat pipes for electronics: Fabrication, modelling and testing, Energy Convers Manag. 255 (2022) 115329. https://doi.org/https://doi.org/10.1016/j.enconman.2022.115329.

Nomenclature

Symbol	Quantity	SI Unit
a	Scale dilation parameter	1/Hz
A	Heat flux amplitude	W/m^2
A_{av}	Average heat flux amplitude	W/m^2
Amp	Amplitude of analytical heat flux	W/m^2K
c_p	Specific heat at constant pressure	J/kg·K
cvf	Coefficient of variation (dominant frequency)	%
cvs	Coefficient of variation (space)	%
cvt	Coefficient of variation (time)	%
cvt_{av}	Mean of the coefficient of variations over the whole device	%
cvt_{std}	Standard deviation of the coefficients of variation over the whole device	%
d	Diameter	m
E	Estimation error (heat flux)	%
f	Frequency	Hz
$\mathcal{F}$	Discrete fast Fourier transform	-
f, g	Signals, functions of time	-
f_D	Dominant frequency	Hz
$fmax$	Wavelet maximum frequency	Hz
$fmin$	Wavelet minimum frequency	Hz
g	Gravity acceleration	m/s^2
h	Convective heat-transfer coefficient	$W/m^2·K$
H	Gaussian filter transfer function	-
i	Channel number	-
k	Thermal conductivity	W/m·K
L	Length	m
$Ladiab$	Length of the adiabatic section	m

M	Number of time samples of the generic thermographic temperature distribution	-
$mean$	Arithmetic mean	-
N	Number of axial coordinates of the generic thermographic temperature distribution	-
n	Channel number	-
num	Total number of channels	-
O	Number of spatial coordinates along the y axis	-
P	Power input to the evaporator	W
P_w	Power spectrum magnitude	$W/m^2/Hz^{3/2}$
Q	Power	W
q	Convective heat flux per unit surface	W/m^2
q_{av}	Heat flux averaged over time	W/m^2
$Q_{conduction}$	Power transferred by conduction between evaporator and condenser	W
q_{exact}	Synthetic heat flux	W/m2
q_{Fou}	Heat exchanged between adjacent channels	W/m2
Q_{net}	Net power input to the evaporator, considering heat dissipation to the environment	W
Q_{ratio}	Power transferred by transverse conduction by a single channel, divided by power transferrable from evaporator to condenser	%
$q_{restored}$	Restored synthetic heat flux	W/m2
Q_{TRcond}	Transverse conduction between channels pairs	W
r	Tube radius	m
r^*	Normalized cross-correlation function	-
$ratio$	Optimal ratio between time and space cut-off frequencies	-
R_{env}	Overall heat-transfer resistance between the external tube wall and the surrounding environment	$m^2 \cdot K/W$
R_{eq}	Equivalent thermal resistance	K/W
s	Wall thickness	m
S'_{eva}	Non-insulated evaporator outer surface	m^2
S_{copper}	Full metallic cross-section	m^2
std	Standard deviation	-
t	Time	s
T	Temperature	K
t^*	Absolute time	s
T_{env}	Environmental temperature	K
T_f	Filtered experimental temperature	K
T_{FPPHP}	Device thickness	m
t_t	Continuity time	s
U	Internal energy	J
u, v	Frequency components	rad^{-1}

u_c, w_c	Cut-off frequencies	rad^{-1}
v_{av}	Average fluid velocity	m/s
W_{FPPHP}	Device width	M
x_{int}	Half of the channel height	M
z	Axial coordinate	m
α	Angular coordinate	rad
ΔP	Fluid pressure difference	Pa
E	Emissivity	-
η	Dimensionless time	-
ρ	Density	kg/m^3
σ	Noise level	K
τ	Time lag	s
Φ	Cumulative distribution function	-
ψ	Wavelet mother	-

Subscripts, superscripts

80	80^{th} percentile
cc	compensation chamber
cond	condenser
env	environment
eva	evaporator
exact	exact value
f	filtered
in	inner
l	liquid
n	n-th channel
out	outer
restored	calculated value
v	vapor
w	wall